Studies into measuring the Higgs CP-state in $H \to \tau\tau$ decays at ATLAS

Dissertation
zur
Erlangung des Doktorgrades (Dr. rer. nat.)
der
Mathematisch-Naturwissenschaftlichen Fakultät
der
Rheinischen Friedrich-Wilhelms-Universität Bonn

von
Maike Christina Hansen
aus
Köln

Bonn, Mai 2020

Dieser Forschungsbericht wurde als Dissertation von der Mathematisch-Naturwissenschaftlichen Fakultät der Universität Bonn angenommen und ist auf dem Hochschulschriftenserver der ULB Bonn unter `https://nbn-resolving.org/urn:nbn:de:hbz:5-59020` elektronisch publiziert.

1. Gutachter:	Prof. Dr. Klaus Desch
2. Gutachter:	Prof. Dr. Ian Brock

Tag der Promotion:	29.06.2020
Erscheinungsjahr:	2020

Abstract

Since the discovery of the Higgs boson in 2012, experimental particle physics made large efforts to measure all properties of the new particle to characterise all its properties as precisely as possible. So far, all observations of the Higgs boson are compatible with the predictions by the Standard Model (SM). However, not all properties are measured with sufficient precision. This thesis studies the Higgs bosons behaviour under Charge-Parity (CP) transformation in its decay to two τ leptons using $36.1\,\mathrm{fb}^{-1}$ of LHC data recorded by the ATLAS experiment in 2015 and 2016. A violation of the CP symmetry is one of the three Sakharov criteria to explain the dominance of matter over antimatter observed in our Universe today. However, the CP violation observed in the quark and lepton sectors of the SM is yet insufficient to explain this imbalance. Therefore, an observation of a new source of CP violation in the Higgs sector would be of particular importance to address this open question in physics. At the same time, it would be a clear sign of new physics beyond the SM, which predicts only one pure CP-even Higgs boson and a conservation of the CP symmetry in the Higgs boson production and decays. In this dissertation the CP state of the Higgs boson is measured in dihadronic $H \to \tau\tau$ decays from the angle φ^*_{CP} between the two τ decay planes. Any deviation from the CP-even nature of the SM Higgs boson would appear as a phase shift in the angular distribution. The presented approach is model-independent and allows for a direct measurement of CP violation in the Higgs coupling to fermions, which makes it unique among other Higgs CP measurements performed at the LHC. Another important part of this thesis is the validation of the applied methods in $Z \to \tau\tau$ decays. The Higgs CP measurement benefits substantially from the τ particle flow reconstruction developed by the ATLAS collaboration for run 2. This dissertation also comprises studies on improving the particle flow method applied to jets. Finally, a maximum likelihood fit is performed to determine the CP-mixing angle ϕ_τ in various signal and control regions. In this measurement, no sign of new physics has been observed. The measured CP-mixing angle of $\phi_\tau = \left(10^{+40}_{-35}\right)^\circ$ is compatible with the SM expectation of $\phi_\tau = 0^\circ$ within its uncertainties. This result allows to exclude a CP-mixing angle larger than 50° and smaller than -25° at 68% CL. A pure CP-odd Higgs boson can be excluded at 89% CL. Furthermore, estimates on the expected sensitivities are given for the full run 2 dataset and larger amounts of data, as they are expected by the high-luminosity LHC.

Contents

CHAPTER 1

Introduction

The first run of the Large Hadron Collider (LHC) 2010-2012 with centre-of-mass energies of 7 and 8 TeV marked an unprecedented advancement in elementary particle physics in the 20th century. The Standard Model (SM) of particle physics has been completed with the discovery of the Higgs boson in 2012 by the ATLAS and CMS collaborations [1, 2]. Since then, many properties of the Higgs boson have been measured and all agree so far with the predictions made by the SM. With the second run period from 2015 to 2017, the LHC operated again at the energy frontier of particle physics. The higher luminosities of the second run period and the higher centre-of-mass energy of 13 TeV offer many new opportunities. Until today all Higgs couplings to gauge bosons and third generation fermions have been discovered, including the Higgs decay to two τ leptons. Nevertheless, there are several open questions in physics that are not answered by the SM. One of them is the domination of matter over antimatter observed in our Universe today. In 1967 Sakharov postulated three conditions which have to be fulfilled to explain this matter-antimatter-asymmetry. One condition is Charge-Parity (CP) violation [3–5]. The CP violation observed so far in the quark and lepton sectors of the SM is not large enough to explain the imbalance. The SM predicts a pure CP-even Higgs boson without any CP mixing or violation. However, prominent Beyond Standard Model (BSM) theories, such as the Minimal Supersymmetric Standard Model (MSSM) or the Two-Higgs-Doublet Model (2HDM) predict CP-even and CP-odd Higgs states. Therefore, it is interesting to measure the CP nature of the Higgs boson and thereby possibly discover new physics. Several measurements in $H \to VV$ [6, 7], tH, $t\bar{t}H$ [8, 9] and the H production in Vector-Boson-Fusion (VBF) [10, 11] have been performed at the LHC and set constraints on anomalous couplings of the Higgs boson, CP-even and CP-odd parameters or the CP-mixing angle. However, these constraints are not model-independent and still leave room for a possible BSM CP violation. The $H \to \tau\tau$ decay offers a unique possibility to study the Higgs boson's behaviour under CP transformation in a model-independent way, which is subject to this dissertation. In $H \to \tau\tau$ decays, the CP state of the Higgs boson can be accessed via transverse spin correlations of the two τ leptons. The CP-mixing angle ϕ_τ can be measured directly from a phase shift in the distribution of the angle φ^*_{CP} between the τ decay planes. In this thesis, two methods are presented to reconstruct the angle φ^*_{CP}: the Impact parameter method, applied to $\tau^\pm \to \pi^\pm \nu$ decays and the ρ decay plane method applied to $\tau^\pm \to \rho^\pm \nu \to \pi \pm \pi^0 \nu$ decays. In the scope of this thesis both methods have been implemented for an ATLAS Analysis, validated and applied to 36.1 fb^{-1} of LHC data recorded by the ATLAS experiment in 2015 and 2016 at a centre-of-mass energy of 13 TeV.

Since the reconstruction of the τ decay planes depends on the τ decay mode, a precise decay mode reconstruction is needed. Also, the reconstructed π^0 four vector is used in the ρ decay plane method. Both quantities are calculated using particle flow reconstruction for τ leptons, which has been developed by the

ATLAS collaboration for run 2. During the work for this thesis, I have also contributed to improvements in the particle flow method applied to jets. In this thesis measures for the performance of the jet particle flow algorithm are defined and the impact of modifications on the reconstruction performance and the reconstructed jet energy resolution are studied.

Furthermore, a measurement of transverse spin correlations in $Z \to \tau\tau$ events is discussed. If the analysed phase space is divided into two regions based on the angle between the negatively charged pion from the τ decay and production plane, a CP-even- and CP-odd-like φ^*_{CP} distribution is obtained in $Z \to \tau\tau$ events. In principle, this can be used as a calibration step for the Higgs CP analysis. However, due to specific trigger requirements in the 2016 data, only the 2015 dataset could be used for this measurement. With this small subset of events it turned out to be impossible to measure the modulation in the φ^*_{CP} distribution in all decay mode combinations and to do the calibration. In the scope of this thesis, the simulation of transverse spin correlations in the $Z \to \tau\tau$ Monte Carlo simulations is validated in a comparison of the results with theoretical calculations. A Z-validation region is constructed to yield the maximal asymmetry in the φ^*_{CP} distribution in $Z \to \tau\tau$ events and a comparison of ATLAS data and the predictions from MC simulations is performed using $\mathcal{L} = 3.21\,\mathrm{fb}^{-1}$ of ATLAS data. Finally, an alternative support trigger chain is suggested, which would allow for the proposed calibration with data from a future data-taking period.

A measurement of the CP-mixing angle in $H \to \tau\tau$ decays is performed using a binned maximum likelihood fit in various signal and control regions. The signal regions are similar to the ones used in the $H \to \tau\tau$ cross section measurement [12]. However, in this analysis only events with two 1-prong τ leptons are used and the signal regions are divided further based on the reconstructed τ decay mode combination. The control regions are used to determine the background normalisation factors r_Z and r_{QCD} for the two dominant background contributions coming from $Z \to \tau\tau$ and QCD multijet events. The fit procedure is validated using pseudo data and different configurations are compared to optimise the setup. Finally, the Higgs CP-mixing angle ϕ_τ is measured in the combined 2015 and 2016 dataset and exclusion limits are set on ϕ_τ. Additionally, estimates are given for expected sensitivities for the full run 2 dataset and larger amounts of data, which are planned to be achieved by the high-luminosity LHC.

This thesis is structured as follows: The theoretical background is introduced in Chapter 2, followed by a description of the experimental setup including the studies on the jet particle flow reconstruction in Chapter 3. Next, a description of the methods and their theoretical foundations used to measure the Higgs CP-state is given in Chapter 4. The event selection for the Higgs CP-measurement and the studies on a suitable Z-validation region for a measurement of transverse spin correlations in $Z \to \tau\tau$ decays is discussed in Chapter 5. The analysed data and simulations, including a validation of the CP sensitive variables in simulations are described in Chapter 6. The measurement of transverse spin correlations in $Z \to \tau\tau$ events and the proposed support trigger chain is presented in Chapter 7. Finally, the measurement of the Higgs CP-mixing angle in data is presented in Chapter 8 including a description of all relevant systematic uncertainties and a validation of the fit procedure using pseudo data. All results and conclusions are summarised in Chapter 9.

CHAPTER **2**

Theoretical background

2.1 The Standard Model of particle physics

The Standard Model (SM) of particle physics comprises all known elementary particles and describes their interactions except gravity. All visible matter is composed of atoms, each consisting of a nucleus surrounded by electrically negatively charged electrons. The nucleus itself is composed of electrically positively charged protons and neutral neutrons. Unlike the electron, neutron and proton are not elementary. They consist of three smaller particles called quarks. The proton is made of two up quarks and one down quark, while the neutron is composed of one up quark and two down quarks. In nuclear decays, protons and neutrons can be transformed into each other through $\beta^{\pm}$ decays. For example in the β^{-} decay, a down quark is transformed into an up quark through a W^{-} boson, which then decays to an electron (e^{-}) and an anti electron-neutrino ($\bar{\nu}_e$). These four particles (up quark, down quark, e^{-} and $\bar{\nu}_e$) form the first generation of matter particles in the SM, displayed as the first column in Fig. 2.1. In addition, there exist two copies of this first generation particles, corresponding to the second and third column in Fig. 2.1. They differ from the particles in the first column only in the particle mass while all other properties are identical compared to the particles in the first column. In total this sums up to 12 matter particles, which can be grouped by their properties into two sets of 6 particles each: quarks (up, down, charm, strange, top, bottom) and leptons (e^{-}, vν_e, μ^{-}, ν_μ, τ^{-}, ν_τ). One of the properties is the charge of a particle. There exist three different types of charges: electric charge, colour charge, and the weak hypercharge. Quarks are the only matter particles which carry colour charge. They have an electric charge of $+2/3$ for up-type quarks and $-1/3$ for down-type quarks and a weak hypercharge of $+1/3$. Leptons are also elementary matter particles but do not carry colour charge. The weak hypercharge is -1 and their electric charge is 0 for the neutrinos and -1 for the charged leptons like the electron. Another property of the particles is the spin: matter particles have a spin of $1/2$ and thus are referenced as fermions[1]. For spin $1/2$ particles there exist always two possible spin states: up and down. Furthermore, for each fermion, there exist an antifermion, with the same mass, but opposite electric charge and parity. In case of the electron, this particle is called positron and was observed for the first time in cosmic ray tracks in a cloud chamber by Andersen in 1933 [14]. The existence of antiparticles provides a physical interpretation for the negative energy solutions to the Dirac equation. The Dirac equation supplies the mathematical framework for the relativistic quantum mechanics of spin-half particles. Negative energy solutions to this equation cannot be avoided or ignored, because quantum mechanics requires a complete set of basic states to span the full vector-space. Our Universe today consists nearly only of matter particles. If an antiparticle is produced, it annihilates shortly after the production with its corresponding

[1] A fermion is a particle with half-integer spin.

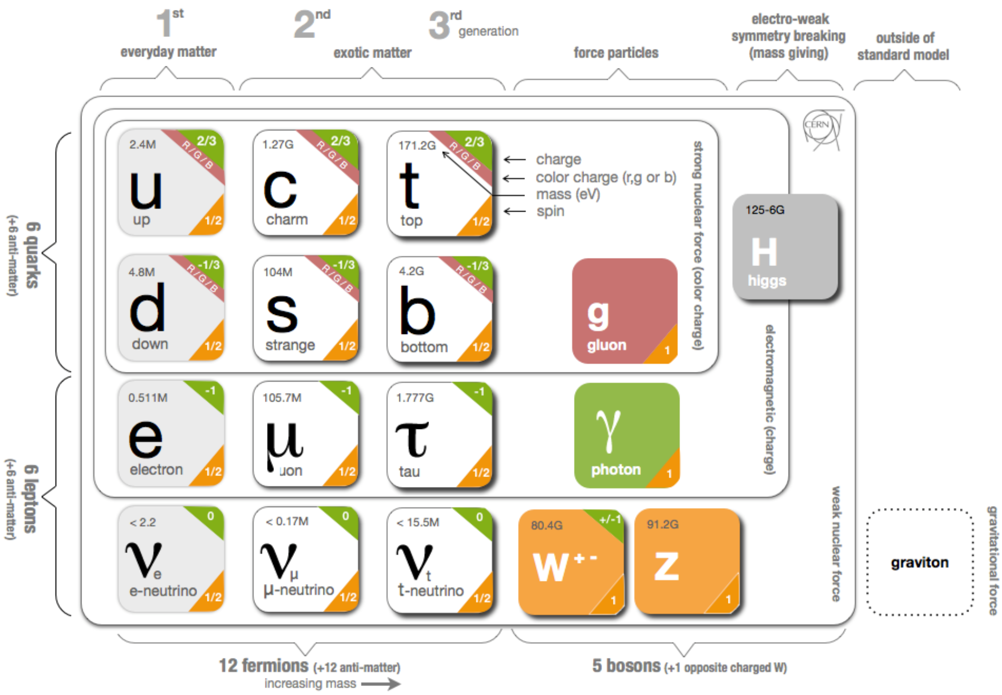

Figure 2.1: The Standard Model of particle physics [13].

antiparticle. The number of elementary matter particles in this world is conserved. Hence, one can produce a new elementary particle only together with a corresponding antiparticle. In order to explain the imbalance of matter and antimatter in our universe today, one needs to assume that initially there has been a small domination of matter over antimatter particles. The necessary conditions for that are explained in more detail in Section 2.2.4. One of them is CP-violation and an important motivation for this thesis is to find and observe further sources of CP-violation.

All matter particles described above interact with each other through different types of interactions. The SM of particle physics comprises three interactions: the weak interaction, the electro-magnetic interaction and the strong interaction. For each interaction, the SM also contains corresponding force-carrier particles listed in Fig. 2.1 which have all integer spins and are hence referenced as bosons[2]. The photon is the exchange boson of the electromagnetic force and couples to all electrically charged particles. The gluon is the exchange boson of the strong force and couples to all particles which carry colour charge, i.e. all quarks and the gluons themselves. $W^{\pm}$ and Z bosons transmit the weak force and thus couple to all quarks and leptons. The Higgs boson couples proportional to the mass of a particle and thus, in the SM, couples to all particles except for the neutrinos. So far, gravity is not included in the SM and no exchange particle has been discovered yet. Hence, Fig. 2.1 includes a graviton with dashed lines as the gravitational exchange particle. All force-carrier particles have spin 1, while the Higgs boson has spin 0. The interactions between the fermions mediated by the respective bosons are formulated in quantum field theories. In case of electromagnetism, the electrostatic force is described by quantum electrodynamics (QED) developed by Tomonaga [15], Schwinger [16], and Feynman [17] in the 1940's.

[2] A boson is a particle with integer spin.

The weak force was originally described by Fermis theory in 1934 [18]. However, Fermis theory did not include massive exchange bosons at that time. They were introduced later by Glashow [19], Salam [20] and Weinberg [21] in the 1960's by the theory of electroweak unification. The strong force is described by quantum chromodynamics (QCD), developed in the 1970' developed by Fritzsch, Gell-Mann and Leutwyler [22]. In the same year, Gross, Wilczek [23] and Politzer [24] discovered the principle of asymptotic freedom, for which they obtained the nobel prize in physics in 2004.

The SM is formulated as a quantum field theory obeying a $SU(3) \otimes SU(2) \otimes U(1)$ symmetry. Particles are described as fields and the Lagrange density is then constructed from the kinetic and potential energies. Hence, the equations of motion are given by the corresponding Euler-Lagrange equations in Eq. (2.1)

$$\frac{\partial \mathcal{L}}{\partial \phi} - \frac{\partial}{\partial x_\mu}\left(\frac{\partial \mathcal{L}}{\partial \phi / \partial x_\mu}\right) = 0, \tag{2.1}$$

whereas $\mathcal{L}$ represents the Lagrange density, ϕ describes the field and x_μ is the spatial coordinate. Lagrange density of the SM has to describe all matter particles and their interactions. It has to be renormalisable and invariant under local gauge and Poincaré transformations.

Renormalisation is a technique in quantum field theory to treat infinities. The renormalisation group specifies relationships between the values of parameters at large scales with the ones at small scales. For example, in QED the interaction strength between electron and photon has the constant value e_0, which results from the coupling associated to the QED vertex. However, the experimentally determined value of e (corresponding to a fine structure constant of $\alpha = \frac{1}{137}$) is an effective strength which contains the sum over all relevant higher order Feynman diagrams in QED. This includes also loops in the photon propagators. Each loop is included as an integral over the four momenta of the contributing particles. This leads to infinite results. However, these infinities can be absorbed in the definition of the electron charge. Due to the local gauge invariance of the theory, all loop corrections to the in/out-going fermions cancel out to all orders in perturbation theory (Ward-identity).

2.1.1 Quantum electrodynamics

Quantum electrodynamics (QED) describes the interactions between electrically charged particles and the photon. The symmetry group of this interaction is $U(1)$. The Lagrange density is required to remain invariant under a local $U(1)$ phase transformation, i.e. it should not change under the following transformation

$$\psi(x) \rightarrow \phi(x) = e^{ie\alpha(x)}\psi(x), \tag{2.2}$$

whereas $\psi(x)$ denotes a fermionic field, e stands for the electron charge and $\alpha(x)$ is a function which specifies the local phase at each point in space x. To establish the invariance under the local phase transformation, a bosonic field A_μ is introduced with a term $e\bar{\psi}\gamma_\mu A_\mu \psi$ in the Lagrange density. Here γ denote the Dirac γ-matrices. This field A_μ transforms as

$$A_\mu \rightarrow A'_\mu = A_\mu + \frac{1}{e}\partial_\mu \alpha(x), \tag{2.3}$$

under the local gauge transformation. A_μ corresponds to the mediating particle of the interaction, i.e. the photon. The resulting Lagrange density for fermionic fields ψ and $\bar{\psi}$, is then given as

$$\mathcal{L}_{QED} = i\bar{\psi}\gamma_\mu D^\mu \psi - m\bar{\psi}\psi - \frac{1}{4}F^{\mu\nu}F_{\mu\nu}, \tag{2.4}$$

whereas $D_\mu = \partial_\mu - ieA_\mu$ is the covariant derivative which transforms as $D_\mu\Psi \to D'_\mu\Psi' = e^{i\alpha(x)}\left(D_\mu\Psi\right)$. $F_{\mu\nu}$ is the field strength tensor defined as

$$F_{\mu\nu} = \partial_\mu A_\nu - \partial_\nu A_\mu. \tag{2.5}$$

As described before, in the renormalisation of QED, photon loops have to be considered and absorbed in the definition of the electric charge. The effective electric charge then depends on momentum transfer by the photon q^2 and can be expressed in terms of the one loop photon self-energy corrections $\Pi(q^2)$ as

$$e^2(q^2) = \frac{e_0^2}{1 - e_0^2\Pi(q^2)}. \tag{2.6}$$

Since scattering cross sections are finite, this expression is finite even if $\Pi(q^2)$ is divergent. Given that the physical electron charge is known at some scale $q^2 = \mu^2$, the exact relation for e^2 is given as

$$e^2(q^2) = \frac{e^2(\mu^2)}{1 - e^2(\mu^2)\cdot\left(\Pi(q^2) - \Pi(\mu^2)\right)}. \tag{2.7}$$

Using $\alpha(q^2) = e^2(q^2)/4\pi$ the scale-dependence of the QED coupling constant α can be predicted to be

$$\alpha(q^2) = \frac{\alpha(\mu^2)}{1 - \alpha(\mu^2)\frac{1}{3\pi}\ln\left(\frac{q^2}{\mu^2}\right)}, \tag{2.8}$$

as also described in [25]. Measurements from atomic physics yield a value of $\alpha \approx \frac{1}{137}$ at $q^2 \approx 0$, while measurements from the OPAL experiment at the LEP accelerator yield $\alpha \approx \frac{1}{127.4}$ at a center-of-mass energy of $\sqrt{s} = 193\,\mathrm{GeV}$ [25]. This confirms the predicted running/ increase of the coupling constant with increasing q^2.

2.1.2 The weak interaction and electroweak unification

The weak interaction was first described in Fermi's theory of the β decay in 1932 [18]. He described the neutron decay $n \to pe^-\bar{\nu}_e$ as a 4-point interaction with a matrix element proportional to the Fermi constant $G_F = 1.166 \times 10^{-5}\,\mathrm{GeV}^{-2}$ [26]. However, with this approach he could neither explain massive exchange bosons nor the parity violating behaviour of the weak interaction. It was found that the weak interaction differentiates between left-handed and right-handed fermions. In particular, the $W^\pm$ bosons couple only to left-handed but not to right handed fermions. The Z^0 boson couples to both, left- and right-handed fermions, but with different strength.

Particle physics intends to develop a complete and unified description of all elementary particles and their interactions. In the 1960's, Glashow, Salam and Weinberg proposed the GSW[3] model that unified electromagnetism and the weak interaction [19–21]. Their GSW model predicts, besides $W^\pm$ and photon, an additional weak, neutral current Z^0. This weak, neutral current was experimentally confirmed in 1973 in neutrino scattering experiments by the Gargamelle collaboration [27, 28]. As a consequence, in 1979, Glashow, Salam and Weinbgerg were awarded with the nobel prize in physics for their electroweak unification theory [29]. In 1983, $W^\pm$ [30, 31] and Z [32, 33] bosons were discovered in a proton-antiproton collider at CERN by the UA1 and UA2 collaborations. The weak interaction is

[3] Glashow-Salam-Weinberg

described as a $SU(2)$ gauge group, the electromagnetic interaction by an $U(1)$ symmetry. The unified model is mathematically described by an $SU(2) \otimes U_Y(1)$ gauge group, with corresponding gauge bosons W^1, W^2, and W^3 of weak isospin from $SU(2)$ and the B boson of weak hypercharge (Y) from $U_Y(1)$, which remains unchanged under a $SU(2)$ transformation. The model contains doublets of left handed particles $L = \begin{pmatrix} \nu_L \\ e_L \end{pmatrix}$ and singlets of right handed particles $R = e_R$. The hypercharge is then defined as $Y(L) = -1$ and $Y(R) = -2$ and it is related to the electric charge Q as

$$Q = T_L^3 + \frac{Y}{2}, \tag{2.9}$$

with T_L^3 being the third component of the weak isospin.

All gauge bosons and particles are however massless and acquire mass through electroweak symmetry breaking introduced by the Higgs mechanism, as described in Section 2.1.4. The physical W^+ and W^- bosons are associated with the two charged gauge bosons W^1 and W^2, while Photon and Z-Boson, which are both neutral currents, can be written as linear combinations of the W^3 and B boson.

The electroweak unification relates the couplings of the electromagnetic and weak interactions, e and g, with the mixing angle θ_W:

$$e = g \sin\theta_W = g' \cos\theta_W \tag{2.10}$$

The relation and can be obtained e.g. from the interactions of electron and electron neutrino.

2.1.3 Quantum chromodynamics

Interactions between particles that carry colour charge are describe by the strong interaction. In quantum chromodynamics (QCD), unlike in QED, the exchange boson (the gluon) carries colour charge itself, allowing gluon-gluon self-interactions. The symmetry group of QCD is $SU(3)$. Similarly to the construction of the QED Lagrangian, invariance under a local SU(3) gauge transformation is required. The local gauge transformation for QCD is given as

$$\psi(x) \to \psi'(x) = e^{ig_s\alpha(x)\cdot\hat{T}}\psi(x), \tag{2.11}$$

where g_s denotes the strong coupling constant and $\hat{T}$ are the eight generators of the SU(3) symmetry group, which relate to the Gellman Matrices as

$$T^k = \frac{1}{2}\lambda^k. \tag{2.12}$$

Due to the $SU(3)$ generators being 3×3 matrices, the wave function shows 3 additional degrees of freedom, which is represented by three different colour states, namely red, green, and blue. In order to guarantee invariance under local phase transformation, eight gauge fields $G_\mu^k(x)$, $k \in (1, ..., 8)$ corresponding to eight gluons are introduced. Under the local gauge transformation, they transform as

$$G_\mu^k \to G_\mu^{'k} - \frac{1}{g}\partial_\mu\alpha^k - g_s f_{ijk}\alpha_i G_\mu^j. \tag{2.13}$$

Here, f_{ijk} denotes for the structure constant of $SU(3)$. The QCD part of the Lagrange density can thus be written as

$$\mathcal{L}_{QCD} = \bar{q}\left(i\gamma^\mu\partial_\mu - m\right)q - g\left(\bar{q}\gamma^\mu T_a q\right)G_\mu^a - \frac{1}{2}G_{\mu\nu}^k G_k^{\mu\nu} \tag{2.14}$$

with the field tensor $G^k_{\mu\nu}$ defined as

$$G^k_{\mu\nu} = \partial_\mu G^k_\nu - \partial_\nu G^k_\mu - f_{klm} G^l_\mu G^m_\nu. \tag{2.15}$$

The generators of $SU(3)$ do not commute, which gives rise to gluon self-interactions. These self-interactions are also believed to be responsible for the so called colour confinement stating that "no objects with non-zero colour charge can propagate as free particles" [25]. If two quarks are pulled apart they interact by the exchange of virtual gluons. The fact that gluons carry colour charge leads to an attractive force between them. The gluon field lines are squeezed into a tube resulting in a constant energy density in the gluon field. Thus, the energy stored in the gluon field is proportional to the distance between the two quarks. As a consequence, separating the two quarks requires an infinite amount of energy. This is the reason why quarks are always confined in colourless hadrons, which can be formed either by three quarks, called baryons, or a combination of a quark and an antiquark, called mesons. Also, gluons can only be found confined in colourless objects and cannot propagate over macroscopic distances due to their colour charge.

The initially free, highly energetic quarks or gluons resulting from high energy collisions start forming colourless objects immediately after their production. Therefore, in a detector they cannot be observed as single particles but rather as bundles of hadrons flying into a similar direction. These bundles are called *jets*. They form when originally coloured quarks or gluons transform into several colourless objects, referred to as *hadronisation process*.

The renormalisation condition in QCD predicts a running of the strong coupling constant α_s, similar to the one in QED. However, one major difference is that gluon-gluon self-interactions are possible, which is not the case for photons in QED. This leads to additional loop diagrams contributing to the gluon propagator. These bosonic loops contribute with the opposite sign with respect to pure fermionic loops. Thus, the bosonic loops give positive contributions to the q^2 dependence of α_s as

$$\alpha_s(q^2) = \frac{\alpha_s(\mu^2)}{1 + B\alpha_a(\mu^2)\ln\left(\frac{q^2}{\mu^2}\right)}, \tag{2.16}$$

where $B = \frac{11N_c - 2N_f}{12\pi}$ with N_c being the number of colours and N_f being the number of quark flavours. The + instead of − sign in the denominator leads to a decreases instead of an increase of α_s with increasing energy/momentum transfer q^2, compared to the QED running coupling-constant in Eq. (2.8). This antiproportional relation between α_s and q^2 has also been measured in various experiments summarised in [26] and agrees with the prediction from QCD. At low energies, i.e. $|q| \propto 1\,\mathrm{GeV}$, α_s is large and perturbation theory cannot be used. In this case, quarks are confined in bound objects (hadrons). However, in modern collider experiments like the LHC, energies of $|q| \propto 100\,\mathrm{GeV}$ or more are reached and in this case one finds $\alpha_s \propto 0.1$. Hence, perturbation theory can be used again and quarks represent quasi-free particles. This effect is called asymptotic freedom.

At the LHC protons are brought to collision with sufficiently large energies such that the quarks and gluons inside the protons (called partons) can interact with each other. The probability to find a certain parton type i within the proton at a momentum fraction $x_i = \frac{p_i}{P_P}$ of the proton's total momentum P_P is described by Parton Distribution Functions (PDFs). The quark and gluon PDFs are shown in Fig. 2.2 as a function of the momentum fraction x at two different scales $\mu^2 = 10\,\mathrm{GeV}^2$ (a) and $\mu^2 = 10 \times 10^4\,\mathrm{GeV}^2$ (b) with $\alpha_s\left(M_Z^2\right) = 0.118$. At large x the PDFs of the valence quarks, i.e. up and down quarks, are the most probable ones. These carry the largest momentum fraction of the proton. At small values of x the gluon PDFs dominate.

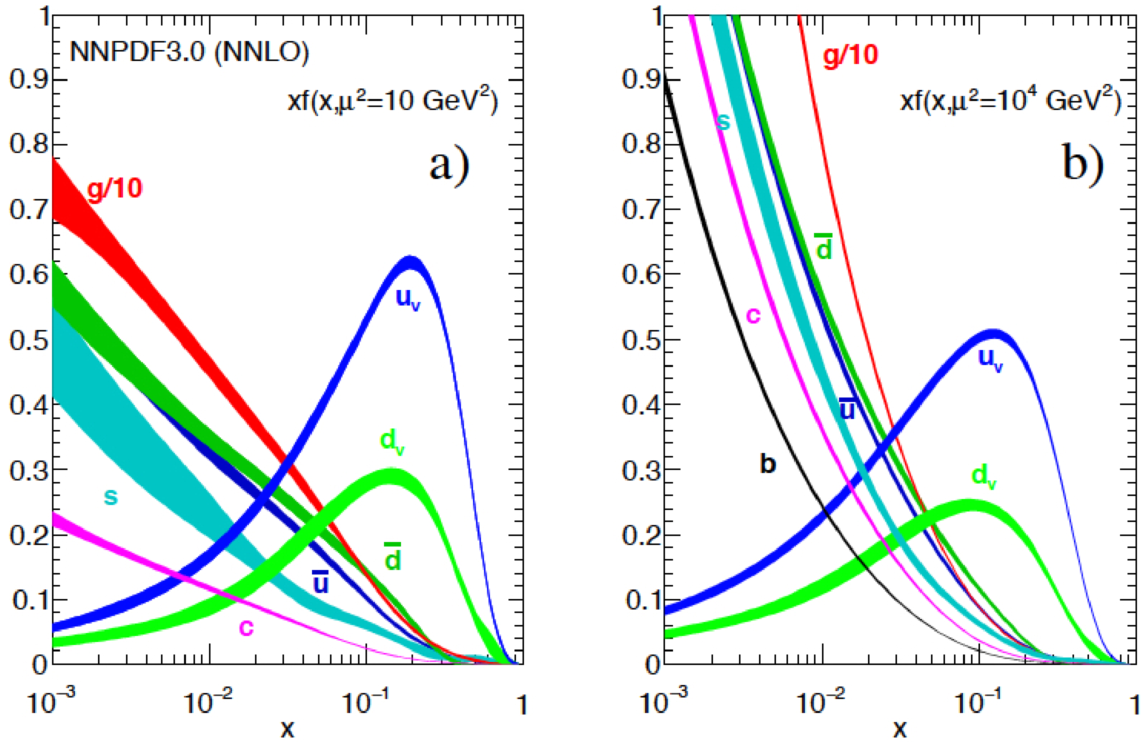

Figure 2.2: The parton distribution functions obtained from a global fit to experimental data using the NNLO NNPDF3.0 parametrisation. The bands denote x times the unpolarised parton distributions $f(x)$ at two different scales $\mu^2 = 10\,\text{GeV}^2$ (a) and $\mu^2 = 10 \times 10^4\,\text{GeV}^2$ (b) with $\alpha_s\left(M_Z^2\right) = 0.118$ [26].

2.1.4 Electroweak symmetry breaking and the Higgs mechanism

The Higgs mechanism, proposed by R.Brought, F.Englert and P.Higgs in 1964 [34–36], allows to explain the non-zero masses of the weak exchange bosons. It breaks electroweak symmetry by introducing a new self-interacting $SU(2)_L$ doublet of complex scalar fields Φ given in Eq. (2.17) with weak hypercharge $Y = 1$, which is related to the electric charge as stated in Eq. (2.9).

$$\phi = \begin{pmatrix} \phi+ \\ \phi^0 \end{pmatrix} = \begin{pmatrix} \phi_1^+ + i\phi_2^+ \\ \phi_1^0 + i\phi_2^0 \end{pmatrix} \tag{2.17}$$

This new doublet (the Higgs doublet) introduces four additional degrees of freedom. After electroweak symmetry breaking, three of them correspond to massless Goldstone bosons, which, by mixing with the gauge fields, produce the three masses of the weak exchange bosons (W^+, W^-, Z^0). The remaining degree of freedom leads to the postulation of a neutral scalar particle, the Higgs boson. The Lagrangian of the Higgs doublet is given as

$$\mathcal{L} = T - V = (D_\mu\phi)^\intercal(D^\mu\phi) - (\mu^2\phi^\intercal\phi + \lambda(\phi^\intercal\phi)^2). \tag{2.18}$$

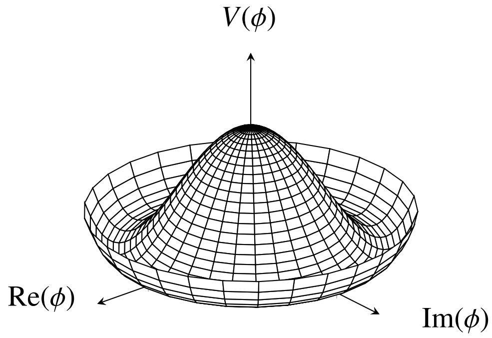

Figure 2.3: Mexican-hat shape of the Higgs potential $V(\Phi)$, whereas Φ denotes the scalar field.

The potential $V(\phi)$ has two free parameters μ and λ and corresponds to the Higgs field. The covariant derivative D_μ is defined as

$$D_\mu = \partial_\mu - i\left(g'\frac{Y}{2}B_\mu + g\frac{\vec{\tau}}{2}\vec{W}_\mu\right). \tag{2.19}$$

The shape of the Higgs potential $V(\phi)$ is sketched in Fig. 2.3. The potential $V(\Phi)$ needs to be bounded from below to have a global minimum, which requires $\lambda > 0$. Additionally, $\mu^2 < 0$ is required to have a non-zero vacuum expectation value (VEV), inducing spontaneous symmetry breaking. After spontaneous symmetry breaking, the photon has to remain massless. In consequence, only the neutral scalar field can have a non-zero vacuum expectation value, corresponding to the minimum of the potential ϕ_{min}, which is given by

$$\phi_{\text{min}} = \begin{pmatrix} 0 \\ \frac{1}{\sqrt{2}v} \end{pmatrix}. \tag{2.20}$$

Here, $v^2 = \frac{\mu^2}{\lambda}$ represents the VEV of the respective scalar field. This allows to expand the remaining neutral scalar field around the minimum, it can be parametrised as

$$\phi_{\text{min}} = \exp\left(i\frac{\vec{\tau}}{2}\cdot\frac{\vec{\chi}}{v}\right)\frac{1}{\sqrt{2}}\begin{pmatrix} 0 \\ v+H \end{pmatrix} \approxeq \frac{1}{\sqrt{2}}\left(1+\frac{i}{2}\frac{\vec{\tau}\cdot\vec{\chi}}{v}\right)\begin{pmatrix} 0 \\ v+H \end{pmatrix} = \frac{1}{\sqrt{2}}\begin{pmatrix} 0 \\ v \end{pmatrix} + \frac{1}{2\sqrt{2}}\begin{pmatrix} \chi_2 + i\chi_1 \\ 2H - i\chi_3 \end{pmatrix}, \tag{2.21}$$

with the Goldstone bosons χ_{1-3}, which can be gauged away, and H representing the Higgs boson. Afterwards, a gauge transformation is applied to ϕ eliminating all dependencies of ϕ except for the ones on v and H

$$\phi \to \exp\left(-i\sum_i \frac{\tau^i}{2}\alpha^i(x)\right)\phi = \frac{v+H}{\sqrt{2}}\begin{pmatrix} 0 \\ 1 \end{pmatrix}, \tag{2.22}$$

with $\alpha^i = \chi^i(x)/v$.

From this, and using the covariant derivative given in Eq. (2.19), the Lagrangian is presented as

$$\mathcal{L} = \left|\left(\partial_\mu - ig'\frac{v}{2}B_\mu - ig\frac{\vec{\tau}}{2}\vec{W}_\mu\right)\frac{v+H}{\sqrt{2}}\begin{pmatrix} 0 \\ 1 \end{pmatrix}\right|^2 - \mu^2\left(\frac{v+H}{\sqrt{2}}\right)^2 - \lambda\left(\frac{v+H}{\sqrt{2}}\right)^4. \tag{2.23}$$

The physical $W^\pm$ are defined as linear combinations of the gauge bosons $W_\mu 1, 2$

$$W_\mu^\pm = \frac{1}{\sqrt{2}}\left(W_\mu^{(1)} \pm iW_\mu^{(2)}\right), \tag{2.24}$$

while the Z boson (Z_μ) and the photon (A_μ) are admixtures of the gauge bosons W_μ^3 and B_μ as already mentioned in Section 2.1.2

$$Z_\mu = \cos\theta_W W_\mu^{(3)} - \sin\theta_W B_\mu, A_\mu = \sin\theta_W W_\mu^{(3)} + \cos\theta_W B_\mu, \tag{2.25}$$

where θ_W represents the weak mixing angle [25]. Using these definitions, the kinetic energy term in the Lagrangian can be rewritten as

$$\frac{1}{2}\left(\partial_\mu H\right)(\partial^\mu H) + \frac{g^4}{4}(v+H)^2\left(W_\mu^- W^{\mu+} + \frac{1}{2\cos^2\theta_W} Z_\mu Z^\mu\right). \tag{2.26}$$

This allows to identify the mass terms for the physical vector bosons in Eq. (2.26) and to deduce the following relations for the W and Z boson masses, respectively:

$$\begin{aligned} M_W &= \frac{1}{2} g v \qquad \text{and} \\ M_Z &= \frac{g v}{2\cos\theta_W} = \frac{M_W}{\cos\theta_W}. \end{aligned} \tag{2.27}$$

In addition, the potential term of the Lagrangian in Eq. (2.23) is rewritten as

$$V = \frac{1}{2}\left(2\mu^2\right)H^2 + \frac{1}{4}\mu^2 v^2\left(\frac{H^3}{v^3} + \frac{H^4}{v^4} - 1\right). \tag{2.28}$$

The first term in Eq. (2.28) appears like a mass term of a scalar field (the Higgs field). Thus, the Higgs mass can be related to the parameters μ and λ as

$$M_H = \sqrt{2}\mu = v\sqrt{2\lambda}. \tag{2.29}$$

The masses of the SM fermions except for the neutrinos are introduced through coupling terms of the scalar Higgs field to the fermion fields. These are added to the Lagrangian as Yukawa couplings, i.e. interactions of fermions with a scalar (Higgs) field. The Yukawa coupling part of the Lagrangian for leptons is given as

$$L^l_{\text{Yukawa}} = -g_l\left\{(\bar{\nu},\bar{e})_L\begin{pmatrix}\phi^+\\ \phi^0\end{pmatrix}e_R + \bar{e_R}\left(\phi^{+*},\phi^{0*}\right)\begin{pmatrix}\nu\\ e\end{pmatrix}_L\right\}. \tag{2.30}$$

Inserting the Higgs doublet as given in Eq. (2.22) in the unitary gauge into the Yukawa part of the Lagrangian, it follows

$$L^l_{\text{Yukawa}} = -g_l\frac{v}{\sqrt{2}}\bar{e_L}e_R - g_l\frac{h}{\sqrt{2}}\bar{e}_R e_L. \tag{2.31}$$

The first term in Eq. (2.31) refers to the lepton coupling to the Higgs field with a non-vanishing VEV. It constitutes a lepton mass-term and relates the lepton mass to its Yukawa coupling as $m_l = g_l\frac{v}{\sqrt{2}}$. The second term in Eq. (2.31) refers to the coupling of the lepton to the Higgs boson itself. The quark Yukawa part of the SM Lagrangian contains the Higgs coupling to quarks and their mass terms, which are constructed in an analogous way. However, since the non-zero VEV occurs only in the Higgs fields lower component, the used combination of fields $\bar{L}\Phi R + \bar{R}\Phi^\intercal L$ will only generate mass terms for the lower components of the $SU(2)_L$ doublets, i.e. the down-type quarks. Hence, in order to introduce mass terms for the up-type quarks, a different combination is needed. These mass terms can simply be added by taking the conjugate doublet Φ_c defined as

$$\Phi_c = -i\sigma_2\Phi* = \begin{pmatrix} -\phi^{0*} \\ \phi^- \end{pmatrix}, \tag{2.32}$$

with σ_i representing the pauli-matrices. As a consequence, the Yukawa coupling part for up-type quarks follows from the combination $g_f\left[\bar{L}\Phi_c R + \bar{R}\Phi_c^\intercal L\right]$ as

$$L^u_{\text{Yukawa}} = -g_u\frac{v}{\sqrt{2}}\bar{u}_L u_R - g_u\frac{h}{\sqrt{2}}\bar{u}_R u_L. \tag{2.33}$$

The fermion Yukawa couplings $g_{l,u,d}$ are free parameters of the SM and not predicted by the theory of electroweak symmetry breaking. However, they are calculated from the experimentally determined fermion masses. The SM VEV is related to the Fermi constant as $v = (\sqrt{2}G_f)^{-1/2} \approxeq 246\,\text{GeV}$ [26].

Finally, the interaction part of the electroweak Lagrangian is expressed as

$$\mathcal{L}^{int}_{\text{EW}} = -g\bar{\Psi}\gamma_\mu\frac{\vec{\tau}}{2}\Psi\vec{W}_\mu - g'\bar{\Psi}\gamma_\mu\frac{Y}{2}\Psi B_\mu. \tag{2.34}$$

2.1.5 The SM Higgs boson

The Standard Model Higgs boson H is a CP-even scalar particle of spin 0. It carries no electric charge and couples to all fermions except for neutrinos with a strength proportional to their masses. The Higgs boson mass itself is a free parameter of the SM, which relates to the VEV as $m_H = 2\lambda v^2$. It has been discovered at the LHC in 2012 by the ATLAS and CMS collaborations [1, 2] and its mass was measured to be $m_H \approx 125\,\text{GeV}$ [26]. The initial discovery of the Higgs boson in July 2012 stems from measurements in the $H \to \gamma\gamma$ and $H \to ZZ* \to 4l$ channels [1, 2]. In ATLAS data from LHC run 2, acquired at a centre-of-mass (CMS) energy of $\sqrt{s} = 13\,\text{TeV}$, the measured significance of the signal strength was 4.4σ in the $H \to \tau\tau$ decay channel [37]. Combining these data with the ones from LHC run 1, acquired at a center-of-mass energy of $\sqrt{s} = 7\,\text{TeV}$ to $8\,\text{TeV}$, yielded a significance of 6.4σ. The CMS collaboration reported a significance of 5.9σ in the $H \to \tau\tau$ decay channel using a combination of the LHC run 1 and run 2 data [38]. In the $H \to b\bar{b}$ channel, an excess was detected at a significance of 2.6σ [26].

Higgs production at the LHC

The main leading order Higgs production mechanisms at a proton-proton collider such as the LHC are gluon-gluon fusion(ggF), vector-boson fusion(VBF) and associated production of a Higgs boson with a vector boson or with a pair of a top and antitop quarks. The Feynman diagrams for these processes are displayed in Fig. 2.4. The coupling of the Higgs boson to the massless gluons is mediated by the exchange of a virtual fermion, mostly a top-quark, since this is the heaviest fermion in the SM and the Higgs boson coupling strength is proportional to the mass of the respective fermion. The production cross sections of a 125 GeV Higgs bosons in pb at the LHC at a CMS energy of $\sqrt{s} = 13\,\text{TeV}$ are listed in Table 2.1.

Higgs decay

The Higgs boson can decay to all massive SM particles. Since coupling strength and branching ratio are proportional to the mass of the decay particle, the Higgs boson decays most frequently to the most massive particles. At the LHC, the dominant Higgs decay modes are $H \to b\bar{b}$ and $H \to WW*$. These

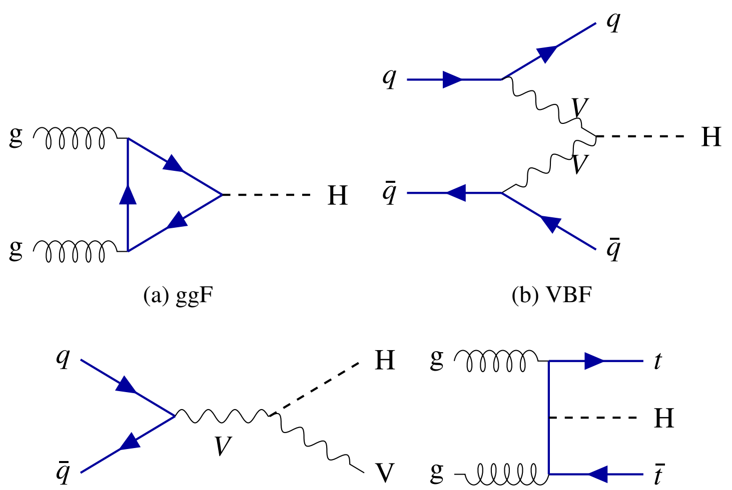

(a) ggF (b) VBF

(c) VH (d) $t\bar{t}$H

Figure 2.4: Feynman diagrams of the main Higgs production processes at the LHC. Here V stands for the vector bosons of the weak interaction i.e. $W^{\pm}$ or Z, g denotes the Gluon, H the Higgs boson, $q/\bar{q}$ a quark/antiquark and $t/\bar{t}$ top-/antitop-quark respectively.

ggF	VBF	WH	ZH	$t\bar{t}H$	total
$48.6 \pm 5\%$	$3.78 \pm 2\%$	$1.37 \pm 2\%$	$0.88 \pm 5\%$	$0.50^{+9\%}_{-13\%}$	55.1

Table 2.1: Higgs production cross sections at the LHC in pb at a centre-of-mass energy of 13 TeV and a Higgs mass of 125 GeV for the dominant leading order production processes [26].

are followed by $H \to gg$, $H \to \tau^+\tau^-$, $H \to c\bar{c}$ and, at much smaller amplitude, $H \to \gamma\gamma$, $H \to \gamma Z$ and $H \to \mu^+\mu-$. The branching ratios of the most prominent decay channels at the LHC are listed in Table 2.2 and the corresponding Feynman diagrams are shown in Fig. 2.5. This thesis focusses mainly on the $H \to \tau\tau$ decay channel with a branching ratio of 6.27×10^{-2}.

$H \to \gamma\gamma$	$H \to W^+W^-$	$H \to ZZ$	$H \to \tau^+\tau^-$	$H \to b\bar{b}$
2.27×10^{-3}	2.14×10^{-1}	2.62×10^{-2}	6.27×10^{-2}	5.84×10^{-1}

Table 2.2: Branching ratios of the most prominent Higgs decay channels at the LHC [26].

2.1.6 The τ lepton

In this thesis the Higgs boson CP properties are studied in its decays to two τ leptons. Hence, also the τ lepton is of special interest for this thesis. The τ lepton weights approximately $3500 \times m_e$ [25] and is the heaviest lepton in the SM. It was discovered in 1975 at the Stanford Linear Accelerator Centre (SLAC) [39] and decays through the weak interaction producing a τ neutrino and a W boson. The W boson further decays to a pair of leptons or a meson formed from the lightest quarks u, d and s. The lowest order Feynman diagrams for the decay of the τ lepton are sketched in Fig. 2.6. The τ branching fractions are summarised in Fig. 2.7. The τ lepton decays are distinguished by the number of charged

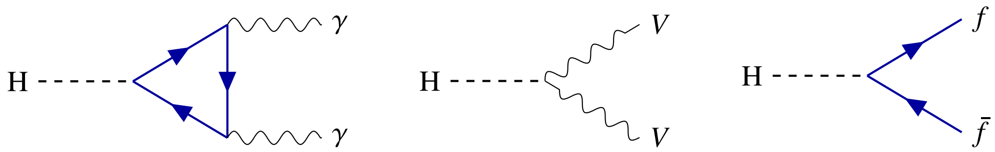

Figure 2.5: Lowest order Higgs decay channels. Here, H denotes the Higgs boson, V the vector bosons of the weak interaction ($W^{\pm}$ and Z) and f stand for any fermion ($\bar{f}$ for the corresponding antifermion) which has a non-zero mass in the SM.

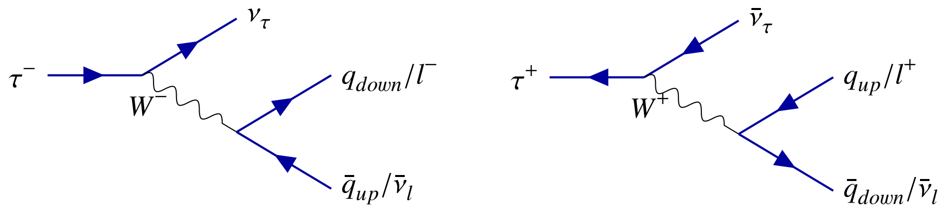

Figure 2.6: Lowest order Feynman diagrams for the decay of the τ lepton. l stands for electron or muon q_{up} for the up-type and q_{down} for the respective down-type quarks.

particles into which the initial τ decayed. τ leptons that decay into one, three or more charged hadrons are referenced as 1-, 3- or X-prong τ leptons. The decay modes of hadronic τ leptons can be further classified according to the number of charged (X) and neutral (Y) pions among the decay products and will be named as XpYn. For example 1p0n means that the τ decayed into one charged and no neutral pions and describes for example the $\tau \to \pi\nu_\tau$ decay.

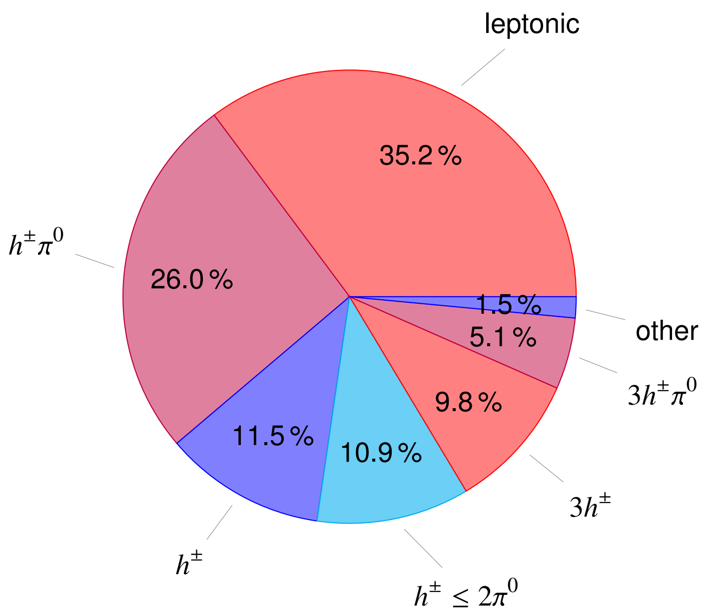

Figure 2.7: Dominant τ decay modes taken from [26].

This thesis is restricted to hadronic decays of the W boson, produced in the τ decay. Additionally, only events with two 1-prong τ leptons in the final state, are analysed.

2.2 Limitations of the Standard Model

Although the SM of particle physics gives a very accurate description of the physics observed, it is still incapable to explain e.g. the existence of Dark Matter (DM) or the Matter-Antimatter asymmetry in the Universe observed today. Also, it does not provide a unification of the three forces in the SM, instead only two of them meet each at different scales. These limitations of the model motivate the endeavour of physics to extend the SM, where this thesis takes part in. In the following, the most prominent motivations for physics beyond the SM are briefly discussed: The existence of Dark Matter, the hierarchy problem, the unification of forces and, most importantly for this thesis, additional violation of the CP symmetry.

2.2.1 Dark Matter

From the observation of the velocity distributions of galaxies inside a cluster, it became clear that the actual mass of a galaxy cluster is much larger than the sum of the masses of the luminous stars, which were thought to make up the biggest part of the galaxies' mass. This was observed for the first time in the 1930's [40] by Zwicky measuring the tangential velocities of galaxy cluster members observing the Doppler shift in their spectra of light. Galaxies inside a cluster are orbiting around the common centre of mass. Zwicky measured the tangential velocity dispersion of the galaxies within the Coma cluster. He estimated the mass of the cluster based on its luminosity and found that the total mass could not support the high velocity dispersion. All galaxies should be able to escape from the cluster, unless there is a significant additional amount of Dark Matter (DM).

By now, this effect was also observed in spiral galaxies. In spiral galaxies, most of the luminous matter is concentrated in the central region. Outside the bulk, the tangential velocity of stars should decrease as $r^{-1/2}$, where r is the distance to the centre. However, the observed distribution decreases only slowly with increasing r. This suggests that the total mass distribution in the galaxy must be proportional to r, which can only be explained by a big part of the galaxies mass being comprised of non-luminous i.e. Dark Matter. Further evidence for DM came from observations of galaxy clusters and the cosmic microwave background (CMB) [41].

Within the current cosmological Standard Model (ΛCDM), only 5% of the Universe is actually composed of baryonic matter[4], while the rest consists of Dark Matter (27%) and dark energy (68%) [42].

The ΛCDM suggests that the majority of cold Dark Matter in the Universe is not made up by normal baryons, i.e. the particles described by the SM of particle physics. One solution is to introduce a new weakly interacting massive particle (WIMP). It is a prototypical example of particle-like Dark Matter. However, the nature of the DM is still unknown. There are many models predicting WIMP candidates such as the Minimal Super Symmetric Standard Model (MSSM) [43] or the Two Higgs Doublet Model (2HDM) [44] and experiments are searching for possible WIMP candidates for example at ATLAS [45] at the LHC, or in Xenon based experiments [46, 47] etc. Up to date, no WIMP candidate have been discovered, neither at the LHC nor by any of the other experiments [48].

2.2.2 Hierarchy problem

The Hierarchy problem is related to loop corrections in the Higgs boson propagator at quantum level, which contribute to the Higgs boson mass. These loop corrections are quadratic in the cut-off scale Λ. Hence, they become significant at large energy scales, such as the scale of Grand Unified Theories $\Lambda_{GUT} = \mathcal{O}(10^{16}\,\text{GeV})$ or the Planck scale $\Lambda_{Planck} = \mathcal{O}(10^{19}\,\text{GeV})$. Therefore, high precision fine tuning is required to keep the Higgs boson mass at the electroweak scale of $\mathcal{O}(10^{2}\,\text{GeV})$ such that the SM of

[4] In cosmology baryonic matter comprises all massive SM particles.

particle physics as (part of) a theory is still applicable at such high mass scales. An elegant way of solving this hierarchy problem is to introduce supersymmetry.This theory provides for every SM loop of particles a corresponding sparticle (supersymmetric partners of the particles) loop. For fermions, the supersymmetric partners are bosons, while for bosons they are fermions. The sparticle loops then add to the propagator with opposite sign and thereby cancel with the loop contributions of the respective particles.

2.2.3 Unification of forces

The unification of forces relates to the dependence of the coupling constants of all three forces in the SM as a function of the energy scale q^2. In the SM, the coupling constants increase or decrease with the energy scale, respectively (see Eqs. (2.8) and (2.16)) and almost meet at a certain high energy scale. However, it would be desirable if there exists a high energy scale at which all couplings have exactly the same strength. This is the idea of the unification of forces.

According to [25], the coupling constants α_i run as a function of the energy scale q^2 as

$$\left[\alpha_i\left(q^2\right)\right]^{-1} = \left[\alpha_i\left(\mu^2\right)\right]^{-1} + \beta \ln\left(\frac{q^2}{\mu^2}\right) \tag{2.35}$$

where μ^2 is the energy scale at which the electron charge is known, and β depends on the number of fermion/boson loops contributing to the gauge boson's self energy. In QED, only fermionic loops are contributing. Hence, the coupling constant increases with increasing energy scale. For QCD and the weak interaction, the gauge boson self interactions have to be considered as well. This leads to bosonic loops in the gauge boson's self energy and thus, to a decrease of the coupling constant with increasing energy scale.

In the SM, there are three characteristic scales at which two of them are connected each. However, several Beyond Standard Model (BSM) theories have been described that allow to converge the coupling constants of all three forces at a very high energy scale. For example, one BSM theory, the Grand Unified Theory (GUT), converges the coupling constants by embedding the three symmetry groups of the SM ($SU(3) \otimes SU(2) \otimes U(1)$) into one single, larger symmetry group. This concept was originally proposed by Georgi and Glashow in the 1970's [49]. They suggested to comprise the gauge symmetries of the SM in a $SU(5)$ symmetry group. In this case, the coupling constants (almost) converge at an energy scale of about $O(10^{15}\,\text{GeV})$ assuming that only SM particles contribute in the loops. If, however, additional particles from physics beyond the SM are incorporated into the loops, for example from supersymmetry, the evolution of the three coupling constants changes. In case of supersymmetry, it can be modified in a way that all three couplings match exactly at a scale of $O(10^{16}\,\text{GeV})$.

2.2.4 CP violation

CP transformation is the combination of Charge (C) conjugation and Parity (P) transformation. Charge conjugation flips the charge of a particle i.e. $e^- \to e^+$, while parity transformation reverses the orientation of space, i.e. $\vec{x} \to -\vec{x}$. When the latter changes, the the so-called helicity or handedness, which is the the projection of the angular momentum on the direction of motion, of a particle changes sign. Hence, under CP transformation, a left-handed electron is transferred into a right-handed positron. C and P are conserved by the strong, electromagnetic and gravitational interaction. On the other hand, they are maximally violated by the weak interaction (see Section 2.1.2). Assuming CP was an exact symmetry, matter and antimatter would follow the same laws of nature. Thus, the violation of this CP symmetry is an important criterion to explain the matter-antimatter asymmetry observed in our Universe today. In 1967, Sakharov [3–5] established three criteria to explain this imbalance, of which one is CP violation. The other two are baryon number violation and the departure from the thermal equilibrium. Without CP violation during the thermal freeze-out of the baryons in the Universe, an equal number of baryons and antibaryons would have been created. This, however, contradicts the observation of our Universe today, where matter dominates clearly over antimatter [50].

In the SM of particle physics, CP violation has so far only been observed in the weak interaction of quarks and leptons. For quarks, CP violation has been widely studied measuring the matrix elements of the Cabibbo-Kobayashi-Maskawa (CKM) matrix. The CKM matrix is a unitary 3×3 matrix which describes the strength at which the quark flavours are changed by the charged currents of the weak interaction ($W^{\pm}$). It was proposed by Kobayashi and Maskawa in 1973 [51] extending the 2×2 mixing matrix proposed by Cabibbo in 1963[52]. CP violation in the quark sector was observed for the first time in neutral kaon decays with the Fitch-Cronin experiment in 1964 [53]. This discovery later resulted in the nobel prize in physics for V. Fitch and J. Cronin in 1980. The observed asymmetry in the $K^0 - \bar{K}^0$ mixing is very small compared to the one measured in $B^0 - \bar{B}^0$ mixing [54, 55]. In addition, CP violation was observed in specific Kaon [56–58], neutral [59–61] and charged [62, 63] B-meson decays and there is evidence for CP violation in D-meson [64] as well as B_s-meson decays [65].

Furthermore, CP violation could also occur in neutrino oscillations. This can be studied by measuring the non-diagonal elements of the Pontecorvo–Maki–Nakagawa–Sakata (PMNS) matrix. The PMNS matrix was introduced in 1962 to explain neutrino oscillations [66]. It describes the mixing between the neutrino eigenstates of the weak interaction and the actual neutrino mass eigenstates. Recent observations of long-baseline neutrino and antineutrino oscillations by the T2K experiment suggest the presence of CP violation also in the leptonic sector [67]. However, the CP-violating effects in the SM of particle physics measured so far are not large enough to generate the observed matter-antimatter asymmetry in our Universe.

Physics beyond the SM could solve this problem by introducing larger sources of CP violation, for example in the Higgs sector. The SM predicts a purely CP-even Higgs boson. However, extensions to the Standard Model, like the Two-Higgs-Doublet Model Section 2.3, predict an admixture of CP-even and CP-odd Higgs bosons. Since the CP nature of the Higgs boson has not yet been determined precisely, there is a possibility to find CP-violating effects and thus, hints for beyond SM physics in this sector. This is one of the main motivations for this thesis and the rational for probing the CP properties of the Higgs boson in $H \to \tau\tau$ decays.

2.3 Extensions to the Standard Model involving non CP-even Higgs bosons

There have been several BSM theories described which include CP violation in the Higgs sector. In the following, two important theories, the general Two Higgs Doublet Model(2HDM) and the Minimal Supersymmetric Standard Model with CP phases (MSSM) are described [26, 68].

2.3.1 CP violation in the Two Higgs Doublet Model

To establish a 2HDM model, the Higgs sector of the SM is extended by a second complex doublet of scalar fields. Hence, in the 2HDM two Higgs doublets Φ_1 and Φ_2 are introduced with opposite hypercharges $Y = \pm 1$. This leads to eight real scalar fields, of which three correspond to the massless Goldstone bosons that mix with the gauge fields and, after electroweak symmetry breakdown, generate the masses of the $W^{\pm}$ and Z bosons, as already explained in Section 2.1.4. Thus, five real scalar fields remain such that the 2HDM contains one pair of charged Higgs bosons $H^{\pm}$ and three neutral Higgs bosons (h^0, H^0 and A^0). The latter three are CP eigenstates, but not necessarily also mass eigenstates. Two of the three neutral Higgs bosons are pure CP-even states, referenced as h^0 and H^0, while A^0 is purely CP-odd . Due to the opposite hypercharges of the two Higgs doublets, the scalar Higgs potential contains mixing mass parameters of the form

$$m_{12}^2 \Phi_1^{\intercal} i\sigma_2 \Phi_2 + h.c. \tag{2.36}$$

Hence, both doublets acquire the VEVs $v_1/\sqrt{2}$ and $v_2/\sqrt{2}$ respectively and the gauge bosons keep their SM expressions. After applying unitarity conditions, the Higgs VEV is replaced by $v = \sqrt{v_1^2 + v_2^2}$. The 2HDM is driven by the choice of the scalar Higgs potential and the Yukawa couplings of the two complex fields to the SM fermions. The most general form of a 2HDM potential in the unitary gauge is given as

$$\mathcal{V} = Y_{ab} \Phi_a^{\intercal} \Phi_b + Z_{abcd} \left(\Phi_a^{\intercal} \Phi_b\right) \left(\Phi_c^{\intercal} \Phi_d\right), \tag{2.37}$$

where $a, b, c, d \in \{1, 2\}$, Y_{ab} contains the coefficients of the quadratic terms, defined as

$$Y = \begin{bmatrix} m_{11}^2 & -m_{12}^2 \\ -\left(m_{12}^2\right)* & m_{22}^2 \end{bmatrix}, \tag{2.38}$$

and Z_{abcd} contains the coefficients of the quartic terms λ_1 to λ_7. The interactions of the Higgs field to the fermion fields are included as Yukawa interactions of the form

$$h_{ij}^a \bar{\Psi}_L^i H_a \Psi_R^j, \tag{2.39}$$

where h_{ij}^a denotes the respective Yukawa coupling. These are, in the 2HDM, related to the fermion masses as

$$m_{ij} = h_{ij}^a v_a / \sqrt{2}. \tag{2.40}$$

However, in this general form, the neutral Higgs bosons could mediate flavour-changing currents between the different fermion mass eigenstates. This contradicts K-, D- and B-meson phenomenology and thus, should be avoided. The simplest way to do this, is to assume a symmetry that ensures that the fermions can couple only to one of the Higgs fields. There are various different realisations of this symmetry, which categorised as type I-IV 2HDM depending on the fermion type coupling to the first and second Higgs doublet as indicated in Table 2.3.

Model	2HDM I	2HDM II	2HDM III	2HDM IV
u	Φ_2	Φ_2	Φ_2	Φ_2
d	Φ_2	Φ_1	Φ_2	Φ_1
e	Φ_2	Φ_1	Φ_1	Φ_2

Table 2.3: Higgs bosons coupling to up, down and charged lepton-type singlet fermions in the four discrete types of 2HDM models [26].

A 2HDM can be CP conserving or CP violating depending on the properties of the 2HDM potential. The CP violation in the Higgs sector can be either explicit or spontaneous. Spontaneous CP violation is the consequence of an explicitly CP conserving Lagrangian and simultaneously a CP violating vacuum state. The general 2HDM scalar potential is explicitly CP violating. However, in most of the 2HDM models, a Z_2 symmetry is imposed, i.e. $\Phi_1 \to \Phi_1$ and $\Phi_2 \to -\Phi_2$, which implies a CP conserving scalar potential. Only if this Z_2 symmetry is broken, CP violation arises. In case of Soft Symmetry Breaking (SSB)[5], CP violation is a consequence of a nontrivial relative phase in the complex parameters m_{12}^2 and λ_5. Both, spontaneous and explicit CP violation yield similar phenomenological effects. If the scalar potential violates CP, the CP eigenstates mix into three mass eigenstates with non-vanishing mixing angles $\tan\alpha$, which is the angle that diagonalises the mass matrix of the CP-even HIggs bosons and $\tan\beta = v2/v1$, which is given by the ratio of the two VEVs. In consequence, the physical neutral Higgs bosons encompass admixtures of the two CP even and the CP odd fields and appear as states of indefinite CP.

2.3.2 Higgs bosons in the Minimal Supersymmetric Standard Model

In the Minimal Supersymmetric Standard Model (MSSM), a supersymmetry (SUSY) partner is associated to each gauge boson and chiral fermion of the SM. The MSSM is the simplest realistic extension to the SM that realises low-energy sypersymmetry. Even tough in this simple extension more than 100 new parameters are introduced, but only a few of the 100 parameters have an impact on the Higgs boson phenomenology. The particle spectrum of the MSSM contains the SM particles and two Higgs doublets (Φ_1 and Φ_2) of complex scalar fields with hypercharges $Y = +1$ and $Y = -1$, respectively, which resembles the general 2HDM. In addition, the MSSM also contains the SUSY partners to all SM particles. The MSSM is a Type-II 2HDM, which means that Φ_1 couples solely to down-type fermions, while Φ_2 couples only to up-type fermions. Hence, Φ_1 generates mass terms for the down-type quarks and leptons and Φ_2 generates mass terms for up-type quarks. The fermion masses are generated if the neutral Higgs components of both fields acquire a VEV.

According to [26], the Higgs potential in the MSSM is given as

$$\begin{aligned} V = {} & m_1^2\Phi_1^\dagger\Phi_1 + m_2^2\Phi_2^\dagger\Phi_2 - m_3^2\left(\Phi_1^\intercal i\sigma_2\Phi_2 + h.c.\right) + \frac{1}{2}\lambda_1\left(\Phi_1^\dagger\Phi_1\right)^2 + \frac{1}{2}\lambda_2\left(\Phi_2^\dagger\Phi_2\right)^2 \\ & + \lambda_3\left(\Phi_1^\dagger\Phi_1\right)\left(\Phi_2^\dagger\Phi_2\right) + \lambda_4\left|\Phi_1^\intercal i\sigma_2\Phi_2\right|^2 + \frac{1}{2}\lambda_5\left[\left(\Phi_1^\intercal i\sigma_2\Phi_2\right)^2 + h.c.\right] \\ & + \left[\left[\lambda_6\Phi_1^\dagger\Phi_1 + \lambda_7\Phi_2^\dagger\Phi_2\right]\Phi_1^\intercal i\sigma_2\Phi_2 + h.c.\right]. \end{aligned} \tag{2.41}$$

The parameters m_i can be related as $m_i^2 = \mu^2 + m_{Hi}^2, i = 1,2$ to the SUSY higgsino mass parameter μ and the soft SUSY breaking mass parameter of the two Higgs doublets m_{Hi}. $m_3^2 = B\mu$ represents the B-term soft SUSY breaking parameter and $\lambda_i, i = 1,..,7$ presents the Higgs' quartic couplings.

After spontaneous symmetry breaking of the electroweak symmetry, three of the eight real fields vanish as massless Goldstone bosons responsible for the W and Z mass terms and five physical Higgs particles are left: two charged Higgs bosons $H^\pm$ and two CP-even neutral Higgs bosons h, H, and one CP-odd neutral Higgs boson A (in the absence of CP violation). The Higgs sector at tree-level is determined by only two free parameters: (1) $\tan\beta = \frac{v_2}{v_1}$, where v_1 and v_2 are the VEVs of the two Higgs doublets and (2) one of the Higgs boson masses, where conventionally m_A is used. The masses of all other Higgs bosons

[5] SSB means that only processes with low energies are changed under the symmetry breaking while the hard high energetic processes still respect the symmetry. This means that terms are added to the Lagrangian, which break the symmetry softly. Their impact on the high energy physics is, however, so small, that no additional divergent contributions to the mass of scalars like the Higgs boson arise from the calculations.

at tree-level are determined by these two parameters. Radiative corrections have a significant effect on the sizes of the Higgs boson masses and couplings, they mainly arise from incomplete cancellations between the top and stop (or bootom/ sbottom and tau/ stau) loops. The phenomenology of the MSSM's Higgs sector is subject to the couplings of the Higgs bosons to the fermions and gauge bosons. These couplings are parametrised in terms of the angles β and α, as defined above. In the limit $\cos(\beta - \alpha) \to 0$, the lightest Higgs boson h in the MSSM shows the same behaviour as the SM Higgs boson. This behaviour is called alignment. The relations between the fermion masses and the Yukawa couplings in the MSSM are defined as

$$\begin{aligned} h_{b,\tau} &= \sqrt{2} m_{b,\tau} / (v \cos\beta) \\ h_t &= \sqrt{2} m_t / (v \sin\beta) , \end{aligned} \tag{2.42}$$

and the Higgs to $f\bar{f}$ couplings relative to the SM value of $gm_f/2M_W$ are described as

$$\begin{aligned} h\tau\tau &: -\sin\alpha / \cos\beta \\ H\tau\tau &: \cos\alpha / \cos\beta \\ A\tau\tau &: \gamma_5 \tan\beta \end{aligned} \tag{2.43}$$

for leptons or down-type quarks and

$$\begin{aligned} ht\bar{t} &: \cos\alpha / \cos\beta \\ Ht\bar{t} &: \sin\alpha / \sin\beta \\ At\bar{t} &: \gamma_5 \cot\beta \end{aligned} \tag{2.44}$$

for up-type quarks. However, there are no tree-level couplings of the CP-odd neutral Higgs boson A or the charged Higgs bosons to vector bosons[26]. Therefore, it is important to measure the CP state in the coupling of the Higgs to fermions as it is subject to this thesis.

Non-trivial phases leading to CP violation in the Higgs sector of the MSSM possibly arise in the gaugino mass parameters ($M_{1,2,3}$), the higgsino mass parameter (μ), the bilinear Higgs square mass parameter ($m^2_{1,2}$) and the trillinear couplings of squark and slepton fields to the Higgs fields (A_f). When explicit CP-violating phases appear, all three neutral Higgs boson mass eigenstates are able to couple to pairs of vector bosons with the coupling strengths

$$\begin{aligned} g_{H_iVV} &= \cos\beta O_{1i} \sin\beta O_{2i} \text{ and} \\ g_{H_iH_jZ} &= O_{3i} \left(\cos\beta O_{2j} - \sin\beta O_{1j} \right) - O_{3j} \left(\cos\beta O_{2i} - \sin\beta O_{1i} \right) , \end{aligned} \tag{2.45}$$

which are normalized to the SM couplings g^{SM}_{VV} and $g^{SM}_{Z}/2$. O_{ij} denotes an orthogonal matrix that relates the weak Higgs eigenstates to the mass eigenstates. If this matrix has non-zero, off-diagonal entries, the three Higgs boson mass eigenstates are admixtures of the two CP-even and the CP-odd Higgs boson

CP eigenstates. The couplings of the Higgs boson mass eigenstates H_i to fermions then depend on the fermion Yukawa-couplings (similar to the CP conserving case), $\tan\beta$ and on O_{ij}.

Another possible source of CP violation affecting the Higgs sector can arise from radiative corrections. They become significant, if one of the following two parameter combinations deviates from zero:

$$\begin{aligned} &\arg\left[\mu A_f (m_{12}^2)^*\right], \\ &\arg\left[\mu M_i (m_{12}^2)^*\right]. \end{aligned} \tag{2.46}$$

These two combinations are invariant under phase redefinition of the MSSM fields [26]. Hence, if they deviate from zero, the mixing of CP-even and CP-odd Higgs boson states becomes possible and CP violation arises.

The Higgs boson production and decay processes in both CP-violating scenarios are similar to the ones in the CP-conserving scenario, unless the mass difference between the light and the two heavy Higgs boson mass eigenstates would be large enough, such that the heavy states H_2 and H_3 can decay into two light Higgs bosons $H_1 H_1$. The discovery of a Higgs boson with mass 125 GeV at CERN and all measurements of its rates and properties, which - so far - cosely resemble the SM-based predictions, set strict constraints on the explicitly CP-violating MSSM scenario. Considering all measurements of the Higgs boson mass, the CP-odd component of the lightest Higgs state may not exceed 10% [26].

2.4 Constraining the Higgs CP nature at the LHC

There are various ways to probe the Higgs CP nature at the LHC. In this thesis, a test of CP invariance in $H \to \tau\tau$ decays is investigated. The τ leptons couple to CP-even and CP-odd Higgs components at leading order. This allows for direct testing of the Higgs CP nature. Furthermore, the $H \to \tau\tau$ channel gives the opportunity to distinguish pure scalar and pseudoscalar bosons from a CP-mix state. The method applied in this thesis is described in detail in Chapter 4. Beside $H \to \tau\tau$ decays, the CP properties of the Higgs boson have been studied in Higgs boson decays to dibosons, the VBF production vertex of $H \to \tau\tau$ decays, the coupling to top quarks in tH or $t\bar{t}H$ production channel or perform a fit to the Higgs boson signal strength. In the following the results of these measurements are briefly discussed.

2.4.1 Constraints on CP properties and anomalous couplings in Higgs-to-diboson decays

ATLAS [69] as well as CMS [70] studied the CP properties of the Higgs boson in its decays to dibosons with all results pointing to the existence of a SM Higgs boson with $J^P = 0^+$. CMS tested the spin-0, spin-1, and spin-2 hypothesis in the $H \to ZZ, Z\gamma*, \gamma\gamma* \to 4l$, $H \to WW \to l\nu l\nu$, and $H \to \gamma\gamma$ decay channels. They found the spin-1 hypothesis to be excluded in $\geq 99.999\% CL$. The spin-2 hypothesis could be excluded at $99.87\% CL$ assuming gravity-like couplings and $\geq 99\% CL$ in all other scenarios. Assuming the exclusion of the spin-1 and spin-2 hypotheses sets constraints on 11 anomalous couplings in the $H \to ZZ$ and $H \to WW$ channel [70]. CMS measured anomalous couplings in the $H \to VV \to 4l$ channel also in run 2 data with a luminosity of $80\,\mathrm{fb}^{-1}$. All anomalous coupling constraints agree with the SM expectation [6].

ATLAS tested the SM 0^+ hypothesis against several alternative spin and parity models using the $H \to ZZ* \to 4l$, $H \to WW \to e\nu\mu\nu$ and $H \to \gamma\gamma$ decay channels. The BSM models investigated include non-SM spin-0 and spin-2 models with universal and non-universal couplings of the Higgs boson to quarks and gluons. From the combination of all decay channels an exclusion of all non-SM hypotheses at $\geq 99.9\% CL$ can be deduced [69]. Furthermore, limits on the presence of BSM terms in the Lagrangian describing the HVV interaction vertex were set. ATLAS set further limits in the $H \rightarrow ZZ^* \rightarrow 4l$ decay channel using the full run 2 dataset using 139 fb^{-1} of data. This analysis interprets the measured coupling strength of the Higgs to Z Bosons in the so-called κ-framework, in which possible deviations from the SM prediction are parametrised in a set of coupling modifiers κ. In addition, the couplings are interpreted in an effective field theory approach probing a non SM-like tensor structure of the Higgs coupling. With these two interpretations limits are set on the beyond SM CP-even and -odd couplings of the Higgs to vector bosons, gluons and top quarks [7]

To summarise, ATLAS and CMS were able to exclude the pure CP-odd hypothesis for the Higgs boson discovered at the LHC in the diboson decay channel and set limits on various anomalous coupling parameters. However, admixtures of CP-even and CP-odd Higgs boson states, which have been predicted in various BSM theories have not yet been disproved.

2.4.2 Test of CP invariance in the VBF producion of a Higgs boson

ATLAS has investigated the CP nature of the Higgs boson in the VBF production vertex of the Higgs boson using the *Optimal Observable Method* [10]. The optimal observable is calculated from leading-order matrix elements for a Higgs boson produced by VBF and thus does not depend on the Higgs decay mode. Since the constructed observable is CP-odd , it is also sensitive to interferences of CP-even and CP-odd Higgs bosons and allows a direct test of CP invariance. The CP-odd contribution to the matrix element is measured from the distribution of the optimal observable in the $H \rightarrow \tau\tau$ leptonic, semileptonic, and hadronic decay channels. The results are, within statistical uncertainties, consistent with the SM hypothesis, which is $\tilde{d} = 0$. In consequence, limits were set on the investigated parameter $\tilde{d}$, such that values larger 0.035 and smaller -0.09 could be excluded at $68\% CL$ [10]. In turn, the hypothesis of a pure CP-odd Higgs boson was refused. However, an interference of CP-even and CP-odd Higgs states remains possible.

The CMS collaboration has also studied the CP properties of the Higgs boson in the VBF production vertex in its decays to two τ leptons [11]. In this measurement, anomalous couplings of the H Boson coupling to the vector bosons are targeted. The anomalous couplings are expressed as cross section fractions and phases. Consequently, limits are set on the resulting parameters using matrix element techniques. The results are then combined with the CP measurement from Higgs to diboson decays in the four-lepton final state presented in [6] to constrain the CP-violating and -conserving parameters even further. The CP-violating parameters are constrained to $f_{a3}\cos(\phi_{a3}) = (0.0 \pm 0.27) \times 10^{-3}$. While the CP-conserving parameters are constrained to $f_{a2}\cos(\phi_{a2}) = \left(0.08^{+1.04}_{-0.21}\right) \times 10^{-3}$, $f_{\Lambda 1}\cos(\phi_{\Lambda 1}) = \left(0.00^{+0.53}_{-0.09}\right) \times 10^{-3}$, and $f^{Z\gamma}_{\Lambda 1}\cos\left(\phi^{Z\gamma}_{\Lambda 1}\right) = \left(0.00^{+1.1}_{-1.3}\right) \times 10^{-3}$ [11].

2.4.3 Constraints on CP properties of the Higgs boson in its coupling to top quarks

Recently, also the CP properties of the Higgs boson are studied in its associated production with a top quark via tH or $t\bar{t}H$ by the ATLAS and CMS collaborations. In the MSSM and also the general 2HDM model, the CP-odd Higgs boson's coupling to vector bosons vanishes at tree-level. Hence, the coupling of a CP-odd component of the Higgs boson might be only detectable in the Higgs couplings to fermions. In ATLAS, the CP-mixing angle is constrained using the diphoton invariant mass measured in $H \rightarrow \gamma\gamma$ decays categorised with two independent boosted decision trees. This results in an exclusion of a CP-mixing angle larger 43 at 95% confidence level exploiting the full run 2 dataset with a luminosity of 139 fb^{-1} [8]. CMS reports the exclusion of a pure CP-odd nature of the Higgs boson at 3.2σ in the same production and decay channel. The fraction of the CP-odd component is compatible with the SM expectation and measured to $f_{\mathrm{CP}}^{t\bar{t}H} = 0.0 \pm 0.33$ [9].

2.4.4 Independent fits to the Higgs signal strength and their ratios

Another way of measuring the Higgs boson's CP properties relies on parametrising the effective Lagrangian of the Higgs couplings in terms of the SM Yukawa couplings and parameters c_i, which comprise possible deviations from the SM couplings as

$$\mathcal{L}_{Higgs} = c_W g_{HWW} H W_\mu^+ W^{-\mu} + c_Z g_{HZZ} H Z_\mu^0 Z^{0\mu} - c_t y_t H \bar{t}_L t_R - c_c y_c H \bar{c}_L c_R - c_b y_b H \bar{b}_L b_R - c_\tau y_\tau \bar{\tau}_L \tau_R + h.c. \tag{2.47}$$

These parameters are fitted to the Higgs signal strength and ratios of the Higgs signal strength measured at the LHC in different production and decay channels. Using decay ratios D_{XX} defined as

$$D_{XX} = \frac{\sigma^P (pp \to H \to XX)}{\sigma^P (pp \to H \to VV)} = \frac{\sigma^P (pp \to H) \times BR(H \to XX)}{\sigma^P (pp \to H) \times BR(H \to VV)} = \frac{\Gamma(H \to XX)}{\Gamma(H \to VV)} \tag{2.48}$$

has various advantages. For example, the dependence on the cross section $\sigma(pp \to H)$ vanishes and hence also the systematic uncertainties on the cross section cancel out. The fit results, presented in [71], rely on minimising

$$\mathcal{X}^2 = \sum_i \frac{\left[\mu_i(c_f, c_V) - \mu_i|_{exp}\right]^2}{(\delta_{\mu_i})^2}, \tag{2.49}$$

and $\mathcal{X}_R^2$ as defined in [71]. For the fit, the results of the respective $H \to XX$ cross section measurements published by ATLAS and CMS with 7 and 8 TeV LHC Data are used. In order to measure the CP nature of the Higgs boson, possible deviations from the c_i parameters of the SM, defined as

$$k_i = 1 - c_i^2, \tag{2.50}$$

are measured. Using these *k-factors*, the HVV coupling is developed to

$$g_{HVV}^{\mu\nu} = -ic_V \left(M_V^2/v\right) g^{\mu\nu}. \tag{2.51}$$

Of particular note, $c_V \neq 1$ does not consequent a CP-odd component of the observed Higgs state. Instead, $c_V \neq 1$ could hint towards contributions from other neutral H states that remain to be discovered. In contrast, the coupling of the Higgs boson to fermions is

$$g_{Hff} = -i\frac{m_f}{v}\left[\Re(c_f) + i\Im(c_f)\gamma_5\right], \tag{2.52}$$

where in the SM $\Re\left(c_f\right) = 1, \Im\left(c_f\right) = 0$. Based on the rates

$$\frac{\Gamma(H \to \gamma\gamma)}{\Gamma(H \to \gamma\gamma)|_{SM}} \approx \frac{\left|\frac{1}{4}c_W A_1\left[m_W\right] + \left(\frac{2}{3}\right)^2 \Re(c_t)\right|^2 + \left|\left(\frac{2}{3}\right)^2 \frac{3}{2}\Im(c_t)\right|^2}{\left|\frac{1}{4}A_1\left[m_W\right] + \left(\frac{2}{3}\right)^2\right|^2} \tag{2.53}$$

a fit is applied to the measured Higgs boson mass and to the product of production and decay rates which both were published by ATLAS and CMS using the full 7 and 8 TeV datasets collected in LHC run 1.

From this fit, it can be concluded, that at 3σ level, a CP-odd Higgs component has to obey $\kappa_{cp} < 0.68$ and the hypothesis of a pure CP-odd Higgs boson state is refused with more than 4σ [71].

CHAPTER 3

Experimental setup

This chapter describes the Large Hadron Collider (LHC) and one of its largest experiments, A Toroidal LHC ApparatuS (ATLAS). The latter recorded the data analysed in this thesis. Beside that, the event reconstruction with the ATLAS detector is outlined in this chapter. focusing in particular on the particle flow concept applied to reconstruct hadronically decaying τ leptons and jets.

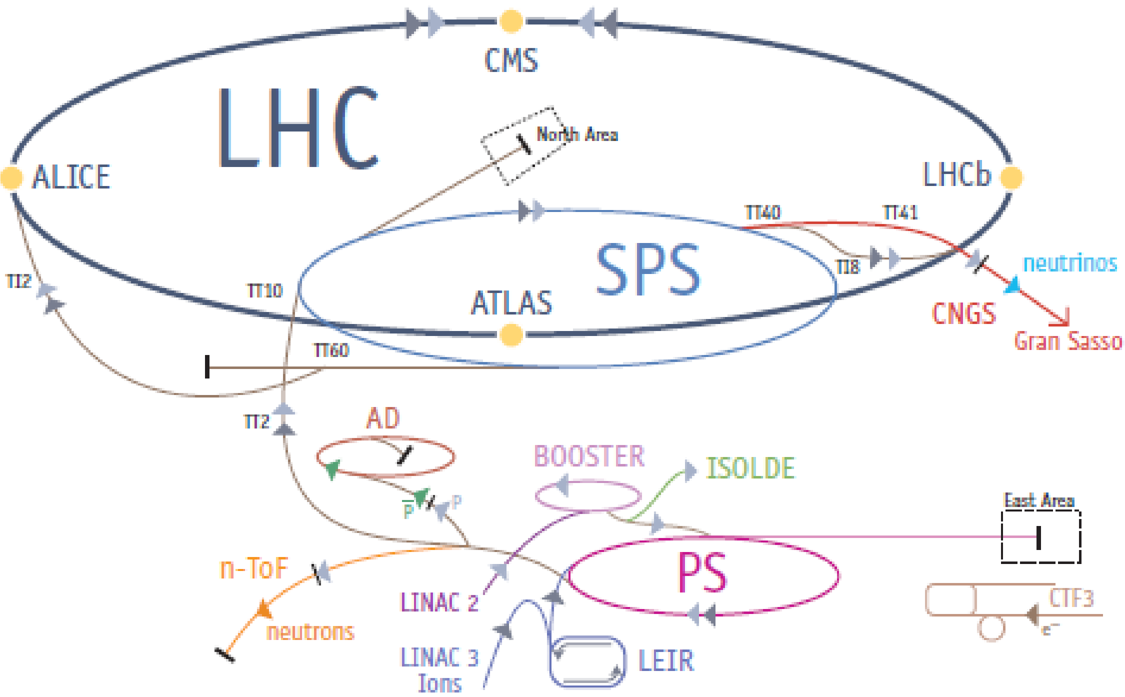

Figure 3.1: The accelerator complex at the European Organization for Nuclear Research with the LHC and associated experiments[72].

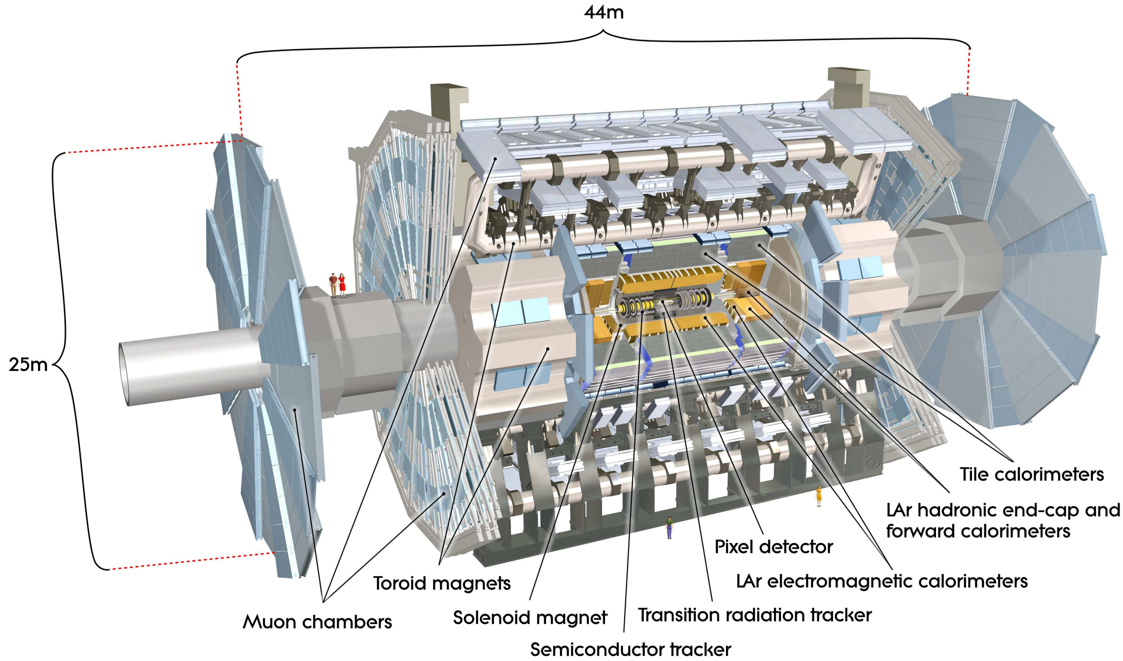

Figure 3.2: Sketch of the ATLAS detector opened on the side parallel to the beam axis for better visualisation [73].

3.1 The Large Hadron Collider

The LHC is part of a large accelerator complex, sketched in Fig. 3.1, at the European Organization for Nuclear Research CERN[1] in Geneva. The LHC has a circumference of 27 km and is located about 100 m below ground. The LHC accelerates protons or lead ions in two beams of opposite directions. In run 1 (2010-2012) center-of-mass (cms) energies of $\sqrt{s} = 7 - 8$ GeV were reached. For run 2 (2015-2018) the cms energy was increased to $\sqrt{s} = 13$ TeV. In spring 2021, the design energy of $\sqrt{s} = 14$ TeV might be reached after the current upgrade.

The accelerated protons stem from hydrogen atoms, from which the orbiting electrons are stripped off. Initially, the protons are accelerated linearly and injected into the Proton Synchroton (PS) Booster at an energy of 50 MeV. Next, the protons are accelerated further by the PS and Super Proton Synchroton (SPS) accelerators to an energy of 450 GeV. At this energy, the protons are filled into the LHC ring in bunches of 10^{11} particles in both clockwise and anticlockwise directions in two separated tubes. The LHC then accelerates them to the final energy of e.g. 6.5 GeV in run 2. The bunch spacing in run 2 reached the planned value of 25 ns. The beam pipes cross at four points, where the protons from each beam can interact. At these points, the four big LHC experiments ATLAS, Compact Muon Solenoid (CMS), Large Hadron Collider beauty (LHCb) and A Large Ion Collider Experiment (ALICE) are located. ATLAS and CMS are general purpose detectors, covering a broad range of physics, and successfully discovered the Higgs boson in 2012 [1, 2]. LHCb is dedicated to B-hadron physics and ALICE to heavy ion physics.

3.2 The ATLAS detector

The ATLAS detector sketched in Fig. 3.2 has a length of 44 m, a diameter of 25 m and a weight of 7 000 t. It has the typical structure of a high-energy collider physics detector, with different subdetectors being placed one after the other, cylindrically around the beam axis. The innermost part of the detector consists of tracking detectors, which measure the momentum of all charged particles by their tracks curvature inside an magnetic field. It is followed by the electromagnetic and hadronic calorimeters which measure the energies of photons, electrons and positrons or hadrons respectively. The muon system makes up the outermost part of the detector and measures the muon tracks. Since muons are minimal ionising particles, they are the only SM particles, except for neutrinos, not being stopped in the calorimeter system.

3.2.1 The ATLAS coordinate system

The nominal interaction point defines the centre of the ATLAS coordinate system. The positive x-axis points to the centre of the accelerator, the positive y-axis points up to the earth surface and the z-axis points along the beam pipe, such that a right-handed coordinate system is defined. The cylindrical architecture of the ATLAS detector suggests to use cylinder-coordinates using the distance from the interaction point $r = \sqrt{x^2 + y^2}$, the Azimuthal angle in the transverse plane ϕ and the angle polar angle between the transverse plane and the $z-$ or beam-axis Θ. Instead of using Θ in ATLAS usually the *pseudorapidity* η is used, which relates to the polar angle as

$$\eta = -\ln\left[\tan\left(\frac{\Theta}{2}\right)\right]. \tag{3.1}$$

In the relativistic limit when $p \cong E$, i.e. the mass of a particle becomes negligible compared to its velocity, the pseudorapidity approaches the rapidity defined as

$$y = \frac{1}{2}\ln\left(\frac{E + p_L c}{E - p_L c}\right), \tag{3.2}$$

where p_L is the particles momentum along the beam axis.

Differences in η are Lorentz invariant which is also true for differences in ϕ. Therefore usually $\delta R = \sqrt{\delta\phi^2 + \delta\eta^2}$ is used as a distance measure between particles in high energy collider physics.

3.2.2 The Inner Detector

The ATLAS Inner Detector (ID) is specialised to measure the tracks of charged particles. Tracks are reconstructed from signatures in the different layers of the detector. They are used to reconstruct the actual interaction vertex and to measure the direction of the particles. The detector is embedded in a solenoid that creates a 2 T magnetic field parallel to the beam axis. Therefore, the charged particles are bent in the magnetic field and one can measure their momenta and charges from the curvature of their tracks.

The Inner Detector system consists of three subdetectors: Pixel detector, Semiconductor Tracker (SCT) and Transition Radiation Tracker (TRT). As shown in Fig. 3.3, the interaction point is surrounded by high granularity pixel modules, which are responsible for the vertex measurement. These are followed by the SCT modules. Both subdetectors cover a range of $|\eta| < 2.5$ and make up the ATLAS precision

[1] The abbreviation is derived from the french name Centre Européenne pour la Recherche Nucléaire

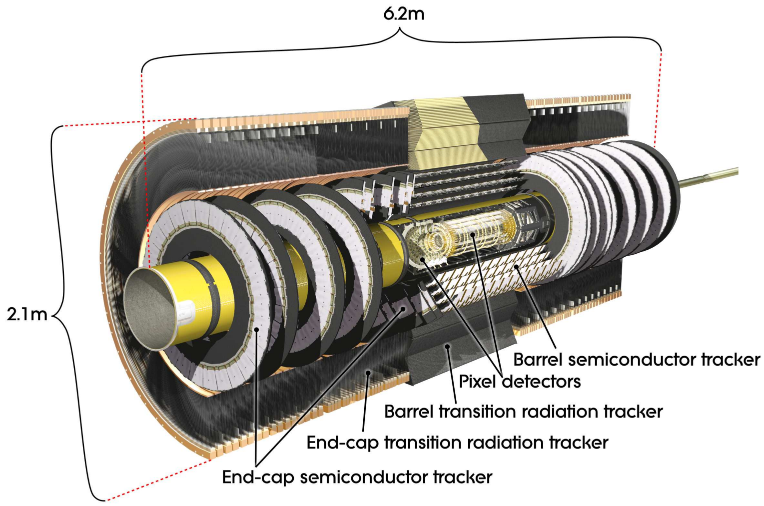

Figure 3.3: Sketch of ATLAS Inner Detector[74]

tracker. These two systems are responsible for vertex and track impact parameter measurements. The impact parameter of a track is the minimum distance between the track and the primary interaction point. They are surrounded by the TRT within $|\eta| < 2.0$. The TRT consists of straw tube detectors. It is used for measurements of charged particles tracks and the identification of electrons. The resolution of the transverse momentum (p_T)in the Inner Detector [75] is

$$\frac{\sigma_{p_\mathrm{T}}}{p_\mathrm{T}} = 0.05\% p_\mathrm{T} \oplus 1\%, \tag{3.3}$$

where σ_{p_T} is the uncertainty on p_T and $\oplus$ means that the two terms are added in quadrature, i.e. $a \oplus b = \sqrt{a^2 + b^2}$.

For run 2 of the LHC, an additional detector layer was inserted between the first layer of the pixel detector and a new beam pipe of smaller radius: The Insertable B-Layer (IBL)[76, 77]. It is mostly dedicated to improve the reconstruction of tracks and vertices and the identification of jets[2] containing B mesons (b-tagging). As shown in [76], there is a significant gain in the reconstruction of the impact parameter with respect to run 1 data due to the IBL.

3.2.3 The calorimeter system

The calorimeter system surrounds the tracking detector. It is responsible for measuring electron, positron, photon and hadron energies and covers a range of $|\eta| < 4.9$. A sketch of the ATLAS calorimeter system is shown in Fig. 3.4. In the $|\eta| < 3.2$ region, the innermost part consists of a high-granularity electromagnetic (EM) liquid argon calorimeter. It is dedicated to the measurement of electron and photon energies. The EM calorimeter consists of alternating layers of lead absorbers and liquid argon and is further split up into one barrel ($|\eta| < 1.475$) and two end-cap regions. While passing through the calorimeter, electrons or photons interact with the liguid Argon and create cascades of photons and electron-positron pairs. These cascades are slowed down by the lead absorbing layers. The energy deposited in the EM calorimeter can

[2] A jet is a bundle of quarks and gluons flying in a similar direction. It originates from the hadronisation of a quark or gluon produced in the collision.

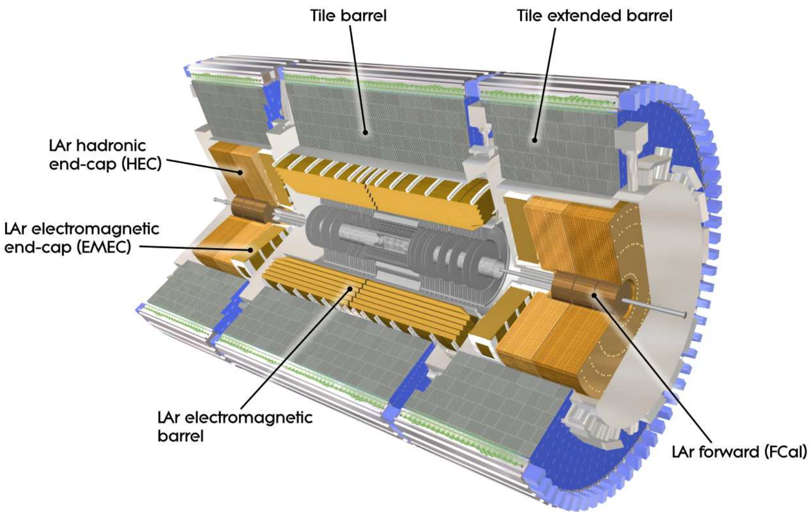

Figure 3.4: Sketch of the ATLAS calorimeter system [74]

be extracted and used to determine the electron/photon energies in an event. The ATLAS EM calorimeter consists of three layers, whereas the first one, the strip layer, has the highest granularity. This plays an important role in the measurement of photons from e.g. π^0 decays as explained in Section 3.3.4. The resolution of the ATLAS EM calorimeter [75] is

$$\frac{\sigma_E}{E} = \frac{10\%}{\sqrt{E}} \oplus 0.7\%. \tag{3.4}$$

Since hadrons usually have a longer interaction length, the EM calorimeter is surrounded by the Hadron calorimeter, which measures the energy of charged and neutral hadrons. It is dedicated to the measurement of jets as well as the missing transverse momentum[3] in an event. In the barrel region, a tile calorimeter is used which is a sampling calorimeter with alternating steel absorbers and scintillating tiles. At the end-caps (i.e. $3.1 < |\eta| < 4.9$), liquid Argon is used again as an interactive medium. The end-cap calorimeter consists of interleaving layers of liquid Argon and copper. It is dedicated to both, EM and hadronic energy measurements in this most forward part of the detector.

In order to measure the particle energies, calorimeter cells are combined to cell clusters. These clusters are associated to certain particles in the event. However, the ATLAS calorimeter system is non-compensating, i.e. electromagnetic and hadronic showers of the same energy leave different signatures in the calorimeter cells. In order to account for that when calculating the energy deposited in a cluster, there is a two-staged calibration applied to the cells. First, a local cluster calibration is applied, i.e. cells are calibrated locally to bring EM and hadronic calorimeter responses to the same level. Second, a calibration of the jet energy scale is performed, that compensates for mismeasurements in the jet energies.

In principle, the calorimeter system is designed in a way that the full shower should be confined in the calorimeters. However, it can happen in some cases, that particles are not fully stopped. In this case they don't deposit their whole energy and can punch through into the muon system. In order to minimise the

[3] Before the collision, the momentum transverse to the beam axis is always zero, since the protons move only along the z-axis. This can be used to calculate the so-called *missing transverse momentum* in an event as the negative sum of all measured particle momenta in the transverse plane. The missing transverse momentum can hint to particles that cannot be measured by the detector and possibly are not part of the SM.

effect of such particles entering the muon system, another absorbing layer of lead is placed around the calorimeters.

The resolution of the ATLAS Hadron calorimeter [75] is

$$\frac{\sigma_E}{E} = \begin{cases} \frac{50\%}{\sqrt{E}} \oplus 3\% & \text{for } |\eta| < 3.2 \\ \frac{100\%}{\sqrt{E}} \oplus 10\% & \text{for } 3.1 < |\eta| < 4.9 \end{cases} . \tag{3.5}$$

3.2.4 The muon system

The muon system (MS) makes up the outer-most part of the ATLAS detector. It is specified to the measurement of muon tracks as well as their momenta. It consists of two types of tracking detectors: The high-precision tracking and the trigger chambers. The high-precision tracking chambers cover a range of $|\eta| < 2.7$ and provide a very precise measurement of the muon tracks. For the momentum measurement, there is again a magnetic field needed. Therefore, a large superconducting air-core toroid magnet system is arranged radially symmetric around the beam axis. It thus provides a magnetic field mostly orthogonal to the muon trajectories.

The trigger chambers cover a range of $|\eta| < 2.4$ and are used for bunch-crossing recognition, well-defined trigger p_{T} thresholds as well as to measure the muon track coordinate orthogonal to the one measured in the high-precision chambers. The design resolution for muons in the MS at $p_{\mathrm{T}} = 1$ TeV [75] is

$$\frac{\sigma_{p_{\mathrm{T}}}}{p_{\mathrm{T}}} = 10\%. \tag{3.6}$$

3.2.5 The trigger system

The LHC is designed to deliver a bunch crossing rate of 40 MHz with a bunch-spacing of 25 ns. In LHC run 1, a bunch-spacing of 50 ns was used, while for the run 2 data that is used in this thesis, the nominal bunch-spacing of 25 ns was reached. The resulting data rate is too large to be recorded by any data acquisition scheme known to date. Hence, a filter system is needed to reduce the data rate by deciding quickly which data need to be recorded and which not. This is done by the ATLAS trigger system [78]. In run 2, the trigger and data acquisition scheme consists of a hardware based first-level trigger (L1) and a software based high-level trigger (HLT).

L1 trigger The ATLAS first-level trigger decision is formed by the central trigger processor (CPT) which is hardware based. It gets inputs from the L1 Muon module, the L1 Calo module, the minimum bias scintillators, the LUCID[4] Cherenkov counters and the Zero-Degree Calorimeters[5]. The L1 Calo module uses calorimeter towers[6] of coarse granularity to define particles and count the number of electrons, photons, τ leptons and jets above various energy thresholds and the (missing) transverse energy in an event. The L1 Muon system counts the number of muons in the barrel and the end-cap regions. The

[4] The Luminosity Measurement Using Cherenkov Integrating Detector (LUCID) is a Cherenkov counter which monitors the luminosity in the ATLAS experiment[79]. It is located close to the beam line 17 m from the point where the two proton beams cross each other.

[5] The Zero-Degree Calorimeters are installed close to the beam line 140 m away from the nominal interaction point of the two proton beams in ATLAS. Its main purpose is the detection of forward neutral particles produced in heavy ion collisions and from this to deduce the centrality of such collisions. Beside that, it can deliver an additional minimum bias trigger for ATLAS [74].

[6] A calorimeter tower is build by dividing the calorimeter in equal segments in $\delta\eta \times \delta\phi$ of e.g. $\delta\eta \times \delta\phi 0.1 \times 0.1$ and summing up all cells in this segment.

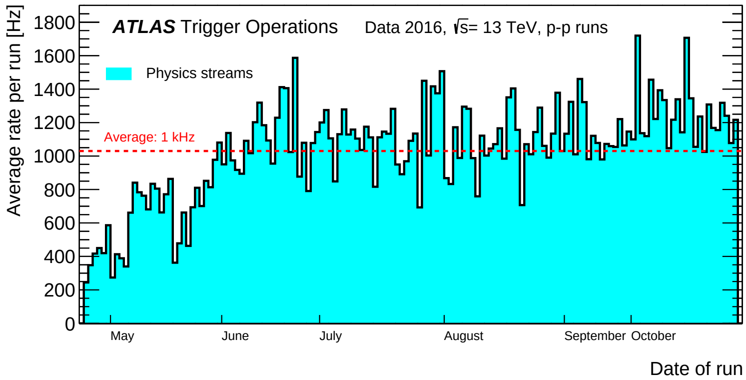

Figure 3.5: Avarage HLT physics stream rate in 2016 data [81].

CPT then combines all the information in the L1 topo module that is able to further filter events based on topological measures like the angular separation between trigger objects[80]. Beside a reduction of the data rate, it is also responsible for applying a preventive dead time to avoid overlapping read-out windows as well as front-end buffers to overflow. In total, it reduces the bunch crossing rate of 40 MHz to a trigger rate of at most 100 kHz. Beside that, it defines specific regions in the detector where particles were identified. These are called *regions of interest*. They are an important input for the following trigger stage.

HLT trigger The software-based high-level trigger performs a full reconstruction of all events passing the previous trigger chain in the previously defined regions of interest. It refines the selection procedure of the L1 trigger and selects events that are recorded for the offline analysis. It thereby breaks down the data rate for physics analysis to on average 1 kHz in run 2 as can be seen from Fig. 3.5 for 2016.

3.3 Event reconstruction with ATLAS

This section explains the reconstruction of physics objects with the ATLAS detector. Since this thesis deals with the reconstruction of $H \to \tau\tau$ events in the fully hadronic channel, this section especially emphasises the reconstruction of τ-leptons, jets and missing transverse energy.

3.3.1 Electrons and photons

Electrons are reconstructed in ATLAS from energy deposits in the EM calorimeter associated to a track in the Inner Detector. Their reconstruction procedure in run 2 is described in [82]. The reconstruction and identification of photons in run 2 is similar to the procedure in run 1, which is described in [83]. Since electrons and photons leave similar signatures in the EM calorimeter, their reconstruction runs in parallel and can be summarised as follows: Each electron or photon candidate is built starting from one initial cluster, called the seed. These seeding clusters are reconstructed using the Sliding Window Algorithm [84], which calculates the energy of a cluster by taking the sum of all cell entries within a rectangular window. The position of this window is chosen such that the energy within the window takes a local maximum. The sliding window for seed finding has a size of 3×5 in units of $\delta\eta \times \delta\phi$, which corresponds to the cell segmentation in the middle layer of the EM calorimeter. The latter is displayed in Fig. 3.6.

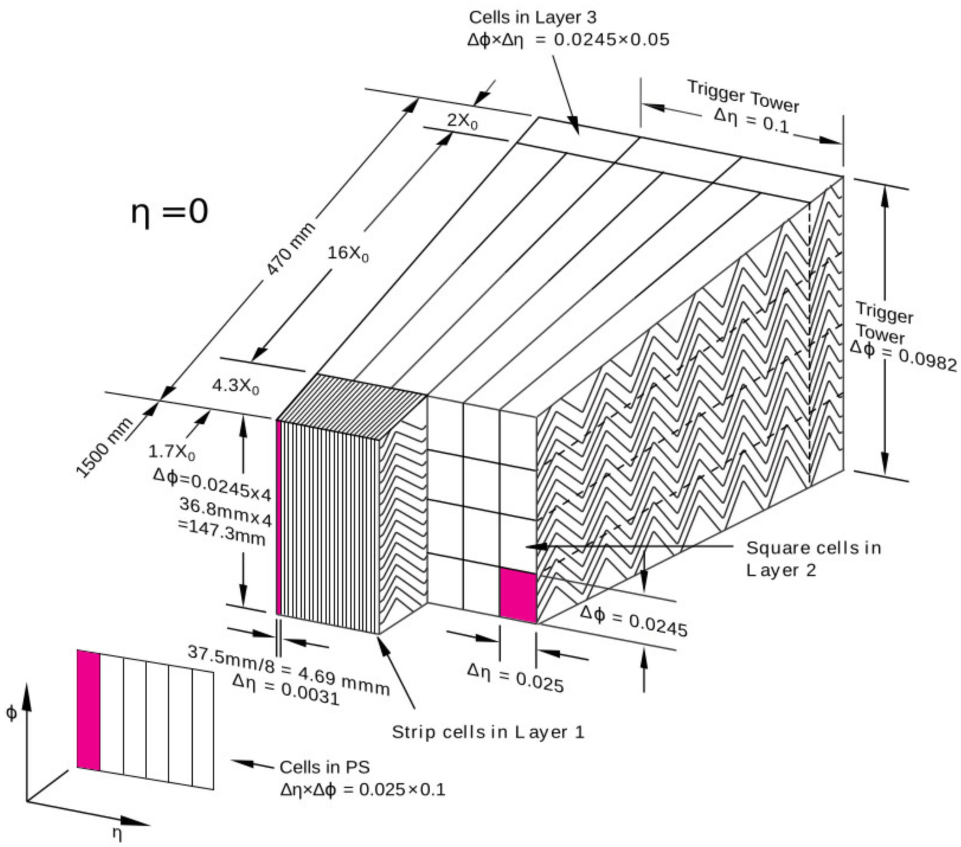

Figure 3.6: Longitudinal and lateral segmentation of the ATLAS high granularity EM calorimeter around $\eta = 0$ [85].

Tracks are reconstructed in the Inner Detector with an *inside-out tracking sequence* [86]. Therefore, in a first step, the pixel and SCT hits are combined to form track candidates. These are then ranked using scoring algorithms in order to resolve badly reconstructed or overlapping ones. Finally the tracks are extrapolated to the TRT, combined with the hits measured there and refitted based on the information of all three sub-detectors. These tracks are then matched to the seed-clusters described above. Electron candidates are then formed by sliding window clusters matched to a track. Photons are formed from clusters with either no matched track, or a matched track in combination with a reconstructed $\gamma \rightarrow e^+e^-$ conversion vertex associated with the respective cluster.

3.3.2 Muons

Muons behave as *minimum ionising particles*. This means, they leave only very little signatures in all subdetectors. They are the only particles (except for neutrinos) that reach the outer-most part of the detector. In order to precisely measure their tracks and momenta, the information of both, the Inner Detector as well as the muon system are combined. In the following, the reconstruction and identification of muons with the ATLAS experiment as presented in [87] is summarised.

In the Inner Detector, muons are measured as tracks. In the Muon System (MS), the reconstruction performs as follows: First, fit patterns for each muon chamber are used to segment the chamber based on the hits. The muon candidates are then created by fitting hits from segments in different layers of the muon chambers. The algorithm uses the hits from the middle layers to seed the muon tracks. Except for the barrel-endcap transition region, there are always at least two matching segments required to build a muon track. In order for the segments to be selected, they need to fulfil certain requirements on the hit multiplicity and the fit quality. The combination of ID and MS is performed with various reconstruction algorithms depending on the input from the ID, MS and calorimeters. According to the used subdetector, four different types of reconstructed muons are defined:

Combined muon For these muons the track reconstruction is performed independently in the ID and MS. Afterwards a combined muon track is formed from a global refit using hits from both subsystems. Most muons are reconstructed following an outside-in pattern recognition algorithm starting from tracks in the MS that are extrapolated to the ID and matched with ID tracks.

Segment-tagged muon Is a track in the ID that is extrapolated to the MS and can be associated with at least one local track segment in the Monitored Drift Tube (MDT) chambers or the cathode strip chambers (CSC). This definition is used if a muon crosses only one layer of the MS chambers due to a low transverse momentum or because it has met a region of the MS with a reduced acceptance.

Calorimeter-tagged muon Is a track in the ID that can be matched to a signature in the calorimeter which is compatible with a minimum ionising particle. This type of muons is optimised for the $\eta < 0.1$ where the MS is only partially instrumented, and for muons with $15 < p_{\mathrm{T}} < 100\,\mathrm{GeV}$.

Extrapolated muon In this case, the muon is reconstructed only from the MS measurement, requiring its direction to be compatible with originating from the interaction point. It needs to transverse at least two layers of the MS to make a track measurement possible. One exception is made for muons in the forward region: here, the muon is required to transverse three layers of the MS. Extrapolated muons are mainly used to increase the acceptance in the region which is not covered by the ID, i.e. $2.5 < \eta < 2.7$.

3.3.3 Jets

A jet is the signature of a quark or gluon produced in the hard interaction of the event. During the hadronisation process, a bunch of particles is produced mostly flying into the same direction. The definition of a jet depends on the chosen algorithm, the input objects to that algorithm and the jet energy resolution. In principle, one distinguishes between two jet finding algorithms: cone algorithms relying on a distance measure in coordinate space and cluster algorithms relying on a distance measure in momentum space. Cluster algorithms are usually preferred since they are infrared and collinear safe. In ATLAS, the anti-k_t algorithm [88] is widely used for jet-finding since it clusters the hard objects first, leading to circular shaped jets. The momentum distance measures d_{ij} between two clusters i and j and d_{iB} between a cluster i and the beam axis as defined in Eqs. (3.7) and (3.8) are calculated for all clusters. Here $\delta R_{ij}^2 = \sqrt{\delta\eta_{ij}^2 + \delta\phi_{ij}^2}$ denotes the spacial distance between the two clusters in the transverse plane and R denotes the cone radius of the jet, which is an input parameter to the algorithm. In ATLAS typically a value of $R = 0.4$ is used in jet reconstruction.

$$d_{ij} = \min\left(p_{T,i}^2, p_{T,j}^2\right) \frac{\delta R_{ij}^2}{R^2} \tag{3.7}$$

$$d_{iB} = p_{T,i}^2 \tag{3.8}$$

The objects i and j with smallest d_{ij} are then merged into one cluster and their four-momenta are summed until d_{iB} is the smaller than d_{ij} for any object j. The object i is considered to be a jet and removed from the list of objects. This way, the hardest objects are clustered first accumulating all soft objects within a cone of radius R.

In general one distinguishes *truth particle jets*, which are only available in simulations, and *calorimeter jets*. *Truth particle jets* are formed by applying the jet algorithm to all neutral and charged final state particles in a simulated event. *Calorimeter jets* are reconstructed applying the jet-clustering algorithm to calorimeter signals, followed by a calibration step [75]. There are two types of calorimeter signals used as inputs: Calorimeter towers and topo-clusters. *Calorimeter towers* are formed by dividing the calorimeter in bins of $\delta\eta \times \delta\phi = 0.1 \times 0.1$ and summing up the signals in all cells per bin. In order to cancel the noise, towers with negative signals (which are noise-dominated) are merged with nearby towers with positive signals until the net-signal in each tower is positive. *Topo-clusters* are formed in a more complex way by the topological cell clustering algorithm [89]. They are seeded by cells for which the absolute energy measurements exceed four times the expected noise, which contains electronic as well as pile-up noise contributions. As a next step, all neighbouring cells are added to the cluster if their energy exceeds two times the expected noise. Finally, all cells adjacent to these secondary seeds are also added to the cluster. Afterwards, a splitting step follows that splits a cluster up if it contains more than one local energy maximum. In contrast to calorimeter towers, topo-clusters do not include cells with no signal at all. Hence they contain substantially less noise. Therefore, for the jets included in the Higgs-CP measurement as well as for the particle flow reconstruction studies, topo-clusters are used as inputs to the anti-k_t jet-finding algorithm.

The energy calibration of jets happens in two stages, a local calibration (LCW) in order to bring EM and hadronic showers to the same scale, and a jet energy scale calibration (JES), in order to account for mismeasurements of the jet energy.

3.3.4 τ leptons

The τ lepton has a short lifetime of roughly 2.9×10^{-13} s. Thus, it cannot be detected directly with the ATLAS detector but only through its decay products. The electron or muon from the leptonic decays cannot be distinguished from promptly produced leptons. Beside that, leptonic decays have two neutrinos in the final state, which makes the reconstruction challenging. Hence, this thesis uses hadronic τ decays only, which sum up to a branching fraction of 65% as summarised in Fig. 2.7. Hadronically decaying τ leptons (τ_{had}) decay mostly to charged and neutral pions and a neutrino. The pions comprise the visible part of the τ lepton ($\tau_{\text{had}}^{\text{vis}}$), as they can be measured in the detector, while the neutrino escapes undetected and hence comprise the invisible part of the τ leptons.

The algorithm to reconstruct the $\tau_{\text{had}}^{\text{vis}}$ and their energy calibration is described in [90] and briefly summarised in the following paragraphs. Hadronically decaying τ leptons are reconstructed from jets using the anti-k_t algorithm with a radius parameter of $R = 0.4$. Furthermore, a core region is defined with a cone of radius $R = 0.2$ around the initial jet axis. The four momentum of the $\tau_{\text{had}}^{\text{vis}}$ is then calculated from clusters within this core region, including a τ specific calibration derived from simulations[91]. This calibration accounts for several effects like energy deposited outside the core region (out-of cone energy), effects from underlying event, pile-up and the typical hadron composition in τ_{had} decays. In addition, Inner Detector tracks are matched to the τ_{had} candidates to calculate the charge of the $\tau_{\text{had}}^{\text{vis}}$ candidates as the sum of the charges of all matched tracks. A track is matched, if its momentum in the transverse plain satisfies $p_{\text{T}} > 1$ GeV, it has at least two hits in the Inner Detector pixel layers, it has at least seven hits in the pixel and silicon microstrip layers all together and its two-dimensional impact parameter[7] fulfils $|d_0| < 1$ mm and $z_0 \sin\theta < 1.5$ mm. In order to discriminate $\tau_{\mathrm{had}}^{\mathrm{vis}}$ candidates from jets, a multivariate algorithm is employed using a boosted decision tree (BDT). This BDT combines information on shower shapes and tracks of jets and hadronically decaying τ leptons. Beside that, there is a discriminant constructed to suppress τ_{had} candidates originating from misidentified electrons. Finally, all $\tau_{\mathrm{had}}^{\mathrm{vis}}$ candidates are asked to fulfil $p_{\mathrm{T}} > 15$ GeV and $|\eta| < 2.5$ to be in the fiducial volume of the Inner Detector and to have one or three associated tracks.

A very precise measurement of the τ decay products and their four vectors is crucial for this analysis. Since the reconstruction of the τ decay plane used in the CP sensitive observables (see Chapter 4) depends also on the specific τ decay mode, a good decay mode classification is needed. In order to access these information, the *Tau Particle Flow Method* [92] is employed afterwards to the $\tau_{\mathrm{had}}^{\mathrm{vis}}$ candidates. This method has been developed for LHC run 2 and is described in Section 3.5.

3.3.5 Missing transverse momentum

The missing transverse momentum ($E_{\mathrm{T}}^{\mathrm{miss}}$) is calculated as the negative vector sum of the transverse momenta of all hard objects in an event i.e. the fully reconstructed and calibrated physics objects like electrons, photons, muons, τ leptons and jets (hard term) plus the negative vector sum of all tracks associated with the hard interaction vertex but not with any of the hard objects (soft term) [93]:

$$\begin{aligned} \vec{E}_{\mathrm{T}}^{\mathrm{miss}} = &- \sum_{\text{selected electrons}} \vec{p}_{\mathrm{T}}^{\,e} - \sum_{\text{accepted photons}} \vec{p}_{\mathrm{T}}^{\,\gamma} - \sum_{\text{selected muons}} \vec{p}_{\mathrm{T}}^{\,\mu} \\ &- \sum_{\text{accepted } \tau \text{ leptons}} \vec{p}_{\mathrm{T}}^{\,\tau} - \sum_{\text{accepted jets}} \vec{p}_{\mathrm{T}}^{\,jet} - \sum_{\text{unused tracks}} \vec{p}_{\mathrm{T}}^{\,\mathrm{track}} \end{aligned} \tag{3.9}$$

The soft term in Eq. (3.9) is comprised of the p_{T} sum of all unused tracks, i.e. ID tracks from the hard scatter vertex that are not associated to any of the hard objects. Therefore, it includes solely the $\vec{p}_{\mathrm{T}}$ flow from soft charged particles. Soft neutral particles reconstructed in the calorimeter systems are not included, since their signals suffer from large pile up contributions, i.e. effects of multiple interactions per bunch-crossing and in neighbouring bunch-crossings.

As described in [93], the following set of variables is provided in ATLAS

$$\vec{E}_{\mathrm{T}}^{\mathrm{miss}}, \tag{3.10}$$

$$E_{\mathrm{T}}^{\mathrm{miss}} = \left|\vec{E}_{\mathrm{T}}^{\mathrm{miss}}\right| = \sqrt{\left(E_{\mathrm{T},x}^{\mathrm{miss}\;2} + E_{\mathrm{T},y}^{\mathrm{miss}\;2}\right)}, \tag{3.11}$$

$$\Phi_{\mathrm{miss}} = \arctan(E_{\mathrm{T},y}^{\mathrm{miss}}/E_{\mathrm{T},x}^{\mathrm{miss}}). \tag{3.12}$$

Finally, it is essential to remove pile up from the considered tracks to achieve a good $E_{\mathrm{T}}^{\mathrm{miss}}$ resolution. This is done using the so-called *jet-vertex tagger technique* as described in [94]. Beside that also the scalar sum of all transverse momenta in an event is calculated as

$$\sum E_{\mathrm{T}} = \sum_{i \in \{\text{hard objects}\}} p_{\mathrm{T}}^{i} + \sum_{j \in \{\text{soft objects}\}} p_{\mathrm{T}}^{j} \tag{3.13}$$

which provides a good estimate of the overall event activity.

[7] The two dimensional impact parameter of a track is characterised by the distance d_0 between the point of closest approach of a track and the primary vertex in the transverse plane and z_0, which is the z-coordinate of this point of closest approach.

3.4 The particle flow method

The particle flow method attempts to combine the information of all detector subsystems to measure a single particle, resulting in the "flow" of the particle through the detector. In LHC run 1, jets as well as hadronically decaying τ leptons were reconstructed solely based on the energy deposits in the calorimeter systems. However, there are multiple advantages to combine the information of all subdetectors, i.e. by using a combination of the tracking and calorimeter measurements.

The ATLAS design calorimeter resolution for charged pions in the centre of the detector is given vy

$$\frac{\sigma(E)}{E} = \frac{50\%}{\sqrt{E}} \oplus 3.4\% \oplus \frac{1\%}{E}, \tag{3.14}$$

while the design resolution of the inverse transverse momentum in the tracking system is [95]

$$\frac{\sigma\left({}^{1}/p_{\mathrm{T}}\right)}{{}^{1}/p_{\mathrm{T}}} = 0.036\% p_{\mathrm{T}} \oplus 1.3\%. \tag{3.15}$$

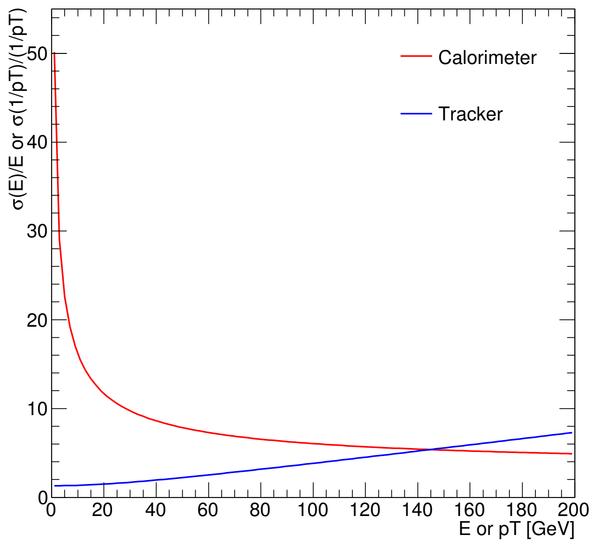

Figure 3.7: Design energy resolution of the ATLAS calorimeter and inverse transverse momentum resolution of the Inner Detector for charged pions in the centre of the detector.

As can be seen from Fig. 3.7, for energies below 140 GeV, the resolution of the tracking system is superior to the calorimeter one. Therefore, it is useful to combine the information for charged hadrons and use always the subsystem, that gives the more accurate result for energy/momentum. This concept is used in ATLAS for hadronically decaying τ leptons [92] and jets [95]. In order to combine the measurements properly, tracks are matched with calorimeter clusters and their energy is subtracted from the clusters in order to avoid double counting.

The particle flow method for hadronically decaying τ leptons is discussed in Section 3.5, while the reconstruction algorithm for jets is outlined in Section 3.6.

3.5 Particle flow for τ leptons

The τ particle flow method is described in [92]. It improves the precision at which four vector of the $\tau_{\text{had}}^{\text{vis}}$ and the neutral pions from the τ_{had} decay are reconstructed. Beside that, it becomes possible to reconstruct the individual charged and neutral decay products of the $\tau_{\text{had}}^{\text{vis}}$ candidates and to classify the different $\tau_{\text{had}}^{\text{vis}}$ decay modes with a high efficiency and purity.

The four momentum of the charged and neutral hadrons from the $\tau_{\text{had}}^{\text{vis}}$ decay are determined from a combination of the tracking detector and the calorimeter measurements. The charged hadrons ($h^{\pm}$) are measured in the tracking system, where also charge and momentum is determined. The neutral hadrons, which are mostly neutral pions (π^0) are measured from the calorimeter system after the expected energy deposited by the charged hadrons has been subtracted to avoid double counting the energy of charged particles. The decay mode is classified based on the number of charged and neutral particle flow (pflow) objects associated to a $\tau_{\text{had}}^{\text{vis}}$ candidate. For the neutral objects, cluster shape variables and the number of shots, i.e. photon clusters in the first EM calorimeter layer, are combined in a Boosted Decision Tree (BDT) in order to decide whether a cluster is likely to be from a neutral pion or any other neutral hadron. Finally, another BDT is used to perform a hypothesis test to improve the determination of the τ decay mode even further.

3.5.1 Charged hadron subtraction

In order to avoid double counting, the energy of the identified $h^{\pm}$ from the $\tau_{\text{had}}^{\text{vis}}$ candidates is subtracted from the calorimeter systems. In 99% of the $\tau_{\text{had}}^{\text{vis}}$ decays, the only neutral hadrons produced are pions. Neutral pions decay with a branching fraction of almost 100% to two photons, which deposit their energy solely in the EM calorimeters. Hence, the whole energy deposited in the hadronic calorimeter is assigned to $h^{\pm}$'s and subtracted from the calorimeters.

In the EM-calorimeter, the subtraction procedure is more complicated. For each track, the closest cluster in the EM-calorimeter is matched and the expected energy deposited in the EM calorimeter is subtracted. If no such cluster can be found, it is assumed that the particle did not leave energy in the EM calorimeter and nothing is subtracted. The expected $h^{\pm}$ energy in the EM calorimeter is calculated from the track energy and the energy in the hadron calorimeter (HAD) as

$$E_{h^{\pm}}^{EM} = E_{h^{\pm}}^{\text{track}} - E_{h^{\pm}}^{HAD}. \tag{3.16}$$

The energy in the HAD calorimeter $E_{h^{\pm}}^{HAD}$ is calculated by assigning all clusters within the core region to the closest $h^{\pm}$. While $h^{\pm}$ is the track extrapolated to the calorimeter layer with the largest amount of clustered energy. The calculated $E_{h^{\pm}}^{EM}$ is then subtracted from the closest cluster in the EM calorimeter, if there is a cluster within $R < 0.04$ of the $h^{\pm}$ direction.

3.5.2 Neutral pion reconstruction

Neutral pions are reconstructed based on their energy deposits in the EM-calorimeter. After the charged hadron subtraction, the remaining energy is reclustered. However, beside the π^0 energies themselves, it still contains $h^{\pm}$ remnants, pile up and noise. In order to get rid of these, only cluster with an energy larger than a certain threshold are considered. The remaining clusters constitute the π^0 candidates. In order to further improve the π^0 identification, a BDT is trained which decides how likely the candidate is originally a π^0. The decision is made based on cluster-variables, such as shower width and depth.

In addition, one can exploit the fact, that π^0's decay almost solely to two photons. Those deposit around 30% of their energy in the very first layer of the EM-calorimeter (EM1). This layer is binned

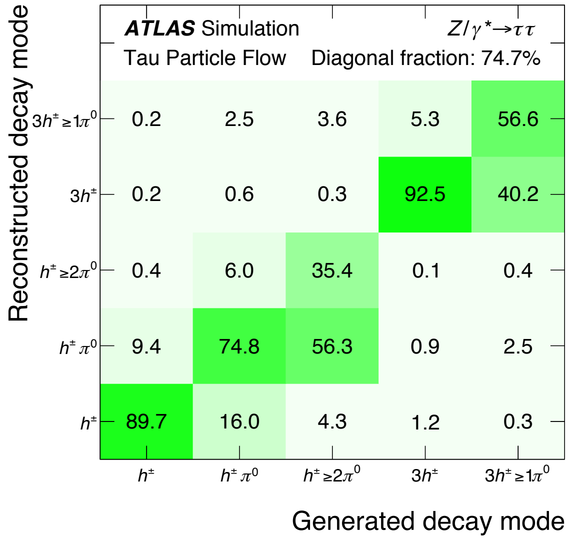

(a) efficiency matrix

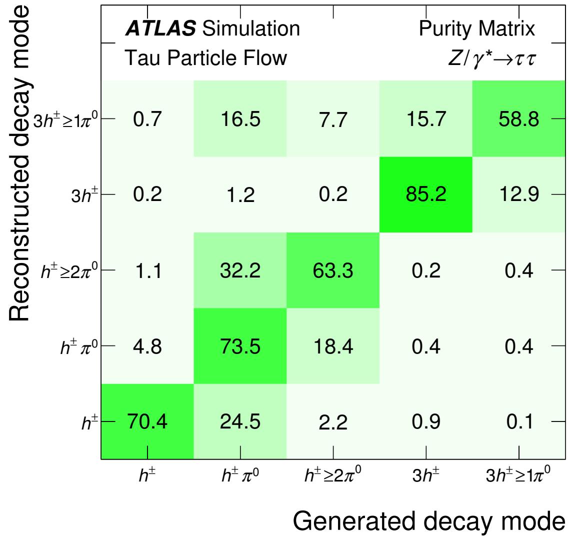

(b) purity matrix

Figure 3.8: Efficiency (a) and purity (b) matrix of the τ particle flow decay mode classification [92].

sufficiently fine in η to reconstruct single photons from the deposits in this first layer called shots. The number of shots associated to a cluster is further used to decide whether two neutral pions are contained in a single cluster. This is also important for the reconstruction of the τ decay mode.

3.5.3 Tau decay mode classification

The τ decay mode is identified based on the number of reconstructed $h^{\pm}$, π^0's and photons (identified in the first EM layer) associated with the respective τ_{had} candidate. In addition to that, the properties of the τ decay-products and the number of reconstructed photons are used and combined in a BDT. The most difficult part of the identification is to reconstruct the number of π^0's correctly. Hence, one of three following decay mode tests is performed: 1p0n vs. 1p1n, 1p1n vs. 1pXn or 3p0n vs. 3pXn. Here, the first number denotes the number of charged, the second one, the number of neutral pions associated to the τ_{had} candidate as explained in Section 2.1.6. Which one, is decided based on the number of $h^{\pm}$'s and π^0's associated to the respective τ_{had}. With this method, in total 74.4% of all τ leptons are reconstructed with the correct decay mode, as can be seen in Fig. 3.8. The decay mode classification efficiency shown in Fig. 3.8 (a) is defined as the probability for a given generated decay mode to be reconstructed as exactly the same decay mode. While the purity shown in Fig. 3.8 (b) is defined as the probability for a $\tau_{\text{had}}^{\text{vis}}$ candidate with a given reconstructed $\tau_{\text{had}}^{\text{vis}}$ decay mode to originate from exactly the same generated decay mode. For the 1p0n, 1p1n and 3p0n decay modes a purity of 70.3%, 73.5% and 85% is reached, respectively[92].

3.5.4 Reconstruction of the visible τ four momentum $\tau_{\text{had}}^{\text{vis}}$

The visible τ four vector is calculated from the $h^{\pm}$'s and π^0's associated to the respective τ as the vector sum of all constituent four vectors. The π^0's are ordered according to their π^0 identification score from the BDT and only the first n π^0's are included in the $\tau_{\text{had}}^{\text{vis}}$ four vector. Here n is determined based on the

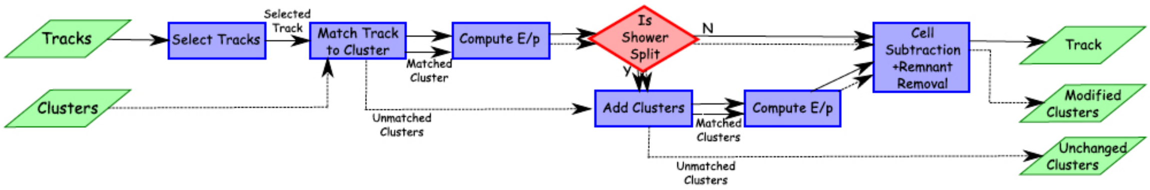

Figure 3.9: Sketch of the jet particle flow algorithm procedure[95].

identified $\tau_{\text{had}}^{\text{vis}}$ decay mode. For each π^0, the mass component of the π^0 four vector is set to the π^0 mass. However, there are two cases which are treated differently: (1) The $\tau_{\text{had}}^{\text{vis}}$ is classified as 1p1n, but there are two π^0's identified. In this case, most likely the π^0's are photons from a single π^0 decay. Hence, the mass in each individual π^0 four vector is set to zero before they are added to the total $\tau_{\text{had}}^{\text{vis}}$ four momentum. (2) The $\tau_{\text{had}}^{\text{vis}}$ is classified as 1pXn and three or more photons are found in a single π^0. Then only this π^0 candidate is added to the $\tau_{\text{had}}^{\text{vis}}$ four momentum and the mass is set to twice the π^0 mass. In this case, most likely two π^0's were reconstructed in one single cluster.

Finally, the τ_{had} four momentum is calibrated using a τ energy calibration method which combines the τ particle flow with additional calorimeter and tracking information in a multivariate analysis technique [91].

3.6 Particle flow for jets

A typical hadronic jet in ATLAS is composed of 60 % charged hadrons, 30% neutral hadrons and 10% photons. The particle flow based jet reconstruction aims to reconstruct all individual particles constituting a jet in the detector part where they can be measured most precisely and then sums up their energies. It can be used to reconstruct hadronic jets and soft activity, which is relevant in the reconstruction of the $E_{\text{T}}^{\text{miss}}$ (see Section 3.3.5). For energies below 140 GeV the resolution of the tracking system is better than the one of the calorimeters. Therefore, for charged hadrons in this energy regime usually only the track measurement is used. For neutral hadrons, there is only a calorimeter measurement available. The decision which topo-clusters originate from charged hadrons requires an accurate matching of tracks to topo-clusters. Followed by a cell-based subtraction algorithm which removes the overlap between the energy determination in the calorimeter and track measurements in the Inner Detector. This prevents the energy of the charged hadrons from being counted twice in an event and improves the reconstruction of the neutral hadrons [95].

During my PhD thesis, I have worked on improving the matching of tracks and calorimeter clusters as well as the cell-subtraction algorithm. Both algorithms are important building blocks of the jet particle flow algorithm referenced as EFLOWREC.

3.6.1 The charged hadron subtraction

This algorithm provides a set of tacks and topo-clusters. The set of topo-clusters contains both, the unmodified topo-clusters and the ones remaining after the subtraction procedure. The different steps of the jet particle flow algorithm as well as needed inputs and outputs are sketched in Fig. 3.9. In a first step, the algorithm selects well-measured tracks and tries to match each of them to a single topo-cluster in the calorimeter. Next, the energy, which is expected to be deposited in the calorimeter by the particle which created the matched track, is calculated. It is estimated based on the position of the topo-cluster and the momentum of the track. However, a single particle deposits its energy often in more than one

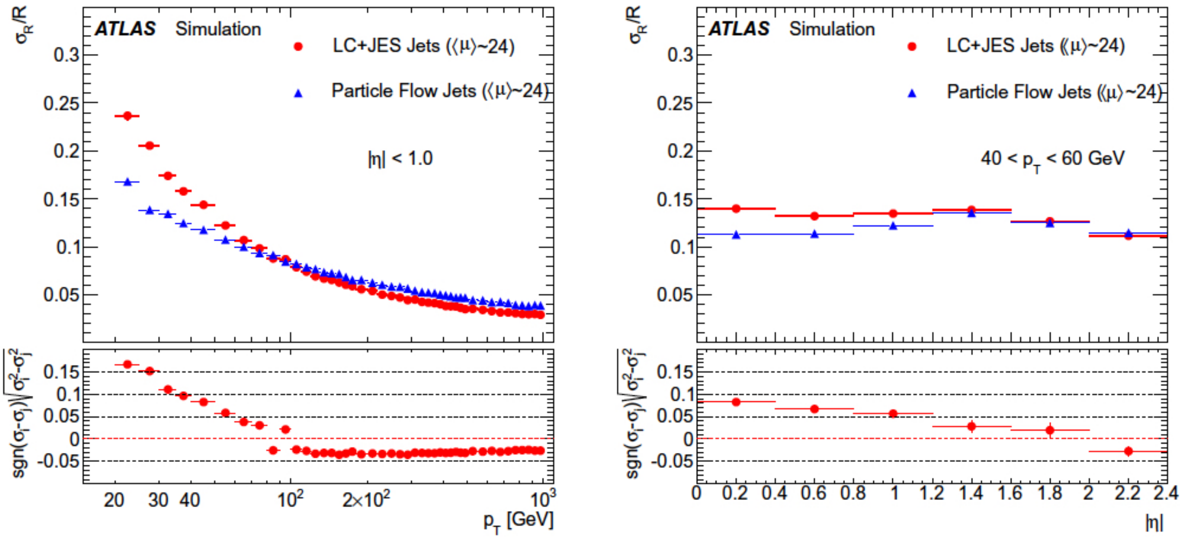

Figure 3.10: Comparison of results from particle flow and calorimeter jets for the jet resolution (left) and pile-up stability (right) using a dijet MC sample[95].

topo-cluster. Therefore, in a next step, the probability that the particle deposited its energy in multiple topo-clusters is evaluated for each track-cluster match. Based on the resulting probability, it is decided whether more topo-clusters are needed to be added to the system, in order to recover the energy of the full shower in the calorimeter. Finally, the following subtraction algorithm is applied to all tracks in descending p_{T} order starting with tracks where only one single cluster was matched: For each track the expected energy deposited in the calorimeter is subtracted from the matched topo-clusters on a cell-by-cell basis. For the topo-cluster remnants, it is evaluated whether the amount of energy is consistent with the shower-fluctuations of a single particle's signal. If so, the whole remnant is removed.

During my PhD thesis, I have worked on improving and evaluating the performance of the cell-subtraction algorithm (see Section 3.6.5) and evaluated the impact of several variations to the track-cluster matching step (see Section 3.6.4).

3.6.2 Jet reconstruction and calibration

Particle flow jets are reconstructed in a similar way to the standard calorimeter jets. The anti-k_t algorithm is used with a radius parameter of $R = 0.4$. However, the inputs differ, as for particle flow jets a different set of tracks and topo-clusters is used. The input tracks are matched to the hard scatter primary vertex and selected based on the z_0 component of the track impact parameter, satisfying $|z_0 \sin\theta| < 2\,\mathrm{mm}$. This criterion removes many tracks resulting from pile-up interactions [95]. In addition, the topo-cluster η and ϕ positions are calculated with respect to the hard-scatter vertex instead of the detector centre. The jet calibration follows the procedure for standard calorimeter jets with a few modifications described in [95].

3.6.3 Jet energy resolution

As shown in [95], the transverse momentum resolution of particle flow jets performs better than calorimeter jets at transverse momenta up to 90 GeV. The angular resolutions and pile-up resistance are also significantly better in this p_{T} range, as can be seen in Fig. 3.10. This is mostly due to the resolution of the tracking system being superior to the calorimeter one at low transverse momenta (up to 140 GeV for single pions).

3.6.4 Improvements to the track-cluster matching

In order to remove the energy of the charged particles from the calorimeter, the selected tracks have to be matched to clusters in the calorimeter. Therefore, they are extrapolated through the magnetic field of the Inner Detector to the second layer of the EM calorimeter (EM2). Next, the distances $\Delta\eta$ and $\Delta\Phi$ of the track position in EM2 to all clusters are computed. The clusters cover a significant area in the calorimeter and can contain energy deposits from multiple clusters. Therefore, a modified distance measure $\Delta R'$ is used, defined as

$$\Delta R^{'} = \sqrt{(\Delta\eta/\sigma_{\eta})^{2} + (\Delta\phi/\sigma_{\phi})^{2}}, \tag{3.17}$$

where $\sigma_{\eta}, \sigma_{\phi}$ denote the standard deviations of the cell positions in the cluster in the η and ϕ directions. This alternative distance measure takes into account a clusters expansion in space. In case multiple particles deposit their energy in the same cluster this expansion can be significant and it is, thus, advantageous to use $\Delta R'$ over using simply ΔR.

For very small clusters a minimum value of 0.05 in σ_{η} and σ_{ϕ} is set. The closest cluster in $\Delta R'$ that fulfils $E/p_{\text{track}} > 0.1$ is proposed for subtraction. If the distance between the track and this cluster is larger than $R^{'} = 1.64$, it is assumed that the charged particle corresponding to the respective track did not produce a cluster in the calorimeter. Hence, no energy is subtracted.

Match to the layer where the maximum energy is deposited

By default, the minimum distance between the cluster and the track is defined as the distance between the cluster centre and the track position extrapolated to the second layer of the EM calorimeter (EM2). However, if a track has two nearby clusters, one of them might appear further away, just because it is not in the layer where the track position is taken from. To account for that, the layer in which most of the cluster energy is located is determined for each cluster and used for matching. The performance of the resulting matching is then compared to the one of the default matching.

In order to determine the layer with the maximum cluster energy, the calibration hits associated with a certain cluster are summed up separately within each layer. The distance between cluster and track is then calculated using the cluster centre and the track position in the layer with the maximum calibration hit energy. This study is performed on single pion samples generated with a particle gun at energies between 600 MeV and 8 GeV. For the EM calorimeter three end-cap (EME1-3) and three barrel (EMB1-3) regions are distinguished. Similarly, for for the hadronic calorimeter, the four layers in the end-cap region (HEC1-4) and three layers in the barrel region (Tile1-3) are considered separately.

The layer that was used in the alternative matching depends on the particle's energy as can be seen from Fig. 3.11. Here the calorimeter layer chosen from matching is shown for single pion MC samples generated at different pion energies between 0.6 to 8 GeV. For low momentum particles, this layer is, as expected, mostly EM1 or EM2. While higher momentum particles, 5 to 8 GeV, sometimes deposit more energy in the Tile than low momentum particles, EM2 still often contains most of the energy.

The distribution of the minimum $\Delta R'$ and ΔR for the default eFlowRec matching and the match to the layer with most energy is compared.

The results are shown in Fig. 3.12. For the high energy samples, i.e. 5 GeV and 8 GeV, no significant difference in the $\Delta R'$ or ΔR distributions is observed. On the other hand, for the low energy particles with energies up to 1 GeV, the distributions calculated with the alternative matching procedure become much

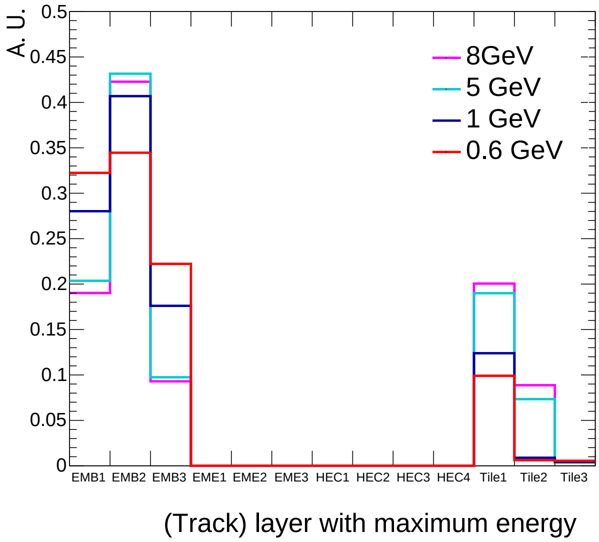

Figure 3.11: Calorimeter layer where most of the pion's energy was deposited. The calculation was performed based on calibration hits for single pion samples generated at four different energies. Here the EME layers denote the EM end-cap, EMB the EM barrel regions, HEC the hadronic end-cap and Tile the hadronic barrel calorimeter regions.

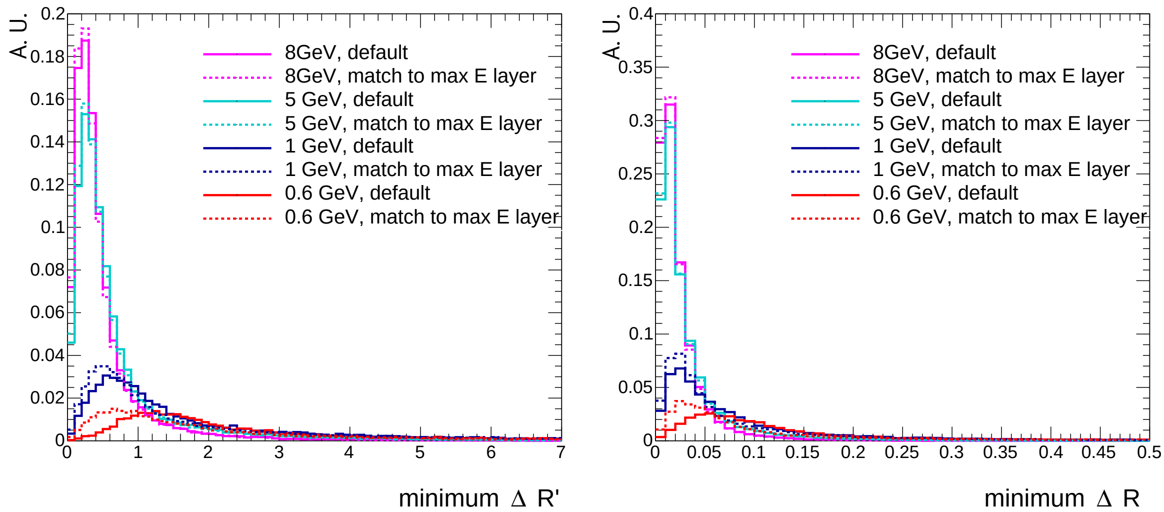

(a)

(b)

Figure 3.12: Comparison of minimum $\Delta R'$ (a) and minimum ΔR (b) values for the default matching and the matching to the layer that contains most of the particle's energy for single pions with energies between 600 MeV and 8 GeV.

narrower. This results in more track-cluster matches, since the cut-off values remain at $\Delta R' < 1.64$ and $\Delta R < 0.2$.

In order to evaluate the different matches, a quality variable is defined as

$$Q = \frac{E_{\text{cluster}} - E_{\text{CalHits}}}{\left(E_{\text{CalHits}} + \left|E_{\text{cluster}} - E_{\text{CalHits}}\right|\right)} = \frac{E_{\text{noise}}}{\left(E_{\text{CalHits}} + \left|E_{\text{noise}}\right|\right)}. \tag{3.18}$$

A good match corresponds to $Q = 0$, which is the equivalent of matching to a cluster with $\varepsilon_i^{\text{clus}} = 1$. Here $\varepsilon_i^{\text{clus}}$ denotes the fraction of true energy deposited by a truth particle in a cluster i. This fraction is defined as

$$\varepsilon_i^{\text{clus}} = \frac{\sum_f E_{if}^{\text{true}}}{\sum_k \sum_l E_{kl}^{\text{true}}} \tag{3.19}$$

where E_{ij}^{true} connotes the energy this particle deposited in cell j of cluster i. This $\varepsilon_i^{\text{clus}}$ is normalised to the overall energy the particle deposited in all cells of all clusters.

The distribution of Q is shown in Fig. 3.13 before and after the cut on $\Delta R'$. It can be seen, that the larger the noise contribution in the matched cluster is, the larger $|Q|$ becomes. It becomes obvious, that the cut on $\Delta R' < 1.67$ excludes all pure noise clusters. Also, the impact of the noise gets smaller with increasing energy and the peak approaches zero, which is expected from the definition of Q.

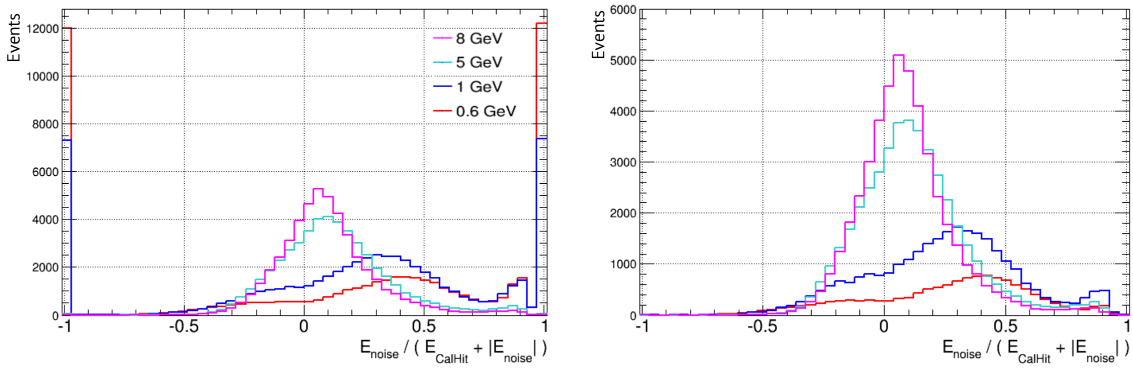

(a) Before the cut on $\Delta R'$ (default matching) (b) After the cut on $\Delta R'$ (default matching)

Figure 3.13: Quality Q defined in Eq. (3.18) for single pions with energies between 0.6 GeV and 8 GeV for the default matching, before and after the cut on $\Delta R'$.

Beside that, the correlation between Q and the corresponding cluster energy is studied. Therefore, the events are divided into four categories: one with more than 95 %; one with more than 50 %; one with less than 50 % of the particle's energy in one cluster; and one where less than 5 % of the particle's energy was clustered at all. The correlation is plotted separately for all four categories. The distributions can be found in Fig. 3.14 for 0.6 GeV and Fig. 3.15 for 8 GeV.

Match always to EM1 layer

In most of the cases the (overall) smallest distances are achieved when matching to the track position in EM1 [95]. Hence, also the effect of matching always to EM1 instead of EM2 was investigated.

The impact on the distribution of the distance between a track and the closest cluster is displayed in Fig. 3.16 for single pions with energies between 0.6 GeV and 8 GeV. For single pions with energies

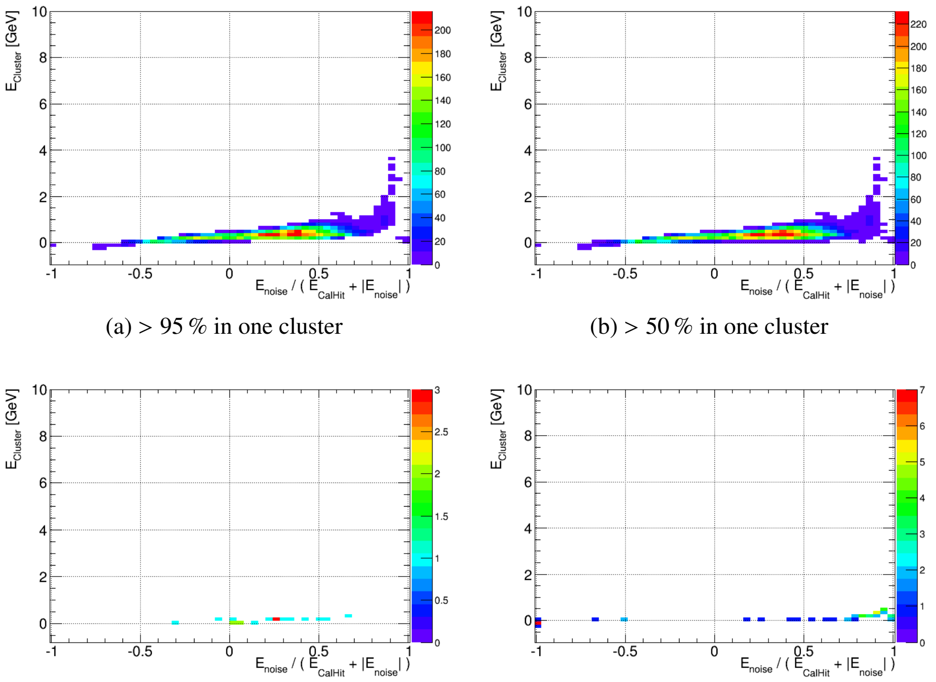

(a) > 95 % in one cluster

(b) > 50 % in one cluster

(c) < 50 % in one cluster

(d) < 5 % E_{particle} clustered

Figure 3.14: E_{cluster} vs. Q defined in Eq. (3.18) for 0.6 GeV pions (default matching) in four track–cluster matching categories. The colour code highlights the absolute number of events in the corresponding bin.

larger than 1 GeV, no significant difference between the EM1 and the default EM2 matching scheme was observed. Only in case of the lowest energetic pions a significant shift towards smaller ΔR and $\Delta R'$ values can be stated. Pions with energies up to 600 MeV are stopped rather early in the calorimeter system and hence deposit most of their energy already in the first layer. This could explain why the reconstruction is better when using EM1 instead of EM2 only at these low energies.

Comparison of all matching schemes

Figure 3.17 shows the distributions of the quality variable for clusters that contain more than 95 % of a charged particle's energy ("perfect case") for all three matching schemes. For single pions, no significant differences in this "perfect case" could be observed.

As a next step, the distribution of layers with the maximum energy for each cluster in dijet events with a hard scattering p_{T} of $8\,\mathrm{GeV} < p_{\mathrm{T}} < 17\,\mathrm{GeV}$ is studied and shown in Fig. 3.18. From this plot, it can be seen that in most of the cases EM1 is chosen for matching. In the studied events, both jets together have at most a p_{T} of 17 GeV. This means that the individual particles inside the two jets have very low energies. Thus, this result matches to what was observed on single pion samples: the lower the energy of the particle, the more often EM1 is picked for matching with this approach.

The minimum $\Delta R'$ and the quality (defined in Eq. (3.18)) distribution is shown in Fig. 3.19. For dijet events no significant differences between the different approaches is observed. Compared to the single pion case, the peak at +1 clearly dominates the Q-distribution. Its origin can be understood from looking at Q if less than 5 % of the particles energy is clustered (Fig. 3.20(b)). It can be seen, that in the case where a match was found, although most likely the particles in the jet did not produce a cluster, there are

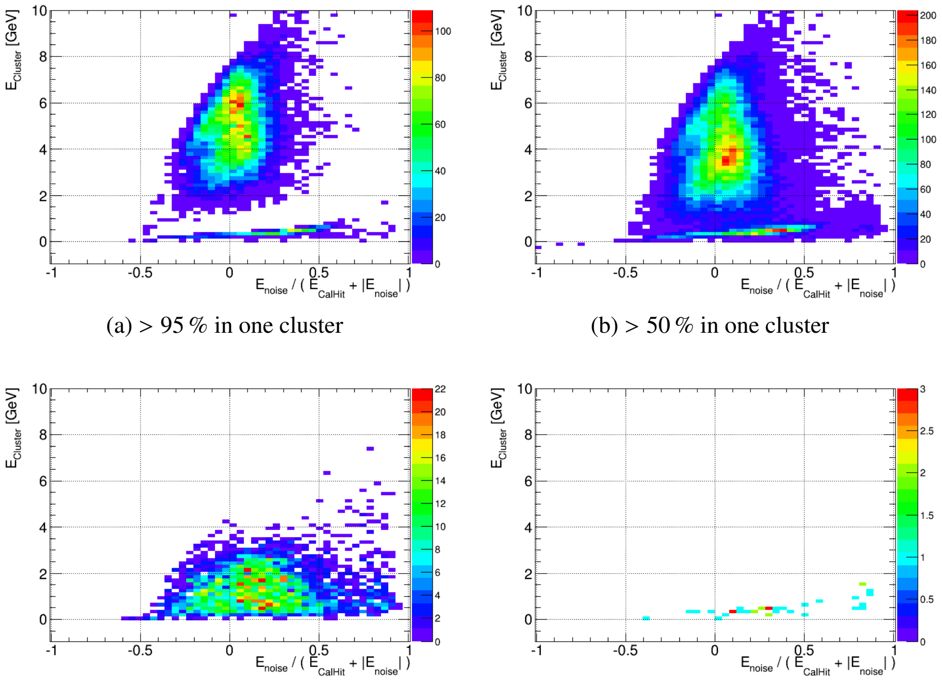

(a) > 95 % in one cluster

(b) > 50 % in one cluster

(c) < 50 % in one cluster

(d) < 5 % E_{particle} clustered

Figure 3.15: E_{cluster} vs. Q defined in Eq. (3.18) for 8 GeV pions (default matching) in four track–cluster matching categories. The colour code highlights the absolute number of events in the corresponding bin.

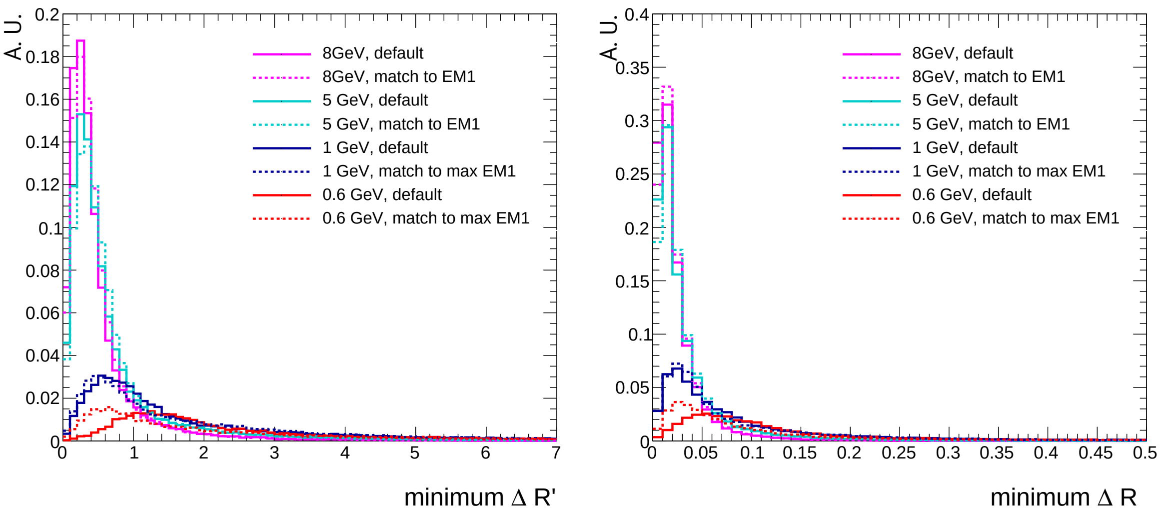

(a)

(b)

Figure 3.16: Comparison of the minimum (a) $\Delta R'$ and (b) ΔR values for the default matching to the track position in EM2 and the matching to the track position in EM1 for single pions with energies between 600 MeV and 8 GeV.

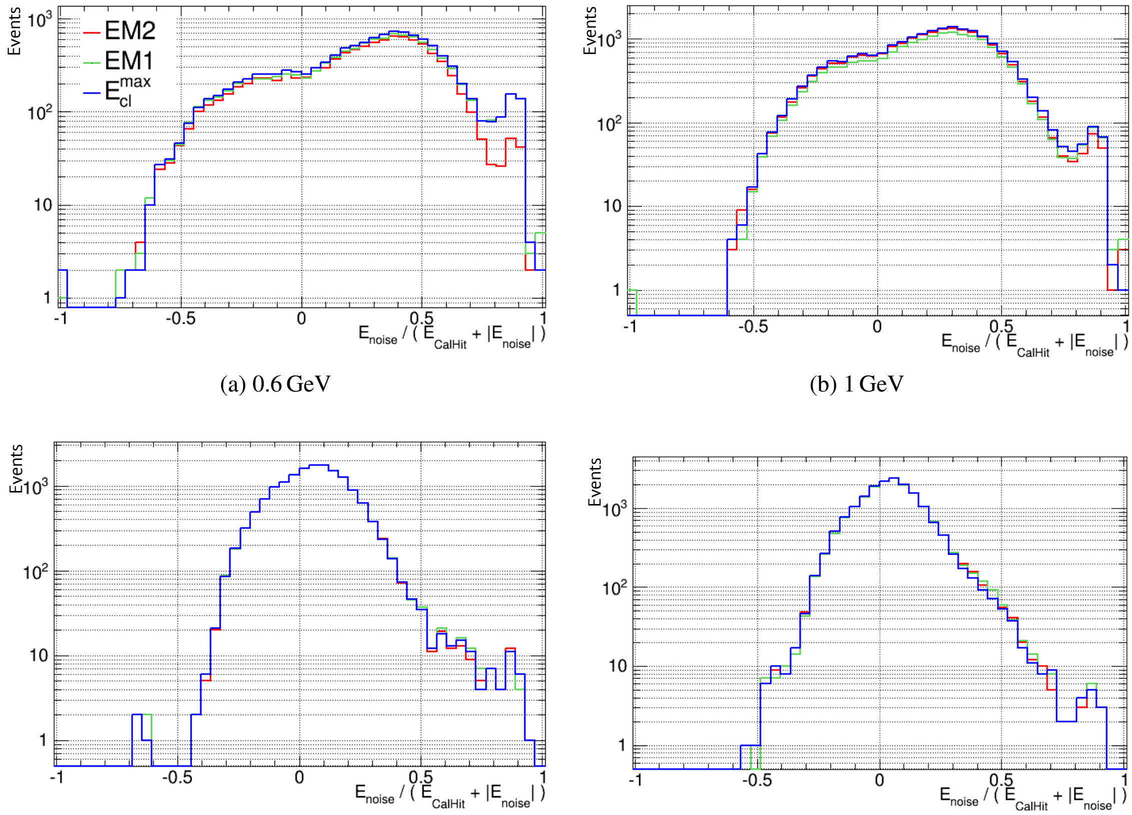

(a) 0.6 GeV

(b) 1 GeV

(c) 5 GeV

(d) 8 GeV

Figure 3.17: Distribution of Q defined in Eq. (3.18), calculated for single pion events with different p_T.

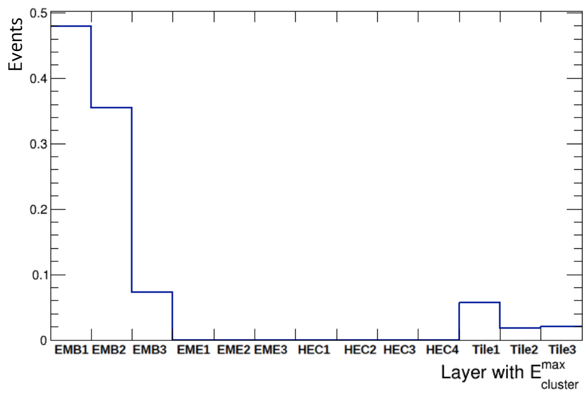

Figure 3.18: Calorimeter layer chosen for matching calculated on dijet events with an event hard scattering p_T of 8 GeV < p_T < 17 GeV.

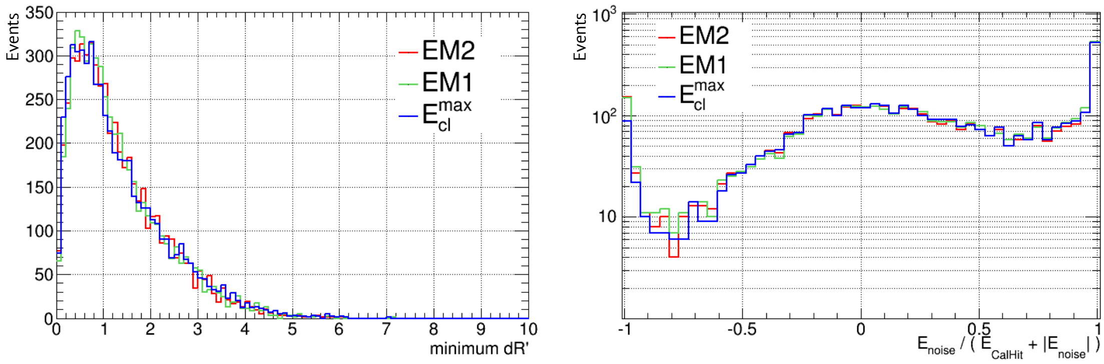

Figure 3.19: Minimum $\Delta R'$ and Q defined in Eq. (3.18) distribution for dijet events with an event hard scattering p_{T} of 8 GeV < p_{T} < 17 GeV for the three tested matching schemes.

strong peaks at -1 and $+1$ in the Q distribution.

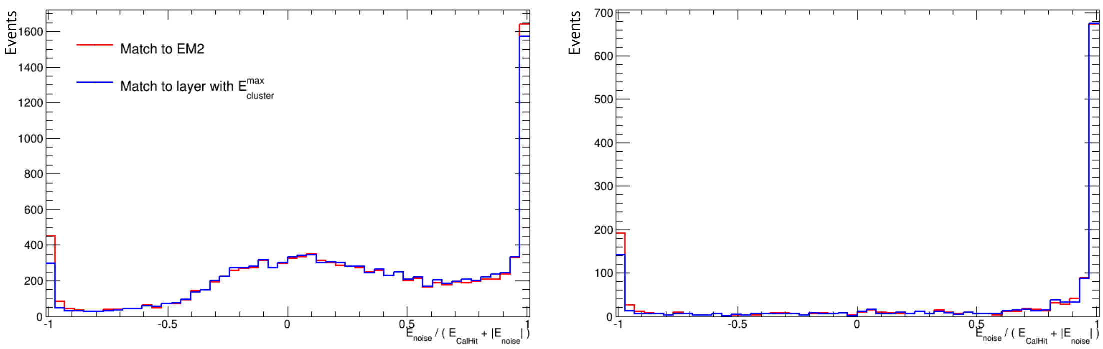

(a) Distribution of Q for all matched clusters $\Delta R' < 1.64$

(b) Distribution of Q for matched clusters with < 5 % of the particle's energy clustered.

Figure 3.20: Distribution of Q defined in Eq. (3.18) calculated on dijet events with an event hard scattering p_{T} of 8 GeV < p_{T} < 17 GeV.

In the single pion case, the peaks at $Q = -1$ and $Q = 1$ represent purely noise dominated clusters. In case of dijet events, they contain most likely erroneously matched clusters from neutral particles. The correlations between Q and the cluster energy for dijet events is shown in Fig. 3.21.

3.6.5 Improvements to the cell-subtraction algorithm

In order to measure the subtraction performance and compare different subtraction procedures, calibration hit information is used. The global performance of the subtraction can be categorised using the fraction of neutral energy left in the calorimeters (R^0) and the charged energy subtracted (R^+) per event. These quantities are calculated as

$$R^0 = \frac{\sum_{\mathrm{neutral}} E_{\mathtt{CalHit}}(\text{after subtraction})}{\sum_{\mathrm{neutral}} E_{\mathtt{CalHit}}(\text{before subtraction})} \tag{3.20}$$

$$(1 - R^+) = 1 - \frac{\sum_{\mathrm{charged}} E_{\mathtt{CalHit}}(\text{after subtraction})}{\sum_{\mathrm{charged}} E_{\mathtt{CalHit}}(\text{before subtraction})}. \tag{3.21}$$

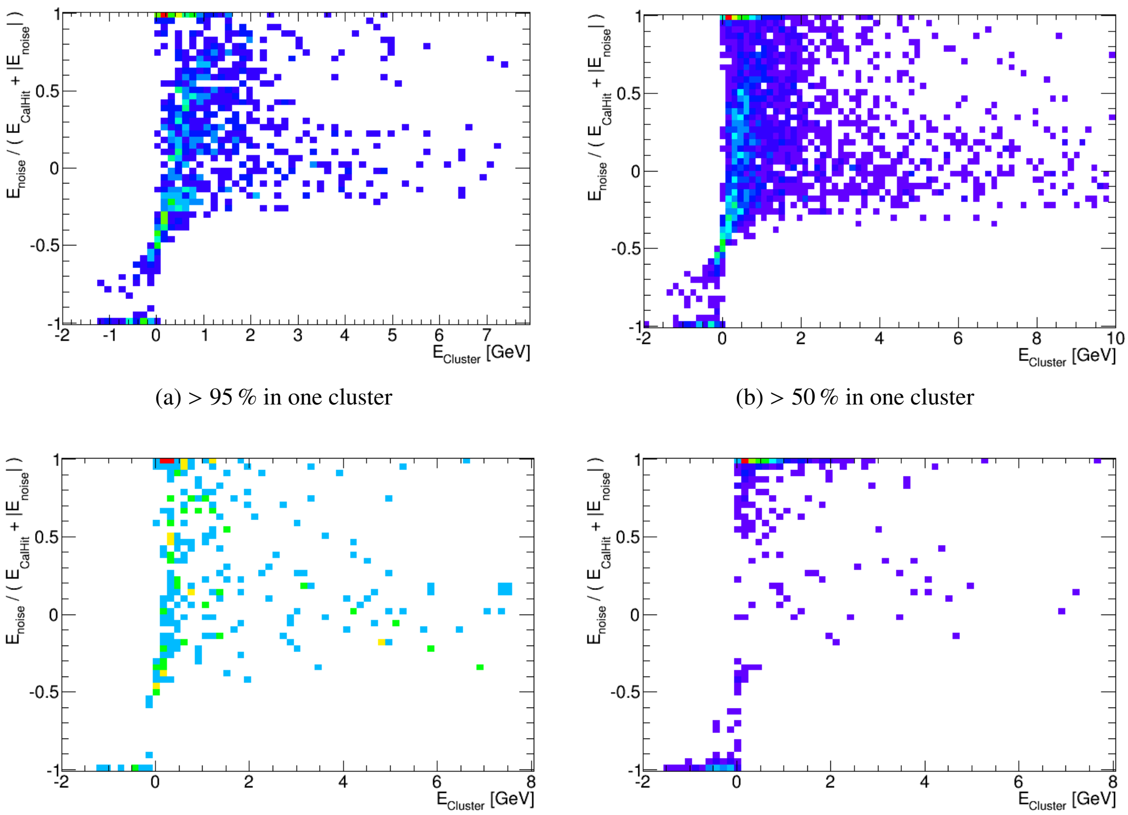

(a) > 95 % in one cluster

(b) > 50 % in one cluster

(c) < 50 % in one cluster

(d) < 5 % E_{particle} clustered

Figure 3.21: Q vs. E_{cluster} for dijet events with an event hard scattering p_{T} of $8\,\text{GeV} < p_{\text{T}} < 17\,\text{GeV}$. The colour code highlights the absolute number of events in the corresponding bin.

In the ideal case, all the neutral energy stays in the calorimeter system, while all the charged energy is subtracted. This corresponds to $R^0 = 1$ and $(1 - R^+) = 1$.

Detailed studies of individual events can be made using an event display that shows the energy deposited separately by charged and neutral particles in ECAL and HCAL, as well as the cluster coordinates and the projected hit position of the tracks. Such displays are very useful in order to test the algorithm and to try to see why certain decisions were made.

Skip first matching step

In the one-to-one matching, it can happen that a wrong cluster is matched to the track, or energy is missed because the charged particle created more than one cluster. Only if the energy of the matched cluster is significantly lower than what is expected from the E/p of the track, all cells within a cone of $\Delta R < 0.2$ are considered for the subtraction (split-shower recovery).

Skipping the first matching step, would clearly simplify the particle flow algorithm. In addition to that, the chances of missing energy coming from the track in the subtraction and thus, leaving it in the calorimeters, are lower. On the other hand, the chance of matching energy coming from a different particle increases especially in the dense particle environments of jets. The impact of this was studied in simulated events, to see which of the aspects dominates and whether it is possible to simplify the algorithm.

Back-to-font subtraction

In addition, the effect of reversing the order of cells from which energy is subtracted was studied. A large fraction of neutral pions decay into two photons, which shower in the EM calorimeter. On the other hand, charged hadrons deposit most of their energy in the hadron calorimeter, which are deeper in the detector system. This observation initiated the second variation of the subtraction procedure: to minimise the amount of erroneously subtracted neutral energy deposits in the early layers, the subtraction procedure was reversed. This means, it starts in the last calorimeter layer containing matched energy instead of in the layer of highest energy density (LHED). This was implemented in eflowRec by reversing the logic in the cell-ordering algorithm such that the layers for subtraction are chosen back-to-front.

Definitions of performance measures at event level

In order to measure the subtraction performance and compare different subtraction procedures, calibration hit information is used. Calibration hits represent the expected energy deposits in the calorimeters given the particle's Monte Carlo information. The global performance of the subtraction can be categorised using the fraction of neutral energy left in the calorimeters (R^0) and charged energy subtracted (R^+) per event. These quantities are calculated as shown in Eqs. (3.20) and (3.21). In the ideal case, all the neutral energy stays in the calorimeter system, while all the charged energy is subtracted. This corresponds to $R^0 = 1$ and $(1 - R^+) = 1$.

Furthermore, one has to take into account that tracks are only reconstructed within $0.0 < \eta < 2.5$ in the calculation of the overall R^0 and R^+. Hence, only calibration hits are included that have a pseudorapidity $|\eta| < (2.5 + \Delta\eta)$ when calculating the sums. $\Delta\eta = 0.2$ was chosen to take into account energy deposits from tracks close to the border of the tracker's range. In addition, the ratios can be calculated per cluster measuring the local performance, denoted by R^0_{cl} and $(1 - R^+_{\mathrm{cl}})$.

Three categories of subtraction performance are defined based on the overall R^0 and R^+. The best category contains all events where more than 95 % of the neutral energy is left over and at the same time more than 95% of the charged energy was subtracted. The medium and bad category are defined similarly as listed in Table 3.1.

	R^0		$(1 - R^+)$
Good	> 95%	&	> 95%
Medium	> 5% < 95%	&	> 5% < 95%
Bad	< 5%	or	< 5%

Table 3.1: Categorisation of the charged hadron subtraction performance.

Next, the efficiency or purity distributions are plotted separately for the different categories. Here the efficiency is a combination of the cluster efficiencies. It is calculated as the sum of all charged calibration hit energies in all clusters involved in the subtraction, divided by the sum of all charged calibration hit energies in the calorimeter.

The combined purity is then defined as the sum of the charged calibration hit energies in all subtracted clusters, divided by the sum of the charged and neutral calibration hit energies in these clusters.

Results on $\pi^+\pi^0$ particle-gun samples

As a first step, $\pi^+\pi^0$ particle-gun samples are analysed. These represent the simplified case of one charged and one neutral particle in the detector. In the sample used, both pions are generated with an energy of 5 GeV. The charged pion is generated with η and ϕ values of $0.0 < \eta < 0.6$, $0.0 < \phi < 0.6$, while the neutral pion is generated with fixed $\eta = 0.3$ and $\phi = 0.6$.

First, R^0 and R^+ are calculated per cluster for all three approaches in order to evaluate the local performance of the subtraction. One needs to take into account that the resulting R^0_{cl} and $(1 - R^+_{\text{cl}})$ distributions also include erroneously matched/not-matched clusters. These are responsible for the large peaks at zero in Fig. 3.22. Apart from that, for both alternative approaches, more clusters can be found in the middle region, i.e. between zero and one and the peak at $(1 - R^+) = 0$ is significantly lower. This means that less charged energy remains, which would then be falsely classified as neutral energy and double counted by eflowRec.

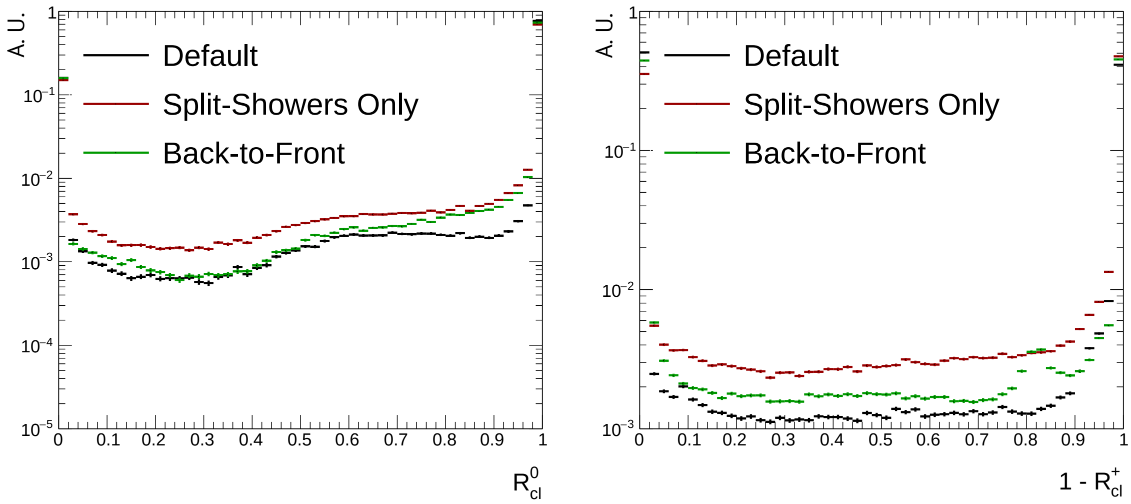

(a) (b)

Figure 3.22: (a) R^0 and (b) $(1 - R^+)$ calculated per cluster for a $\pi^+\pi^0$ particle gun sample generated with 5 GeV each for the default and the two alternative subtraction procedures.

However, these clusters can also contain only a very low fraction of the particle's energy. Thus, one has to relate these distributions to the fraction of neutral/charged energy in the considered cluster. The correlation between R^0 and R^+ with the neutral/charged energy is displayed in Figs. 3.23 and 3.24 split up into the three event categories defined in Table 3.1. From the plots, it can be seen that clusters with a high R^0 often also contain more neutral energy, while the ones with very low R^0 usually have energies smaller 1 GeV. For events from the worst category, an accumulation of clusters with low R^0 but 4 to 5 GeV of neutral energy is seen. The same holds for the plots showing the charged energy per cluster in Fig. 3.24.

Figure 3.25 shows $(1 - R^+)$ and R^0 calculated per event for the $\pi^+\pi^0$ sample. It contains three lines corresponding to the default procedure and the two variations described in Sections 3.6.5 and 3.6.5. Both distributions show a strong pronounced peak at one, as expected. The comparison of the three curves shows that the fraction of events for which all charged energy is taken out is larger for the two alternative approaches. In addition, for the back-to-front approach, the charged distribution is smoother at low $(1 - R^+)$ values. On the other hand, the fraction with all neutral energy left $(1 - R^+) = 1$ is smaller and the R^0 distributions are broader for both alternatives.

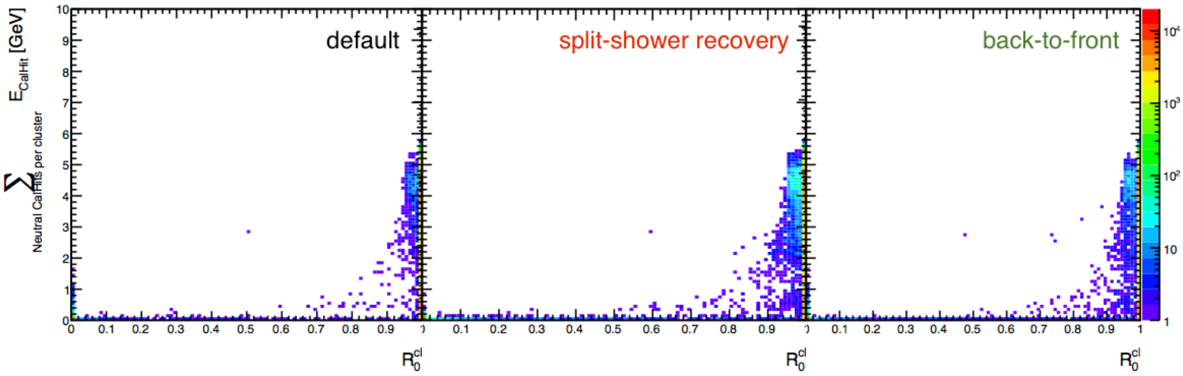

(a) Good: R^0 > 95% & 1-R^+ > 95%

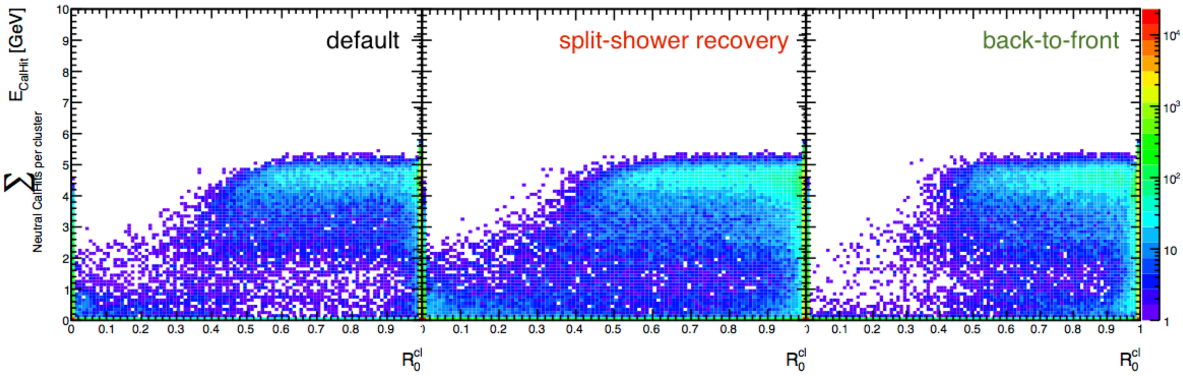

(b) Medium: 5% < R^0 < 95% & 5% <1-R^+ < 95%

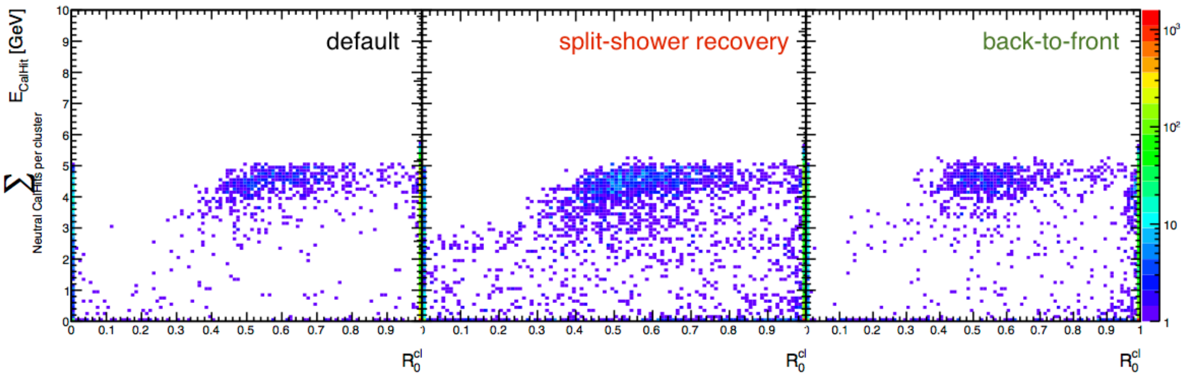

(c) Worst: R^0 < 5% or 1-R^+ < 5%

Figure 3.23: Correlation between R^0 and the neutral energy per cluster, calculated for a $\pi^+\pi^0$ particle gun sample generated with 5 GeV each for the three subtraction procedures. The events are separated into the (a) good, (b) medium and (c) worst categories. Going from left to right, each row of plots shows the default, split-shower recovery only and back-to-front approach. The colour code highlights the absolute number of events in the corresponding bin.

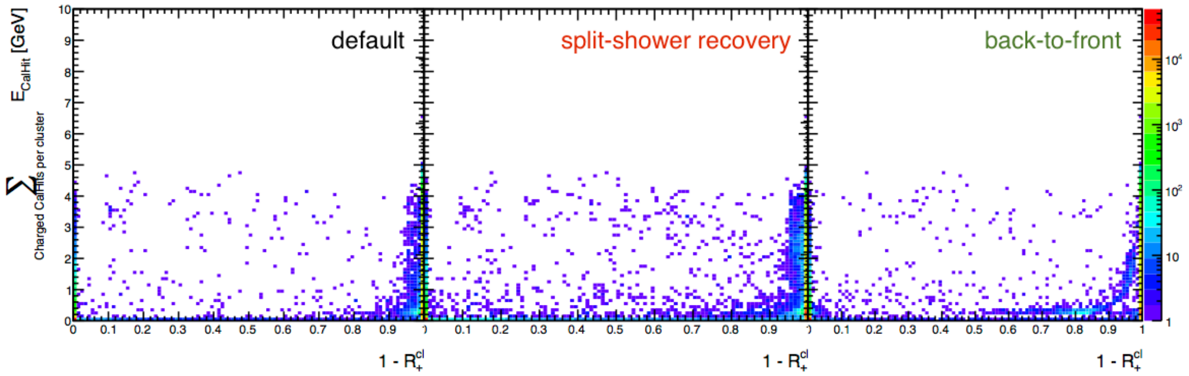

(a) Good: R^0 > 95% & 1-R^+ > 95%

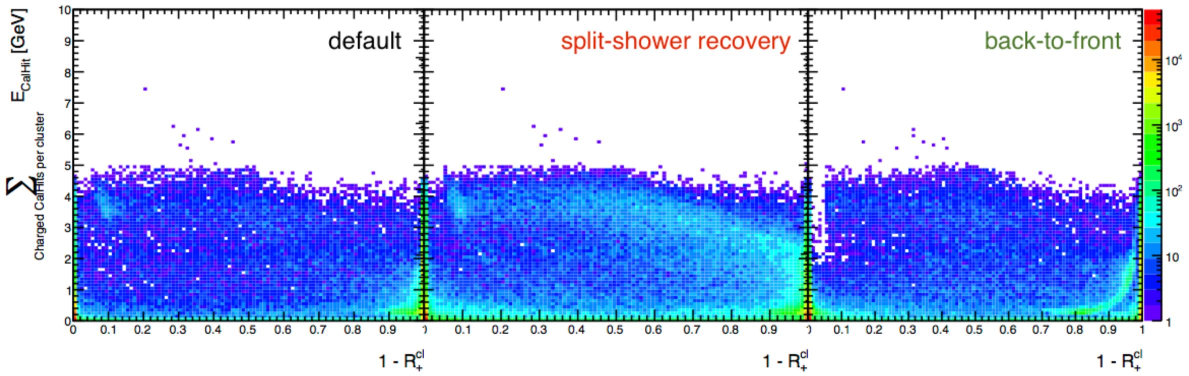

(b) Medium: 5% < R^0 < 95% & 5% <1-R^+ < 95%

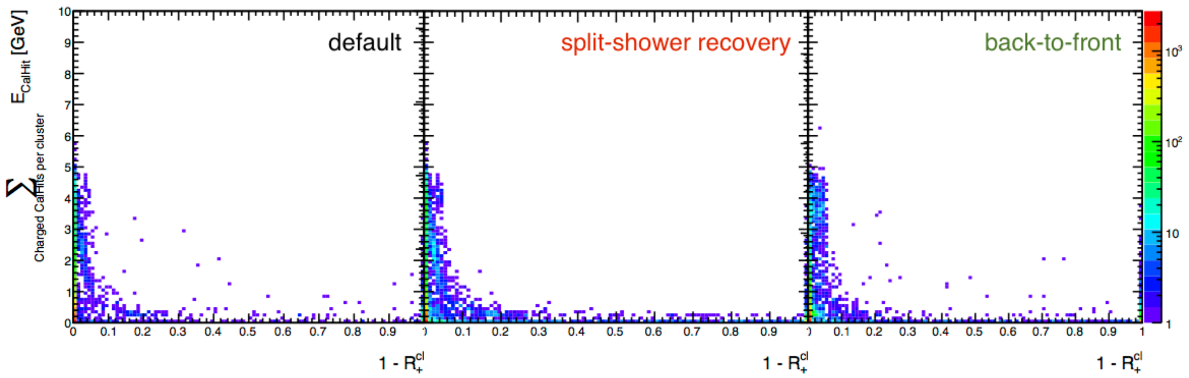

(c) Worst: R^0 < 5% or 1-R^+ < 5%

Figure 3.24: Correlation between $(1 - R^+)$ and the charged energy per cluster, calculated for a $\pi^+\pi^0$ particle gun sample generated with 5 GeV each for all three subtraction procedures. The events are separated into the (a) good, (b) medium and (c) worst categories. Going from left to right, each row of plots shows the default, split-shower recovery only and back-to-front approach. The colour code highlights the absolute number of events in the corresponding bin.

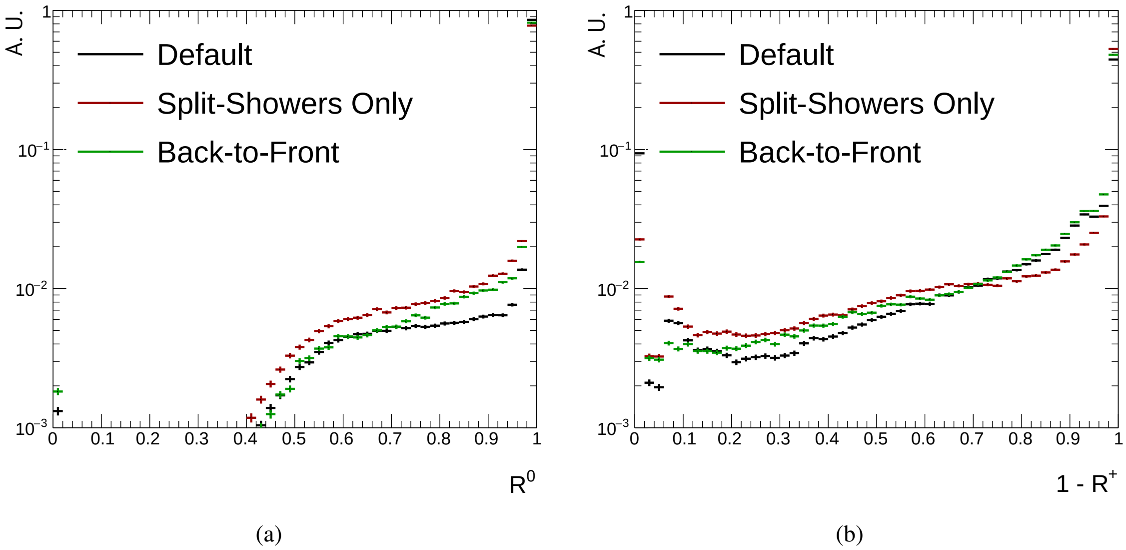

Figure 3.25: (a) R^0 and (b) $(1-R^+)$ distribution on a $\pi^+\pi^0$ particle gun sample generated with 5 GeV each.

Figure 3.26 shows the correlation between R^0 and $(1-R^+)$ in a 2-dimensional plot. Comparing the three subtraction approaches, one spots a crowded region at $(1-R^+) < 10\,\%$ and $R^0 \approx 60\,\%$. This is most pronounced for the first change (split-shower recovery only). For the back-to-front subtraction this region vanishes almost completely. Beside that, the peak in the upper-right corner is broadest in the back-to-front case.

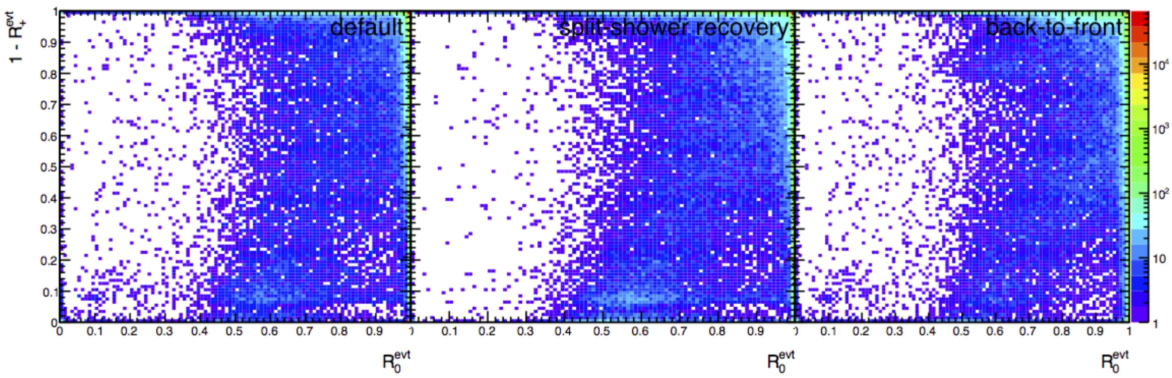

Figure 3.26: Correlation between R^0 versus $(1-R^+)$ on a $\pi^+\pi^0$ particle gun sample generated with 5 GeV each for the default, split-shower recovery only and back-to-front approach. The colour code highlights the absolute number of events in the corresponding bin.

The overall changes in the subtraction performance can be estimated better by comparing the fractions of events in each of the performance categories. They can be derived from the distributions in Fig. 3.26 and are listed in Tables 3.2 and 3.4. The number of events in the best category, i.e. R^0 and $(1-R^+)$ larger than 95 %, is enlarged for both alternative subtraction procedures. At the same time, the number of events in the worst category is reduced from 10 % to 2 to 3 %. This looks very promising and motivated to run eflowRec with these changes implemented also on dijet events.

In order to find out why and where the subtraction performs better/worse, we plot the ΔR between

R^0 \(1- R^+)	> 0.95 [%]	<= 0.95 & >= 0.05 [%]	< 0.05 [%]	Sum [%]
> 0.95	46	32	9.2	87
<= 0.95 & >= 0.05	3.3	8.7	0.6	13
< 0.05	0.03	0.06	0.05	0
Sum	49	41	10	100

Table 3.2: Categorisation of the $\pi^+\pi^0$ particle-gun sample at 5 GeV each by R^0 and R^+ with the default eflowRec subtraction.

R^0 \(1- R^+)	> 0.95 [%]	<= 0.95 & >= 0.05 [%]	< 0.05 [%]	Sum [%]
> 0.95	52	27	1.6	81
<= 0.95 & >= 0.05	5.6	13	1.1	19
< 0.05	0.04	0.02	0.01	0
Sum	58	40	3	100

Table 3.3: Categorisation of the $\pi^+\pi^0$ particle-gun sample at 5 GeV each by R^0 and R^+ with the split-shower recovery only eflowRec subtraction.

R^0 \(1- R^+)	> 0.95 [%]	<= 0.95 & >= 0.05 [%]	< 0.05 [%]	Sum [%]
> 0.95	50	33	1.3	84
<= 0.95 & >= 0.05	4.8	10.1	0.61	16
< 0.05	0.07	0.08	0.06	0
Sum	55	43	2	100

Table 3.4: Categorisation of the $\pi^+\pi^0$ particle-gun sample at 5 GeV each by R^0 and R^+ with the back-to-front eflowRec subtraction.

the neutral pion and the track, efficiency and purity distributions, split up into the three performance categories as defined in Table 3.1. Figures 3.27 and 3.29 show the distributions for the default, split-shower recovery and back-to-front approaches. All plots are area normalised. Events from the best category show very high efficiency and purity, since 78 % of the events have an efficiency and 96 % a purity equal to one (for the default subtraction). For the medium category this is already significantly reduced to 25 % of the events having an efficiency and 56 % a purity of one. Furthermore, the ΔR distributions in Fig. 3.27 show that the subtraction works best, if the distance between the neutral pion and the track is rather large. This is clear, since in this case, we have no overlap of the clusters and thus as little confusion as possible. The split-shower recovery only subtraction, corresponding to the middle plots in Figs. 3.27 and 3.29, results in an increase of the peak at one in the efficiency distribution for all categories. At the same time, the peak at zero efficiency decreases for the worst category. The latter observation also holds for the back-to-front subtraction. Regarding the purity, both changes result in the peaks at zero and one being more pronounced for the worst category. This is mainly due to the fact that the statistics in this category drops (from 10 % of all events to 2 to 3 %). This can be interpreted as matches were either right or completely wrong with the two alternative subtractions.

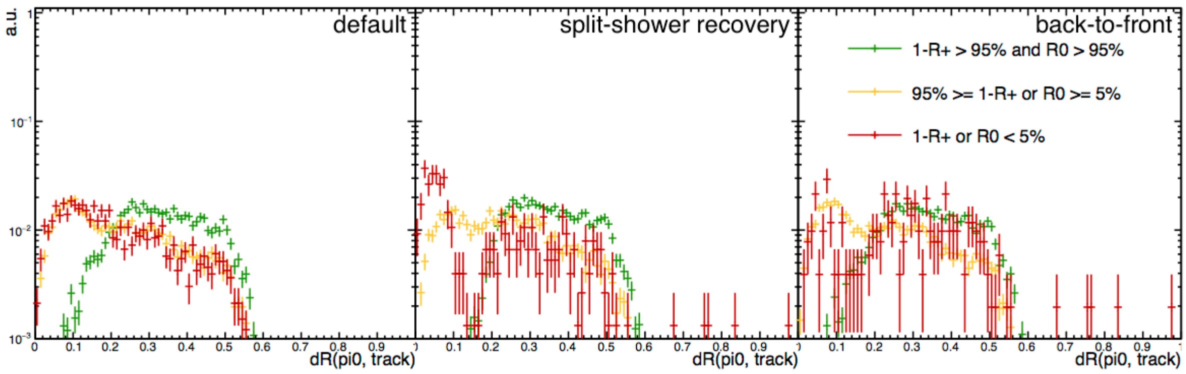

Figure 3.27: ΔR between the neutral pion and the track calculated for a $\pi^+\pi^0$ sample with 5 GeV each for the default, split-shower recovery only and back-to-front subtraction.

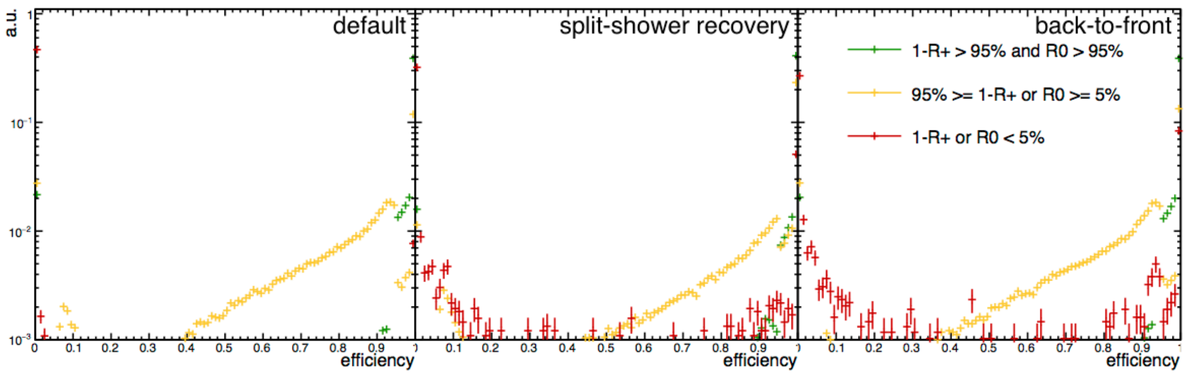

Figure 3.28: Combined efficiency calculated for a $\pi^+\pi^0$ sample with 5 GeV each for the default, split-shower recovery only and back-to-front subtraction.

Apart from that, the event displays are used to check how the calibration hit energy is distributed in the calorimeters in case the subtraction went clearly wrong. One example event display can be found

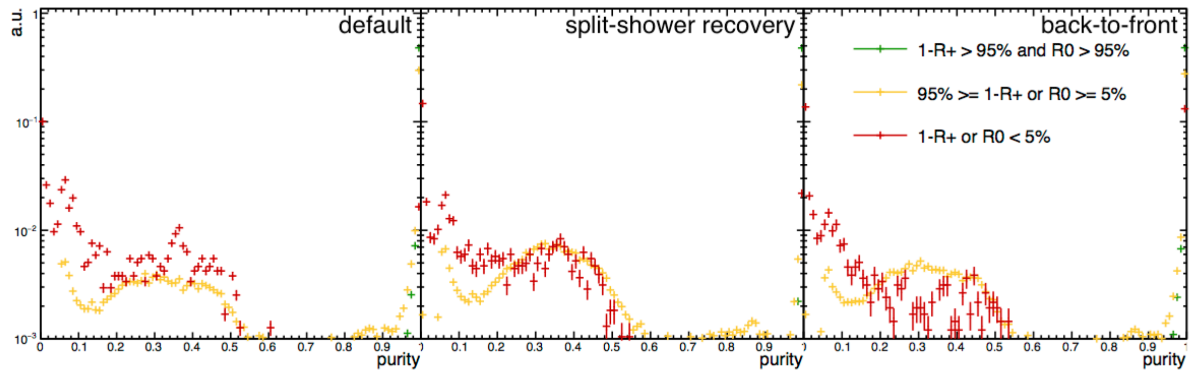

Figure 3.29: Combined purity calculated for a $\pi^+\pi^0$ sample with 5 GeV each for the default, split-shower recovery only and back-to-front subtraction.

in Fig. 3.30. It shows the distribution of the calibration hit energy in η–ϕ space. The colour of a box indicates the charge of the cluster (blue neutral, red charged), while the size scales with the amount of energy. The event is taken from the worst subtraction category. The plus signs indicate the track extrapolation to EM1-3. The circles show cluster positions and the crosses indicate whether a cluster was matched to a track or not. This example indicates that mainly neutral energy (blue squares) is deposited in the electromagnetic calorimeters, while all the charged energy is measured in the hadron calorimeter. Both clusters are very close together in η and ϕ. Since the subtraction starts close to the layer of highest energy density, a large amount of energy is subtracted from the ECAL. This energy originates mainly from the neutral pion, while most of the charged energy in the HCAL is left over.

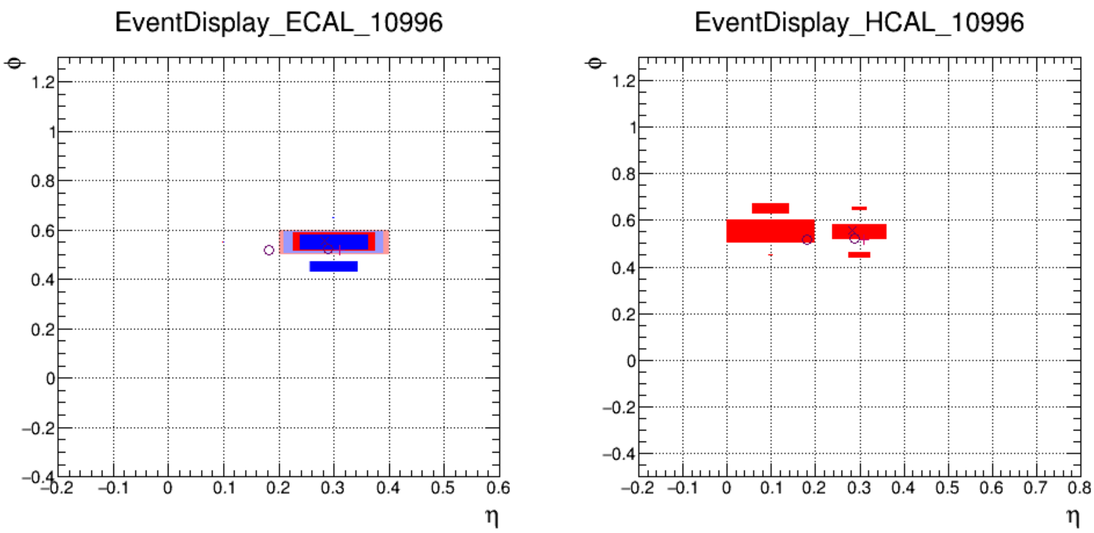

(a)

(b)

Figure 3.30: Example event display showing the distribution of the calibration hit energy in η–ϕ space for (a) ECAL and (b) HCAL. The event is taken from the worst subtraction category and a $\pi^+\pi^0$ sample with 5 GeV pion energy each. The + indicate the track positions in EM1-3. The ∘ show the cluster positions and the x indicates whether a cluster was matched to a track or not.

To disentangle the effects of track–cluster matching and subtraction performance, events with a combined matching efficiency larger than 95 % are studied. In this case the fraction of events with a high subtraction performance is significantly larger. It increases from 46 % to 78 %, as can be seen from Table 3.5.

R^0 \(1- R^+)	> 0.95 [%]	<= 0.95 & >= 0.05 [%]	< 0.05 [%]	Sum [%]
> 0.95	78	8.7	0.02	87
<= 0.95 & >= 0.05	5.6	7.0	0.22	13
< 0.05	0.05	0	0	0
Sum	84	16	0	100

Table 3.5: Categorisation of the $\pi^+\pi^0$ particle-gun sample at 5 GeV each by R^0 and R^+ with the default eflowRec subtraction, but for events with $\varepsilon > 95$ % only.

The ΔR distribution gives an even clearer picture for this case, as can be seen from Fig. 3.31: the smaller the radial distance between the neutral and the charged particle, the worse the performance. The crowded spot at low $(1 - R^+)$ which was present before in the R^0–$(1 - R^+)$ correlation plot vanishes if only events with high matching efficiency are taken into account, as can seen in Fig. 3.31. This means that it was an artefact of matching the wrong cluster in the first matching step and not an issue of the subtraction itself.

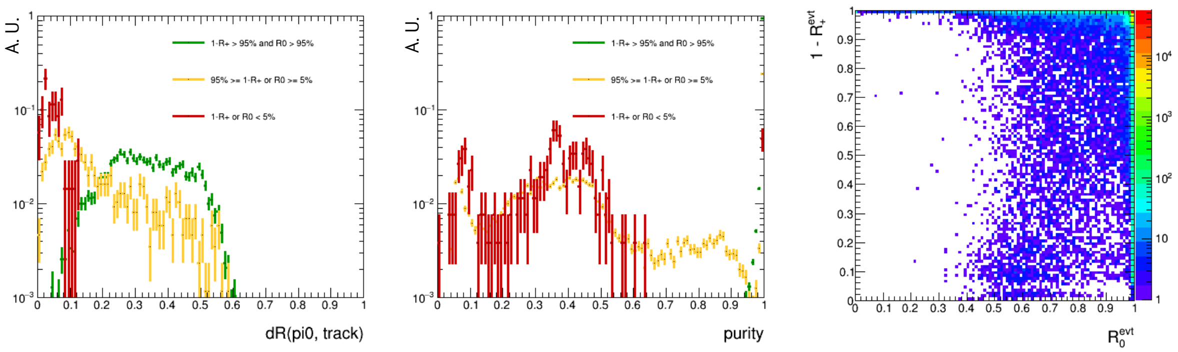

Figure 3.31: ΔR between the neutral pion and the track, combined purity and R^0-R^+-correlation calculated on a $\pi^+\pi^0$ sample with 5 GeV each for the default subtraction.

eflowRec uses tracks as charged ingredients of the jets and clusters as neutral ones. Thus, it is important to check that the neutral particles' resolution does not worsen when changing the algorithm. Figure 3.32 shows the energy, η and ϕ resolution of the neutral pions. The energy resolution is calculated as the difference of the neutral particle flow object's energy and the sum of all neutral calibration hits, which in the case of a $\pi^+\pi^0$ sample necessarily come from the neutral pion. No significant change in neither the energy nor the angular resolutions is observed.

Results on dijet samples

In order to estimate the real impact of the changes on jets, R^0 and R^+ are calculated on events with two jets (dijet events). Figure 3.33 shows their distributions for the default subtraction and the two variations in comparison. In general, the peaks of both distributions are significantly broader than in the clean

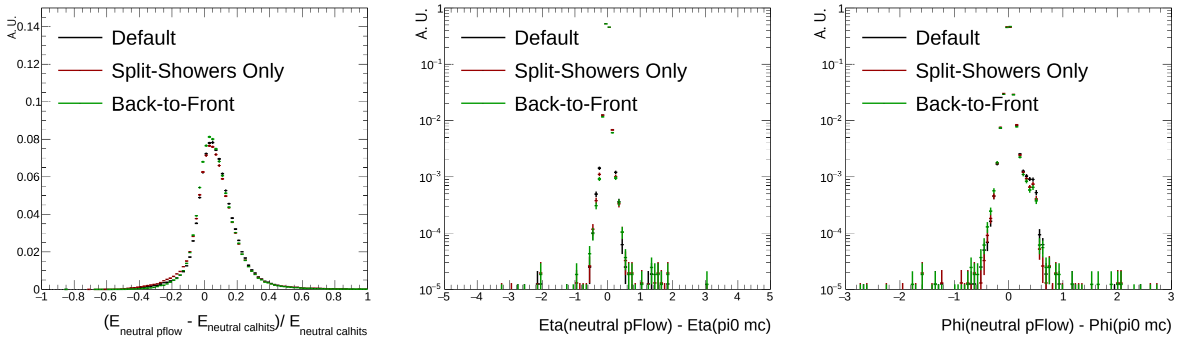

Figure 3.32: Energy, η and Φ Resolution of the neutral pion for the $\pi^+\pi^0$ particle-gun sample generated at 5 GeV each.

two-particle case, as expected. In addition, they are shifted to smaller values, which is most obvious for the $(1 - R^+)$ distribution. On dijet events, only about 80 % of the charged energy per event is subtracted, while still more than 90 % of the neutral energy is left in the calorimeter. Applying split-shower recovery only, both peaks are shifted towards lower values and thus decreases the subtraction performance. This shows that although it worked very well in the ideal case of one charged and one neutral pion, in the dense environment of jets this introduces too much confusion. This can e.g. be due to more neutral energy being erroneously subtracted. However, the second change, subtracting back-to-front, seems to point in the right direction. Although the peak of the R^0 distribution is slightly shifted towards lower values, the correctly subtracted charged energy is increased by 10 %. In order to implement this in eflowRec, the ordering of the cells was completely reversed. This means that those cells were subtracted first that were deepest in the calorimeter and furthest from the track. It would probably be better to keep the subtraction inside-out and just change the starting point to the back for the future.

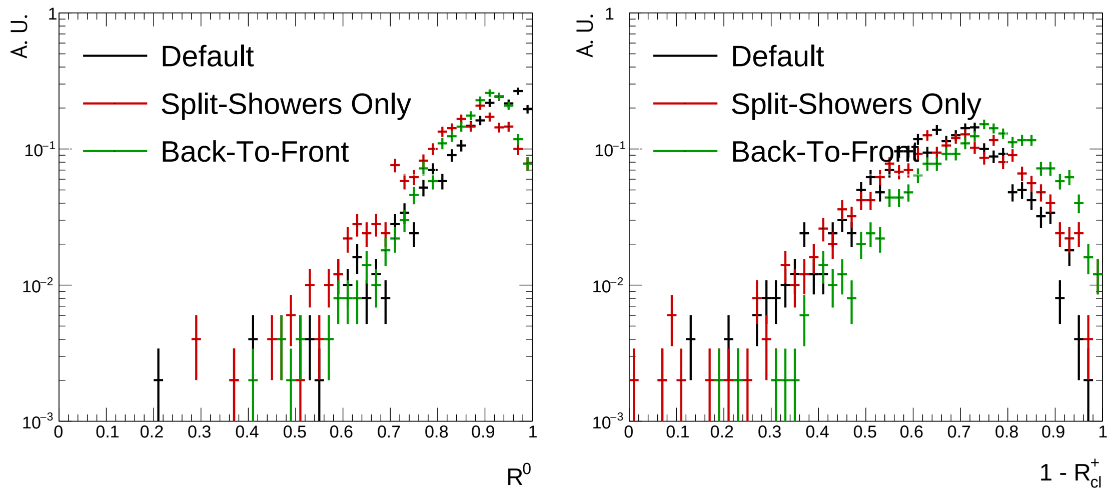

Figure 3.33: R^0 and R^+ on dijet events with a hard scattering p_{T} of 17 GeV < p_{T} < 35 GeV.

From the correlation plots in Fig. 3.34 it follows that for the split-shower recovery only approach, the points are much more scattered in the x- and y-directions compared to the other two cases. This further disfavours this approach. However, regarding the back-to-front approach, the two-dimensional

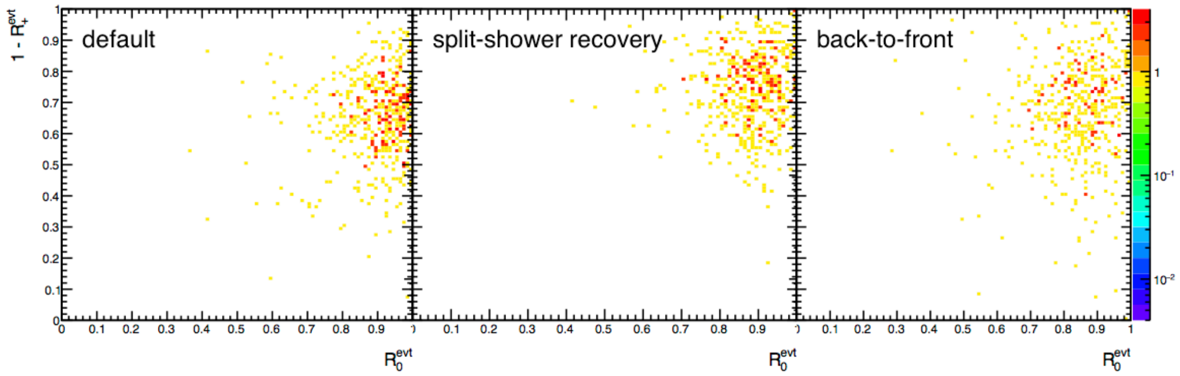

Figure 3.34: Correlation between R^0 versus R^+ on dijet events with a hard scattering p_T of 17 GeV < p_T < 35 GeV for the default, split-shower recovery only and back-to-front approach. The colour code indicates the normalised number of events in each bin.

distribution is much narrower.

Again, the correlation between R^0 and $(1 - R^+)$ (Fig. 3.34) is investigated. In contrast to the two-pion sample, there are no events in the worst category anymore and significantly fewer in the best one. Most of the events actually end up in the medium class. The actual percentages are listed in Table 3.6.

	Good [%]	Medium [%]	Bad [%]
Default	0.2	99.8	0.0
Split shower recovery only	0.7	99.2	0.1
Back-to-front	0.9	99.1	0.0

Table 3.6: Categorisation of dijet events with a hard scattering p_T of 17 to 35 GeV.

Regarding the fact that now almost all events end up in the medium category, the cut values for the three categories defined in Section 3.6.5 seem not to be appropriate any more. According to the distributions of the two ratios, different values are chosen for dijet events which can be found in Table 3.7.

	R^0		$(1 - R^+)$
Good	> 90%	&	> 90%
Medium	> 50% < 90%	&	> 50% < 90%
Bad	< 50%	or	< 50%

Table 3.7: Categorisation of the charged hadron subtraction performance.

Applying these values for the categorisation, the fraction of events in each category (Table 3.8), efficiencies (Fig. 3.35) and purities (Fig. 3.36) are computed. Again, the same effect is observed that was also present in the two pion case, i.e. the back-to-front approach shows significantly more events in the best category (a factor 5 more) and fewer in the worst. Comparing the efficiency and purity distributions with the ones from the two-pion case, one observes, that the purity is close to zero for all three approaches. The efficiency is, similar to what was observed in the two-pion case, higher in the split-shower recovery only and lower in the back-to-front approach.

	Good [%]	Medium [%]	Bad [%]
Default	1	87	12
Split-shower recovery only	2	85	13
Back-to-front	5	92	7

Table 3.8: Categorisation of dijet events with a hard scattering p_T of 17 to 35 GeV.

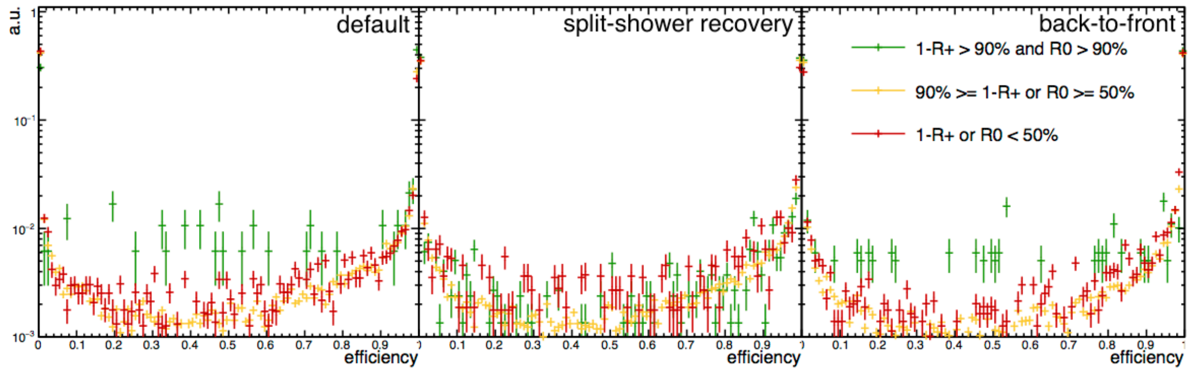

Figure 3.35: Efficiency calculated on dijet events with a hard scattering p_T of 17 GeV < p_T < 35 GeV for the default, split-shower recovery only and back-to-front approaches.

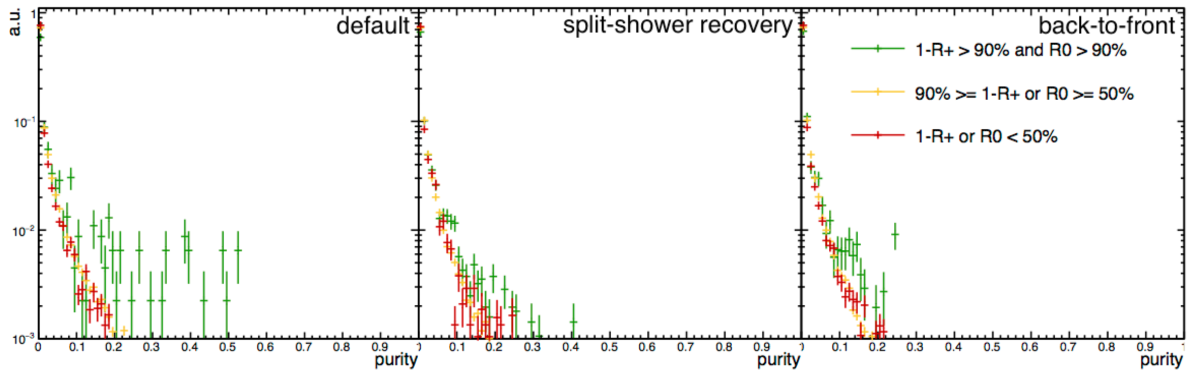

Figure 3.36: Purity calculated on dijet events with a hard scattering p_T of 17 GeV < p_T < 35 GeV for the default, split-shower recovery only and back-to-front approaches.

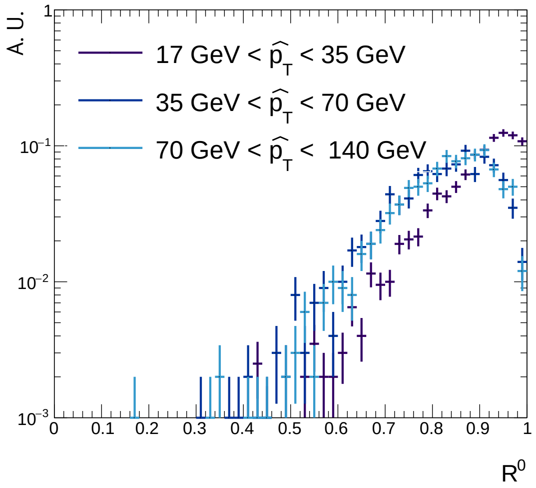

(a)

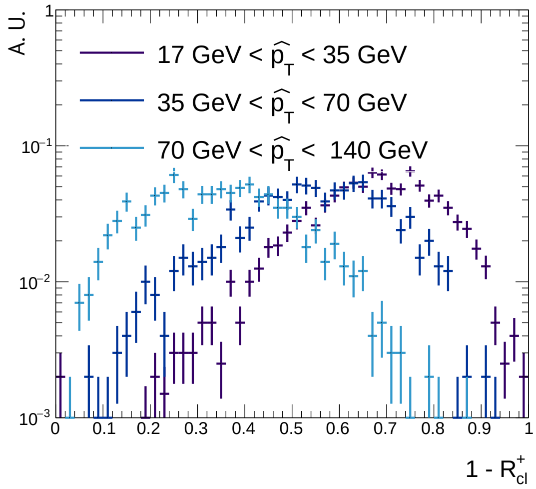

(b)

Figure 3.37: (a) R^0 and (b) R^+ binned in terms of the hard scattering p_T per event calculated on dijet events.

Figure 3.37 shows the two ratios calculated for different jet energy ranges using the default subtraction. One observes that the performance depends on the jet energy. As the hard scattering p_T is increased and together with it the jet p_T, the peaks of both distributions are flattened and move to lower values.

In order to better understand the origin of these differences, R^0 and R^+ are defined per calorimeter-layer. The results are given in the appendix in Figs. E.1 and E.5. The events are split into three subsets according to their hard-scattering p_T. These plots show that R^+ peaks at one in most of the layers. Only the Presampler and EMB 1–3 show a different behaviour. For the EMB layers a broad peak at 0.7 is observed. This could be explained by the fact that most of the particles shower at least partially in these regions and thus the chance of subtracting wrong energy-deposits is largest there.

In addition to that, the dependence on the pseudorapidity η was investigated, as shown in Fig. 3.38. However, no significant difference between the barrel ($0.0 < \eta < 0.8$) and the endcap region ($0.8 < \eta < 2.5$) is observed.

Since, an important global performance measure is the jet energy resolution, this is used to compare the different subtraction schemes: Fig. 3.39 shows the jet energy scale and resolution in dijet events calculated with different approaches. It allows the current ATLAS default (GSC) to be compared with the particle flow approach. In addition, it contains the values obtained using the back-to-front subtraction procedure. From these plots one can see that for particle flow in general the performance is better at low p_T and behaves worse for high jet-momenta. For the back-to-front subtraction, the energy resolution is as good or a bit better at very low momenta. However, it is worse than the default particle flow procedure at $p_T^{\text{jet}} = 120\,\text{GeV}$. Since this behaviour is not fully understood so far and for the future one would rather like to just reverse the order of the layers and not the cells within one layer, this is not implemented into eflowRec yet. However, it looks promising and worth further investigation, since going back-to-front leads to significantly more charged energy being subtracted.

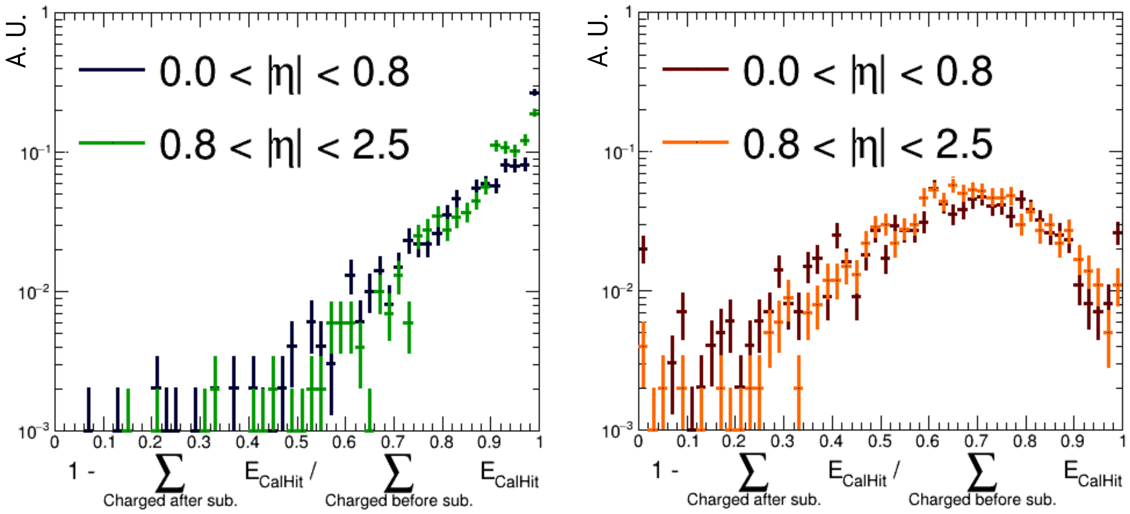

Figure 3.38: R^0 and R^+ binned in terms the pseudorapidity η per event calculated on dijet events with a hard scattering p_T of 17 GeV < p_T < 35 GeV.

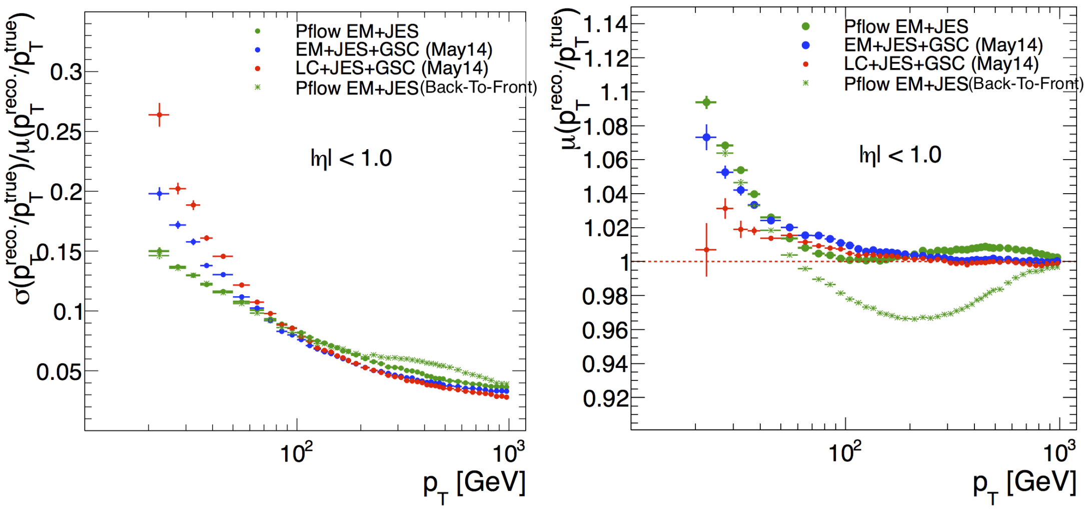

Figure 3.39: Jet energy resolution calculated on dijet events. The green dots denote the default particle flow subtraction procedure, while the green stars represent the results obtained with the back-to-front subtraction.

CHAPTER 4

Methods and observables

This chapter presents methods and observables used to determine the Higgs CP nature in $H \to \tau\tau$ decays at the LHC. The theoretical background and the methods to measure the Higgs CP state from transverse τ spin correlations are presented. Two methods for reconstructing the τ decay plane are used, depending on the decay mode of the τ: the impact parameter and the ρ decay plane method. Additionally, transverse τ spin correlation in $Z \to \tau\tau$ decays are discussed and the possibility to measure them at the LHC is outlined.

4.1 Methods to measure the Higgs CP-state in $H \to \tau\tau$ decays

The $H \to \tau\tau$ decay channel allows for a direct measurement of the Higgs CP-state from transverse spin correlations in the coupling of the Higgs boson to τ leptons. The description of τ spin-correlations follows the one presented in [96, 97]. Neglecting higher order electroweak corrections, the differential cross section of $H \to \tau\tau$ factorises into a product of the Higgs production and decay matrix element [96]. The interaction of τ leptons with a Higgs boson of arbitrary CP-state can be expressed by a Yukawa term in the Langrangian [97]:

$$\mathcal{L}_Y = -\frac{m_\tau}{v}\kappa_\tau \left(\cos\phi_\tau \bar{\tau}\tau + \sin\phi_\tau \bar{\tau} i\gamma_5 \tau\right) h. \tag{4.1}$$

Here m_τ denotes the mass of the τ lepton, $v = 246\,\text{GeV}$ the SM VEV, κ_τ the reduced Yukawa coupling strength and ϕ_τ denotes the scalar-pseudoscalar mixing angle between CP-even and CP-odd components of the Higgs boson coupling to the τ lepton. In the case of a purely CP-even SM Higgs boson, $\phi_\tau = 0$ and in case of a purely CP-odd Higgs boson, it is $\phi_\tau = 90$.

The methods to reveal the CP nature of the Higgs boson rely on characteristic features of the τ spin correlations. Here, the charged τ decay-products operate as τ spin analysers. For polarised τ decays, where a τ lepton decays into a $\pi^\pm$, ρ, a_1, electron or muon, the differential decay width in the $\tau^\pm$ rest frame is expressed by

$$\frac{1}{\Gamma_a} d\Gamma_{\tau\pm\to a^\pm + X} = n(E_\pm)\left[1 \mp b(E_\pm)\hat{s}^\pm \cdot \hat{q}^\pm\right] dE_\pm \frac{d\Omega_\pm}{4\pi}, \tag{4.2}$$

where $\hat{s}^\pm$ denotes the normalised spin vector of the $\tau^\pm$, $\hat{q}^\pm$ the direction of flight and $E_\pm$ the energy of the charged τ decay-product $a^\pm$ in the $\tau^\pm$ rest frame. Here $a^\pm$ can be a $\pi^\pm$, ρ, a_1, or a charged lepton. $n(E_\pm)$ and $b(E_\pm)$ describe the spectral functions of the polarised τ decay: n characterises the decay rate and b the τ or $a^\pm$ spin analysing power. For direct τ decays, i.e. $\tau^\pm \to \pi^\pm\nu_\tau$ or $\tau^\pm \to a_1^{L,T,\pm}\nu_\tau \to 2\pi^\pm\pi^\mp\nu_\tau$

with L and T representing the longitudinal and transversal helicity states, respectively, the spin analysing power is maximal, i.e. unity. For all other decay modes, the τ spin analysing power is a function of the $a^{\pm}$ energy, as can be seen for example for $\tau^{\pm} \rightarrow \rho^{\pm}\nu$ decays in Fig. 4.6.

The differential cross section $d\sigma_{H\rightarrow\tau\tau}$ for a Higgs production and its decay to two τ leptons is obtained by convolving the parton distribution functions (PDFs) with the partonic differential cross section $d\hat{\sigma}^{ij}_{H\rightarrow\tau\tau}$. Neglecting higher order electroweak corrections, the cross section factorises into the production and decay matrix elements [96]. The characteristics of the τ spin-correlations only depend on the Higgs CP-nature, but not on its production details. Hence, it is sufficient to study the differential decay width of the Higgs decaying into two τ leptons. In the rest frame of the Higgs, the differential decay width can be expressed using the τ spin components [98]:

$$d\Gamma_{H\rightarrow\tau\tau} \propto 1 - s_z^- s_z^+ + \cos(2\phi_\tau)\left(s_\perp^- \cdot s_\perp^+\right) + \sin(2\phi_\tau)\left[\left(s_\perp^- \times s_\perp^+\right)\hat{k}^-\right]. \tag{4.3}$$

Here $\hat{k}^-$ represents the normalised three momentum of the τ in the Higgs rest frame pointing in positive z-direction. $s_z^{\pm}$, $s_\perp^{\pm}$ denote the longitudinal and transversal components of the normalised $\tau^{\pm}$ spin vectors boosted into the respective $\tau^{\pm}$ rest frame. Equation (4.3) exposes the insensitivity of the longitudinal τ spin components to the CP-mixing angle, while pointing out the sensitivity of the transverse τ-spin components. The differential decay width can thus be reformulated as

$$d\Gamma_{H\rightarrow\tau\tau} \propto 1 - s_z^- s_z^+ + \left|s_\perp^-\right|\left|s_\perp^+\right|\cos(\phi - 2\phi_\tau), \tag{4.4}$$

where ϕ denotes the angle between the transverse spin components, oriented from $s_\perp^+$ to $s_\perp^-$. Due to the parity violation in the weak interaction, the directions of the charged τ decay-products are correlated with the $s_\perp^+$ and $s_\perp^-$ directions as it is sketched in Fig. 4.1. This allows to determine the CP properties

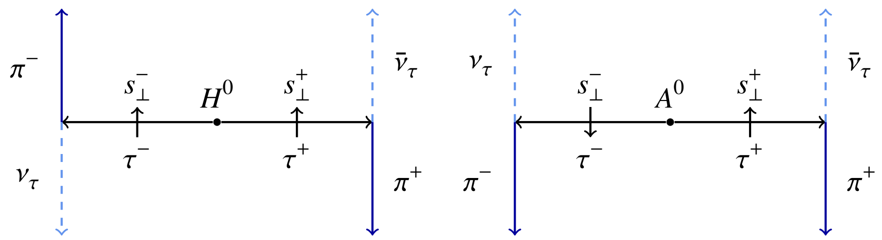

Figure 4.1: Correlations between the transverse spin components of the τ leptons and the τ decay products in $H \rightarrow \tau\tau$ decays for a scalar (a) and pseudoscalar (b) Higgs boson.

of the decaying Higgs from angular correlations between the directions of the visible τ decay-products. In the $\tau^+\tau^-$ zero-momentum frame (ZMF), the charged decay products tend to be emitted into opposite directions in case of a scalar Higgs boson, while for a pseudoscalar Higgs boson they are emitted into the same direction. Exploiting this correlation between the directions in which the charged τ decay-products are emitted and the CP-nature of the Higgs boson, it is possible to directly measure the Higgs CP state from the angle ϕ between the decay planes spanned by the visible τ decay-products: Eq. (4.4) indicates that any CP-mixing in the Higgs sector, will lead to a phase shift of this angular distribution. This is illustrated in Fig. 4.2, showing the φ^*_{CP}[1] distributions for a CP-even (dashed line), a CP-odd (dotted line), and an exemplary CP-mixed Higgs boson state (dashed-dotted line). Applying Eq. (4.4), the

[1] φ^*_{CP} is the signed decay plane angle boosted in the a^+a^- ZMF. The explicit relation between φ^*_{CP} and ϕ is explained e.g. in Eq. (4.7).

scalar-pseudo-scalar mixing angle ϕ_τ can be measured as twice the phase shift between the observed φ^*_{CP} distribution and a pure CP-even distribution as indicated in Fig. 4.2.

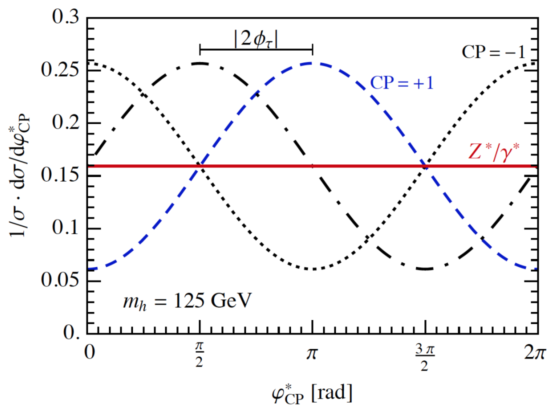

Figure 4.2: Differential cross section as a function of the decay plane angle φ^*_{CP} for 1p0n-1p0n decays. Any admixture of a CP-even and CP-odd Higgs boson would show up in a phase shift of the measured φ^*_{CP} distribution compared to the CP-even one as indicated for an example CP-mixed state, shown as the dashed-dotted line[96].

The reconstruction of the τ decay-plane for each τ depends on its decay mode: For 1p0n τ leptons, the plane is reconstructed based on the charged pion's track impact parameter. This method is called *impact parameter method* [96, 99]. For 1p1n τ leptons, the *ρ decay plane method* is used: the τ decay-plane is approximated by the decay plane of the intermediate ρ meson, which can be reconstructed from the charged and the neutral pion four-vectors [100–102]. In order to deal with di-τ decays for which one of the two τ leptons decays as 1p0n, while the other decays as 1p1n, the method has been reformulated, such that it is compatible with the impact Parameter method [97]. In the following these two methods are described: first the impact parameter method in Section 4.1.1, second the ρ decay plane method in Section 4.1.2 and third a combination of both methods in Section 4.1.3. To compare φ^*_{CP} distribution in different regions of phase space or measured with different methods, the asymmetry defined in Section 4.1.4 is used.

4.1.1 Impact parameter method

The impact parameter (IP) method is based on calculating the IP of the charged pion, i.e. the point of closest approach of the pion's track to the production vertex of the two τ leptons. The latter is almost identical to the Higgs boson production vertex, which is given by the Primary Vertex (PV) in an event. The method was originally described for $\tau^\pm \to \rho^\pm \nu$ decays at a linear collider [99]. However, it can be reformulated for any τ decay mode at the LHC [103].

The charged pion's IP vector $\vec{n}$ in the laboratory frame can be reconstructed by dropping a perpendicular from the PV onto the charged pion direction, as indicated in Fig. 4.3. The normal vector of the τ decay plane then follows from the IP vector $\vec{n}$ and the $\pi^\pm$ direction of flight. Hence, reconstructing the τ decay-plane with the IP method requires the Primary Vertex (PV), the charged pion's track, and the 3D IP to be measured. However, the ATLAS detector is only capable of measuring d_0 and z_0 describing the pion track 2D point of closest approach. Here, d_0 denotes the distance between the point of closest approach and the primary vertex in the x-y-plane of the ATLAS coordinate system and z_0 describes the z-coordinate of this point. Thus, approximating the 3D impact parameter relies on parametrising the pion track with a straight line that is positioned by the vector pointing to the 2D point of closest approach as a

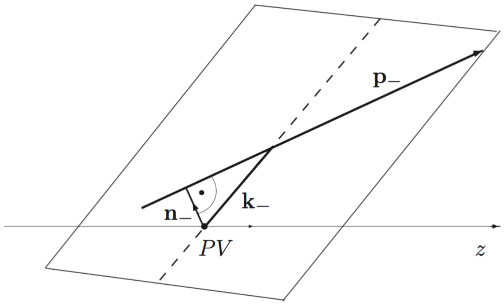

Figure 4.3: Reconstructing the τ decay-plane from the track's impact parameter [103].

support-vector and directed by the pion momentum vector. The full calculation of the 3D IP is outlined in Appendix A.

Since the sensitivity of measuring the CP-mixing angle is considerably larger in the $\pi^+ - \pi^-$-ZMF than in the laboratory (lab) frame, the IP method is applied in the $\pi^+ - \pi^-$-ZMF [97]. To this end, all four-vectors are boosted into the $\pi^+ - \pi^-$-ZMF. As a consequence, the angle between the two τ decay-planes then follows from the transverse components of the boosted IPs in the $\pi^+ - \pi^-$-ZMF as

$$\phi^* = \arccos\left(\vec{n}^*_{\perp,+} \cdot \vec{n}^*_{\perp,-}\right). \tag{4.5}$$

Depending on the CP-odd triple correlation (0^*_{CP}) defined as

$$0^*_{CP} = \vec{P_{\pi^-}}^* \cdot \left(\vec{n}^*_{\perp,+} \times \vec{n}^*_{\perp,-}\right), \tag{4.6}$$

where $\vec{P_{\pi^-}}^*$ is the boosted π^- direction, the signed decay plane angle acquires the following form

$$\varphi^*_{CP} = \begin{cases} \phi^* & \text{if } 0^*_{CP} \geq 0 \\ 2\pi - \phi^* & \text{if } 0^*_{CP} < 0 \end{cases}. \tag{4.7}$$

The CP-odd triple correlation measures the spin-spin correlation of the τ^+ and τ^- transverse to their direction of flight [104].

In this thesis, the IP method is only applied to $\tau \to \pi\nu$ decays. In principle, for any other 1-prong or 3-prong τ decay-mode and even in the leptonic decay modes, all quantities of the IP method can be calculated in an analogous way [96]. However, the IP method is very sensitive to the IP resolution. Thus, to analyse 1p1n τ decays, the IP method is outcompeted by the ρ decay plane method (see Section 4.1.2), which does not suffer from the low IP resolution.

4.1.2 The ρ decay plane method

The ρ decay plane method is dedicated to $\tau^\pm \to \rho^\pm\nu \to \pi^\pm\pi^0\nu$ decays. It was developed for a Higgs CP-measurement at a linear collider [100–102]. A description adapted to the LHC and compatible with the IP method was presented in [97]. The ρ decay plane method allows to measure the Higgs CP-state using the angle between the two ρ (instead of the τ) decay planes in the $\rho - \rho$ rest frame. It is appropriate to use the $\rho - \rho$ rest-frame, since the ρ meson carries a larger fraction of the energy of the decaying Higgs than the neutrino does in the Higgs rest frame. Advantageously, the $\rho - \rho$ rest frame is directly reconstructable from measurable quantities since all ρ decay-products are visible in the detector. The ρ

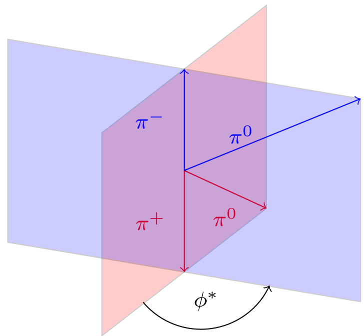

Figure 4.4: Sketch of the two ρ decay planes in the $\rho - \rho$ rest frame.

decay planes are spanned by the four vectors of the immediate two ρ decay products, a charged and a neutral pion. However, the angle φ^*_{CP} between the two planes alone does not yet distinguish the different CP components, since the spin sensitivity in 1p1n τ-decays is proportional to the energy difference $y^\pm$ of the $\pi\pm$ and π^0[100] defined as

$$y^\pm = \frac{E_{\pi\pm} - E_{\pi 0}}{E_{\pi\pm} + E_{\pi 0}}. \tag{4.8}$$

This energy difference can be used to split the phase space into two zones. This leads to two clearly distinguishable distributions for a CP-even and CP-odd Higgs, as can be seen in Fig. 4.5.

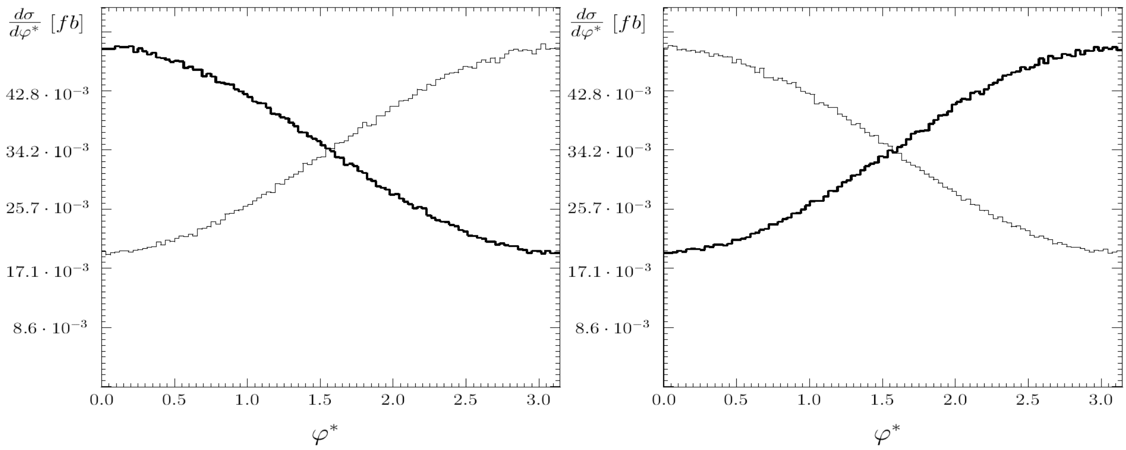

Figure 4.5: Decay plane angle φ^*_{CP} for the product of the energy differences between the charged and neutral pion $Y_+Y_- > 0$ and $Y_+Y_- < 0$ in the first and second plane, respectively [100].

Without splitting the phase space based on the product of the energy differences between the charged and neutral pions, however, the sensitivity is completely lost. This is due to the distributions for $Y_+Y_- < 0$ and $Y_+Y_- > 0$ being exactly complementary. It originates from the dependence of the differential decay width on the spectral functions $n(E_{\pi^\pm})$ and $b(E_{\pi^\pm})$ in the τ rest-frame [105] given in Eq. (4.2). In contrast to $\tau^\pm \to \pi^\pm + \nu_\tau$ decays, where the spin analysing power is always maximal, i.e. unity, in $\tau^\pm \to \rho^\pm + \nu_\tau$ decays the spin analysing power depends on the spectral functions n and b. The dependence of the spectral functions on the charged pion energy for $\tau^\pm(\hat{s}^\pm) \to \rho + X \to \pi^\pm(q^\pm) + X$ decays is displayed in Fig. 4.6. It shows that the spectral function $b(E_{\pi^\pm})$ crosses sign at $E_{\pi^\pm} \approx 0.55\,\text{GeV}$.

For a direct comparison of the ρ decay plane method and the IP-method, the CP sensitive variables

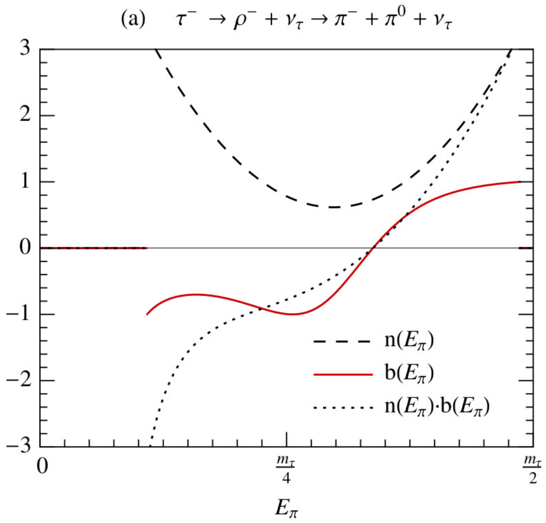

Figure 4.6: Spectral function of the charged pion in hadronic $\tau^- \to \rho^- + \nu_\tau \to \pi^- + \pi^0 + \nu_\tau$ decays. The y-axis indicates the spectral functions $b(E_{\pi^\pm})$, $n(E_{\pi^\pm})$ and $n(E_{\pi^\pm})b(E_{\pi^\pm})$, where the latter two are given in units GeV^{-1}[105].

need to be reconstructed in the same frame in either of the two methods. This allows to use a combination of both methods that enables the reconstruction of $H \to \tau\tau \to \pi\nu\rho\nu \to \pi^+\pi^-\pi^0 2\nu$ decays. Hence, the $\rho - \rho$ ZMF is replaced by the $\pi^+ - \pi^-$ ZMF in the ρ decay plane method [97] and all variables needed for the ρ decay plane method are recalculated in the $\pi^+ - \pi^-$ ZMF. The π^+, π^-, and π^0 four momenta are boosted in the $\pi^+ - \pi^-$ ZMF and, as a consequence, the angle between the decay planes appears as

$$\phi^* = \arccos\left(\hat{q}_\perp^{*0+} \cdot \hat{q}_\perp^{*0-}\right). \tag{4.9}$$

Here $\hat{q}_\perp^{*0+}$ and $\hat{q}_\perp^{*0-}$ are the normal vectors of the planes spanned by the charged an neutral pions in the $\pi^+ - \pi^-$ ZMF. The signed angle can be derived from this quantity using the CP-odd triple correlation 0^*_{CP}:

$$0^*_{CP} = \hat{q}^{*-} \cdot \left(\hat{q}_\perp^{*0+} \times \hat{q}_\perp^{*0-}\right). \tag{4.10}$$

Here, $\hat{q}^{*-}$ denotes the normalised π^- 3-momentum in the $\pi^+ - \pi^-$ ZMF. Consequently, the signed angle $\phi^{*'}$ is defined as

$$\phi^{*'} = \begin{cases} \phi^* & \text{if } 0^*_{CP} \geq 0 \\ 2\pi - \phi^* & \text{if } 0^*_{CP} < 0 \end{cases}. \tag{4.11}$$

The proportionality of the spin sensitivity and the energy difference $y^\pm$ in 1p1n τ-decays requires differentiating two categories depending on the sign of the product of the energy asymmetries as described earlier. In order to reduce the statistical uncertainty in the measured φ^*_{CP} distribution, the two categories are combined in the measurement by shifting the φ^*_{CP} distribution by π for all events with $Y_+Y_- < 0$ In turn, the combined φ^*_{CP} variable is defined as

$$\varphi^*_{CP} = \begin{cases} \phi^{*'} + \pi & \text{if } Y_+Y_- < 0 \\ \phi^{*'} & \text{else} \end{cases}. \tag{4.12}$$

The energy differences $y^{\pm}$ need to be calculated in the corresponding τ rest-frames. However, since it is impossible to reconstruct the true τ rest-frame from current measurements, they are calculated in the lab frame. The impact of using different frames in the reconstruction of Y_+Y_- on the sensitivity on the CP-mixing angle was studied in [106]. For example, if the lab frame or the $\rho-\rho$ ZMF is used for the $y^{\pm}$ calculation rather than the true τ rest-frames, the amplitude of the φ^*_{CP} distribution decreases by a factor three, when approaching small Y_+Y_- values e.g. $Y_+Y_- < 0.11$.

4.1.3 Combining the IP- and ρ decay plane methods

The combination of the IP- and ρ decay plane methods in $H \to \tau\tau$ decays at the LHC was first described in [97]. In this analysis it is applied only to $H \to \tau\tau$ decays in which one of the two τ leptons decays as 1p0n, while the other decays as 1p1n. In principle, the combined method can be employed to any decay mode combination, since the IP method is defined for all one- and three-prong τ decays, as long as the respective charged τ decay-product $a^{\pm}$ has a non-vanishing IP and at least one of the τ leptons decays as 1p1n.

In the combined method, all 4-momenta are boosted into the ZMF of the final two charged τ decay-products a^+ and a'^-. In this thesis, only 1p0n and 1p1n τ decays are analysed, hence, the 4-momenta are always boosted into π^+-π^- ZMF. Applying the IP method to the τ^-, the decay plane angle ϕ^* emerges as

$$\phi^* = \arccos\left(\hat{q}_{\perp}^{*0+} \cdot \hat{n}_{\perp}^{*-}\right) \tag{4.13}$$

and the triple correlation is defined as

$$0^*_{CP} = \hat{q}^{*-} \cdot \left(\hat{q}_{\perp}^{*0+} \times \hat{n}_{\perp}^{*-}\right). \tag{4.14}$$

Similarly, applying the IP method to the τ^+ results in the decay plane angle ϕ^* defined as

$$\phi^* = \arccos\left(\hat{q}_{\perp}^{*0-} \cdot \hat{n}_{\perp}^{*+}\right) \tag{4.15}$$

and the triple correlation becomes

$$0^*_{CP} = \hat{q}^{*-} \cdot \left(\hat{n}_{\perp}^{*+} \times \hat{q}_{\perp}^{*0-}\right). \tag{4.16}$$

In either of the two cases, the phase space needs to be split according to the energy asymmetry as described in Section 4.1.2. Since the ρ decay plane method is only applied to one of the τ decays, only the respective $y^{\pm}$, instead of the product Y_+Y_- of the two, is used to split the phase space. Compared to the pure ρ decay plane method, the expected asymmetry of the φ^*_{CP} distribution is larger because the τ spin analysing power is maximal for direct $\tau^{\pm} \to \pi^{\pm}\nu$ decays. Additionally, since only one ρ meson is involved, the asymmetry reduction is smaller because $y^{\pm}$ is calculated in the lab frame rather than the τ ZMF.

4.1.4 Definition of the φ^*_{CP} asymmetry

The φ^*_{CP} distributions are fitted with a cosine function of the form $f(x) = u\cos(x+v) + w$ in order to quantify the size of the modulation in the distribution. The normalisation of this function is inherited from the Higgs production cross section $\sigma_{aa'}$, which includes the branching fractions of the respective $\tau^+\tau^-$ decays, i.e.

$$\int_0^{2\pi} d\varphi^*_{CP} f = 2\pi w = \sigma_{aa'}. \tag{4.17}$$

The distributions in different production and decay channels are not comparable unless the asymmetry $A^{aa'}$ is introduced. It is defined as

$$A^{aa'} = -\frac{1}{\sigma_{aa'}} \int_0^{2\pi} d\varphi^*_{CP} \left(d\sigma_{aa'} \left[u \cos\left(\varphi^*_{CP} - 2\phi_\tau\right) > 0\right] - d\sigma_{aa'} \left[u \cos\left(\varphi^*_{CP} - 2\phi_\tau\right) < 0\right]\right), \tag{4.18}$$

where a and a' denote the charged decay particles of the τ^+ and τ^-, respectively. Using Eq. (4.17), $A^{aa'}$ can be calculated based on the parameters obtained by fitting a cosine function [97] as

$$A^{aa'} = -\frac{4u}{2\pi w}. \tag{4.19}$$

4.2 Tau spin correlations in $Z/\gamma* \to \tau\tau$ decays

The τ spin correlations in $Z/\gamma* \to \tau\tau$ decays differ from those in $H \to \tau\tau$ decays described in Section 4.1. In contrast, in $Z \to \tau\tau$ decays the differential cross section is independent of the angle φ^*_{CP} [96], since the dependence on the transverse τ spin-correlations cancels out in the calculation. Hence, the expected φ^*_{CP} distribution in $Z/\gamma* \to \tau\tau$ decays is flat, as shown in Fig. 4.2. However, one can split the phase space based on the angle between the π^- (from the τ^- decay) and the τ production-plane. Thereby the dependence of the differential decay width on the angle φ^*_{CP} can be restored in the two halves of the entire phase space and a CP-even and CP-odd like φ^*_{CP} distribution is obtained, respectively. This dependency on the angle φ^*_{CP} can be exploited to calibrate the measurement of the Higgs CP-mixing angle in $Z \to \tau\tau$ decays.

4.2.1 Differential cross section at leading order

As described in [96], major differences appear in the matrix element and the cross sections when comparing $H \to \tau\tau$ and $Z/\gamma* \to \tau\tau$ decays. In contrast to $H \to \tau\tau$ decays, the matrix element does not factorise into the production and decay process for $Z/\gamma* \to \tau\tau$ decays. Hence, calculating the differential cross section, requires determining the full $\tau^+\tau^-$ spin density matrix. As a consequence, taking into account the transverse τ spin correlations in simulations of Z+jets events is much more complicated and computationally intensive than for $H \to \tau\tau$ events. The differential cross section of $Z/\gamma* \to \tau\tau$ decays at leading order in the $\tau^+\tau^-$ ZMF is given as

$$\frac{d\sigma_{Z\to\tau\tau}}{d\phi_+ d\phi_-} \propto 1 + \frac{\pi^2}{32} b(E_+) b(E_-) \kappa(B1, B2) \cos\left(\phi_+ + \phi_-\right), \tag{4.20}$$

where $\phi_\pm$ denote the azimuthal angles of the $a^\pm$ momenta in a coordinate system where the x-axis points along the direction of the τ^- momentum and the initial quark momentum lies in the $x - z$-plane [96]. $\kappa(B1, B2)$ characterises the τ coupling strength, defined as

$$\kappa(B1, B2) = \left(a_\tau^{B1} a_\tau^{B2} - v_\tau^{B1} v_\tau^{B2}\right) / \left(a_\tau^{B1} a_\tau^{B2} + v_\tau^{B1} v_\tau^{B2}\right), \tag{4.21}$$

where $B1, B2$ run over Z, γ and a_τ and v_τ are defined as

$$a_f^\gamma = 0 \text{ and } v_f^\gamma = Q_f e, \text{ respectively,} \tag{4.22}$$

in case of a photon and as

$$a_f^Z = e\frac{T_{3f}}{2\sin\Theta_w\cos\Theta_w} \text{ and } v_f^Z = e\frac{T_{3f} - 2Q_f\sin^2\Theta_w}{2\sin\Theta_w\cos\Theta_w}, \text{ respectively,} \tag{4.23}$$

in case of a Z boson. Furthermore, the angle ϕ is defined as the difference between ϕ_- and ϕ_+: $\phi = \phi_- - \phi_+$. After substituting $\phi_+ = \phi_- - \phi$ in Eq. (4.20) and integrating out ϕ_-, the differential cross section does no longer depend on ϕ. Hence, the φ^*_{CP} distribution is expected to be flat for $Z/\gamma* \to \tau\tau$ decays without splitting the phase space [96].

However, this is only true if ϕ is integrated across the full phase space of the τ decay-products. If the phase space of the τ^- charged decay product is split up based on its momentum being either preferably parallel or perpendicular to the τ^- production plane, an asymmetrical φ^*_{CP} distribution is obtained [96]. This is realised using the angle α^- between the π^- and τ production-plane defined as

$$\cos\left(\alpha^-, \mathrm{IP}\right) = \left|\frac{\hat{e}_z \times \hat{\mathrm{p}}_{\pi^-}}{\left|\hat{e}_z \times \hat{\mathrm{p}}_{\pi^-}\right|} \cdot \frac{\hat{n}_\perp^- \times \hat{\mathrm{p}}_{\pi^-}}{\left|\hat{n}_\perp^- \times \hat{\mathrm{p}}_{\pi^-}\right|}\right| \qquad \cos\left(\alpha^-, \rho\right) = \left|\frac{\hat{e}_z \times \hat{\mathrm{p}}_{\rho-}}{\left|\hat{e}_z \times \hat{\mathrm{p}}_{\rho^-}\right|} \cdot \frac{\hat{\mathrm{p}}_{\pi^-} \times \hat{\mathrm{p}}_{\rho^-}}{\left|\hat{\mathrm{p}}_{\pi^-} \times \hat{\mathrm{p}}_{\rho^-}\right|}\right|, \tag{4.24}$$

for the IP and ρ decay plane methods, respectively. Here, $\hat{n}_\perp^-$ represents the normal component of the π^- track IP and $\hat{\mathrm{p}}_{\pi^-}$ ($\hat{\mathrm{p}}_{\rho^-}$) denotes the normalised π^- (or ρ^-) momentum in the lab frame. To visualise the abstract angle α^- defined in Eq. (4.24), it is sketched in Fig. 4.7 together with the τ/ρ production- and decay-planes for 1p0n and 1p1n τ decays, respectively. Events for which the τ^- charged decay product is

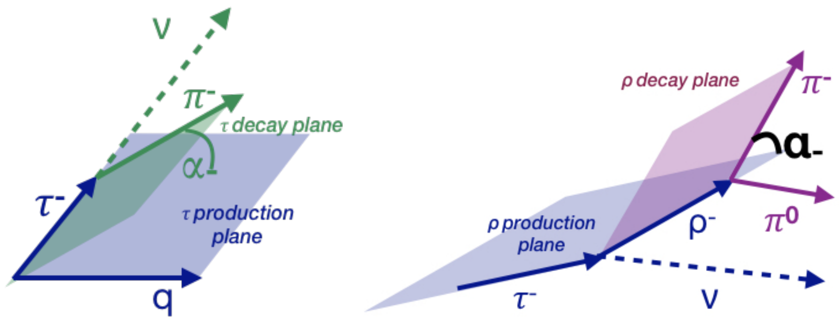

(a) 1p0n τ decay (b) 1p1n τ decay

Figure 4.7: Sketch of the angle α^- used to split the phase space to restore the dependence on the transverse τ spin correlations in $Z \to \tau\tau$ events for 1p0n and 1p1n τ decays, respectively.

rather parallel (perpendicular) to the τ^- production plane feature an angle α^- which is smaller or larger $\frac{\pi}{4}$, respectively. If these events are considered separately, the φ^*_{CP} distributions are enhanced around $\varphi^*_{CP} \approx \pi$ or $\varphi^*_{CP} \approx 0$ (and 2π). Thus, the behaviour is similar to the one expected for a CP-even and CP-odd Higgs boson as it can be seen in Fig. 4.8 for Drell-Yan $Z/\gamma* \to \tau\tau$ and in Fig. 4.9 for Z+1jet events. Please note the different y-axis scales in the two plots. From these distributions it becomes obvious, that the difference in the amplitudes of the two split φ^*_{CP} distributions is significantly reduced for Z+1jet events. This can be explained by the different initial states that contribute to Z+1jet events. If the extra jet in the event originates from the initial state because e.g. a gluon from one of the protons interacts with a quark from the other proton, the τ production plane is not well-defined anymore and the relation between the angle α^- and the charged pions being emitted preferably parallel or antiparallel does not hold. Hence, the amplitude of the φ^*_{CP} distribution decreases for events with jets. In Section 6.3, I have shown how the amplitude in the φ^*_{CP} distribution in $Z \to \tau\tau$ events changes from pure Drell-Yan $Z \to \tau\tau$ (zero jets from

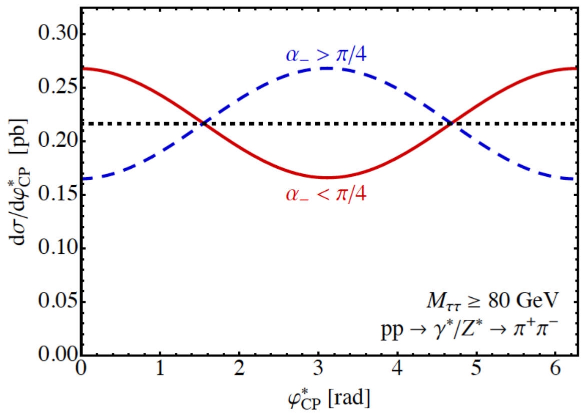

Figure 4.8: Distribution of φ^*_{CP} for Drell-Yan $Z/\gamma* \to \tau\tau$ events which are separated into two categories of events using α^-[96].

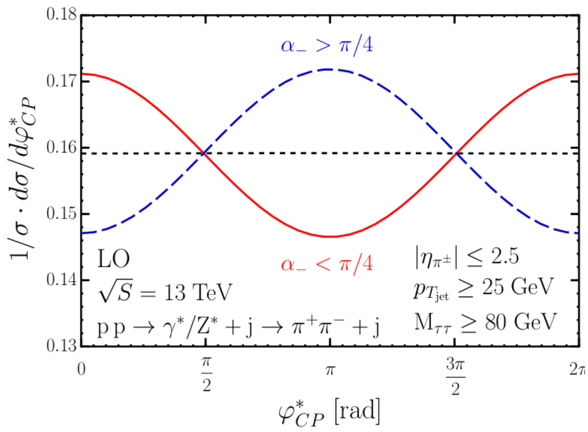

Figure 4.9: Distribution of φ^*_{CP} for Z+1jet events which are separated into two categories of events using α^-[107].

the initial state) to quark-gluon (one jet from the initial state) or gluon-gluon (two jets from the initial state) production. In case of one jet from the initial state, the amplitude in the $Z \to \tau\tau$ φ^*_{CP} distribution, constructed through the cut on α^-, is significantly reduced, while for two jets it vanishes completely.

Beside that, requirements on the di-τ invariant mass ($m_{\tau\tau}$) have to be chosen carefully, since the φ^*_{CP} distributions for pure γ^* and pure Z exchange are exactly reverse as can be seen comparing Fig. 4.10 and Fig. 4.8. The reason for this reversed behaviour is that the coupling $\kappa(Z, Z)$ is close to 1, while $\kappa(\gamma, \gamma)$ is close to -1 [96]. In other words, in the case of a decaying photon, the τ pair is produced in an s-wave, while for a Z boson the production takes place through an axial vector current and thus in a p-wave. This results in the τ spin-projections on the quark axis being predominantly correlated or anti-correlated, respectively. If the (true) invariant mass of two τ leptons from the $Z/\gamma* \to \tau\tau$ decay is demanded to be $m_{\tau\tau} > 80$ GeV, the Drell-Yan process is dominated by Z-boson exchange. In turn, the relative contribution from the photon is small. It can increase though, if a different $m_{\tau\tau}$ mass range, further away from the Z-peak is chosen. In this case, the expected asymmetry of the φ^*_{CP} distribution will decrease.

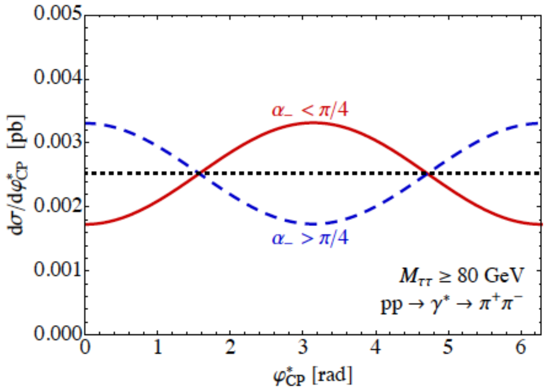

Figure 4.10: Distribution of φ^*_{CP} for Drell-Yan $\gamma \to \tau\tau$ events separated into two categories of events using α^-[96].

4.2.2 Asymmetry dependence on the jet p_T in Z+jets events

The calculation of the asymmetry defined in Eq. (4.18) from the differential cross section illustrates that $A^{aa'}$ is independent of the mixing angle ϕ_τ, but depends on the product of the τ − spin analysing powers of the charged decay products a and a' [96]. Since the τ spin analysing power is maximal for direct τ decays, $A^{aa'}$ is maximal if both τ leptons decay directly to $\pi^\pm$ or $a_1^{L,T,\pm}$. In all other cases, the τ spin analysing powers and hence also the asymmetry depends on the event selection cuts applied to the pion (or lepton) energies.

For Z+1 jet events, $A^{aa'}$ depends on the minimum required p_T^{jet}, as it was shown in [107] and can be seen in Fig. 4.11. Therefore, any p_T^{jet} threshold, applied in the analysis, has to be chosen with caution,

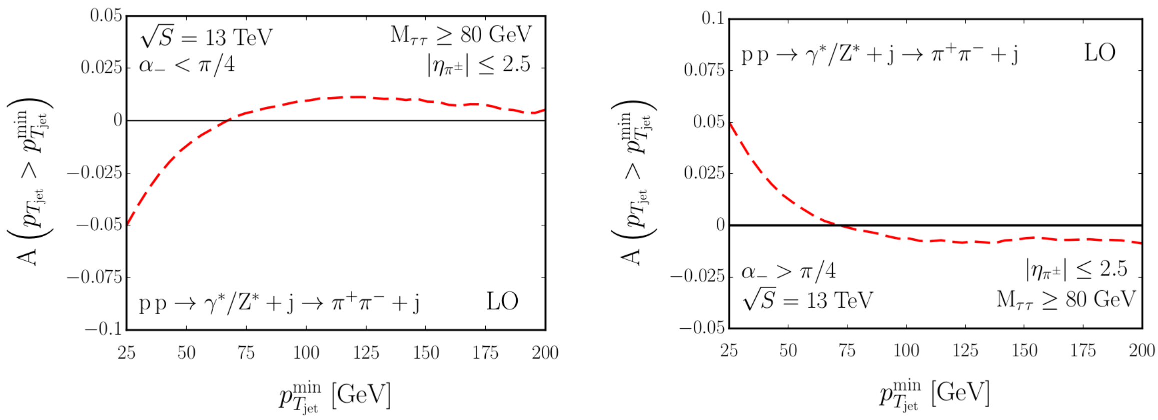

Figure 4.11: Asymmetry as a function of the minimum p_T^{jet} cut for Z + 1jet events for $\alpha^- < \pi/4$ and $\alpha^- > \pi/4$ in the first and second plane, respectively [107].

taking into account that it will reduce the asymmetry significantly and could even eliminate the gain from splitting up the phase space completely.

CHAPTER 5

Event selection

In this chapter the event selection for the Higgs CP analysis is presented. All signal and control region requirements are described. The control regions are used to derive normalisation factors on the $Z \to \tau\tau$ and QCD backgrounds. In addition, a $Z \to \tau\tau$ validation-region is defined, used to measure transverse spin correlations in $Z \to \tau\tau$ events. In order to define which events should be selected for this Z-validation region, a series of optimisation studies has been performed to maximise the asymmetry in the φ^*_{CP} distribution in $Z \to \tau\tau$ events.

5.1 Event selection for the Higgs CP measurement in $H \to \tau\tau$ decays

For the measurement of the Higgs CP state, events with a Higgs boson decaying into two τ leptons, with subsequent decays to a charged hadron ($\pi^\pm$ or $\rho^\pm$) and neutrinos are investigated. The event selection is similar to the one used in the $H \to \tau\tau$ cross section measurement [12] with additional criteria separating the events into the different $\tau^+\tau^-$ decay mode combinations. All signal and control regions are summarised in Table 5.1 and described in more detail in the following paragraph.

For the Higgs CP measurement events are selected that match the following requirements:

Trigger and $p_{\mathrm{T}}^{\mathrm{jet}}$ requirements The events have to pass the di-τ trigger for two hadronically decaying τ leptons[1]. In 2015 and 2016 data the requirements in the level-1 trigger slightly changed with respect to the 2015 data. The 2016 trigger requires at least one jet at the trigger level 1. In order for the di-τ trigger to be in the efficiency plateau, an event is required to have at least one jet with a minimum p_{T} of $p_T^j > 70\,\mathrm{GeV}$ and $|\eta_j| < 3.2$ to be selected. Alternatively, the analysis could ask for one matched level 1 jet in the event. The impact of the $p_{\mathrm{T}}^{\mathrm{jet}}$ cut or its alternatives is discussed in more detail in Section 5.2.2.

Two oppositely charged τ leptons in the event From the event topology, two oppositely charged τ leptons are expected. Since only 1p0n or 1p1n τ leptons are considered, the τ leptons are required to be classified as such by the τ particle flow reconstruction described in Section 3.5. In addition, they are asked to be associated to the same reconstructed primary vertex, since they should originate from the decay of one Higgs boson. Both of them have to fulfil the *medium* τ identification (ID) criterion and at least one of them also has to pass the *tight* τ ID criterion.

[1] Hadronically decaying means that the two W-bosons from the τ decays both decay hadronically.

<table>
<tr><th colspan="6">Higgs preselection requirements</th></tr>
<tr><td colspan="6">Event passes di-τ had-had trigger requirements
Two τ_{had} candidates with opposite sign, classified as 1p0n or 1p1n present
Both τ_{had} candidates associated to same reconstructed primary vertex
$p_{\text{T}}(\tau_1) > 40\,\text{GeV}$, $p_{\text{T}}(\tau_2) > 30\,\text{GeV}$
Both passing medium and at least one tight τ identification
No electron or muons
$\Delta\eta_{\tau\tau} < 1.5$ and $0.8 < \Delta R_{\tau\tau} < 2.5$
$E_{\text{T}}^{\text{miss}} > 20\,\text{GeV}$
$70 < m_{\tau\tau}^{\text{MMC}} < 150\,\text{GeV}$
At least one jet with $p_T^j > 70\,\text{GeV}$ and $|\eta_j| < 3.2$
$0.1 < x_{0/1} < 1.4$</td></tr>
<tr><th colspan="6">VBF region</th></tr>
<tr><td colspan="6">At least two jets with $p_T^{j1} > 50\,\text{GeV}$ and $p_T^{j2} > 30\,\text{GeV}$
$m_{jj} > 400\,\text{GeV}$
$\Delta\eta_{j1,j2} > 3.0$, $\eta_{j1} \times \eta_{j2} < 0$
Both τ_{had} candidates must lie between the two leading jets in η</td></tr>
<tr><th colspan="6">Boosted regions</th></tr>
<tr><td colspan="6">Failed VBF selection
$p_T^H > 100\,\text{GeV}$</td></tr>
<tr><td colspan="3">Boosted high p_{T}
$p_{\text{T}}^{\text{H}} \geq 175\,\text{GeV}$</td><td colspan="3">Boosted low p_{T}
$p_{\text{T}}^{\text{H}} < 175\,\text{GeV}$</td></tr>
<tr><th colspan="3">Higgs signal regions</th><th colspan="3">Background estimation regions</th></tr>
<tr><td colspan="3">VBF or boosted requirements
$100 < m_{\tau\tau}^{\text{MMC}} < 150\,\text{GeV}$</td><td colspan="3">VBF or boosted requirements
$70 < m_{\tau\tau}^{\text{MMC}} < 100\,\text{GeV}$</td></tr>
<tr><th colspan="6">Decay mode selection</th></tr>
<tr><td colspan="2">IP-IP
1p0n, 1p0n</td><td colspan="2">IP-ρ
1p0n, 1p1n</td><td colspan="2">ρ-ρ
1p1n, 1p1n</td></tr>
<tr><th>High d_0^{sig}</th><th>Low d_0^{sig}</th><th>High d_0^{sig}/y</th><th>Low d_0^{sig}/y</th><th>High $y0y1$</th><th>Low $y0y1$</th></tr>
<tr><td>$d_0^{\text{sig}}(\tau_0) \geq 1.4$
and
$d_0^{\text{sig}}(\tau_1) \geq 1.4$</td><td>$d_0^{\text{sig}}(\tau_0) < 1.4$
or
$d_0^{\text{sig}}(\tau_1) < 1.4$</td><td>$d_0^{\text{sig}}(\tau_{1\text{p0n}}) \geq 1.4$
and
$y(\tau_{1\text{p1n}}) \geq 0.3$</td><td>$d_0^{\text{sig}}(\tau_{1\text{p0n}}) < 1.4$
or
$y(\tau_{1\text{p1n}}) < 0.3$</td><td>$|y_0 y_1| \geq 0.2$</td><td>$|y_0 y_1| < 0.2$</td></tr>
</table>

Table 5.1: Summary of signal and control regions and the respective event selections criteria for the Higgs CP measurement.

Veto on electrons or muons Since this analysis uses the dihadronic (referenced as had-had) decay channel, electrons and muons are vetoed. This suppresses $Z \to \ell\ell$, W+Jets and top backgrounds, which contain one or even two light leptons in the final state. Also, this cut would ensure the orthogonality to the lep-had and lep-lep decay channels, if they were included in a future analysis.

Tau p_T thresholds The leading τ lepton is required to have a transverse momentum of at least $p_\mathrm{T}^{\tau,vis} > 40\,\mathrm{GeV}$. A lower threshold of $p_\mathrm{T}^{\tau,vis} > 30\,\mathrm{GeV}$ is required for the subleading τ.

$E_\mathrm{T}^\mathrm{miss}$ requirement In order to suppress the large amount of QCD background in the had-had channel, the missing transverse energy is required to be at least 20 GeV. From the two τ-lepton decays, there are also two neutrinos present in the event. This leads to a significant amount of expected missing transverse energy.

The collinear approximation condition To suppress events with large $E_\mathrm{T}^\mathrm{miss}$ contributions, which do not originate from ditau decays, an additional requirement is made on the momentum fraction inherited by the two visible τ leptons, which can be calculated with the collinear approximation defined as

$$x_{0/1} = \frac{p_{0/1}^\mathrm{vis}}{p_{0/1}^\mathrm{vis} + p_{0/1}^\mathrm{miss}}. \tag{5.1}$$

Here, $p_{0/1}^\mathrm{vis}$ is the visible τ_had momentum, while $p_{0/1}^\mathrm{miss}$ is the missing τ_had momentum carried away by the neutrinos in the event. This quantity is asked to be between $0.1 < x_{0/1} < 1.4$ for ditau decays.

Conditions on $\Delta\eta_{\tau\tau}$ and $\Delta R_{\tau\tau}$ The requirements on the angular distance between the two τ candidates targets also at the suppression of the QCD background. τ's coming from a Z boson or Higgs decay tend to produce lager distances in $\Delta R_{\tau\tau}$ and smaller $\Delta\eta_{\tau\tau}$ due to the boost from the decaying heavy particle. Therefore, it is asked for $0.8 < \Delta R_{\tau\tau} < 2.5$ and $\Delta\eta_{\tau\tau} < 1.5$.

Requirements on the ditau mass ($m_{\tau\tau}^\mathrm{MMC}$) The $m_{\tau\tau}^\mathrm{MMC}$ variable approximates the ditau invariant mass. It is calculated with the Missing Mass Calculator (MMC) [108], which makes the following assumptions:

- The particle (here the H or Z boson) from which the two τ's originate, is much heavier than the τ s themselves. Therefore, the τ's are boosted and their decay products are collimated.
- The direction of the τ and its decay products do not have to be exactly the same, i.e. $\Delta\Theta$ between them can be larger than zero. However, $\Delta\Theta$ should depend only on the four-momentum and the decay modes of the two τ's. The following categories of decay mode combinations are used: both leptonically, one leptonically and one hadronically, both hadronically. In case of hadronically decaying τ s, also 1-prong and 3-prong decays are distinguished.
- The missing energy $E_\mathrm{T}^\mathrm{miss}$ in the event is solely caused by the neutrinos from the two τ decays. The MMC parametrises the estimated mass in $E_\mathrm{T}^\mathrm{miss}$ taking into account the $E_\mathrm{T}^\mathrm{miss}$ resolution.

In order to find the best solution for the ditau invariant mass, a maximum likelihood approach is used and the parameter space is scanned with a Markov chain. Details on the scanned parameters and a comparison of the MMC with other reconstruction techniques for the ditau mass are presented in [106].

In the Higgs signal regions the ditau mass range is restricted to $100 < m_{\tau\tau}^{\mathrm{MMC}} < 150\,\mathrm{GeV}$. Hence, they contain the Higgs mass peak, but reject QCD and $Z \rightarrow \tau\tau$ events.

The $Z \rightarrow \tau\tau$ and QCD control regions are used to perform the data-driven background estimates. They are defined similar to the Higgs signal regions but within a different $m_{\tau\tau}^{\mathrm{MMC}}$ mass window of $70 < m_{\tau\tau}^{\mathrm{MMC}} < 100\,\mathrm{GeV}$. This way, they are orthogonal to the signal regions.

Selection criteria for the VBF categories The VBF signal region cuts are dedicated to the VBF Higgs production topology. In order to enrich $H \rightarrow \tau\tau$ events where the Higgs was produced via the vector-boson fusion, one requires at least two jets in the event with $p_T^{j1} > 50\,\mathrm{GeV}$ and $p_T^{j2} > 30\,\mathrm{GeV}$, $m_{jj} > 400\,\mathrm{GeV}$, $\Delta\eta_{jj} > 3.0$ and that the product of the pseudorapidities of the two jets is smaller than zero. In addition to that, both τ_{had} candidates must lie between the two leading jets in pseudorapidity.

Selection criteria for the boosted regions The boosted signal region requirements are dedicated to select boosted $H \rightarrow \tau\tau$ events. Those are primarily produced via gluon-gluon fusion. Such events have to fail the VBF requirements and to fulfil $p_{\mathrm{T}}^{\mathrm{H}} > 100\,\mathrm{GeV}$. Where $p_{\mathrm{T}}^{\mathrm{H}}$ denotes the transverse momentum of the di-τ system approximated by the sum of the two visible τ leptons four-momenta and the missing transverse energy $E_{\mathrm{T}}^{\mathrm{miss}}$. The boosted signal region is further split into a **boost low-p_{T}** and **boost high-p_{T}** region requiring $100\,\mathrm{GeV} < p_{\mathrm{T}}^{\mathrm{H}} < 175\,\mathrm{GeV}$ or $p_{\mathrm{T}}^{\mathrm{H}} \geq 175\,\mathrm{GeV}$, respectively.

The high/low d_0^{sig} requirements In simulations it has been shown that, without further cuts on the d_0-significance (d_0^{sig}), there is almost no separation power between the φ_{CP}^* distributions created by a CP-even or a CP-odd $H \rightarrow \tau\tau$ signal. The variable d_0 denotes the transverse component of the 2D impact parameter of the τ lepton's leading track. The IP method suffers significantly from mismeasurements of the IP which occur mostly for small track IP significances. However, separating the signal regions into high and low d_0^{sig} categories, leads to a better separation between the different mixing angles in the high d_0^{sig} category and increases the significance of the IP method. The d_0^{sig} is defined as

$$d_0^{\mathrm{sig}} = \frac{|d_0|}{\sigma_{d_0}}. \tag{5.2}$$

The high (low) d_0^{sig} requirements are defined as $d_0^{\mathrm{sig}}(\tau_i) \geq 1.4$ ($d_0^{\mathrm{sig}}(\tau_i) < 1.4$) where $i \in 0, 1$ is the index of the τ lepton for which the IP method is used. They are applied to the VBF, boost high-p_{T} and boost-low-p_{T} regions, such that for each of the signal regions, a low and high d_0^{sig} category is defined for the IP-IP method.

The high/low y^+y^- requirements For $\rho - \rho$ method one can also benefit from splitting up the VBF and boosted signal regions further. In this case, a cut on the product of the energy asymmetries y^+ and y^- between the charged and neutral pion from the $\rho^{\pm}$ decay defined in Eq. (4.8) is applied. This is beneficial because the closer $y^{\pm}$ approaches zero, the more likely it is reconstructed with the wrong sign. Hence, the choice of phase for φ_{CP}^* is wrong. Thus, splitting up the region into a tight ($y^+y^- \geq 0.2$) and loose ($y^+y^- < 0.2$) region in the fit improves the overall performance of the analysis.

The combined y and d_0^{sig} requirements For the combination of methods also two categories are defined out of each signal region. The high $d_0^{\mathrm{sig}}/Y_{\pm}$ region requires a high d_0^{sig} for the 1p0n τ and a high

$y^{\rho} \geq 0.3$ for the 1p1n τ, while the low $d_0^{\text{sig}}/Y_{\pm}$ region collects the remaining events where either the 1p0n τ has a low d_0^{sig} or the 1p1n τ has a low $y^{\rho} < 0.3$.

5.1.1 Definition of the Higgs CP signal-regions

The Higgs CP-state is measured from the distribution of the angle φ^*_{CP}. The signal regions in which this angle is measured are derived from the VBF, boosted low-p_{T} and boosted high-p_{T} categories selecting only events with a di-τ invariant mass close to the Higgs mass by requiring $100\,\text{GeV} < m_{\tau\tau}^{\text{MMC}} < 150\,\text{GeV}$. Each of these three regions is further segmented based on the three decay-mode combinations and the respective high/low $d_0^{\text{sig}}/Y_{\pm}$ requirements into:

- IP-IP (low d_0^{sig})
- IP-IP (high d_0^{sig})
- IP-ρ (low $d_0^{\text{sig}}/Y_{\pm}$)
- IP-ρ (high $d_0^{\text{sig}}/Y_{\pm}$)
- $\rho - \rho$ (low Y_+Y_-)
- $\rho - \rho$ (high Y_+Y_-).

Due to statistical limitations, the VBF region is only segmented into four regions: IP-IP, IP-ρ, $\rho - \rho$ (low Y_+Y_-) and $\rho - \rho$ (high Y_+Y_-). To this end, 16 distinct signal regions are defined for the Higgs CP-measurement.

5.1.2 Definition of the Higgs CP control-regions

The QCD and $Z \to \tau\tau$ backgrounds are estimated from data as explained in Section 6.2.3 and Section 6.2.4. Normalisation factors on both backgrounds are included in the Higgs CP-measurement named r_{QCD} and r_Z and determined in a fit to the $\Delta\eta_{\tau\tau}$ distribution in three control regions. These regions are defined from the VBF, boosted low-p_{T} and boosted high-p_{T} categories selecting only events with a di-τ invariant mass fulfilling $70\,\text{GeV} < m_{\tau\tau}^{\text{MMC}} < 100\,\text{GeV}$, in order to be orthogonal to the signal regions. The three control regions are referenced as

- VBF CR
- boosted low-p_{T} CR
- boosted high-p_{T} CR

5.2 Definition of the Z-validation region

Based on reconstructing the transverse spin correlations of the τ's in $Z \to \tau\tau$ decays, cosine shaped φ^*_{CP} distributions can be constructed after splitting up the phase space using α^- defined in Eq. (4.24). If measured in data, it can be used to constrain any systematic effect on φ^*_{CP}. Beside that, the measurement of these distributions can be used to calibrate the methods to determine the CP mixing angle in $H \to \tau\tau$ events. Hence, a well defined $Z \to \tau\tau$ validation region is needed, for which the cuts are chosen in a way that the constructed modulation of the φ^*_{CP} distribution is maximal. In addition, it should have a good signal, i.e. $Z \rightarrow \tau\tau$ purity and it needs to be orthogonal to the Higgs signal regions. The $Z \rightarrow \tau\tau$ purity is subordinated though, as long as all other backgrounds in this region, especially the QCD background, are flat in φ^*_{CP}. The orthogonality can simply be achieved by requiring the ditau invariant mass to be $m_{\tau\tau}^{\mathrm{MMC}} < 100\,\mathrm{GeV}$. To enhance statistics in the Z-validation region, the distribution obtained when requiring $\alpha^- < \pi/4$ is shifted by π and added to the distribution for $\alpha^- > \pi/4$.

Z-validation region	
Two τ_{had} candidates with opposite sign, classified as 1p0n or 1p1n	
Both τ_{had} candidates associated to same reconstructed primary vertex	
$p_{\mathrm{T}}(\tau_1) > 40\,\mathrm{GeV}$, $p_{\mathrm{T}}(\tau_2) > 30\,\mathrm{GeV}$	
Both passing *tight* τ identification	
No electron or muons	
$\Delta\eta_{\tau\tau} < 1.0$	
$0.8 < \Delta R_{\tau\tau} < 3.0$	
$E_{\mathrm{T}}^{\mathrm{miss}} \geq 10\,\mathrm{GeV}$	
$70\,\mathrm{GeV} < m_{\tau\tau}^{\mathrm{MMC}} < 100\,\mathrm{GeV}$	
$\alpha^- \geq \pi/4$ or $\alpha^- < \pi/4$	
Z-CR 2015	**Z-CR 2016**
passing 2015 trigger	passing 2016 trigger
	At least one jet with $p_T^{j1} > 70\,\mathrm{GeV}$

Table 5.2: Categories and event selection used for the $Z \rightarrow \tau\tau$ validation region.

5.2.1 Optimisation of the event selection for the $Z \rightarrow \tau\tau$ region

In order to find the optimal event selection for studying the modulation in $Z \rightarrow \tau\tau$ events, the $H \rightarrow \tau\tau$ preselection is varied in order to determine the set of cuts which yields the maximal amplitude of the fitted cosine distribution (A), the minimal relative uncertainty $|\Delta A/A|$ on the amplitude (i.e. the maximum $|A/\Delta A|$) and a phase shift which is still compatible with 0.

This is done in an iterative process starting with a very loose set of cuts und evaluating the three parameters for all variations. Next, the cut values are set to the optimal ones from this iteration and the procedure is repeated. The resulting event selection is displayed in Table 5.2. It is very similar to the $H \rightarrow \tau\tau$ preselection except for the ΔR, $m_{\tau\tau}^{\mathrm{MMC}}$ and $E_{\mathrm{T}}^{\mathrm{miss}}$ requirements. If using only 2015 data, the level 1 jet requirements are dropped, since they decrease the amplitude significantly.

Figure 5.1 shows that the leading and subleading τ p_{T} cuts should not be increased further with respect to the default p_{T}-thresholds of $p_{\mathrm{T}} > 40\,\mathrm{GeV}$ for the leading and $p_{\mathrm{T}} > 30\,\mathrm{GeV}$ for the subleading τ leptons. The asymmetry in the φ^*_{CP} distribution clearly decreases with increasing the minimum $E_{\mathrm{T}}^{\mathrm{miss}}$ requirement. However, it is necessary to require a minimum $E_{\mathrm{T}}^{\mathrm{miss}}$ present in the event to suppress the QCD background as much as possible. Also, in true $Z \rightarrow \tau\tau$ events there are at least two neutrinos from the two τ decays present and hence true $E_{\mathrm{T}}^{\mathrm{miss}}$ is expected carried away by the neutrino momenta. On the other hand, for QCD events, the $E_{\mathrm{T}}^{\mathrm{miss}}$ comes mainly from mismeasurements of the jet energies, which is comparably small. For the requirement on maximum $\Delta\eta_{\tau\tau}$, it becomes obvious, that the asymmetry is larger if $\Delta\eta_{\tau\tau} < 1.0$. It decreases slightly and saturates around 0.05, if this cut is loosened.

The dependence of the asymmetry on the minimum and maximum$\Delta R_{\tau\tau}$ and $m_{\tau\tau}^{\mathrm{MMC}}$ minimum and maximum requirements are displayed in Section 5.2.1. For $\Delta R_{\tau\tau}$ it appears advantageous to select a region between $2.0 < \Delta R_{\tau\tau} < 3.0$. However, requiring the minimum$\Delta R_{\tau\tau}$ to be larger 1.0 reduced the absolute number of selected events too drastically. Thus, the minimum$\Delta R_{\tau\tau}$ cut is not tightened further with respect to the default $H \to \tau\tau$ event selection. The maximum$\Delta R_{\tau\tau}$ cut is loosened as much as possible in order to increase the asymmetry to a maximum. Thus, the final requirement on the angular distance between the two τ leptons results to be $0.8 < \Delta R_{\tau\tau} < 3.0$. The dependence of the asymmetry on the minimum $m_{\tau\tau}^{\mathrm{MMC}}$ requirement is rather weak. For the maximum $m_{\tau\tau}^{\mathrm{MMC}}$ mass requirement the asymmetry changes sign, increases and then decreases again. This can be explained due to the asymmetry being contrary for $Z \to \tau\tau$ and $\gamma\tau\tau$ events. It is important to select the Z-peak and suppress the $\gamma\tau\tau$ events as much as possible. The asymmetry is maximised if a $m_{\tau\tau}^{\mathrm{MMC}}$ mass window of $70\,\mathrm{GeV} < m_{\tau\tau}^{\mathrm{MMC}} < 100\,\mathrm{GeV}$.

5.2.2 Impact of the level 1 jet requirement on the $Z \to \tau\tau\ \varphi_{CP}^{*}$ distribution

The 2016 ditau had-had trigger requires at least one jet with $p_{\mathrm{T}}^{\mathrm{jet}} > 25\,\mathrm{GeV}$ to be present at level 1. In order for the trigger to be in the efficiency plateau, a threshold of $p_{\mathrm{T}}^{\mathrm{jet}} > 70\,\mathrm{GeV}$ is needed. However, as can be seen in Fig. 5.3 and Fig. 5.4, a cut on $p_{\mathrm{T}}^{\mathrm{jet}}$ decreases the amplitude significantly. The same holds for all cuts which can be used to replace the $p_{\mathrm{T}}^{\mathrm{jet}} > 70\,\mathrm{GeV}$ requirement, which are asking the p_{T} of the decaying particle to be larger 100 GeV, i.e $p_{\mathrm{T}}^{\mathrm{H}} > 100\,\mathrm{GeV}$ or requiring a matched jet on level 1.

Thus, for future measurements a different or additional trigger is needed that does not contain the jet-requirement at L1 level and thus, does not require such a high cut on the $p_{\mathrm{T}}^{\mathrm{jet}}$. A suggestion of a future support trigger without the jet requirement is discussed in Section 7.2.

5.2.3 Dependence of the asymmetry on the $p_{\mathrm{T}}^{\mathrm{jet}}$ cut in $Z \to \tau\tau$ events

Theoretical calculations predict, that the φ_{CP}^{*}-asymmetry in $Z \to \tau\tau$ events depends significantly on the $p_{\mathrm{T}}^{\mathrm{jet}}$ cut [107]. This is also observed in the MC simulations used in this thesis: The asymmetry displayed in Fig. 5.5 decreases with increasing $p_{\mathrm{T}}^{\mathrm{jet}}$ cut, crosses zero, and saturates around $A^{\rho\rho'} \approx -0.02$. The asymmetry crosses zero between 55 GeV and 60 GeV, which is a bit lower than what was predicted in [107]. This difference can be explained by the fact, that in Fig. 5.5 the reconstructed jet momentum is used, while [107] shows the dependence on the generator-level momentum of the truth-jet. In addition, the $Z \to \tau\tau$ MC sample used in Fig. 5.5 contains not only Z+1jet events, but includes all Z+Xjet events, whereas $x \geq 0$, while the theoretical reference plots are produced using a set of pure Z+1jet events.

5.2.4 Impact of the cut variations on the $H \to \tau\tau$ distribution

In order to study the cuts impacts on the CP-even signal distribution, the optimisation is repeated on a pure CP-even $H \to \tau\tau$ signal sample. There are a few differences, which are briefly outlined in the following. Unlike for $Z \to \tau\tau$, the $H \to \tau\tau$ signal is almost not affected by the cut on $E_{\mathrm{T}}^{\mathrm{miss}}$, the maximum $\Delta R_{\tau\tau}$ and the leading τ p_{T} cuts. The effects of varying the $\Delta\eta_{\tau\tau}$ and the minimum $\Delta R_{\tau\tau}$ requirements on the amplitude in $H \to \tau\tau$ events is larger than what is observed in $Z \to \tau\tau$ events. The corresponding plots are displayed in Appendix B. The cut on the minimum jet p_{T} at 70 GeV decreases the amplitude only slightly in $H \to \tau\tau$ events and leaves the phase unchanged (see Fig. 5.6). As a consequence, the Higgs CP measurement does not directly suffer from the $p_{\mathrm{T}}^{\mathrm{jet}}$ requirement on trigger level in the 2016 data. The differences between the impact of the $p_{\mathrm{T}}^{\mathrm{jet}}$ requirement in $Z \to \tau\tau$ and $H \to \tau\tau$ events can

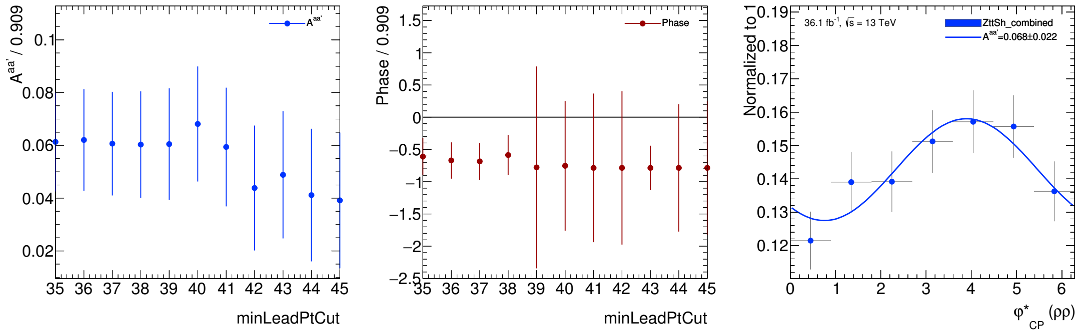

(a) Vary the minimum leading p_{T} cut. The φ^*_{CP} distribution presented requires the $Z \to \tau\tau$ selection and a leading τ $p_{\mathrm{T}} > 40\,\mathrm{GeV}$.

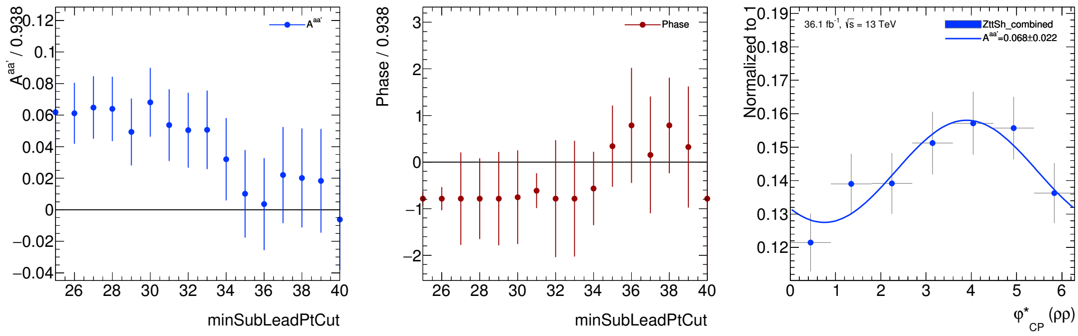

(b) Vary the minimum subleading p_{T} cut.The φ^*_{CP} distribution presented requires the $Z \to \tau\tau$ selection and a leading τ $p_{\mathrm{T}} > 30\,\mathrm{GeV}$.

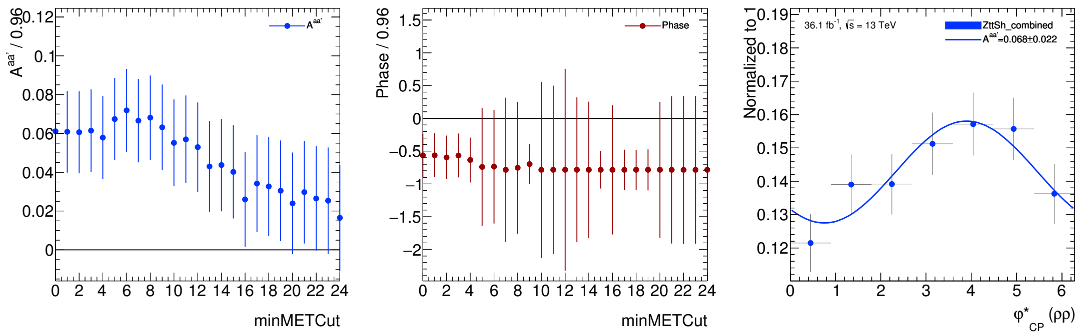

(c) Vary the minimum $E_{\mathrm{T}}^{\mathrm{miss}}$ cut. The φ^*_{CP} distribution presented requires the $Z \to \tau\tau$ selection and $E_{\mathrm{T}}^{\mathrm{miss}} > 8\,\mathrm{GeV}$.

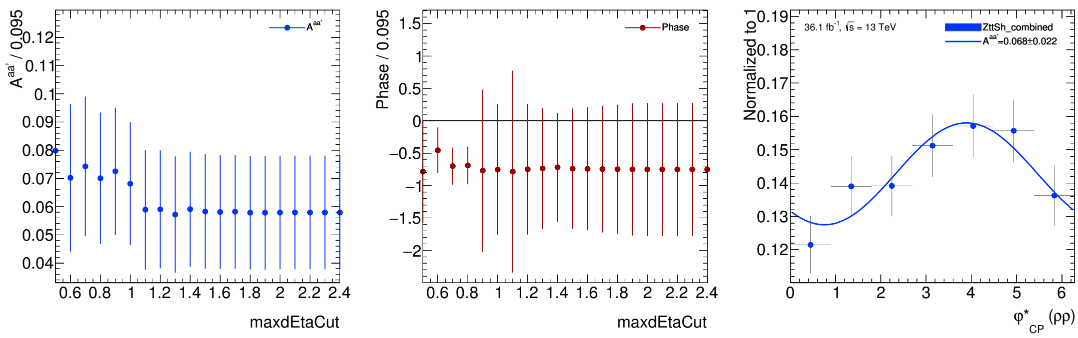

(d) Vary the maximum $\Delta\eta_{\tau\tau}$ cut. The φ^*_{CP} distribution presented requires the $Z \to \tau\tau$ selection and $\Delta\eta_{\tau\tau} < 1.0$

Figure 5.1: Asymmetry and phase of the φ^*_{CP} distribution as a function of the leading and subleading τ p_{T} thresholds, the $E_{\mathrm{T}}^{\mathrm{miss}}$ and the $\Delta\eta_{\tau\tau}$ requirements as well as the φ^*_{CP} distribution in 1p1n-1p1n $Z \to \tau\tau$ events at the final cut value.

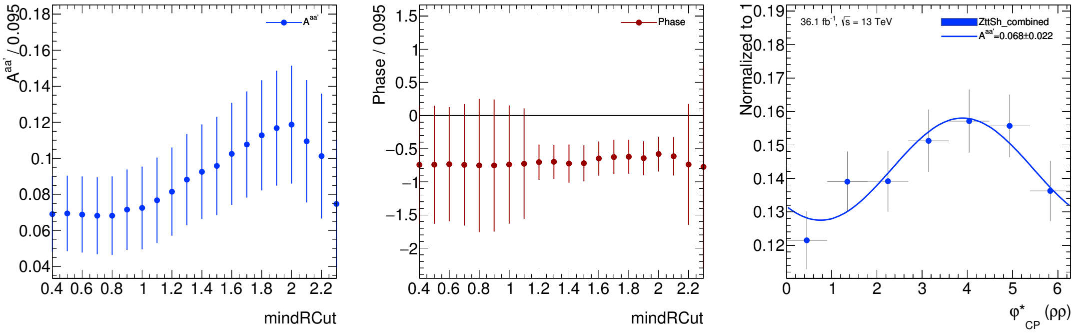

(a) Vary the minimum $\Delta R_{\tau\tau}$ cut. The φ^*_{CP} distribution presented requires the $Z \to \tau\tau$ selection and $\Delta R_{\tau\tau} > 0.8$.

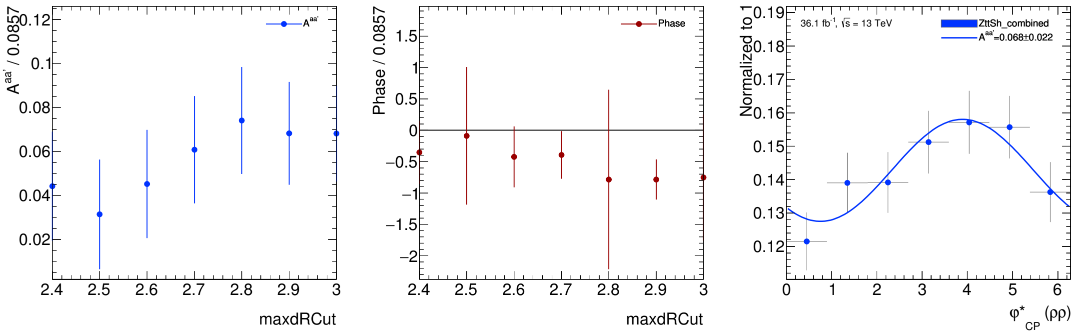

(b) Vary the maximum $\Delta R_{\tau\tau}$ cut. The φ^*_{CP} distribution presented requires the $Z \to \tau\tau$ selection and $\Delta R_{\tau\tau} < 3.0$.

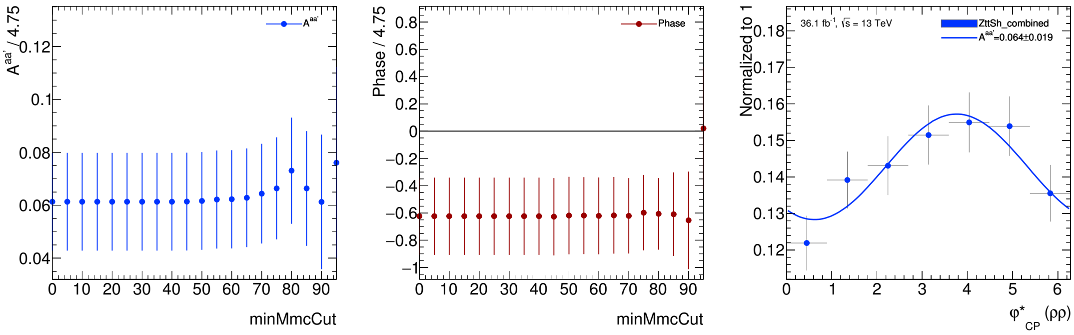

(c) Vary the minimum $m_{\tau\tau}^{\text{MMC}}$ mass cut. The φ^*_{CP} distribution presented requires the $Z \to \tau\tau$ selection and $m_{\tau\tau}^{\text{MMC}} >$ 70 GeV.

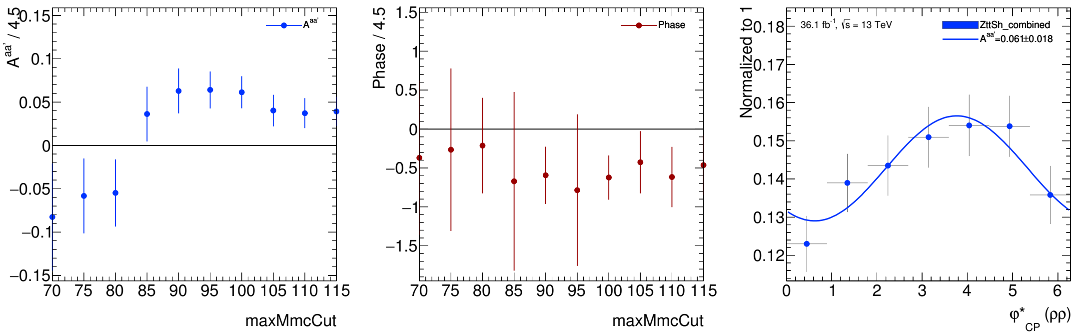

(d) Vary the maximum $m_{\tau\tau}^{\text{MMC}}$ mass cut. The φ^*_{CP} distribution presented requires the $Z \to \tau\tau$ selection and $m_{\tau\tau}^{\text{MMC}} <$ 100 GeV.

Figure 5.2: Asymmetry and phase of the φ^*_{CP} distribution as a function of the requirements on $\Delta\eta_{\tau\tau}$, $\Delta R_{\tau\tau}$ and the $m_{\tau\tau}^{\text{MMC}}$ mass as well as the φ^*_{CP} distribution in 1p1n-1p1n $Z \to \tau\tau$ events at the final cut value.

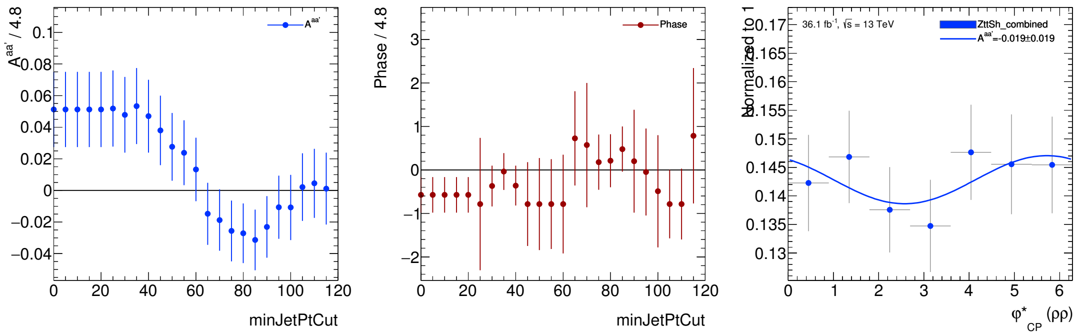

Figure 5.3: Asymmetry and phase of the φ^*_{CP} distribution after variation of the minimum jet p_{T} cut. The presented φ^*_{CP} distribution requires $p_{\mathrm{T}}^{\mathrm{jet}} > 70\,\mathrm{GeV}$ as it is needed if using the 2016 trigger in the analysis.

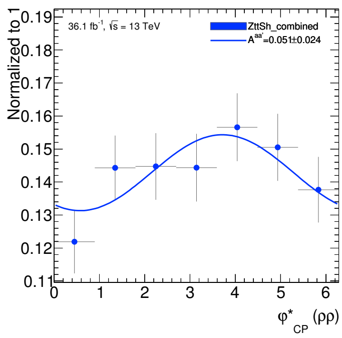

(a) $p_{\mathrm{T}}^{\mathrm{jet}} > 0\,\mathrm{GeV}$

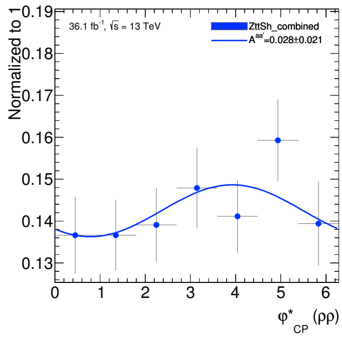

(b) $p_{\mathrm{T}}^{\mathrm{jet}} > 50\,\mathrm{GeV}$

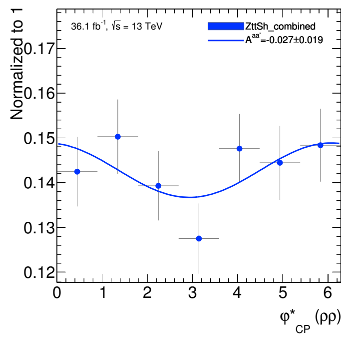

(c) $p_{\mathrm{T}}^{\mathrm{jet}} > 80\,\mathrm{GeV}$

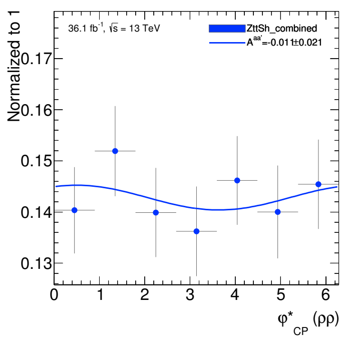

(d) $p_{\mathrm{T}}^{\mathrm{jet}} > 100\,\mathrm{GeV}$

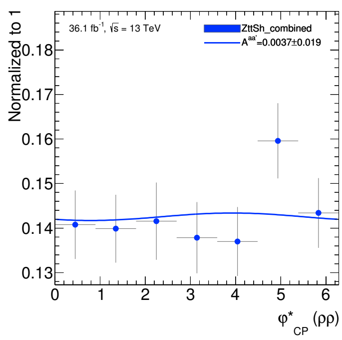

(e) Requiring a matched L1 jet

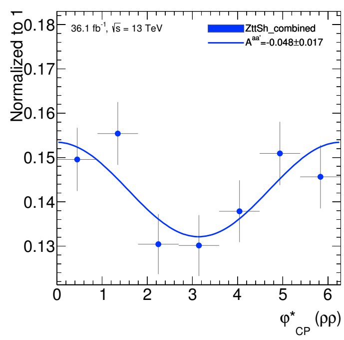

(f) $p_{\mathrm{T}}^{\mathrm{H}} > 100\,\mathrm{GeV}$

Figure 5.4: φ^*_{CP} distribution in $Z \rightarrow \tau\tau$ events after the Z region selection for different cuts on $p_{\mathrm{T}}^{\mathrm{jet}}$, $p_{\mathrm{T}}^{\mathrm{H}}$ and a matched L1 jet.

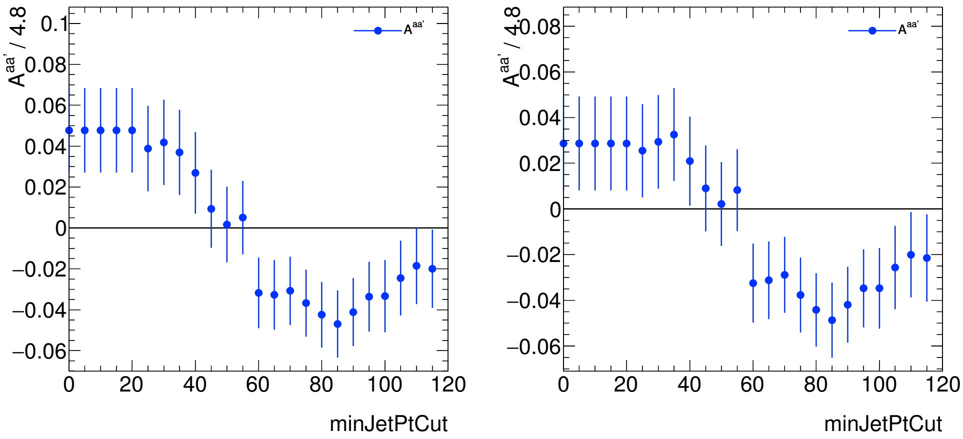

(a) 2015 trigger

(b) 2016 trigger

Figure 5.5: Asymmetry in $Z \rightarrow \tau\tau$ after the 2015(a) and 2016(b) Z-validation region as a function of the $p_{\mathrm{T}}^{\mathrm{jet}}$ cut.

be understood taking into account the fact that production and decay process factorise in the matrix element in case of a scalar Higgs boson, but not for a Z boson. Thus, for $H \rightarrow \tau\tau$ there are no scalar products between jets originating from the production process and the final state τ s or pions included in the calculation of the cross section. For $Z \rightarrow \tau\tau$, the production and decay part of the matrix element do not decouple. Hence, there are scalar products between the jet and τ momenta involved and the cross section for $Z \rightarrow \tau\tau$ is much more sensitive to kinematic cuts on the jet variables than it is the case for the $H \rightarrow \tau\tau$ one.

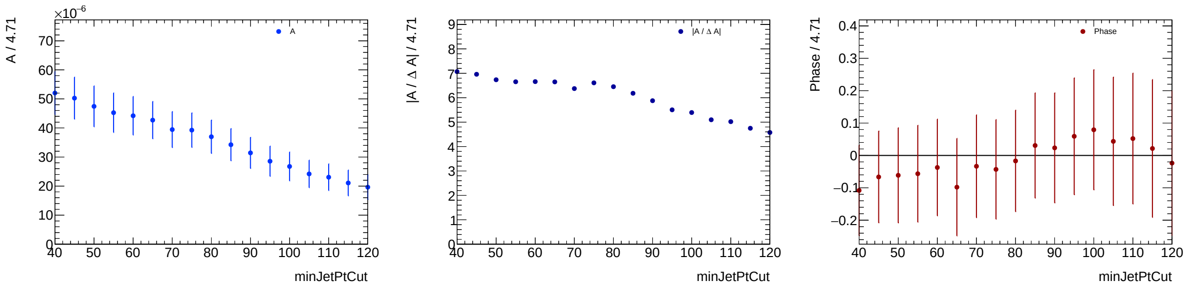

Figure 5.6: Impact of the minimum jet p_{T} requirement on the amplitude and phase of the φ_{CP}^{*} distribution in $H \rightarrow \tau\tau$ events.

CHAPTER 6

Data and simulation

This chapter deals with the datasets used for this analysis. The simulation of signal and background processes using Monte Carlo (MC) generators is discussed as well as the estimation of background processes from data. Since transverse spin correlations play a major role in the presented analysis, it is important to make sure that they are correctly modelled in the respective MC samples. Therefore, a comparison of different $Z \to \tau\tau$ MC simulations with leading-order matrix element calculations is performed.

6.1 Data

This analysis uses LHC data recorded by the ATLAS experiment in the years 2015 and 2016, at a centre-of-mass energy of $\sqrt{s} = 13\,\text{TeV}$. After applying data quality requirements, the corresponding integrated luminosities are $3.2\,\text{fb}^{-1}$ for 2015 and $32.9\,\text{fb}^{-1}$ for 2016 data. The total integrated luminosity collected with ATLAS in this time period is displayed in Fig. 6.1.

The events in this analysis have to pass a di-τ trigger. The trigger chains employed to filter the 2015 and 2016 data used for this analysis are listed in Table 6.1. Both trigger chains demand two medium ID τ s in the event. The τ s that are present in an event are sorted by their transverse momentum (p_{T})

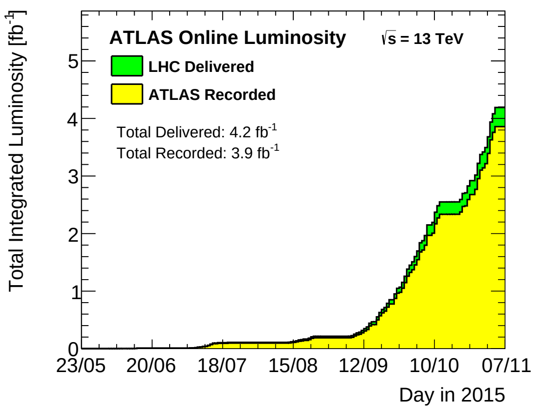

(a) 2015

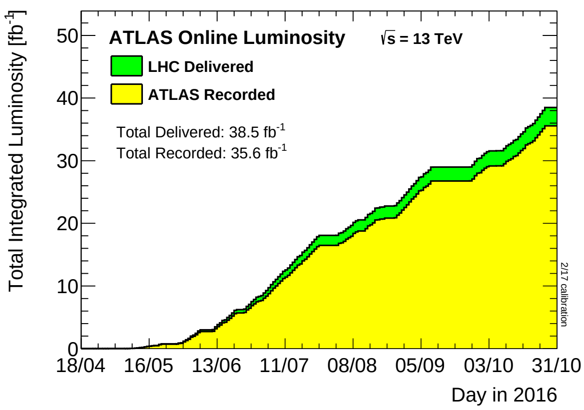

(b) 2016

Figure 6.1: Total integrated luminosity in 2015 and 2016 data measured with the ATLAS detector[109].

Year	Trigger name
2015	`HLT_tau35_medium1_tracktwo_tau25_medium1_tracktwo_L1TAU20IM_2TAU12IM`
2016	`HLT_tau35_medium1_tracktwo_tau25_medium1_tracktwo_L1TAU20IM_2TAU12IM-J25`

Table 6.1: Trigger chains used to filter the 2015 and 2016 data used in this analysis requiring two hadronically decaying τ leptons.

in descending order. Thus, the leading τ is the τ with the highest p_T value. Both trigger chains require the leading τ in the event to fulfil $p_T > 35\,\text{GeV}$ while the subleading τ has to have $p_T > 25\,\text{GeV}$. For 2016 data the di-τ trigger requires the presence of an additional jet with $p_T > 25\,\text{GeV}$ within $\eta_j < 3.2$ at level-1. These requirement allows to reduce the event rate to a reasonable value, and, at the same time keep the p_T thresholds of the two τ leptons as low as possible. This is useful, because the rate of selected $H \to \tau\tau$ signal events decreases with increasing p_T thresholds of the leading and subleading τ leptons.

6.2 Simulation

For the design and performance of any data analysis, simulations of the relevant signal and background processes are of special importance. In the scope of this thesis, they are used to optimise the event selection, calibrate the used methods and to estimate systematic uncertainties.

In order to predict the signal yields or the shape of a certain distribution in the respective region, several steps are necessary: First, the Matrix element (ME) of the hard interaction process is generated with a suitable Monte Carlo generator. In the next step, the particle decays and parton showers are simulated with a parton showering algorithm. Afterwards, a full simulation of the detector response is performed to all Monte Carlo samples using GEANT4 [110–112]. Finally, the events are reconstructed with the same event reconstruction algorithms used for the Run-2 ATLAS data which are described in Section 3.3.

Some of the background processes, however, cannot be estimated sufficiently well from MC. One typical example is the QCD multijet background. In such events, QCD jets are misclassified as (hadronically decaying) τ leptons. Due to the large cross section of such QCD events at the LHC, simulating them in a sufficient amount as MC samples is computationally very expensive. To simulate QCD multijet events, many different processes need to be taken into account for the simulation. This makes the simulation computationally expensive and time consuming. In such cases, data-driven techniques are applied to get a handle on the expected background processes.

Beside that, also the effect of multiple interactions per bunch-crossing and in neighbouring bunch-crossings, called *pileup*, needs to be taken into account in the simulations. For the data recorded in 2015, there have been on average 14 interactions per bunch crossing, while for the data in 2016 it has been on average 25 interactions per bunch crossing as can be seen from Fig. 6.2. To account for the effect of pileup in simulations, so-called *minimum bias* (MB) events are overlaid to each simulated signal and background event. MB events are events, in which the initial hadrons usually scatter without any actual hard collision happening. In order to select MB events in data a very loose trigger chain is used creating as little bias as possible. However, the MB events in the simulations used in this analysis are simulated with Pythia8 [113]. The number of MB events that are overlaid to the simulated signal and background events is chosen in a way such that the resulting distribution of the number of interactions per bunch crossing in simulations agrees with the one observed in data.

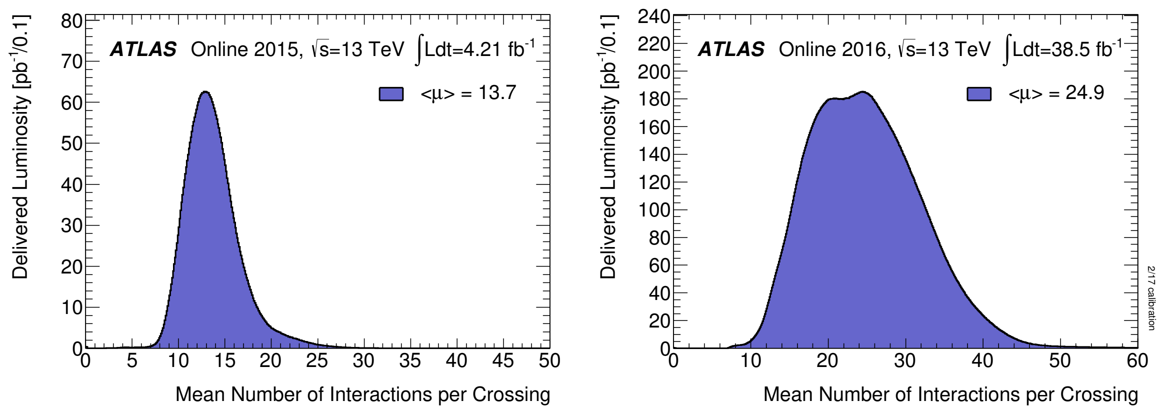

(a) 2015 (b) 2016

Figure 6.2: Average number of interactions per bunch crossing for the data collected in 2015 and 2016 [109].

6.2.1 Estimation of signal and background processes from MC

For this analysis, signal and background processes are simulated using various MC generators at a centre-of-mass energy of 13 TeV, listed in Table 6.2. The two main Higgs boson production processes at the LHC i.e. the ggF and VBF H production processes are included in the signal contribution. Both processes are simulated with Powheg [114–117] interfaced to Pythia8 [113]. The contributions from $t\bar{t}H$, ZH and $W^{\pm}H$ are negligibly small and hence not considered in this thesis.

The dominant background contributions arise from $Z \to \tau\tau$ events with both τ leptons decaying hadronically and from QCD multijet events. All other backgrounds like $Z \to \ell\ell$, W+Jets, Top-Antitop and Single Top have very small or even no significant contribution to the signal regions. The $Z \to \tau\tau$ background contains at least two real τ leptons. For the measurement of the transverse spin correlations in $Z \to \tau\tau$ events (see Chapter 7) it constitutes the signal process. In this case, the $Z \to \tau\tau$ events are simulated using Sherpa2.2. For the Higgs CP measurement itself, a data-driven approach is performed in order to reduce the statistical uncertainty of the Z + jets estimation. The corresponding procedure is described in Section 6.2.4.

QCD multijet events originate from QCD processes, where at least two QCD jets are misclassified as τ s. Shape and yield of the expected QCD distribution are determined from data using the same-sign minus opposite-sign method as described in Section 6.2.3.

The remaining backgrounds can be grouped into two sets of events: The first set comprises W+Jets, $Z \to \ell\ell$ and Single Top events. For these events, there is at least one true τ lepton in the final state and at least one misclassified QCD jet. These processes are estimated from MC simulations, requiring at least one of the τ candidates to be matched to a hadronically decaying τ lepton in the truth record of the simulation. The second set includes processes with two real τ s in the final state e.g. Diboson or Top-Antitop events. They are also estimated from MC simulations. A list of all processes estimated from simulations including the respective Dataset IDs, MC Generators and PDF sets is provided in Table 6.2. As a parametrisation of the parton distribution functions (see Section 2.1.3), the PDF sets CT10 [118] and NNPDF3.0 [119] are used, depending on the respective process.

Signal $H \to \tau\tau$	DSID	MC generator	PDF (ME/UE)
ggH, CP-even ggH, unpolarised	345123 345128	Powheg +Pythia8	NNLOPS
VBF, CP-even VBF, unpolarised	345076 345129	Powheg +Pythia8	AZNLO CTEQ6L1
Background	**DSID**	**MC generator**	**PDF (ME/UE)**
$Z \to \tau\tau$	344775 344779 344782 364137 364138 364139 364140 364141	Sherpa2.2	NNPDF3.0 NNLO
$Z \to \tau\tau$ low-mass DY	364210-364215		
$Z \to \tau\tau$ EWK	344443		
Zee $Z\mu\mu$	364114-364127, 344442 364100-364113, 344441	Sherpa2.2	NNPDF3.0
$t\bar{t}$ Single top	410000-410006 410011-410014	Powheg +Pythia8	CT10
Diboson	363355-363360, 363489-363494	Sherpa2.2	NNPDF3.0
W+jets	364156-364197, 344438-344440	Sherpa2.2	NNPDF3.0

Table 6.2: Signal and background MC samples used in this thesis. For each of the samples, the respective Dataset ID (DSID), the MC generators, and the PDF sets are listed.

6.2.2 $H \to \tau\tau$ signal events with different CP-mixing angles

For the signal processes CP-even , CP-odd and unpolarised $H \to \tau\tau$ MC events are available for the two main Higgs production processes at the LHC i.e. VBF and ggF. The CP-even and CP-odd samples of events are used for validation purposes only. In the CP measurement the unpolarised VBF and ggF $H \to \tau\tau$ samples are utilized. They are able to describe any CP mixing angle ϕ_τ if the respective *TauSpinner*[120] weights are applied. A CP mixing angle of $\phi_\tau = 0^\circ$ corresponds to the pure CP-even SM prediction and $\phi_\tau = 90^\circ$ to a pure CP-odd BSM physics model.

The CP-even and CP-odd weights are applied to the unpolarised $H \to \tau\tau$ samples and the resulting φ^*_{CP} distributions are compared to the ones predicted by the CP even and CP-odd $H \to \tau\tau$ samples in Fig. 6.3 to verify that the transverse spin correlations in $H \to \tau\tau$ are described correctly in the reweighted signal samples. The plots indicate that the reweighted samples agree with the CP-even and CP-odd signal samples within the statistical uncertainties. To investigate whether the shape differences in some of the distributions, e.g. in the IP-ρ (high $d_0^{\mathrm{sig}}/Y_\pm$) category are of statistical or systematic origin, teach of the $H \to \tau\tau$ samples is divided into two randomly chosen and equally sized subsets. The φ^*_{CP} distributions are compared between the two subsets each. The resulting plots are displayed in Appendix C. The distributions of the two subsets are compatible for all categories and samples. Hence, it can be concluded, that the shape differences are purely of statistical and no further corrections have to be applied.

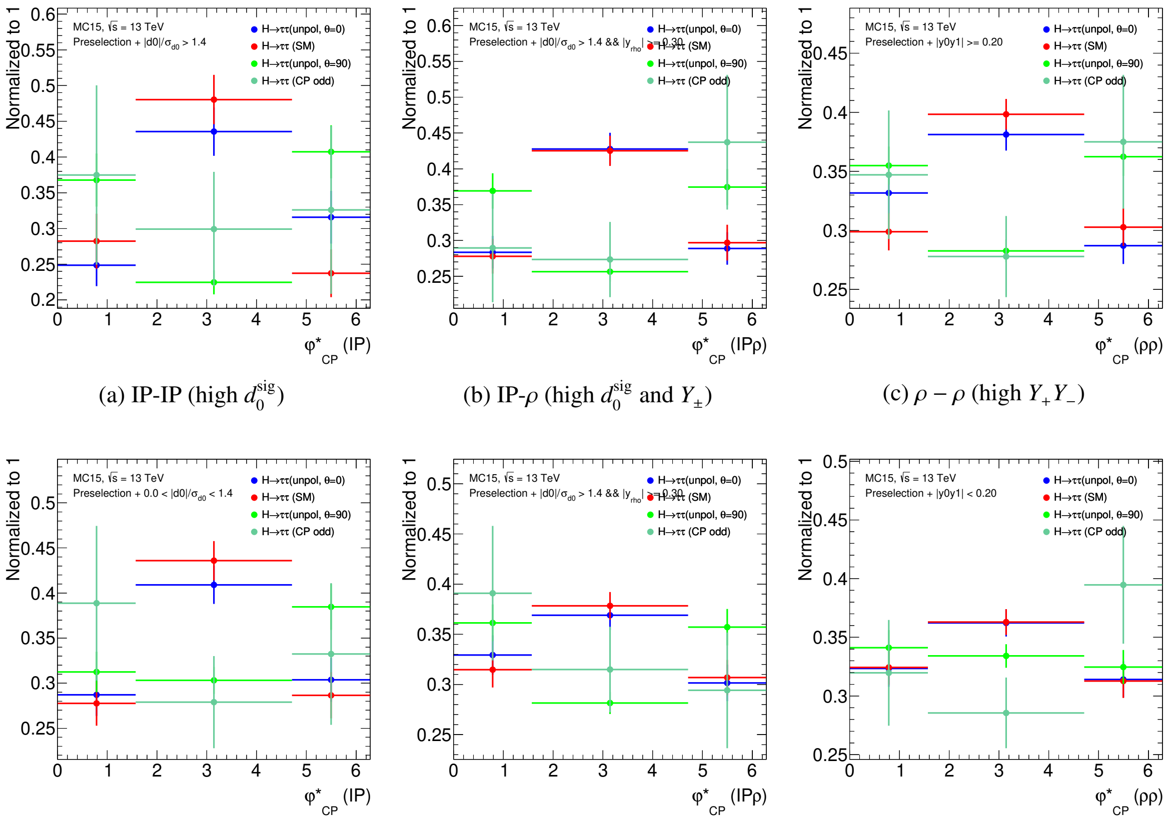

(a) IP-IP (high d_0^{sig}) (b) IP-ρ (high d_0^{sig} and $Y_{\pm}$) (c) $\rho-\rho$ (high Y_+Y_-)

(d) IP-IP (low d_0^{sig}) (e) IP-ρ (low d_0^{sig} and $Y_{\pm}$) (f) $\rho-\rho$ (low Y_+Y_-)

Figure 6.3: Distribution of φ^*_{CP} in the Higgs preselection region split up by decay mode combination for the CP-even , CP-odd , and unpolarised $H \to \tau\tau$ samples weighted to describe a CP mixing angle of zero or 90° denoted by $\theta = 0^\circ$ and $\theta = 90^\circ$ in the plots.

The φ^*_{CP} distributions for $\phi_\tau \in [0, 10, ..., 90]^\circ$ in the different high and low d_0^{sig}/ Y categories are displayed in Fig. 6.4. The events included in these distributions fulfil either the the VBF or Boosted event selection requirements.

6.2.3 Estimation of the QCD multijet background

The QCD multijet background is estimated in a data-driven way using the same-sign minus opposite-sign (OS-SS) method. As described in Chapter 5, events selected in this analysis are required to contain two opposite-sign (OS) τ candidates. In addition, the τ candidates are required to have one or three tracks, both need to pass at least the medium τ identification criterion and one of them has to pass the tight identification requirement. If the requirement on the charge product of the two τ leptons is reversed and they are required to have the same-sign (SS), the selected events are very likely to stem from the QCD multijet background. Since the main other contributions in the SRs, $Z \to \tau\tau$ and $H \to \tau\tau$ processes, require OS τ leptons due to charge conservation. To ensure, that no events are double counted, SS events from other background processes are subtracted from the data in the SS region. However, their contribution is small as can be seen from Fig. 6.5. It shows the φ^*_{CP} distributions of data and all backgrounds estimated from MC in the VBF and boosted inclusive categories asking the two τ leptons to

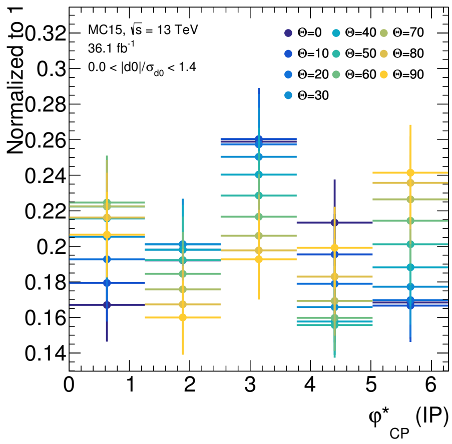

(a) IP-IP (low d_0^{sig})

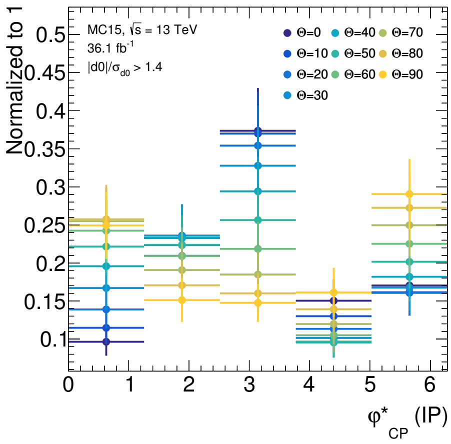

(b) IP-IP (high d_0^{sig})

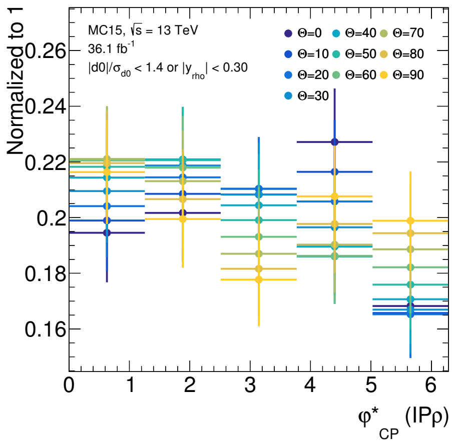

(c) IP-ρ (low d_0^{sig} and $Y_{\pm}$)

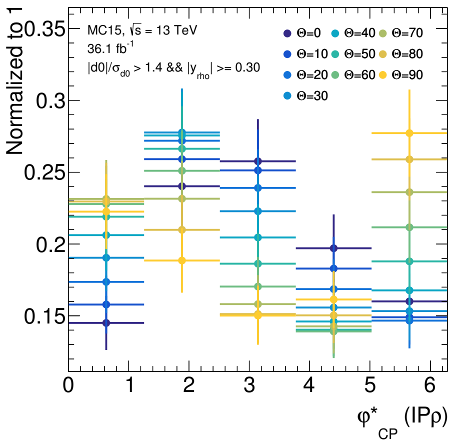

(d) IP-ρ (high d_0^{sig} and $Y_{\pm}$)

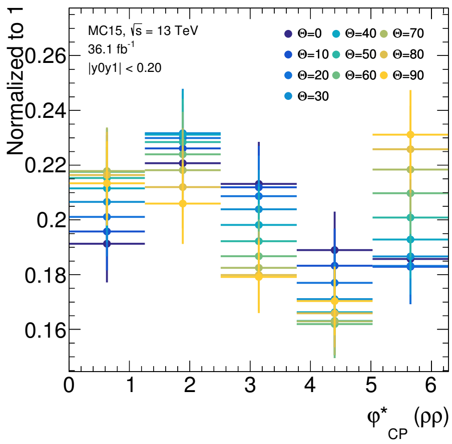

(e) $\rho - \rho$ (low Y_+Y_-)

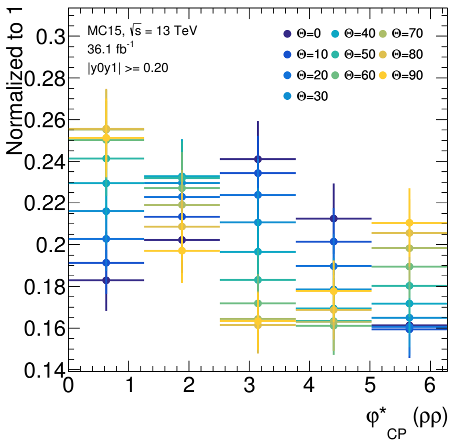

(f) $\rho - \rho$ (high Y_+Y_-)

Figure 6.4: $H \to \tau\tau$ signal events from the unpolarised VBF and ggF production processes reweighted to describe CP mixing angles in a range of $\phi_\tau \in [0, ..., 90]^\circ$ split into the different decay mode combinations and $d_0^{\mathrm{sig}}/\ Y_{\pm}$ categories. The selected events fulfil either the VBF or boosted event selection requirements.

have the same sign.

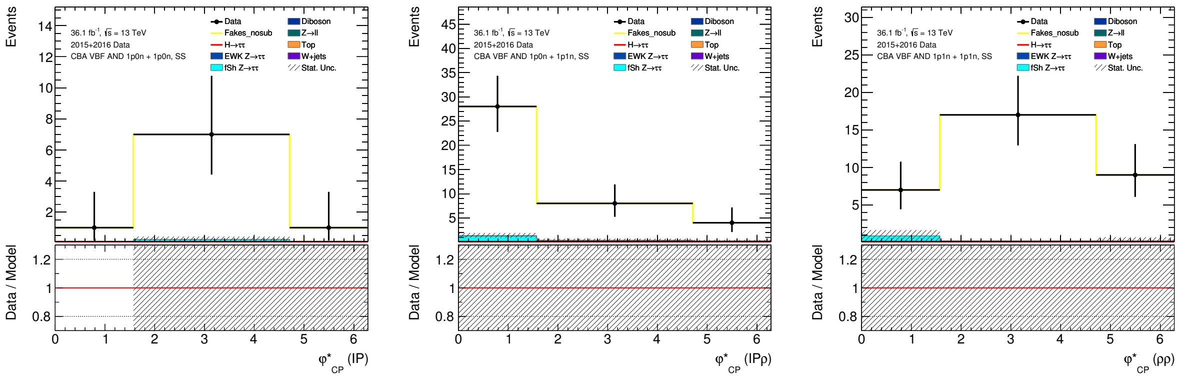

(a) VBF region

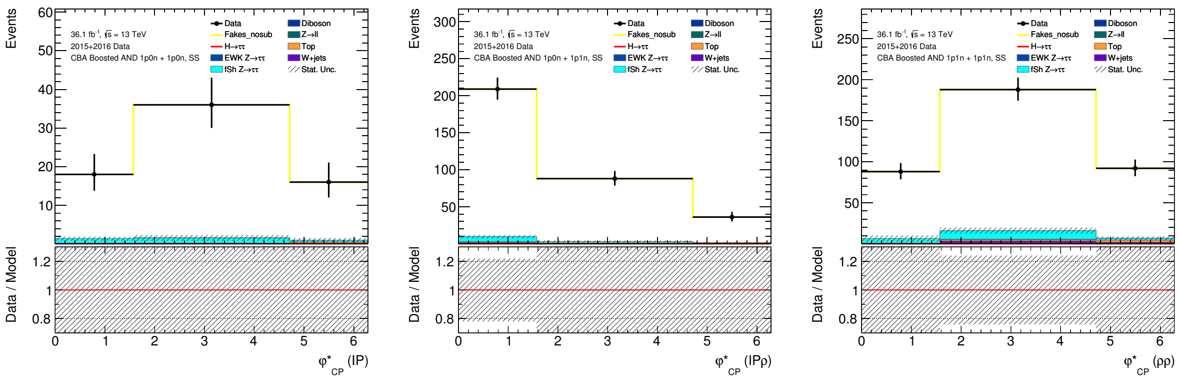

(b) boosted inclusive region

Figure 6.5: The φ^*_{CP} distributions in the VBF (a) and boosted inclusive (b) categories requiring two SS τ leptons in all three considered τ decay-mode combinations.

Thus, the QCD multijet background in the signal regions is estimated from SS data in the respective regions. In order to correct for the yield differences between the SS and OS regions, the ratio between the number of QCD multijet events in the OS to SS region r_{QCD} needs to be measured. It is defined as

$$r_{\text{QCD}} = \frac{N^{OS}_{QCD}}{N^{SS}_{QCD}} \tag{6.1}$$

and included as normalisation factor in the final measurement. Simultaneously, the normalisation of the $Z \to \tau\tau$ background (r_Z) is determined to improve the overall agreement of data and simulations. Even though, in $Z \to \tau\tau$ simulations the cross section is already taken into account correctly, it has been measured in a different phase space than the one used in this thesis. Hence, it makes sense to allow for a variation on the expected $Z \to \tau\tau$ yield in the final measurement. The expected data yield in the OS region then follows as

$$N^{OS}_{\text{Data}} = r_Z N^{OS}_Z + \sum_{\text{other BG } i} N^{OS}_i + r_{\text{QCD}} \left(N^{SS}_{\text{Data}} - r_Z N^{SS}_Z - \sum_{\text{other BG } i} N^{SS}_i \right). \tag{6.2}$$

The ratios r_{QCD} and r_Z are measured in the VBF, boosted low-p_{T} and boosted high-p_{T} control regions simultaneously from a fit to the $\Delta\eta_{\tau\tau}$ distribution. $\Delta\eta_{\tau\tau}$ represents the longitudinal boost of the di-τ system. It is suitable for this measurement because the shapes of the QCD multijet and $Z \to \tau\tau$ backgrounds differ significantly in this variable: the distribution of the QCD multijet background is rather flat in $\Delta\eta_{\tau\tau}$, while the $Z \to \tau\tau$ background decreases for larger values of $\Delta\eta_{\tau\tau}$ as can be seen in Fig. 6.6.

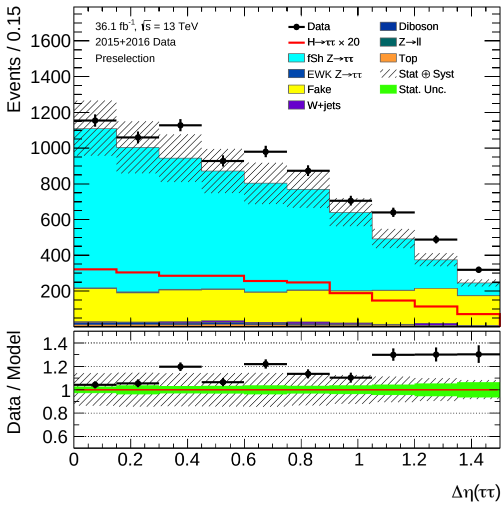

Figure 6.6: Prefit $\Delta\eta_{\tau\tau}$ distribution in the Higgs preselection region using $\mathcal{L}$ = 36.1 fb^{-1} of ATLAS data. The QCD multijet background is referenced as *Fake* in the plot.

A comparison of the φ^*_{CP} distributions of OS and SS events is performed to validate that the extrapolation of the QCD multijet background shape from the SS to the OS region is justified. The shapes in SS and OS events are overlaid in Fig. 6.7 for events that fulfil the VBF or boosted requirements and the standard τ ID criteria, i.e. requiring one medium and at least one tight τ. The events passing the OS or SS requirement agree in all bins within their statistical uncertainties. The compatibility is further quantified by performing a $\mathcal{X}^2$ test of the two distributions. The p-values in the τ-id regions range from 0.48-0.88, which means that all distributions are statistically compatible.

6.2.4 Estimation of the $Z \to \tau\tau$ background

The $Z \to \tau\tau$ background in the φ^*_{CP} signal regions (SR) is also estimated from data. The shape is obtained from data in the $Z \to \tau\tau$ control regions (CR).For each signal region, there is a $Z \to \tau\tau$ CR defined with the same requirements as the SR except for the one on the $m^{\mathrm{MMC}}_{\tau\tau}$ mass. In the Z CRs, the mass is asked to be within 70 GeV < $m^{\mathrm{MMC}}_{\tau\tau}$ < 100 GeV instead of 100 GeV < $m^{\mathrm{MMC}}_{\tau\tau}$ < 140 GeV. The yields of the $Z \to \tau\tau$ events in the SRs is estimated using MC simulations. The data from the CRs are then scaled to the $Z \to \tau\tau$ yield in the respective SR expected from MC.

In principle the φ^*_{CP} distribution is expected to be flat for $Z \to \tau\tau$ events in all mass ranges, such that it is justified to use the data from the Z control regions as estimate for the shape of the $Z \to \tau\tau$ background in the respective signal region. However, this assumption has to be approved, by comparing the shape of the φ^*_{CP} distributions in simulated $Z \to \tau\tau$ events in the two different mass ranges. Figure 6.8 shows the φ^*_{CP} observable using $Z \to \tau\tau$ events after applying the Higgs preselection requirements in the Z- and Higgs-mass windows for all three decay mode combinations in the respective low/high d_0^{sig} or $Y_\pm$ categories. It can be seen that the shape of the $Z \to \tau\tau$ background agrees in all categories within their

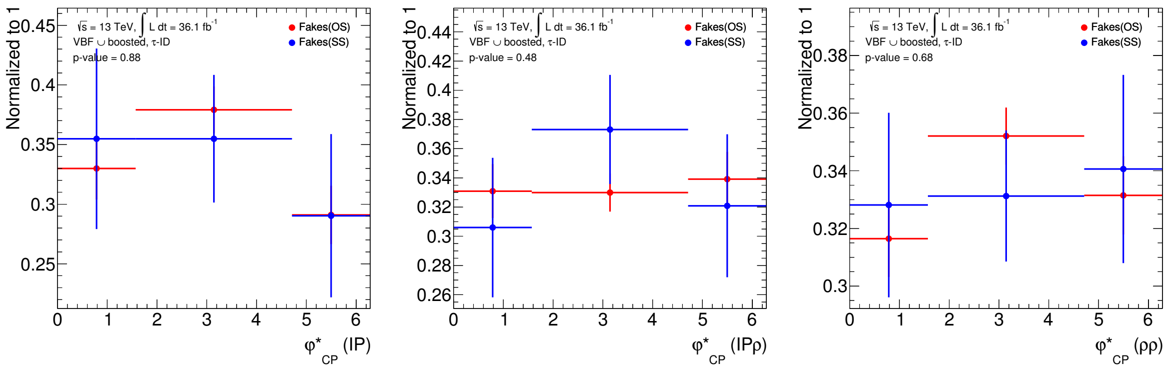

(a) IP-IP (b) IP-ρ (c) $\rho - \rho$

Figure 6.7: Comparison of the shape of OS and SS data after subtraction of all mc backgrounds. Events are selected that fulfil the VBF or the boosted signal region requirements with the standard τ ID conditions for all three considered τ decay-mode combinations.

statistical uncertainties. The p-values for comparing the distributions in the two mass ranges range from 0.2 to 0.99.

6.3 Validation of transverse spin correlations in $Z \to \tau\tau$ MC samples

The $Z \to \tau\tau$ decays constitute a large, irreducible background for the $H \to \tau\tau$ CP-measurement. Thus, it is crucial to correctly model their distribution in the φ^*_{CP} observable. Their distribution in φ^*_{CP} is predicted to be flat [96], but this needs to be carefully checked. A mismodelling in the simulation of transverse τ spin-correlations in $Z \to \tau\tau$ events in the signal regions, can lead to non trivial distributions that can mimic a CP-violating signal.

Beside that it is studied in this thesis whether $Z \to \tau\tau$ events can be used to calibrate the Higgs CP measurement. For this purpose a modified φ^*_{CP} distribution is measured in a $Z \to \tau\tau$ enhanced region which exploits transverse τ spin correlations in $Z \to \tau\tau$ events. The events are separated into two categories based on the angle α^- described in Section 4.2. For this study it is also important to validate the modelling of the transverse τ spin correlations in simulations.

$Z \to \tau\tau$ events are simulated at ATLAS using three different MC generators to simulate the hard interaction: Sherpa2.2, Powheg +Pythia8 and MadGraph +Pythia8. Sherpa2.2 is expected to model the transverse spin correlations correctly also in events with extra jets in the final state [121], since Sherpa2.2 implements spin correlations across the propagator of the decaying particle according to the algorithm described in [122]. This also includes the transverse τ spin correlations in hadronic τ decays. Powheg and MadGraph are both interfaced with Pythia8, which models the τ decays and performs the parton showering. Pythia8 includes a proper treatment of transverse spin correlations at LO for $f + \bar{f} \to \gamma, Z^0, Z^{0'}, \gamma^*/Z^0/Z^{0'}, H, W, B, D \to \tau\tau$ processes, where f denotes any fermion of the SM [123]. However, transverse spin correlations in production processes involving extra jets, like $q/\bar{q}+g \to Z \to \tau\tau$ can only be treated properly with Pythia8 if the intermediate $q\bar{q}$ vertex is stored, which is usually not the case [124]. Hence, the Powheg +Pythia8 and MadGraph +Pythia8 simulations do not model the transverse τ spin correlations correctly in Z+jets events.

This section is organised as follows: First, I compare Sherpa2.2 simulations with exact ME calculations from [125] for different Z production processes involving 0,1 and 2 jets in the final state at generator

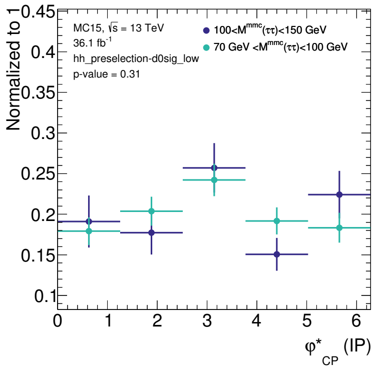

(a) IP-IP (low $d_0^{\rm sig}$)

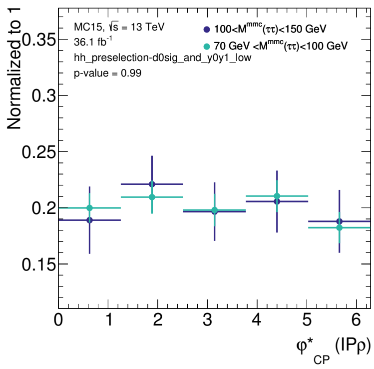

(b) IP-ρ (low $d_0^{\rm sig}$, low $Y_\pm$)

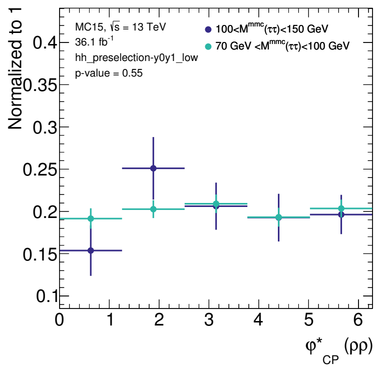

(c) $\rho-\rho$ (low Y_+Y_-)

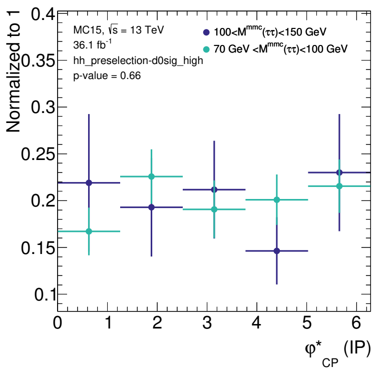

(d) IP-IP (high $d_0^{\rm sig}$)

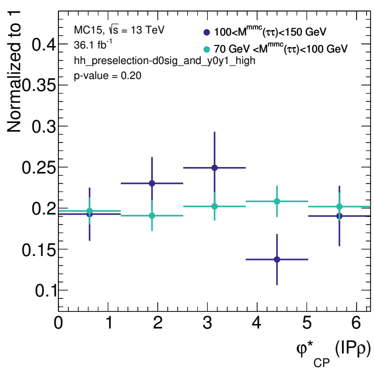

(e) IP-ρ (high $d_0^{\rm sig}$/ $Y_\pm$)

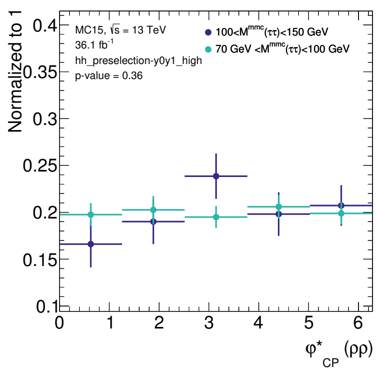

(f) $\rho-\rho$ (high Y_+Y_-)

Figure 6.8: φ^*_{CP} distribution of Sherpa2.2 $Z\to\tau\tau$ at preselection in the H and Z mass window.

level. Next, I confirm that the modelling of transverse τ spin correlations agrees in simulations of $Z\to\tau\tau$ events with no extra jet produced with Sherpa2.2 and MadGraph +Pythia8. Finally, I compare the inclusive Sherpa2.2, Powheg +Pythia8 and MadGraph +Pythia8 $Z\to\tau\tau$ +jets simulations on generator level as well as after the full ATLAS event reconstruction.

6.3.1 Comparison of Sherpa2.2 with ME Calculations (in 0,1 and 2-jet bin)

The modelling of the transverse τ spin correlations in $Z\to\tau\tau$ events, simulated with Sherpa2.2, is validated by comparing the generator level φ^*_{CP} distributions with those predicted in [125]. These distributions are obtained from the exact calculation of the differential cross section, including the transverse τ spin correlations. The comparison is performed separately for events with 0,1 or 2 additional partons in the final state, as listed in Table 6.3. For each of these sub-processes, a private sample of 5 million events is generated using Sherpa2.2 with the same software configuration used for the nominal Sherpa2.2 $Z\to\tau\tau$ samples listed in Table 6.2. The resulting φ^*_{CP} distributions at generator level are shown in Fig. 6.9 and include the basic event selection of the visible τ transverse momentum and the invariant mass of the two τ leptons as listed in Table 6.4. These requirements are applied to generator-level quantities, i.e. to the true $p_{\rm T}^{\tau,vis}$ and the di-τ invariant mass. For the actual analysis, when the quantities of fully reconstructed objects are used, higher $p_{\rm T}^{\tau,vis}$ values are required. In this case, it is asked for $p_{\rm T}^{\tau,vis}>40$ GeV of the leading and $p_{\rm T}^{\tau,vis}>30$ GeV of the subleading τ lepton (see Chapter 5).

Number of partons	Generated process
0	$q + \bar{q} \to Z \to \tau\tau$
1	$q + g \to Z + q \to \tau\tau + q \,/\, \bar{q} + g \to Z + \bar{q} \to \tau\tau + \bar{q}$
2	$g + g \to Z + q + \bar{q} \to \tau\tau + q + \bar{q}$

Table 6.3: Generated processes for generator comparison of SHERPA2.2 with the exact calculations of transverse tau spin correlations in $Z \to \tau\tau$ events [125].

Since both distributions are symmetric (with a shift of π), the CP-odd like distribution is shifted by π and

variable	selection
$p_T^{\tau,vis}$	$p_T^{\tau,vis} > 20\,\text{GeV}$
$\eta^{\tau,vis}$	$\eta^{\tau,vis} < 2.5$
$m_{\tau\tau}$	$m_{\tau\tau} > 80\,\text{GeV}$

Table 6.4: Minimal event selection used in the SHERPA2.2 validation at generator level.

added to the CP-even like distribution, as shown in Fig. 6.10. This increases the statistics in each bin and thus reduces the overall statistical uncertainty.

The φ^*_{CP} distributions are fitted with a cosine, as described in Section 4.1.4 and from the resulting fit parameters, the asymmetries (see Eq. (4.19)) of the distributions are derived and compared to the asymmetries determined from the exact calculations in [125]. For Z+0jets and Z+1jet, the results are summarised in Table 6.5. They are found to be in agreement within statistical uncertainties. In Z+2jets events, there is no φ^*_{CP} dependence observed, as expected. The reason for this is that the two gluons in the initial state are both spin-1 particles. Therefore, the intermediate state, i.e. the Z boson together with the quark-antiquark pair, can have spin 0 or spin 2. This means that the beam-axis must no longer be parallel to the Z/γ spin. However, this fact is important to the definition of the τ-production plane used to calculate the angle α^-. Hence, in this case, splitting the phase space becomes inappropriate and the $Z \to \tau\tau$ distribution is flat as it is the case without any splitting. In order to support this hypothesis, a linear function is fitted to the distribution in this case. The extracted rise is compatible with 0 for all decay mode combinations as can be seen in Fig. 6.10(c).

For Z+1 jet events, there is no expected value given in Table 6.5, since there is no reference value from theoretical calculations. However, the matrix elements are calculated for one single case, i.e. the IP-IP method in the 1p0n-1p0n decay mode combination, requiring a minimum $p_{\mathrm{T}}^{\mathrm{jet}}$ of 25 GeV on generator

	# Partons	IP-IP (1p1n-1p1n)	IP-ρ (1p1n-1p1n)	$\rho - \rho$ (1p1n-1p1n)
A(exp.)	0	7.15%	8.77%	10.75%
A(meas., Sh 2.2)		(7.6 ± 1.3)%	(8.9 ± 1.3)%	(9.6 ± 1.3)%
A(meas.)	1	(1.38 ± 0.35)%	(1.92 ± 0.35)%	(2.79 ± 0.35)%

Table 6.5: A comparison of the asymmetries determined from simulations A(meas.) and the expected ones A(exp.) determined in exact calculation of the matrix elements [125].

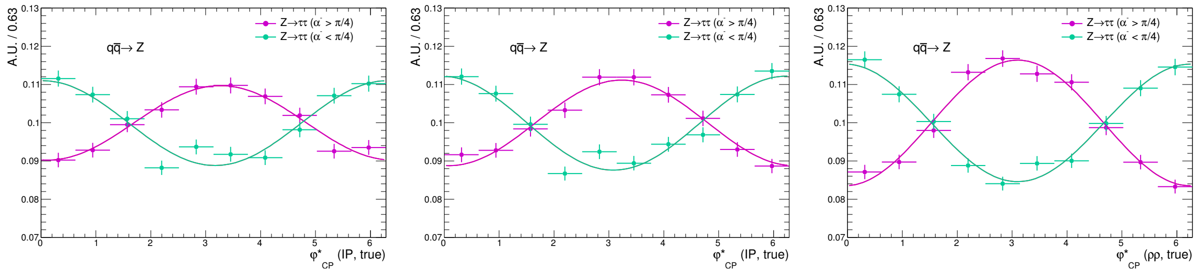

(a) $q + \bar{q} \to Z \to \tau\tau$

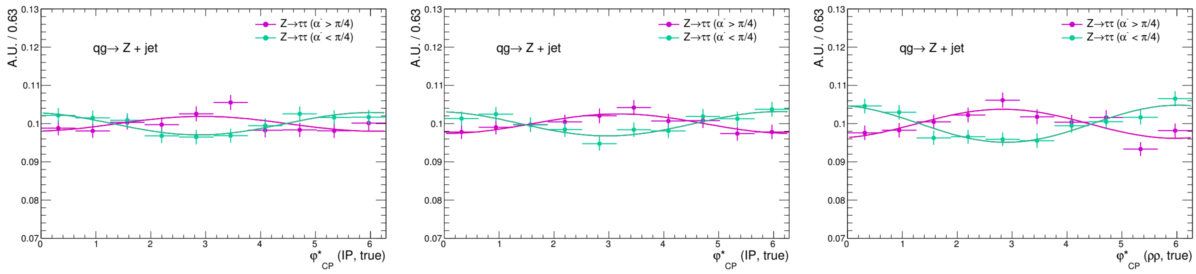

(b) $q/\bar{q} + g \to Z \to \tau\tau$

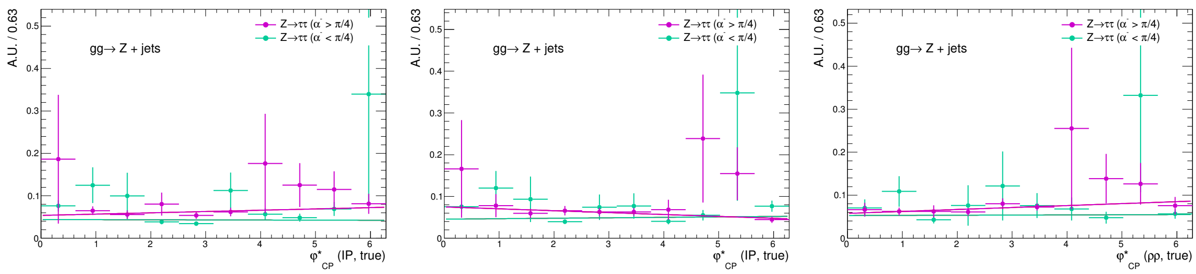

(c) $gg \to Z \to \tau\tau$

Figure 6.9: The CP-even and CP-odd like φ^*_{CP} dependence in Sherpa2.2 events with two 1p1n τ leptons reconstructed using the IP-IP, IP-ρ and $\rho - \rho$ methods in the 0-jet(a), 1-jet(b) and 2-jet (c) bin. In case (a) and (b) cosine distributions are fitted, while for (c) a linear function is used since there is no cosine distribution expected or observed.

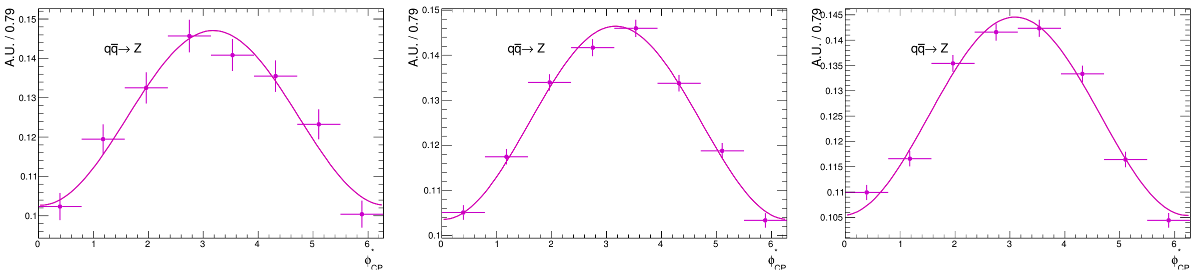

(a) $q + \bar{q} \to Z \to \tau\tau$

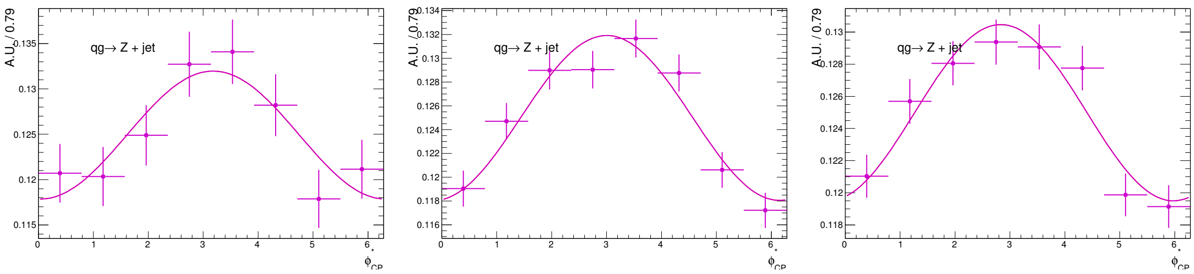

(b) $q/\bar{q} + g \to Z \to \tau\tau$

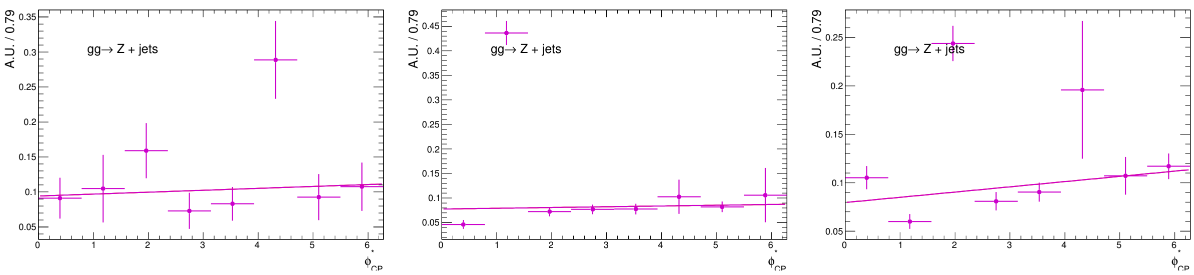

(c) $gg \to Z \to \tau\tau$

Figure 6.10: φ^*_{CP} distributions in Sherpa2.2 events with two 1p1n taus reconstructed using the IP-IP, IP-ρ and ρ-ρ methods. The φ^*_{CP} distribution with $\alpha^- < \frac{\pi}{4}$ is shifted by π and added to the distribution for $\alpha^- \geq \frac{\pi}{4}$.

level [107]. As can be seen from Fig. 4.11, the expected asymmetry asking for a minimum $p_{\mathrm{T}}^{\mathrm{jet}}$ of 25 GeV is 5% and it increases for decreasing $p_{\mathrm{T}}^{\mathrm{jet}}$. In order to compare the results in this thesis with this theoretical reference value, the generator-level studies are repeated for Sherpa2.2 with 1p0n-1p0n decays. Since the MC generated for this validation study requires a minimum $p_{\mathrm{T}}^{\mathrm{jet}}$ of 20 GeV (in order to compare all other decay-mode combinations with the reference values from [125]), it was not possible to compare with the exact same initial conditions in this case. However, from Fig. 4.11 it becomes clear, that the asymmetry is expected to rise for smaller values of $p_{\mathrm{T}}^{\mathrm{jet}}$. Thus, Fig. 4.11 can be used to estimate if the order of magnitude is correct and that the asymmetry must be at least 5%. The measured value from simulations is

$$A(\text{meas., Sh 2.2, 1p0n-1p0n, Z+1jet}) = (6.1 \pm 1.8)\%.$$

This is consistent with a lower limit from the theoretical calculations of 5%.

	IP-IP (1p1n-1p1n)	IP-ρ (1p1n-1p1n)	ρ-ρ (1p1n-1p1n)
A(meas., Sh 2.2)	$(7.6 \pm 1.3)\%$	$(8.9 \pm 1.3)\%$	$(9.6 \pm 1.3)\%$
A(meas., MG)	$(6.1 \pm 0.6)\%$	$(7.4 \pm 0.6)\%$	$(9.6 \pm 0.6)\%$

Table 6.6: A comparison of the fitted asymmetries in SHERPA2.2 and MADGRAPH in events with no extra jets.

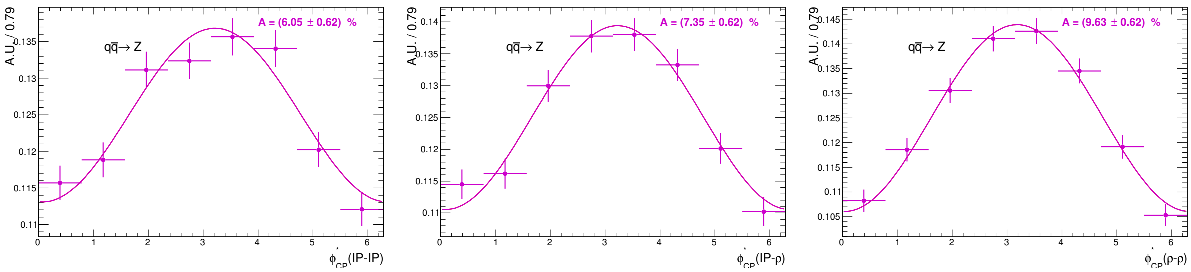

Figure 6.11: The φ^*_{CP} dependence in MADGRAPH +PYTHIA8 events with two 1p1n τ leptons reconstructed using the IP-IP, IP-ρ and ρ-ρ methods. The φ^*_{CP} distribution with $\alpha^- < \frac{\pi}{4}$ is shifted by π and added to the distribution for $\alpha^- \geq \frac{\pi}{4}$ in the $q + \bar{q} \to Z \to \tau\tau$ production mode.

6.3.2 The φ^*_{CP} dependence in Z+0jet events using MADGRAPH +PYTHIA8 for the event generation

In the following, the predicted φ^*_{CP} distributions from the baseline MADGRAPH simulation are investigated and compared with the SHERPA2.2 predictions. SHERPA2.2 calculates the τ spin correlations using full helicity matrices in the matrix element at LO[126]. MADGRAPH, instead, leaves the τ decay to be simulated by PYTHIA8 +TAUOLA, which does the parton showering and recalculates the matrix element including also the transverse spin correlations assuming the Drell-Yan(DY) production of the Z/γ^*[123, 127]. SHERPA2.2 and MADGRAPH predict similar φ^*_{CP} distributions in $Z \to \tau\tau$ events with no additional jet, but a difference can be expected in Z+jets events. Simulations with SHERPA2.2 and MADGRAPH should agree in DY events. This is confirmed by a comparison of the asymmetries in events with no additional partons reported in Table 6.6. The fitted distributions are shown in Fig. 6.11.

6.3.3 Comparison of SHERPA2.2, MADGRAPH +PYTHIA8 and POWHEG +PYTHIA8 for inclusive Z + jets events

As described in Section 6.3, the three used MC generators differ in their treatment of transverse τ spin correlations in Z + jets events. SHERPA2.2 models the longitudinal and transversal spin correlations also in Z + jets events correctly, while MADGRAPH and POWHEG would simulate the τ decays always assuming the DY production only.

In Table 6.7 and Fig. 6.12, the generator-level predictions from SHERPA2.2, POWHEG and MADGRAPH, for the inclusive Z + jets production are compared in order to assess the size of such differences. Again, the minimal event selection described in Table 6.4 is applied, the distribution at $\alpha^- < \frac{\pi}{4}$ is shifted by π and is added to the one at $\alpha^- \geq \frac{\pi}{4}$.

Significant differences in the fitted asymmetries are obtained between SHERPA2.2 and MADGRAPH. The asymmetries in events simulated with SHERPA2.2 are almost twice as large as the ones predicted by MADGRAPH. On the other hand, POWHEG and MADGRAPH show comparable results, which is also what is expected because both generators use PYTHIA8 for the decay of the τ and the parton showering.

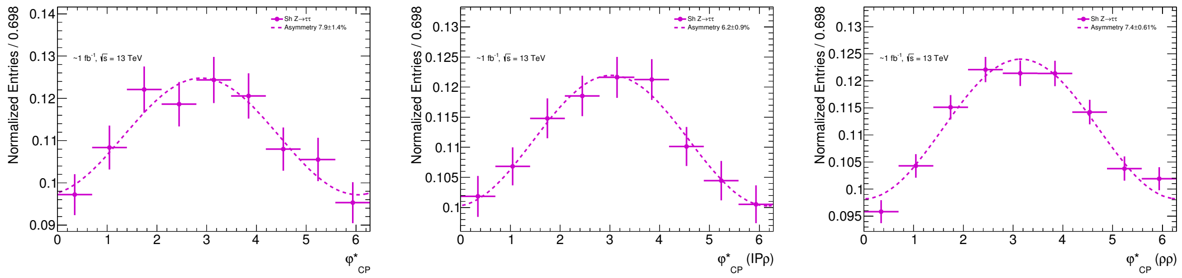

(a) Sherpa2.2

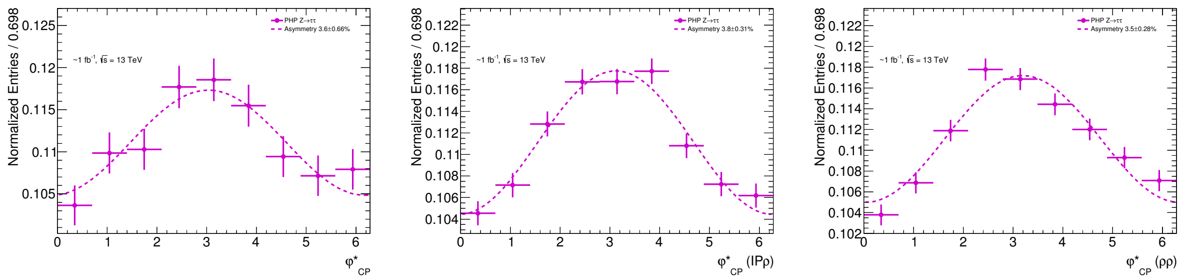

(b) Powheg

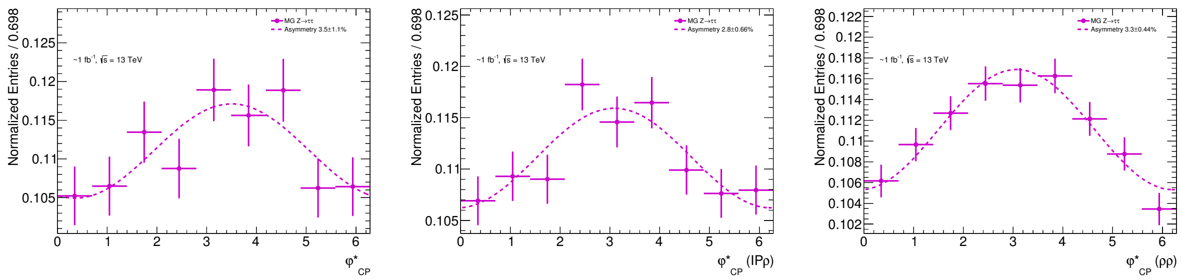

(c) MadGraph

Figure 6.12: The generator-level φ^*_{CP} distributions in the 1p0n-1p0n, 1p0n-1p1n and 1p1n-1p1n τ decay modes reconstructed with the IP, IP-ρ and $\rho - \rho$ methods, respectively, based on (a) Sherpa2.2, (b) Powheg and (c) MadGraph ATLAS MC samples. The event selection described in Table 6.4 is applied. The asymmetry is obtained from a cosine fit to the simulated data.

	Asymmetry in %		
Generator	1p0n-1p0n	1p0n-1p1n	1p1n-1p1n
Sherpa2.2	7.9 ± 1.4	6.2 ± 0.9	7.4 ± 0.61
Powheg	3.6 ± 0.66	3.8 ± 0.31	3.5 ± 0.28
MadGraph	3.5 ± 1.1	1.8 ± 0.66	3.4 ± 0.44

Table 6.7: Results of the fit to the simulated events shown in Fig. 6.12 at generator-level for (a) Sherpa2.2 and (b) Powheg and (c) MadGraph.

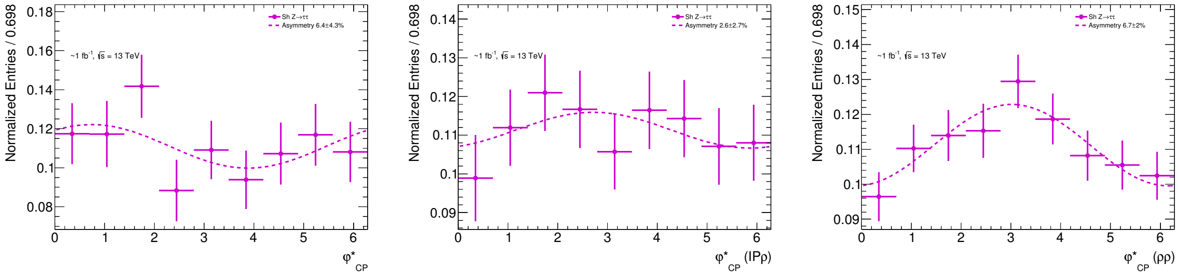

(a) SHERPA2.2

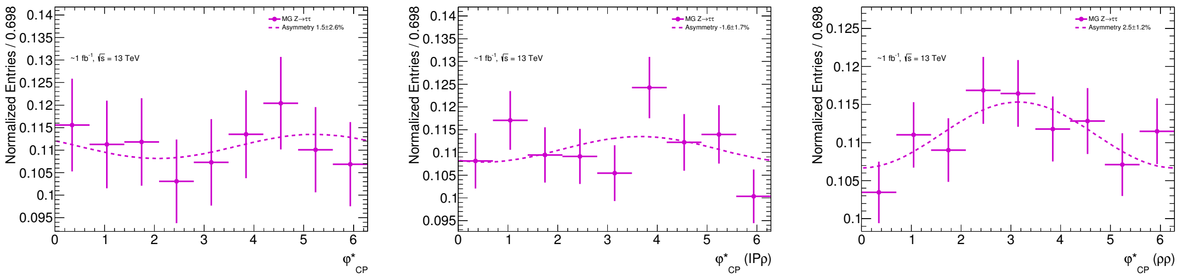

(b) MADGRAPH

Figure 6.13: Generator-level φ^*_{CP} distributions in the 1p0n-1p0n, 1p0n-1p1n and 1p1n-1p1n τ decay modes reconstructed with the IP, IP-ρ and $\rho-\rho$ methods, respectively, based on (a) SHERPA2.2 and (b) MADGRAPH ATLAS MC samples. For these distributions events are selected which fulfil $p_{\mathrm{T}}^{\mathrm{true}}(\tau_{0/1}^{vis}) > 40/30\,\mathrm{GeV}$, $m_{\tau\tau}^{\mathrm{true}} > 80\,\mathrm{GeV}$ and $0.8 < \Delta R_{\tau\tau}^{\mathrm{true}} < 3.0$ in order to compare the two in a phase space region closer to the actual Z-validation region. The asymmetry is obtained from a cosine fit to the simulated data.

In the end, the transverse τ spin correlations in $Z \to \tau\tau$ events are measured in the Z-validation region, defined in Table 5.2. Hence, to address the question whether the same level of disagreement is expected also in events selected for the actual measurement, the same comparison is repeated in a region of the phase space that is closer to the Z-validation region. This can be reached by increasing the p_{T}-thresholds of the leading and subleading τ leptons and restricting the range in $\Delta R_{\tau\tau}$ in which events are accepted. The complete set of requirements is listed in Table 6.8.

variable	selection
leading $p_T^{\tau,vis}$	$p_T^{\tau,vis} > 40\,\mathrm{GeV}$
subleading $p_T^{\tau,vis}$	$p_T^{\tau,vis} > 30\,\mathrm{GeV}$
$\Delta R_{\tau\tau}$	$0.8 < \Delta R_{\tau\tau} < 3.0$
$m_{\tau\tau}$	$m_{\tau\tau} > 80\,\mathrm{GeV}$

Table 6.8: Generator-level event selection for validation selecting a region of the phase space that is close to the signal regions.

The resulting φ^*_{CP} distributions after applying the selection from Table 6.8, are shown in Fig. 6.13 and the asymmetries are reported in Table 6.9.

Next, the same test is repeated, after applying the full simulation of the ATLAS detector to the simulated events. Figure 6.14 and Table 6.10 show the expected asymmetries applying a minimal event selection equivalent to the one used in Table 6.4 but using the reconstructed τ p_{T}, τ η and $m_{\tau\tau}$ instead.

Generator	Asymmetry in %		
	1p0n-1p0n	1p0n-1p1n	1p1n-1p1n
SHERPA2.2	6.4 ± 4.3	2.6 ± 2.7	6.7 ± 2.0
MADGRAPH	1.5 ± 2.6	-1.6 ± 1.7	2.5 ± 1.2

Table 6.9: Results of the fit to the simulated events shown in Fig. 6.13 at generator-level for (a) SHERPA2.2 and (b) MADGRAPH requiring $p_{\mathrm{T}}^{\mathrm{true}}(\tau_{0/1}^{vis}) > 40/30\,\mathrm{GeV}$, $m_{\tau\tau}^{\mathrm{true}} > 80\,\mathrm{GeV}$ and $0.8 < \Delta R_{\tau\tau}^{\mathrm{true}} < 3.0$.

Thus, the events are required to fulfil $p_{\mathrm{T}}(\tau_{0/1}^{vis}) > 20\,\mathrm{GeV}$, $\eta(\tau_{0/1}^{vis}) < 2.5$ and $m_{\tau\tau}^{\mathrm{MMC}} > 80\,\mathrm{GeV}$.

For the IP-IP method an additional requirement on the d_0^{sig} is made (see Section 5.1). In the IP-ρ case, the τ which is reconstructed as 1p0n, is asked to fulfil the same d_0^{sig} requirement. For the τ lepton reconstructed as 1p1n, an additional requirement on the $Y_\pm$ is made (see Section 5.1). Finally, in the $\rho-\rho$ case, a condition on the product of Y_+Y_- is asked to be fulfilled (see Section 5.1).

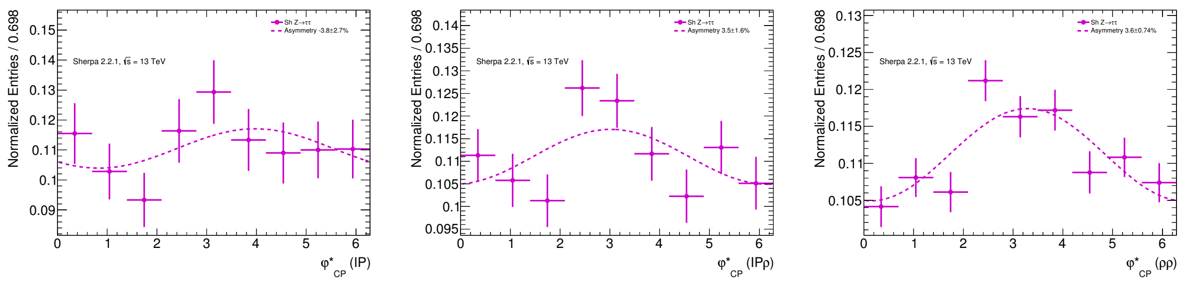

(a) SHERPA2.2

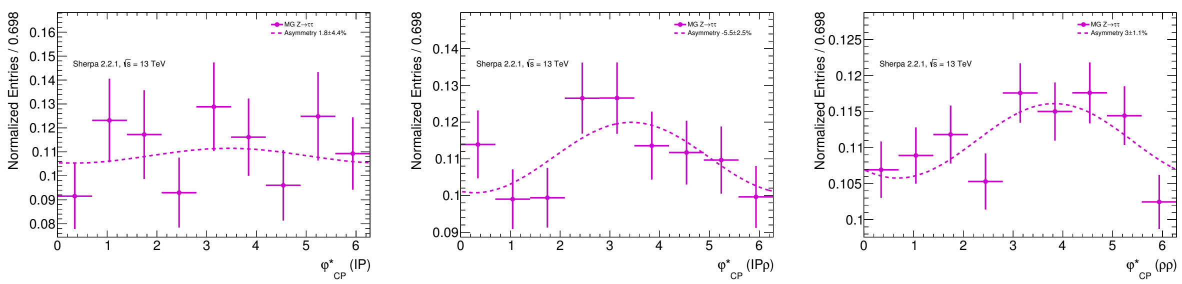

(b) MADGRAPH

Figure 6.14: The expected φ_{CP}^* distributions with full detector simulation in the 1p0n-1p0n, 1p0n-1p1n and 1p1n-1p1n τ decay modes reconstructed with the IP, IP-ρ and $\rho-\rho$ methods, respectively, based on (a) SHERPA2.2 and (b) MADGRAPH ATLAS MC samples. Events are selected that fulfil $p_{\mathrm{T}}(\tau_{0/1}^{vis}) > 20\,\mathrm{GeV}$, $\eta(\tau_{0/1}^{vis}) < 2.5$ and $m_{\tau\tau}^{\mathrm{MMC}} > 80\,\mathrm{GeV}$. The asymmetry is obtained from a cosine fit to the simulated data.

These distributions show that the modulation in the φ_{CP}^* distribution is visible in reconstructed events at least for the $\rho-\rho$ decay mode combination. The distributions are smeared out by reconstruction effects, such that fitting a cosine curve is difficult, especially in the IP-IP case. Beside that, one can conclude that the relative uncertainty on the measured asymmetry is still smaller for SHERPA2.2 than for MADGRAPH. However, with the given statistics, the asymmetry values obtained with SHERPA2.2 and MADGRAPH after reconstruction and the listed event selection are statistically compatible. The φ_{CP}^* distributions requiring the events to pass the Z-validation region selection are displayed in Fig. 6.15.

Generator	Asymmetry in %		
	1p0n-1p0n	1p0n-1p1n	1p1n-1p1n
SHERPA2.2	3.8 ± 2.7	3.5 ± 1.6	3.6 ± 0.74
MADGRAPH	1.8 ± 4.4	5.5 ± 2.5	3.0 ± 1.1

Table 6.10: Results of the cosine fit to the simulated events shown in Fig. 6.14 after reconstruction for the different MC generators.

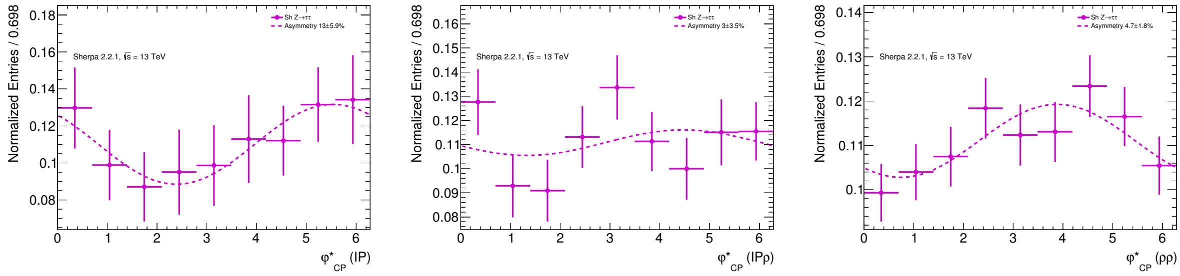

(a) SHERPA2.2

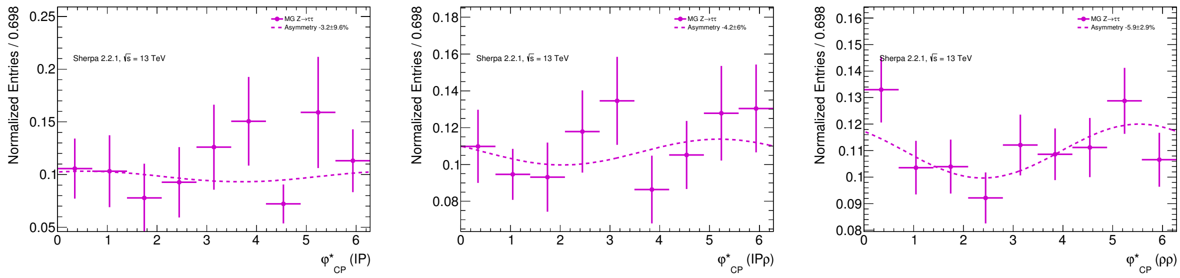

(b) MADGRAPH

Figure 6.15: The simulated φ^*_{CP} distributions requiring the had-had preselection in the 1p0n-1p0n, 1p0n-1p1n and 1p1n-1p1n τ decay modes reconstructed with the IP, IP-ρ and $\rho-\rho$ method based on (a) SHERPA2.2 (b) MADGRAPH ATLAS MC samples. The asymmetry is obtained from a cosine fit to the simulated data.

6.3.4 Expected SHERPA2.2 $Z \to \tau\tau$ distribution in the Z validation region

Figure 6.16 shows the expected φ^*_{CP} distribution in the Z-validation region using reconstructed SHERPA2.2 $Z \to \tau\tau$ events, applying the 2015 di-τ-Trigger requirements for all events (first column) and after applying the respective d_0^{sig}, d_0^{sig}-$Y_\pm$ or Y_+Y_- requirements (second and third column), respectively. In this case of the $\rho-\rho$ method, Fig. 6.16 shows that the shift in the phase of the expected cosine distribution is due to the events with small Y_+Y_- in which the reconstruction of the sign of Y_+Y_- is not always correct. On the other hand, the φ^*_{CP} distribution of the events with a large Y_+Y_-, is much more centred around π as it is expected from theory.

The separate φ^*_{CP} distribution for $Z \to \tau\tau$ events with $\alpha^- < \pi/4$ and $\alpha^- \geq \pi/4$ are shown in Fig. 6.17. Again, the first column shows all events of the respective decay-mode combination, while the second column shows the events in the low d_0^{sig} or $Y_\pm$ categories and the last column shows the distribution for events in the high d_0^{sig} or $Y_\pm$ categories, respectively.

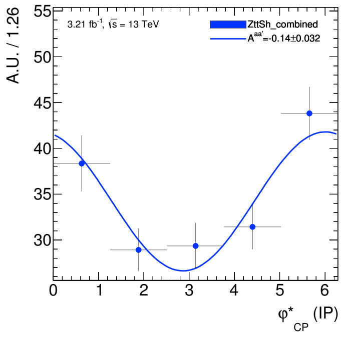

(a) All IP-IP events

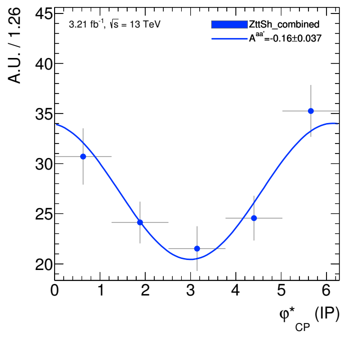

(b) low d_0^{sig}

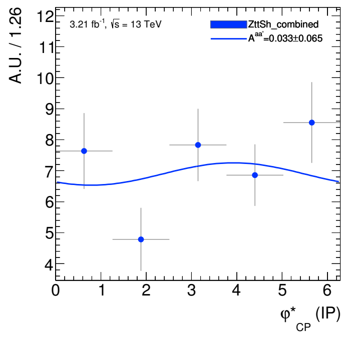

(c) high d_0^{sig}

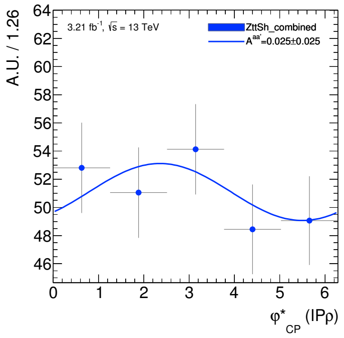

(d) All IP-ρ events

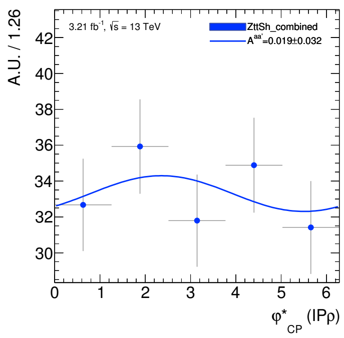

(e) low d_0^{sig}-$Y_{\pm}$

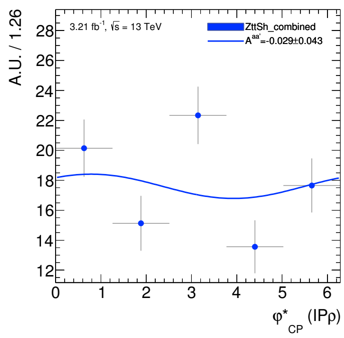

(f) high d_0^{sig}-$Y_{\pm}$

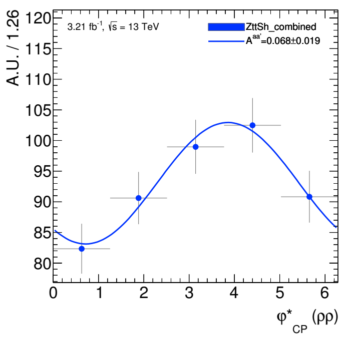

(g) All $\rho-\rho$ events

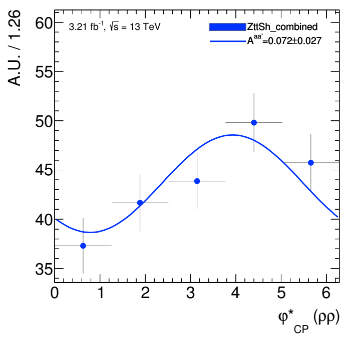

(h) low Y_+Y_-

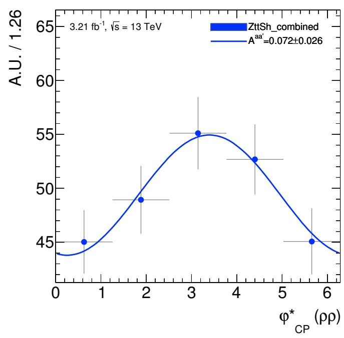

(i) high Y_+Y_-

Figure 6.16: Expected SHERPA2.2 $Z \to \tau\tau$ distribution in the Z validation region for 2015 data.

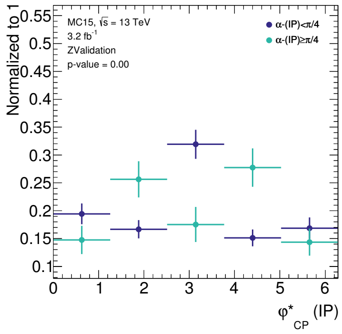

(a) All IP-IP events

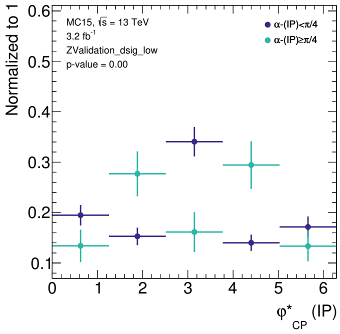

(b) low d_0^{sig}

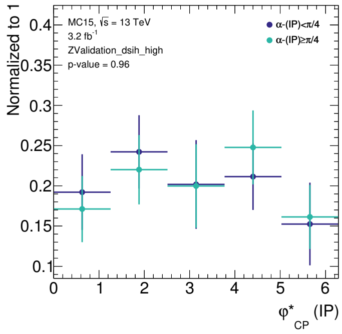

(c) high d_0^{sig}

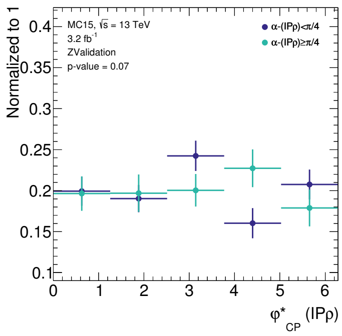

(d) All IP-ρ events

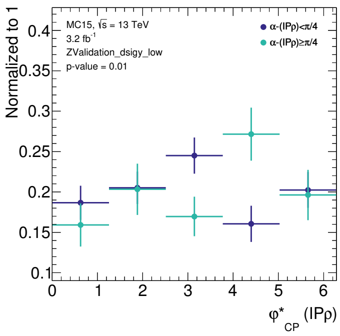

(e) low d_0^{sig}-$Y_{\pm}$

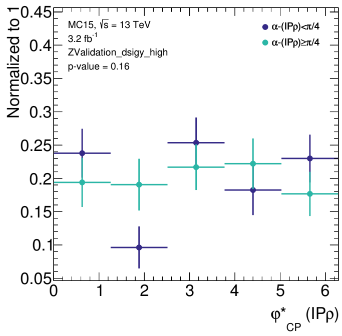

(f) high d_0^{sig}-$Y_{\pm}$

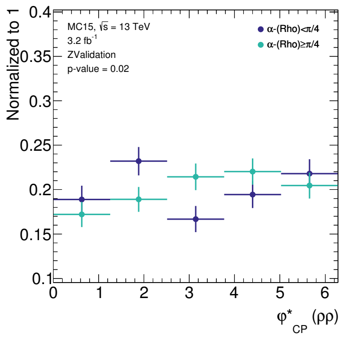

(g) All $\rho-\rho$ events

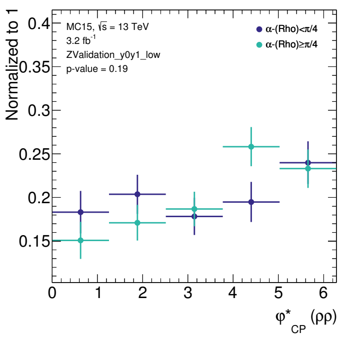

(h) low $Y_{+}Y_{-}$

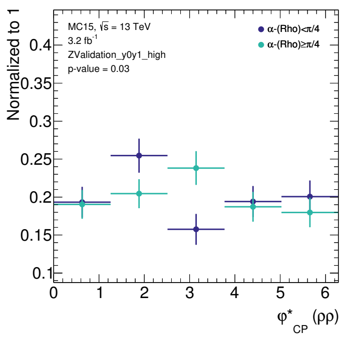

(i) high $Y_{+}Y_{-}$

Figure 6.17: Expected Sherpa2.2 $Z \to \tau\tau$ distribution in the Z validation region for 2015 data split up with α^{-}.

CHAPTER 7

Measurement of transverse spin correlation in $Z \to \tau\tau$ decays

In this chapter the studies of transverse spin correlations in $Z \to \tau\tau$ events and their possible applications for the Higgs CP measurement are discussed. As presented in Section 4.2, effects of transverse spin correlations on the differential cross section can also be measured for $Z \to \tau\tau$ events if φ^*_{CP} is measured separately in two halves of the phase space split with the angle α^- between the charged pion from the τ^- decay and the τ production-plane. The reconstruction of the CP sensitive variable φ^*_{CP} is identical to the one applied in $H \to \tau\tau$ decays. Thus, it can be used for a calibration of the Higgs CP-measurement and to constrain systematic effects on φ^*_{CP} as briefly described in the following paragraphs.

Calibration of the used methods in $Z \to \tau\tau$ events In order to calibrate the IP- and $\rho - \rho$ method in $Z \to \tau\tau$ events, artificial φ^*_{CP} templates are generated shifting the phase in the $Z \to \tau\tau$ nominal distribution expected from MC simulations. For each template a binned maximum likelihood fit is applied in the same way as for the Higgs CP-measurement. The $-\log(\mathcal{L})$ values are extracted, plotted as a function of the template's phase shift and the global minimum of the resulting distribution is used as best-fit value for the phase shift. Ideally, a phase shift compatible with zero results from this measurement. If a non-vanishing phase shift ϕ^{corr} is observed, it can be used to calibrate the final Higgs CP-measurement.

Method to determine systematic effects on φ^*_{CP} The measurement of transverse spin correlations in $Z \to \tau\tau$ events offers a unique possibility to determine and constrain systematic uncertainties on the φ^*_{CP} variable originating from the resolution of the τ particle flow variables. In the decay channels involving the $\tau \to \rho + \nu \to \pi + \pi^0 + \nu$ decay, the π^0 angular components play a major role in the determination of the τ decay planes. The resolution of these components directly impacts the φ^*_{CP} distribution and has to be taken into account as a systematic uncertainty. Therefore, measuring the φ^*_{CP} distribution in $Z \to \tau\tau$ events in the $\rho - \rho$ decay channel in the Z-validation region, one would be able to constrain these uncertainties for the Higgs CP-measurement and thereby improve the sensitivity on the Higgs CP-state.

For the studies presented in this chapter only the 2015 data of $\mathcal{L} = 3.21\,\text{fb}^{-1}$ are used, because the trigger used to record the 2016 data requires an additional jet with a transverse momentum of $p_{\text{T}}^{\text{jet}}$ >70 GeV, which eliminates the asymmetry in the split $Z \to \tau\tau$ distributions. The reason for this is that the τ production plane used in the α^- definition is no longer well defined in processes where additional partons contribute to the hard matrix element as discussed in Section 5.2.3. However, using only the 2015 data and thus exploiting only approximately 8% of the data available for this analysis leads to large statistical fluctuations in all distributions. In fact, it is neither possible to calibrate the Higgs CP-measurement in $Z \to \tau\tau$ decays, nor to derive the π^0 systematic uncertainties. The statistical uncertainties are too large to measure a significant asymmetry in all decay mode combinations. Nonetheless, the modelling of the CP sensitive variables can be analysed and validated using the 2015 dataset as it is presented in Section 7.1. Also, an alternative trigger chain is proposed in Section 7.2 to be used in future data taking. This trigger chain achieves a similar rate of recorded di-τ events as the 2016 trigger, but does not affect the asymmetry in $Z \to \tau\tau$ events significantly. An alternative approach to determine the systematic uncertainties from the π^0 angular resolutions is discussed in Section 8.4.3.

7.1 Measurement of transverse τ spin correlations in $Z \to \tau\tau$ decays

In order to measure transverse spin correlations in in $Z \to \tau\tau$ decays, the phase space needs to be divided into two parts using α^- defined in Eq. (4.24). The Z-validation region event selection is optimised to yield the maximal asymmetry in the $\rho-\rho\ \varphi^*_{CP}$ distribution of $Z \to \tau\tau$ decays in Chapter 5. The expected asymmetry of the $\rho-\rho\ \varphi^*_{CP}$ distribution in this region is $A_{\text{Trigger15}} = 0.068 \pm 0.019$ using a luminosity of $\mathcal{L} = 3.21\ \text{fb}^{-1}$ as can be seen in Fig. 7.1(c). The measured φ^*_{CP} distribution for the 1p1n-1p1n decay

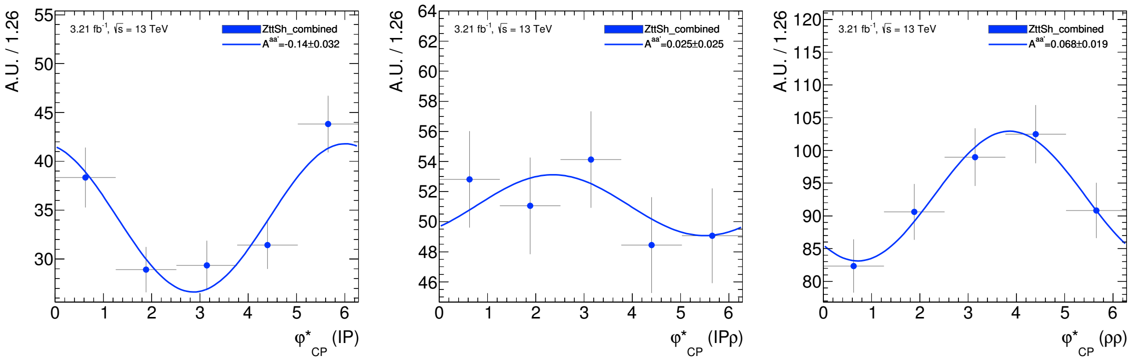

(a) 1p0n-1p0n (b) 1p0n-1p1n (c) 1p1n-1p1n

Figure 7.1: Expected φ^*_{CP} modulation in $Z \to \tau\tau$ events after the Z-validation region split up by decay mode combination for $\mathcal{L} = 3.21\ \text{fb}^{-1}$ recorded with ATLAS in 2015.

mode combination is displayed in Fig. 7.2. Here r_Z and r_{QCD} are determined from a fit to the $\Delta\eta_{\tau\tau}$ distribution in the Z-validation region and their values amount to $r_Z = 1.23 \pm 0.49$ and $r_Z = 1.61 \pm 0.94$. Within the statistical uncertainties these values are compatible with the values obtained in the Higgs CP-measurement presented in Section 8.3. Differences between the measured normalisation factors in the two measurements can be explained by the different regions of the phase space they are determined from. The backgrounds are estimated in the same way as for the Higgs CP-measurement, except for the $Z \to \tau\tau$ background. The $Z \to \tau\tau$ background in the Z-validation region is estimated from MC simulations instead of using the data-driven approach used in the Higgs measurement Section 8.3. The systematic uncertainties are the same as for the Higgs CP-measurement described in Section 8.4.

The modelling of the α^- variables in the Z-validation region split by the respective τ decay mode combinations is displayed in Fig. 7.3. Data and prediction agree within the uncertainties in most of the bins. Figure 7.4 shows a reasonable agreement between the 2015 data and the prediction in the φ^*_{CP} distributions within the uncertainties. So far, the background normalisation factors are determined in the Z-validation region, which was optimised to yield the maximal asymmetry in the $\rho-\rho\ \varphi^*_{CP}$

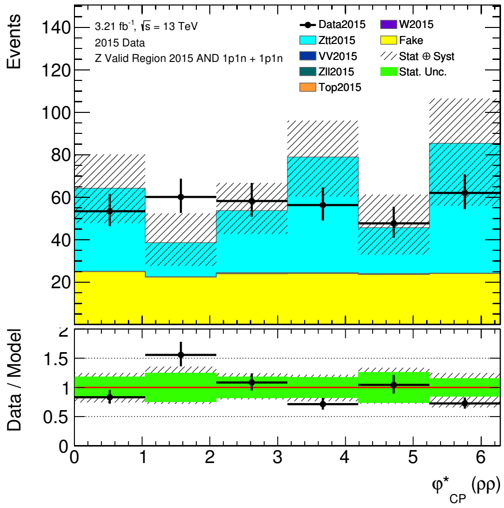

Figure 7.2: Measured φ^*_{CP} distribution in the 1p1n-1p1n decay channel using $\mathcal{L} = 3.21\,\text{fb}^{-1}$ of ATLAS data. The two α^- categories are combined in one distribution.

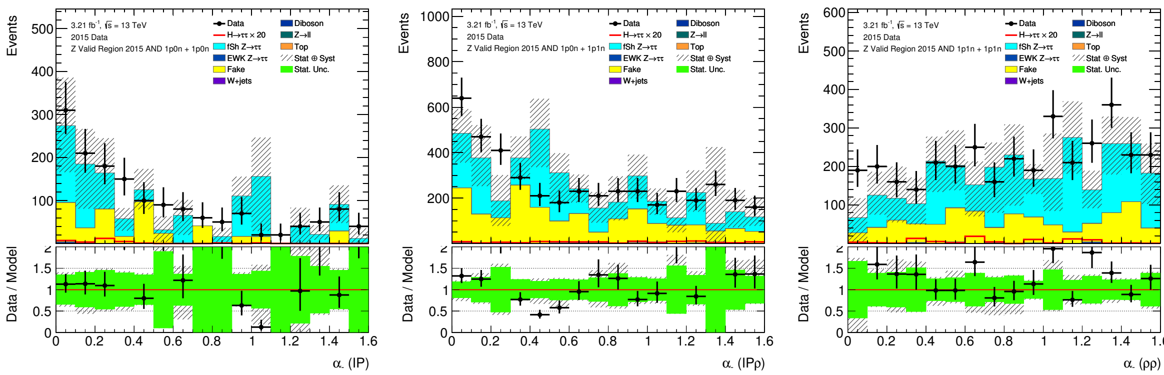

(a) 1p0n-1p0n (b) 1p0n-1p1n (c) 1p1n-1p1n

Figure 7.3: Modelling of α^- variable used to divide the phase space in all three decay-mode combinations.

distribution. The agreement between data and prediction might be improved if the region used to estimate the backgrounds is varied or chosen more inclusively. Beside that, in a future measurement, the Z-validation region event selection should be optimised separately also for the other decay mode combinations.

The distributions of $\Delta R_{\tau\tau}$, $\Delta\eta_{\tau\tau}$, p_{T} and η of the leading/subleading τ are displayed in Fig. 7.5. The overall agreement between data and simulations is reasonable within the statistical uncertainties. The $\Delta R_{\tau\tau}$ distribution in data is shifted with respect to the predicted one. This would need to be investigated further with a larger dataset.

7.2 Proposal for a new support trigger

To measure transverse spin correlations in $Z \to \tau\tau$ in the future with a higher precision and to use the results for a calibration of the measurement of the Higgs CP-state, a new support trigger is suggested.

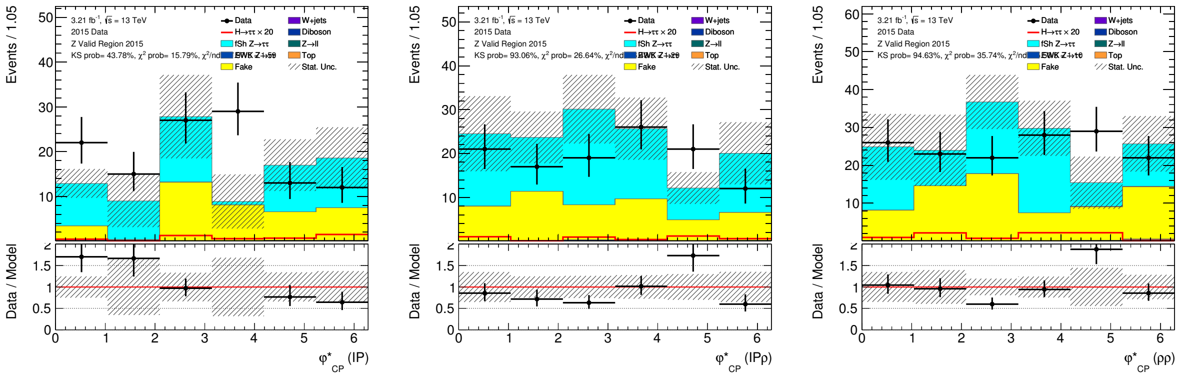

(a) $\alpha^- < \pi/4$

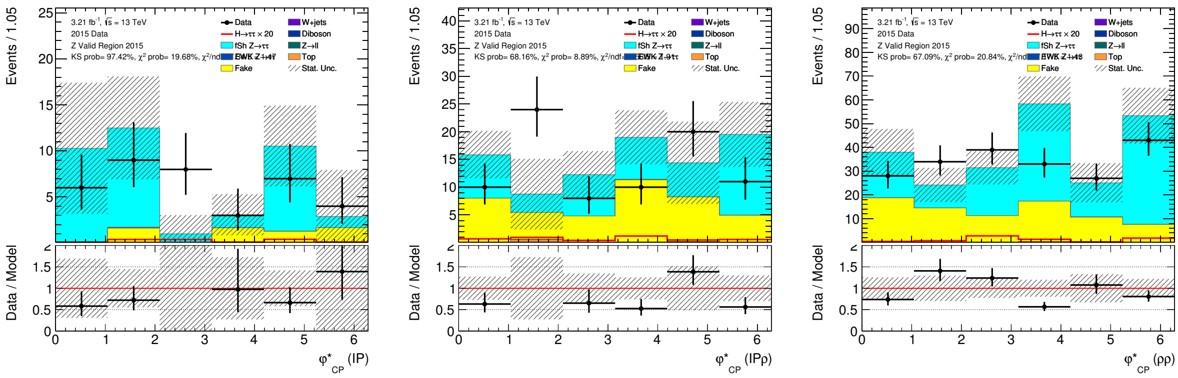

(b) $\alpha^- \geq \pi/4$

Figure 7.4: Modelling of φ^*_{CP} in all decay mode combinations for $\alpha^- < \pi/4$ and $\alpha^- \geq \pi/4$.

Trigger chain	Topological cuts
L1_DR-TAU20ITAU12I	$0.8 < \Delta R_{\tau\tau} < 2.8$, $p_T(\tau 0) > 20\,\text{GeV}$, $p_T(\tau 1) > 12\,\text{GeV}$, both taus pass medium ID
L1_DR-TAU20ITAU12I-J25	$0.8 < \Delta R_{\tau\tau} < 2.8$, $p_T(\tau 0) > 20\,\text{GeV}$, $p_T(\tau 1) > 12\,\text{GeV}$, both taus pass medium ID, ≤ 1 jet with $p_T > 25\,\text{GeV}$ and $|\eta| < 3.2$

Table 7.1: Definition of the available di-τ had-had topological trigger chains.

This trigger chain could be used to select events with two hadronically decaying τ leptons in addition to the common di-τ had-had trigger. To optimise the requirements on trigger level, the trigger chain without the jet-requirement (bottom row in Table 7.1) is modified and the impact of various changes to this trigger chain are compared to the one with jet-requirement. The impact of the changed requirements is studied on an Enhanced Bias (EB) sample using 2016 ATLAS data and on a simulated $Z \to \tau\tau$ MC sample.

From Section 5.2.1 it can be concluded, that the amplitude in $Z \to \tau\tau$ is stable under variations in $\Delta R_{\tau\tau}$ and $\Delta\eta_{\tau\tau}$. Hence, requirements on the minimum $\Delta R_{\tau\tau}$ and the maximum $\Delta\eta_{\tau\tau}$ are added to the trigger chain. For example the CMS di-τ trigger [128] does not ask for additional jets. Instead a requirement on $|\eta| < 2.1$ is included with higher cuts on the τ transverse momenta. Therefore, the impact of restricting $|\eta|$ in the ATLAS di-τ trigger chain is evaluated. Furthermore, the use of stricter τ-ID requirements already

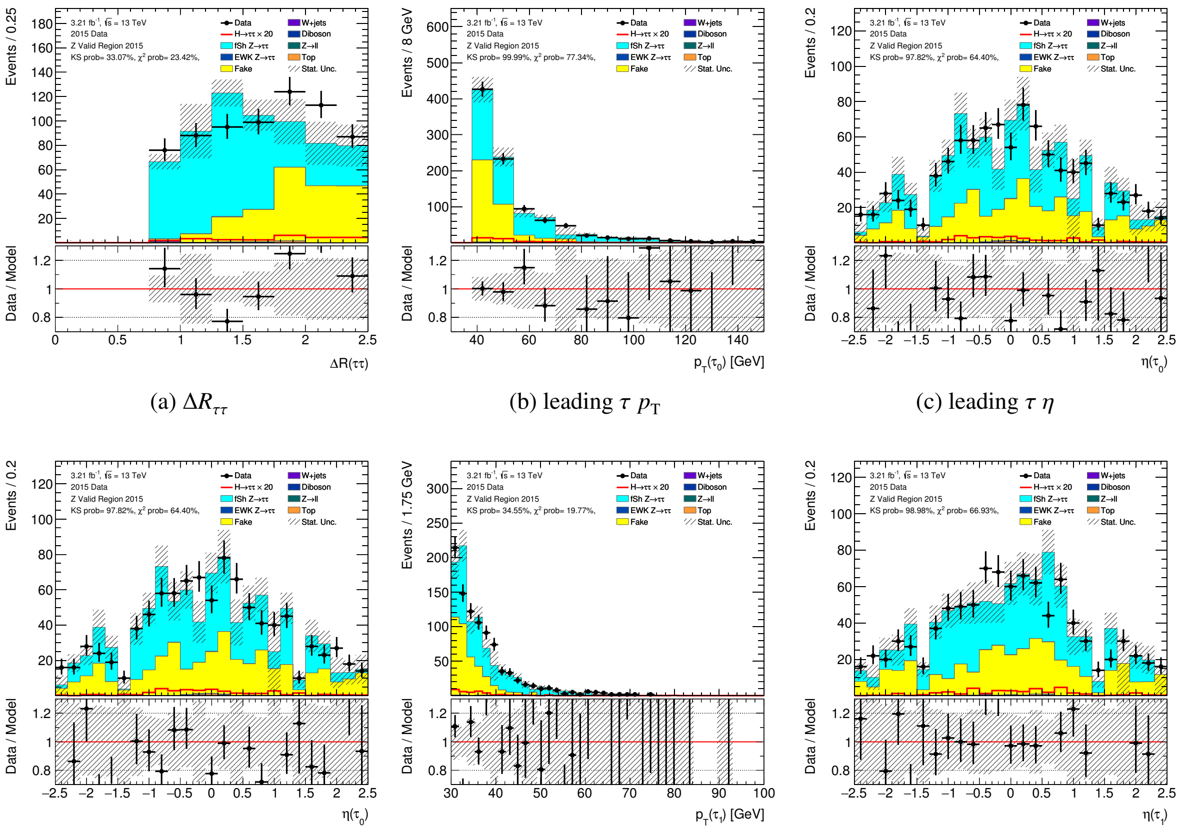

(a) $\Delta R_{\tau\tau}$ (b) leading τ p_{T} (c) leading τ η

(d) $\Delta\eta_{\tau\tau}$ (e) subleading τ p_{T} (f) subleading τ η

Figure 7.5: Modelling of the di-τ angular separation $\Delta R_{\tau\tau}$ and $\Delta\eta_{\tau\tau}$, the leading and subleading τ p_{T} and η in the Z-validation region.

on trigger level is studied, requiring two tight τ leptons instead of one medium and one tight τ.

The L1_DR-Tau20ITau12I trigger chain is modified using the Tau Trigger Emulation Tool [129]. This tool allows to validate available trigger chains in data and mc samples and to predict the decision and rates of new trigger chains.

For each variation, the fraction of events that match the requirements of the new trigger chain is calculated. Furthermore, the number of additional events which are not triggered by the default ATLAS ditau had-had trigger with the jet requirement (top line in Table 7.1) is calculated. The resulting fractions and numbers are listed in Table 7.2.

The proposed trigger chain should be used as a support trigger, this means it will be used in addition to the default di-τ trigger, which includes the jet requirements. Hence, the exclusive trigger rate on the EB sample should be as small as possible. A new support trigger, will only be implementable if the exclusive rate on the EB sample does not exceed 20% of the nominal trigger rate. The minimal exclusive rate is achieved when asking for $\Delta\eta_{\tau\tau} < 1.0$, $1.5 < \Delta R_{\tau\tau} < 3.0$, $|\eta| < 2.1$, and that both τ leptons pass the tight τ-ID requirements in the L1 trigger chain.

In addition, the impact of stricter cuts on $|\eta|$, p_{T} (τ_{had}) and the tighter τ-ID requirements on the signal acceptance was studied. As can be seen from Figs. 7.6 to 7.9, increasing the requirement on the leading tau p_{T} to $p_{\mathrm{T}} > 50$ GeV as used by CMS [128] decreases the acceptance in gg$H \to \tau\tau$ events by about 20% at preselection level. Restricting $|\eta|$ to 2.1 reduces the acceptance by 5% for the gg$H \to \tau\tau$ signal.

Cut	EB sample	Add. events	Rate in %	Excl. rate in %	$Z \to \tau\tau$ sample	Add. events	Rate in %	Excl. rate in %
none	89853		100.00		240000			
L1_DR-Tau20ITau12I-J25	828		0.92		24224		10.09	0.00
L1_DR-Tau20ITau12I	1075		1.20		32177		13.41	0.00
$\Delta\eta_{\tau\tau} < 1.8$, $0.8 < \Delta R_{\tau\tau} < 2.8$	829	198	0.92	0.22	30452		12.69	0.00
$\Delta\eta_{\tau\tau} < 1.5$, $0.8 < \Delta R_{\tau\tau} < 3.0$	1014	421	1.13	0.47	34833	12302	14.51	5.13
$\Delta\eta_{\tau\tau} < 1.2$, $0.8 < \Delta R_{\tau\tau} < 3.0$	922	379	1.03	0.42	32520	11348	13.55	4.73
$\Delta\eta_{\tau\tau} < 1.2$, $1.0 < \Delta R_{\tau\tau} < 3.0$	869	371	0.97	0.41	31858	11316	13.27	4.72
$\Delta\eta_{\tau\tau} < 1.2$, $1.5 < \Delta R_{\tau\tau} < 3.0$	763	350	0.85	0.39	29066	11066	12.11	4.61
$\Delta\eta_{\tau\tau} < 1.2$, $1.5 < \Delta R_{\tau\tau} < 3.0$, $\|\eta\| < 2.47$	763	350	0.85	0.39			0.00	0.00
$\Delta\eta_{\tau\tau} < 1.2$, $1.5 < \Delta R_{\tau\tau} < 3.0$, $\|\eta\| < 2.1$	652	298	0.73	0.33	25726	9753	10.72	4.06
$\Delta\eta_{\tau\tau} < 1.2$, $1.5 < \Delta R_{\tau\tau} < 3.0$, $\|\eta\| < 2.1$, tight-tight	566	255	0.63	0.28	24540	9265	10.23	3.68
$\Delta\eta_{\tau\tau} < 1.0$, $1.5 < \Delta R_{\tau\tau} < 3.0$	664	314	0.74	0.35	26660	10044	11.11	4.19
$\Delta\eta_{\tau\tau} < 1.0$, $1.5 < \Delta R_{\tau\tau} < 3.0$, $\|\eta\| < 2.1$	570	269	0.63	0.30	23604	8860	9.84	3.69
$\Delta\eta_{\tau\tau} < 1.0$, $1.5 < \Delta R_{\tau\tau} < 3.0$, $\|\eta\| < 2.1$, tigh-tight	497	231	0.55	0.26	22484	8409	9.37	3.50

Table 7.2: Trigger rates for different modifications to the level 1 di-τ trigger and the number of additional events triggered by the new chain but not by the default one calculated on an EB and a $Z \to \tau\tau$ sample.

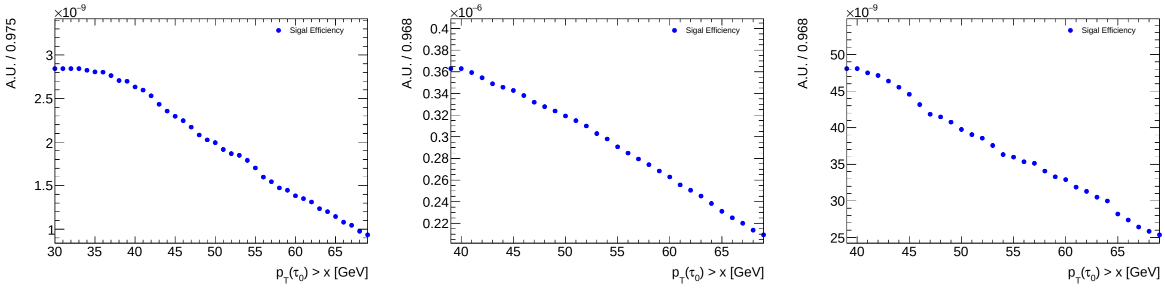

(a) $Z \to \tau\tau$ (PHP) (b) $H \to \tau\tau$ (VBFH) (c) $H \to \tau\tau$ (ggH)

Figure 7.6: Fraction of accepted events as a function of the cut on the p_T of the leading τ, calculated on a sample of simulated $Z \to \tau\tau$ (a), VBF $H \to \tau\tau$ (b) and ggF $H \to \tau\tau$ (c) events.

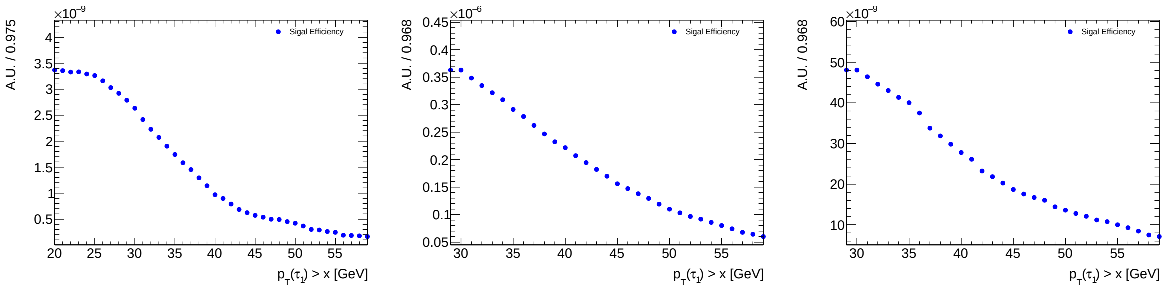

(a) $Z \to \tau\tau$ (PHP) (b) $H \to \tau\tau$ (VBFH) (c) $H \to \tau\tau$ (ggH)

Figure 7.7: Fraction of accepted events as a function of the cut on the p_T of the subleading τ, calculated on a sample of simulated $Z \to \tau\tau$ (a), VBF $H \to \tau\tau$ (b) and ggF $H \to \tau\tau$ (c) events.

However, the trigger was designed for the application to $Z \to \tau\tau$ events and there the acceptance loss amounts only to 7.5% at preselection level.

Requiring two τ leptons to fulfil the tight τ-ID requirement on analysis level, reduces the signal acceptance after the $H \to \tau\tau$ preselection cuts by 22% for the gg$H \to \tau\tau$ and 33% for the Powheg+Pythia $Z \to \tau\tau$ sample as can be seen in Fig. 7.10, while the background rejection is significantly improved.

Requiring two tight τ leptons on trigger level helps to decrease the trigger rate in the EB sample by 13% (see Table 7.2). Also, it increases the asymmetry in the $Z \to \tau\tau$ φ^*_{CP} distribution in the Z-validation region by 33% (see Fig. 7.11).

To conclude, the studies of the different trigger chains suggest to implement a new support trigger to allow for a measurement of transverse spin correlations in $Z \to \tau\tau$ decays. The new trigger chain should include the same requirements as the current di-τ had-had topological trigger without the jet-p_T requirements and instead asking for $\Delta\eta_{\tau\tau} < 1.0$, $1.5 < \Delta R_{\tau\tau} < 3.0$, $|\eta| < 2.1$, and both τ leptons having tight τ-ID. A similar background rejection of this new trigger might be achieved even without the strict requirement of two tight τ leptons, if the definition of the isolation itself is varied, as suggested in [130].

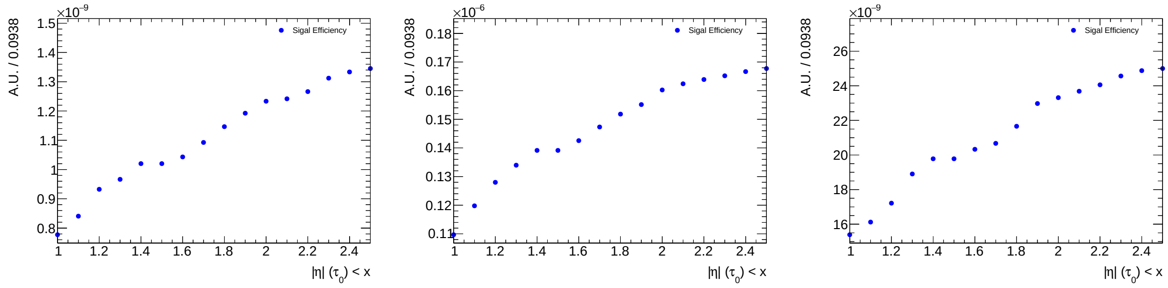

(a) $Z \to \tau\tau$ (PHP) (b) $H \to \tau\tau$ (VBFH) (c) $H \to \tau\tau$ (ggH)

Figure 7.8: Fraction of accepted events as a function of the cut on $|\eta|$ of the leading τ, calculated on a sample of simulated $Z \to \tau\tau$ (a), VBF $H \to \tau\tau$ (b) and ggF $H \to \tau\tau$ (c) events.

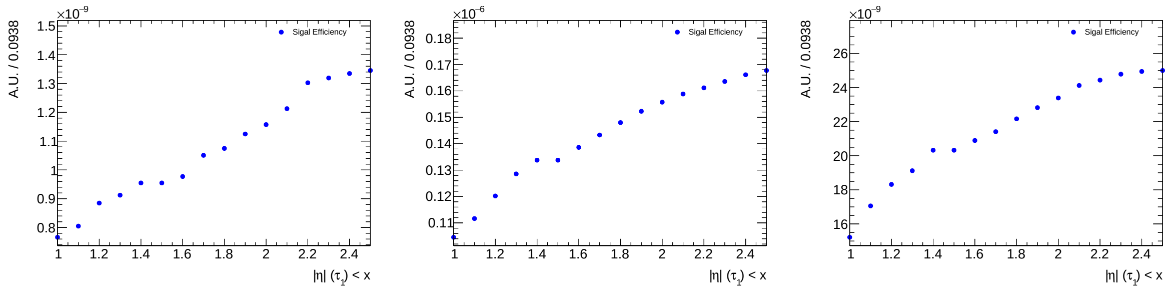

(a) $Z \to \tau\tau$ (PHP) (b) $H \to \tau\tau$ (VBFH) (c) $H \to \tau\tau$ (ggH)

Figure 7.9: Fraction of accepted events as a function of the cut on $|\eta|$ of the subleading τ, calculated on a sample of simulated $Z \to \tau\tau$ (a), VBF $H \to \tau\tau$ (b) and ggF $H \to \tau\tau$ (c) events.

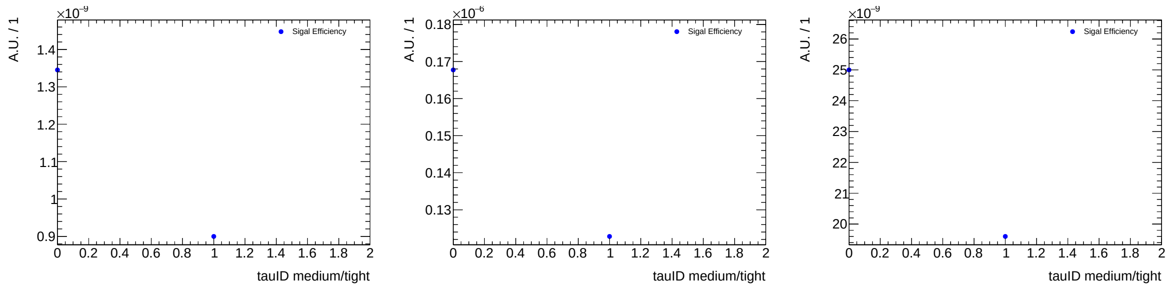

(a) $Z \to \tau\tau$ (PHP) (b) $H \to \tau\tau$ (VBFH) (c) $H \to \tau\tau$ (ggH)

Figure 7.10: Fraction of accepted events requiring one medium and one tight τ (first bin) and two tight τ leptons (second bin) calculated on a sample of simulated $Z \to \tau\tau$ (a), VBF $H \to \tau\tau$ (b) and ggF $H \to \tau\tau$ (c) events.

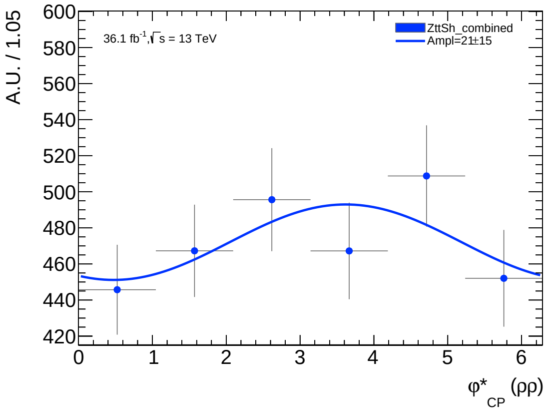

(a) medium-tight τ-ID

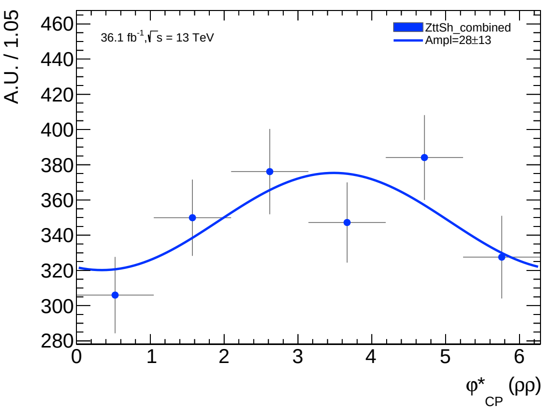

(b) tight-tight τ-ID

Figure 7.11: φ^*_{CP} modulation in $Z \to \tau\tau$ events after applying the Z-validation region event selection requiring a medium-tight (a) and a tight-tight (b) τ-ID.

CHAPTER 8

Studies of the Higgs CP-state in $H \rightarrow \tau\tau$ decays

In this chapter, a measurement of the Higgs CP-state in $H \rightarrow \tau\tau$ decays is discussed. First, the analysis strategy, including background estimation and systematic uncertainties is explained. Second, the fit procedure is validated using pseudo data and different fit configurations are compared. Finally, the measurement of the CP-mixing angle in the 2015+2016 datasets with a luminosity of $36.1\,\text{fb}^{-1}$ is presented. Also, an outlook on the measurement using the full LHC run 2 dataset or even more data collected at a future high-luminosity LHC is given. Within my ATLAS analysis team working on CP violation in $H \rightarrow \tau\tau$ decays, two related theses were presented [131, 132]. The focus of my work lies in particular on the implementation and validation of the CP sensitive observables, a validation of the applied likelihood fit and a study of its performance and the dependence on various effects coming e.g. from statistical limitations in the signal and background modellings.

8.1 The Maximum Likelihood Approach

The maximum likelihood method estimates parameter values $\theta = (\theta_1, ..., \theta_N)$ from a finite data sample, given a random variable x, which is distributed according to a probability distribution function $f(x;\theta)$ [133]. The so-called *likelihood function* $L(\theta)$ describes the joint probability distribution function for N independent measurements x_i and is defined as

$$L(\theta) = \prod_{i=1}^{N} f(x_i;\theta). \tag{8.1}$$

The parameters θ are then defined as those parameter values $\hat{\theta}$, for which the likelihood takes on its maximum. This occurs, if the following criteria are fulfilled:

$$\frac{\partial L}{\partial \theta_i} = 0, i = 1, ...N \tag{8.2}$$

and

$$\frac{\partial^2 L}{\partial \theta_i \partial \theta_j}\,|_{\theta=\hat{\theta}} = U_{ij}\left(\hat{\theta}\right), \tag{8.3}$$

given that the likelihood is differentiable for all parameters $\theta_1, ..., \theta_N$ and that the maximum is not at the boundary of the parameter range [133]. The global maximum of the likelihood is used as best estimator for the parameter set θ.

Because the likelihood as the product of probabilities covers only a small value range between 0 and 1, it is presented in the log scale allowing a more precise discrimination of different likelihood values. Accordingly the likelihood function is defined as

$$\log L(\theta) = \sum_{i=1}^{N} \log f(x_i; \theta). \tag{8.4}$$

In counting experiments, the data $x_1, ..., x_N$ are Poisson distributed random variables themselves with median value ν. Hence, the likelihood function becomes the product of the Poisson probabilities to count N:

$$L(\nu, \theta) = \frac{\nu^N}{N!} e^{-\nu} \prod_{i=1}^{N} f(x_i \theta) = \frac{e^{-\nu}}{N!} \prod_{i=1}^{N} \nu f(x_i \theta) \tag{8.5}$$

This function is called the *extended likelihood* function. In case of samples with many measurements, usually histograms with a certain number of entries $N = (n_1, ..., n_M)$ in M bins are used instead of using the value of each measurement individually. The expectation value of each bin, i.e. the expected number of events per bin is described by $\nu = (\nu_1, ..., \nu_M)$, where $\nu_i(\theta) = N_{\text{Total}} \int_{x_i^{min}}^{x_i^{max}} f(x; \theta)\, dx$ with the lower and upper borders of each bin x_i^{min} and x_i^{max}, respectively. Accordingly, the extended likelihood function for binned data is

$$\log L(\nu_{\text{total}}, \theta) = \nu_{\text{total}} + \sum_{i=1}^{M} n_i \log \nu_i(\nu_{\text{total}}, \theta). \tag{8.6}$$

The parameter Θ is referenced as *Parameter Of Interest* (POI). Besides this parameter, further so-called *Nuisance parameters* (NPs) can be introduced to account for systematic or statistical uncertainties. Including a single systematic and a single statistical uncertainty, the likelihood function for a simple counting experiment with n observed data, b expected background events and s signal events to be observed, i.e. the POI, develops to [134]:

$$L(s, \alpha, \gamma) = P(n \mid s + \gamma b + \alpha\Delta) \times P(m, \gamma m) \times G(\alpha \mid 0, 1). \tag{8.7}$$

$P(m, \lambda)$ describes a Poisson distribution of the ratio $m = \frac{b^2}{\delta^2}$ and the NP γ of the statistical uncertainty δ. $G(\alpha|0, 1)$ describes a Gaussian distribution for the NP α of the systematic uncertainty Δ.

To assess the outcome of the fit for the likelihood estimators, a χ^2 statistical test is applied. The χ^2 can be derived from the negative log likelihood ratio ΔNLL defined as

$$\Delta\text{NLL} = -\log \frac{\mathcal{L}(\Theta)}{\mathcal{L}(\hat{\Theta})} = -\left(\log(\mathcal{L}(\Theta)) - \log\left(\mathcal{L}\left(\hat{\Theta}\right)\right)\right), \tag{8.8}$$

where $\hat{\Theta}$ denotes the best-fit estimator of the POI and Θ is the hypothesis under test. The relation between χ^2 and ΔNLL is given as

$$\chi^2 = -2\Delta\text{NLL}. \tag{8.9}$$

The width of the ΔNLL distribution at ΔNLL = 0.5 then yields the 1σ uncertainty on the best-fit estimator $\hat{\Theta}$. The *p-value*, often used to quote significance levels in hypothesis testing, is defined as the probability that the hypothesis under test would lead to a χ^2 value lower than the observed one. Mathematically, the *p-value* is defined as

$$P = \int_{\chi^2}^{\infty} f(z, n_{\text{dof}}) dz, \tag{8.10}$$

where f denotes the probability density function of a χ^2-distributed random variable z with n_{dof} degrees of freedom. Determining the χ^2 from the observed ΔNLL distribution, allows to compute this *p-value* for a certain hypothesis. The Confidence Level (CL) at which this hypothesis can be rejected, is then calculated as

$$1 - P(\chi^2 \mid \Theta), \tag{8.11}$$

for the hypothesis under test Θ.

8.2 Analysis strategy

The SM of particle physics predicts a pure CP-even Higgs boson. However, as discussed in Section 2.3, prominent BSM models like the 2HDM or the MSSM predict a mixing of CP-even and CP-odd states in the Higgs sector. In the Higgs boson decay to two τ leptons, the CP-mixing angle between the CP-even and CP-odd states can be measured directly from the angle φ^*_{CP} between the τ decay planes. The reconstruction of φ^*_{CP} depends on the τ decay mode. Hence, each of the three signal regions described in Chapter 5 is further segmented depending on the τ decay mode combination as described in Section 5.1.1. Thus, there are 16 signal regions in which the angle φ^*_{CP} is simultaneously measured. In addition, three control regions are defined in Section 5.1.1. In these basically signal-free control regions, $\Delta\eta_{\tau\tau}$ is measured in order to constrain the normalisations of the $Z \to \tau\tau$ and QCD backgrounds. This measurement is repeated 17 times, assuming a CP-mixing angle hypothesis of $0, 10, 20, ..., 170$ degrees, respectively. To this end, the $H \to \tau\tau$ signal template in each of the 17 measurements is replaced by the unpolarised $H \to \tau\tau$ signal sample, using the respective *TauSpinner*[120] weights.

A binned maximum likelihood fit of the respective signal and background predictions is applied to the combined 2015+2016 dataset. This maximum likelihood fit is performed in all signal regions simultaneously using the $H \to \tau\tau$ signal strength as parameter of interest (POI) and the $Z \to \tau\tau$ and QCD normalisations as nuisance parameters. In addition, nuisance parameters for the systematic uncertainties are included, as described in Section 8.4. The maximum likelihood fit is performed using the FitBox [135] statistical software framework, which fits the statistical model provided to it as a ROOFit/ROOStats [136] Workspace. The statistical model is build via HistFactory [137]. The likelihood function $\mathcal{L}(\mathbf{x}; \phi_\tau)$ is evaluated for each dataset $\mathbf{x}$ and each of the considered mixing angles ϕ_τ, with all nuisance parameters profiled at their best-fit values. The negative log-likelihood (NLL) curve is constructed plotting the (negative) maximal log-likelihood value $\log \mathcal{L}_{\max}$ as a function of the mixing angle hypothesis used in the simulation. The global minimum of this distribution then yields the best-fit value of the CP-mixing angle ϕ_τ. The NLL value at the global minimum is subtracted to obtain the likelihood ratio ΔNLL as described in Section 8.1. The approximate central confidence interval at 68% CL around the best estimator ϕ_τ can be determined from the points where $\Delta\mathrm{NLL} \equiv \log \mathcal{L}_{\max} - \log \mathcal{L}(\hat{\phi}_\tau \pm \sigma_{\hat{\phi}_\tau}) = 0.5$. And $\sigma_{\hat{\phi}_\tau}$ then yields the 1σ uncertainty on the measured mixing angle.

8.3 Estimation of the background processes

The two major background processes for the Higgs CP-measurement are Z+jets and QCD events. Both processes are estimated in a data-driven way as described in Sections 6.2.3 and 6.2.4. All other background processes are estimated from MC as described in Section 6.2.1. After the Higgs preselection (defined in Section 5.1), their contribution is almost negligible, as can be seen from Figs. 8.1 and 8.2. Figure 8.1 shows the distributions of the leading- and subleading-τ transverse momentum, η and the reconstructed τ decay mode. Figure 8.2 displays the modelling of several di-τ variables: the angular separations ΔR and $\Delta\eta_{\tau\tau}$ between the two τ leptons, the reconstructed di-τ invariant mass, and the transverse momentum of the reconstructed Higgs boson (derived from the two τ transverse momenta and $E_{\mathrm{T}}^{\mathrm{miss}}$). The distributions contain all events in the Higgs preselection region. Compared to the $H \to \tau\tau$ cross section measurement, a medium-tight τ-ID is required instead of a tight-tight τ-ID and only events with two 1-prong τ candidates are selected. Also, the applied normalisation factors for the QCD and $Z \to \tau\tau$ backgrounds differ, since they are fitted in a different region of the phase space. This can explain the differences in the modelling with respect to the results presented in [138]. $Z \to \tau\tau$ background displayed in Figs. 8.1 and 8.2 is taken from MC and r_{QCD} and r_Z are determined in a separate binned maximum likelihood fit to the $\Delta\eta_{\tau\tau}$ distribution in the VBF, boosted low-p_{T} , and boosted high-p_{T} regions. The resulting values amount to $r_{\mathrm{QCD}} = 1.59 \pm 0.52$ and $r_Z = 1.01 \pm 0.04$. However, in the final configuration of the analysis, they are estimated simultaneously to the CP-mixing angle ϕ_τ as described in Section 8.2.

8.4 Systematic uncertainties

Systematic uncertainties account for approximations or simplifying assumptions in theoretical calculations and the experimental setup. All systematic uncertainties contribute to the final fit as Nuisance Parameters (NPs).

The theoretical uncertainties originate from assumptions that are applied during the calculations of the Higgs production cross section, the $H \to \tau\tau$ branching fraction, the electroweak fraction of the Z boson production, the Matrix elements, the underlying event and the hadronisation process. Beside that, they emerge from experimentally measured input parameters to the calculations such as the measured parton distribution functions.

The experimental uncertainties in this analysis can be grouped into three major categories: First, the experimental uncertainties related to the object reconstruction, i.e. Tau, Jet and MET systematic-uncertainties. Second, uncertainties related to the setup of the collider, e.g. uncertainties from the luminosity measurement and difference between the simulated pile-up distribution and the actual data. Third, systematic uncertainties specific to the Higgs CP-measurement, i.e. Track-, IP- and τ particle flow related uncertainties. Both, the first and second group of systematic uncertainties were also included in the $H \to \tau\tau$ cross section measurement[139] and are estimated in the same way.

8.4.1 Systematic uncertainties from object reconstruction

τ systematic-uncertainties To estimate the τ systematic uncertainties, the recommendations of the ATLAS τ working group [140] are applied. In general, scale and efficiency uncertainties are distinguished: The uncertainties on the τ energy scale are determined from a fit of the Z-boson mass (reconstructed from the visible tau decay products) in $Z \to \tau\tau$ events and represent an uncertainty of 2-3% [91]. It is mainly dominated by the uncertainty of the background modelling. For τ_{had} with $p_{\mathrm{T}}^{\tau,vis} > 50\,\mathrm{GeV}$, additional uncertainties on the modelling of the calorimeter response to single particles are added [141]. For the τ energy scale, the following NPs are implemented in the fit:

- *Tau_TES_Detector* corrects for differences in the single-particle response and for threshold uncertainties evoked by the the detector modelling applied to the MC samples.

- *Tau_TES_MODEL* refers to uncertainties in the modelling of hadronic showers in the calorimeters, estimated by comparing the energy scale for different Geant4 physics lists.

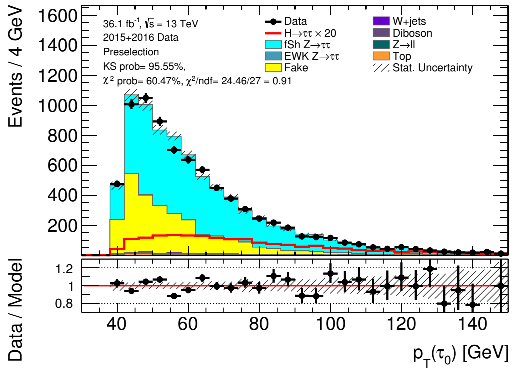

(a) Leading τ p_{T}

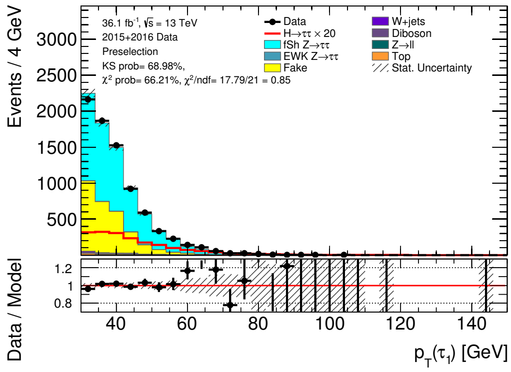

(b) Subleading τ p_{T}

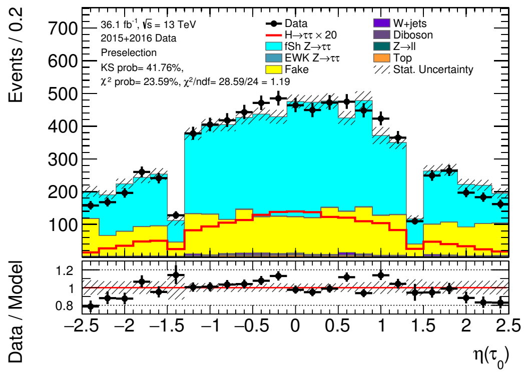

(c) Leading τ η

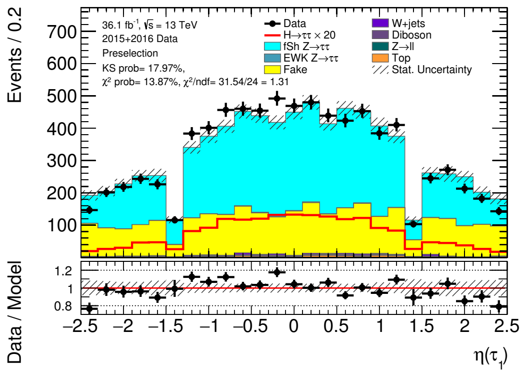

(d) Subleading τ η

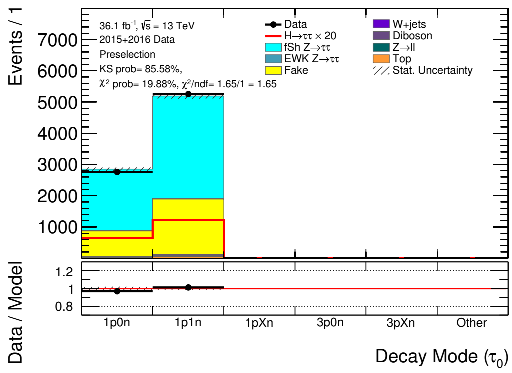

(e) Decay Mode of the leading τ

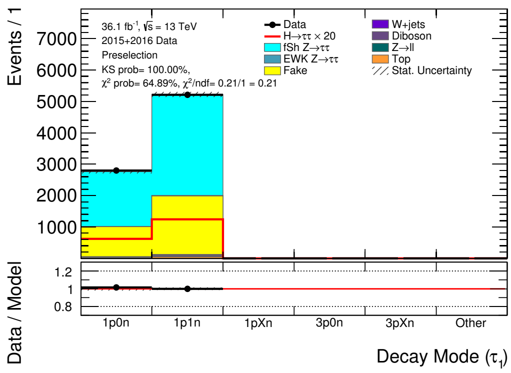

(f) Decay Mode of the subleading τ

Figure 8.1: Distribution of the leading and subleading τ transverse momenta, η and decay mode distributions in the Higgs preselection region. The $Z \to \tau\tau$ background prediction (fSh $Z \to \tau\tau$) is taken from MC and the QCD and $Z \to \tau\tau$ background normalisation factors are determined in a binned maximum likelihood fit to the $\Delta\eta_{\tau\tau}$ distribution in the Higgs preselection region. The signal contribution is shown as a red line. All signal and background expectations are stacked on each other in the plots and compared to data.

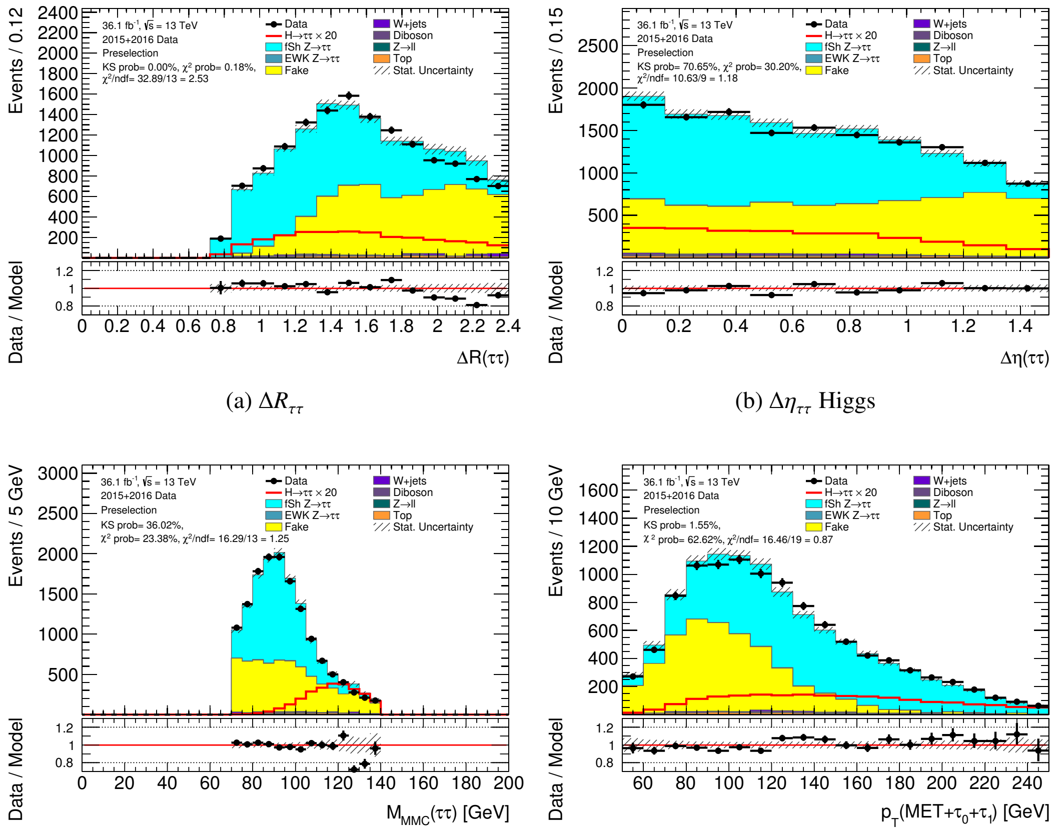

(a) $\Delta R_{\tau\tau}$ (b) $\Delta\eta_{\tau\tau}$ Higgs

(c) $m_{\tau\tau}^{\mathrm{MMC}}$ mass (d) p_{T} Higgs

Figure 8.2: $\Delta R_{\tau\tau}$ and $m_{\tau\tau}^{\mathrm{MMC}}$ distributions in the Higgs preselection region. The $Z \to \tau\tau$ background prediction is taken from MC and the QCD and $Z \to \tau\tau$ background normalisation factors are determined in a binned maximum likelihood fit to the $\Delta\eta_{\tau\tau}$ distribution in the Higgs preselection region.

- *Tau_TES_Insitu* is a total systematic uncertainty of the τ energy scale determined with a tag-and-probe measurement comparing the MC simulations to the acquired data.

The precision of the identification efficiency of hadronically decaying tau leptons is 2–4.5% for the reconstruction efficiency [90], 3–14% (depending on the p_{T} of the visible τ_{had}) for the trigger efficiency, 5–6% for the identification efficiency, and 3–14% (depending on the $\tau_{\mathrm{had}}^{vis}$ η) for the misidentification rate at which an electron is identified as a τ_{had} [91]. Accordingly, the following NPs are included in the fit to account for identification, reconstruction and trigger inaccuracies:
TAU_EFF_ELEORL_TRUEELE, TAU_EFF_ELEORL_TRUEHADTAU, TAU_EFF_ID_HIGHPT, TAU_EFF_ID_TOTAL, TAU_EFF_RECO_HIGHPT, TAU_EFF_RECO_TOTAL, TAU_EFF_TRIG_STATDATA2015, TAU_EFF_TRIG_STATDATA2016,TAU_EFF_TRIG_STATMC2015, TAU_EFF_TRIG_STATMC2016, TAU_EFF_TRIG_SYST2015, TAU_EFF_TRIG_SYST2016.
Beside that, uncertainties on the efficiency of passing the jet-vertex-tagger(JVT) and forward JVT requirements are included in the analysis as NPs *JVT* and *Forward_JVT*. The jet-vertex-tagger [142] is a multivariate combination of track-based variables used e.g. for pileup suppression and in the reconstruction of hadronically decaying τ leptons.

Systematic uncertainties form jet reconstruction For jets, uncertainties on the jet energy scale and on the jet energy resolution are applied. They depend on the jet's p_T and η and are estimated by comparing the MC simulations to the acquired data [143]. The uncertainties on the jet energy scale amount to 1-6% depending on the jet's p_T and they are taken into account in the analysis by the following NPs: *JES_BJES, JES_EffectiveNP_1 - JES_EffectiveNP_8, JES_EtaInter_Model, JES_EtaInter_NonClosure, JES_EtaInter_Stat, JES_Flavor_Comp, JES_Flavor_Resp, JES_HighPt, JES_PU_OffsetMu, JES_PU_OffsetNPV, JES_PU_PtTerm, JES_PU_Rho, JES_PunchThrough*. The uncertainties on the jet energy resolution amount to 1-4.5% depending on the jet's p_T and η [144] and they are considered in the fit by the following NPs: *jet_jer_crosscalibfwd,jet_jer_noisefwd,jet_jer_np0-jet_jer_np8*

Systematic uncertainties from E_T^{miss} reconstruction For the missing transverse energy E_T^{miss}, uncertainties apply to the E_T^{miss} scale and to the resolution of the soft track term. The E_T^{miss} systematic uncertainties are determined comparing the MC simulations to the acquired data for the parallel and perpendicular projections of E_T^{miss} on the vector sum of all hard object transverse momenta [93]. The parallel projection is used to determine the uncertainty on the scale as well as the longitudinal resolution. The transverse resolution is obtained from the width of the perpendicular projection In this analysis, three E_T^{miss}-related NPs are considered, accounting for uncertainties on the MET soft track's parallel resolution (*MET_SoftTrk_ResoPara*), perpendicular resolution (*MET_SoftTrk_ResoPerp*), and scale (*MET_SoftTrk_Scale*).

8.4.2 Luminosity and pileup-related uncertainties

All simulated MC samples are affected by the uncertainty on the integrated luminosity. The uncertainty on the integrated luminosity amounts to 2.1% for the combined 2015+2016 dataset [139]. A similar method compared to the one used in LHC run 1 [145] is applied to determine the uncertainty for the 2015+2016 dataset. The LUCID-2 detector is used to measure the luminosity and calibrated with x-y beam separation scans. The uncertainty on the luminosity measurement is included in the maximum likelihood fit of the CP-mixing angle by the NP *LumiUncCombined*.

Beside that, all MC simulations used to describe the expected signal or background processes are reweighted to the observed pileup profile of the 2015 and 2016 datasets. This is done by applying a correction factor to the number of bunch crossings in all simulated events. The uncertainty on this correction factor is represented by the NP *PRW_DATASF*.

8.4.3 Analysis-specific systematic uncertainties

Additional analysis-specific uncertainties originate e.g. from the τ particle-flow algorithm used to reconstruct the tau decay modes and the π^0 four-vectors. The analysis-specific systematic uncertainties can be grouped in three main categories: Tracking-, π^0- and τ-ID-systematic uncertainties.

Tracking uncertainties primarily originate from the finite resolutions of the transverse and longitudinal components d_0 and z_0 of the 2D track impact parameter. Another tracking uncertainty originates from the alignment of so-called weak modes, i.e. modes in which the detector is misaligned but the global χ^2 in the alignment procedure is unchanged. This requires a bias correction to the tracks, which is adjusted according to the angular position of the track [146]. In this analysis, the track-related uncertainties are represented by the following NPs: *TRK_bias_d0_WM, TRK_bias_qoverp_sagitta_WM, TRK_res_d0_dead, TRK_res_d0_meas, TRK_res_z0_dead, TRK_res_z0_meas*

The systematic uncertainties related to the π^0 reconstruction only affect 1p1n τ decays for which the ρ decay plane method is applied. One way to determine the π^0 uncertainties from a measurement of transverse spin correlations in $Z \to \tau\tau$ events is described in Chapter 7. However, it is impossible to apply this method for the 2015+2016 dataset, since the majority of the data was collected with a trigger that made the measurement in $Z \to \tau\tau$ events impossible, as described in Chapter 7.

To determine the π^0 uncertainties in the 2015+2016 datasets, an alternative method has been described in [147], which is based on blurring the π^0 angular components and studying the impact of this obscuring on the angular distances between the charged and the neutral pions from the τ decay. The uncertainties are measured in a $Z \to \tau\tau$ CR which applies the same $H \to \tau\tau$ preselection requirements presented in Section 5.1 with an additional cut on the $m_{\tau\tau}^{\mathrm{MMC}}$ mass of $m_{\tau\tau}^{\mathrm{MMC}} < 110\,\mathrm{GeV}$. The angular distances $\delta\eta$ and $\delta\phi$ between the charged and the neutral pions from $\tau^{\pm} \to \rho^{\pm}\nu \to \pi^{\pm}\pi^{0}\nu$ decays are used as observables. If both τ leptons decay via an intermediate ρ meson, both τ leptons are used. A Gaussian blur is applied to the reconstructed components of π^0, using a Gaussian centred around zero with a width of $k \cdot \sigma_{resolution}$. The width of the resolution in $\delta\eta$ and $\delta\phi$ is determined in a separate fit. The angular components of π^0 are decomposed into one component parallel and one perpendicular to the axis connecting π^0 and $\pi^{\pm}$. These parallel and perpendicular components are related to η and ϕ via a rotation matrix with angle α. Both components are blurred separately and hence, the dataset is divided into two equal-sized subsets in order to make sure no events are double counted. Two NPs are introduced in a maximum likelihood fit to the $\delta\eta$ and $\delta\phi$ distributions to consider the blurring of the variations on the parallel and perpendicular components described above. The uncertainty in parallel and perpendicular direction is determined using the full run 2 dataset corresponding to $147\,\mathrm{fb}^{-1}$ of ATLAS data.

The uncertainties on the π^0 resolutions are then determined from the constraints on these two NPs and amount to $17.3\%\sigma_{\mathrm{para}}(p_{\mathrm{T}})$ in parallel and $29.2\%\sigma_{\mathrm{perp}}(p_{\mathrm{T}})$in perpendicular direction [147]. They vary as a function of the π^0 transverse momentum, since the resolution of the parallel and perpendicular components of the π^0 depend on the p_{T} (π^0). Especially the transverse or perpendicular component is relevant for the calculation of the angle φ^*_{CP} in case of the $\tau \to \rho\nu$ decay. Hence, the impact of these π^0 uncertainties on the distribution of the φ^*_{CP} observable need to be studied in the future. In principle, the results of this study allow to include the presented fit in the measurement of the φ^*_{CP} observable, using additional Z CRs to determine the impact of the π^0 uncertainties simultaneously to the CP-mixing angle ϕ_τ. These additional CRs and thus the π^0 systematic uncertainties have not been included in the analysis presented in this thesis. However, they should be included in a future analysis using the full run 2 dataset.

In addition to the π^0 directional uncertainties, a τ-ID shape systematic uncertainty accounts for the impact of discrepancies between data and MC in the input variables of the τ-ID BDT on the φ^*_{CP} observable. Their impact can be measured in a $Z \to \tau\tau$ CR from a comparison of the data-MC agreement in the τ-ID BDT distributions between different bins in φ^*_{CP}. The amount of the impact of this systematic has not yet been evaluated, but should also be included in a future measurement of the CP-mixing angle.

8.4.4 Systematic uncertainties from the QCD multijet background estimate

The distribution of the QCD multijet background in the SR is derived from SS data as described in Section 6.2.3. It is estimated using the SS data in each signal region and subtracting all signal and background events predicted by MC simulations. Hence, a systematic uncertainty from the MC subtraction needs to be included. To this end, for each systematic uncertainty acting of the subtracted MC background samples, a separate up-/down-variation histogram is created. This up- or down- variation histogram contains the SS data minus the sum of all up- or down-varied background histograms, respectively. The so derived histograms are associated with the NP *hh_fake_contamination*.

Additionally, a possible uncertainty on the extrapolation of the QCD multijet template from the SS

name	applied selection
at least 2 loose τ leptons	$n_{\text{loose }\tau} > 1$ and not medium-tight
2 loose τ leptons	$n_{\text{loose }\tau} > 1$, τ_0 and τ_1 don't pass medium τ-ID
1 loose, 1 medium	$n_{\text{loose }\tau} > 0$, τ_0 or τ_1 passes medium τ-ID, but none of them tight
2 medium τ leptons	tau_0 and tau_1 pass medium τ-ID, but none of them tight
1 loose, 1 tight tau	$n_{\text{loose }\tau} > 0$, τ_0 or τ_1 passes tight Id, while the other one does not pass medium

Table 8.1: Definition of all studied anti-τ-ID regions. Except for the first one, all of them are statistically independent.

to the OS region can be derived separately for each of the three decay mode combinations. To this end, different anti-τ-ID regions are defined in Table 8.1, which all are reconstructed orthogonally to the medium-tight τ-ID region used in this analysis. The medium-tight τ-ID is defined as follows: τ_0 and τ_1 need to pass the medium τ-ID BDT score and at least one of them passes also the tight τ-ID BDT score.

Next, the ratio of OS to SS data is calculated subtracting all MC processes from the data and applying the $H \to \tau\tau$ preselection requirements with the respective modified (anti-) τ-ID cuts. The OS/SS ratio vs the φ^*_{CP} observable split up into the three decay mode combinations is shown in Fig. 8.3. Ideally, the

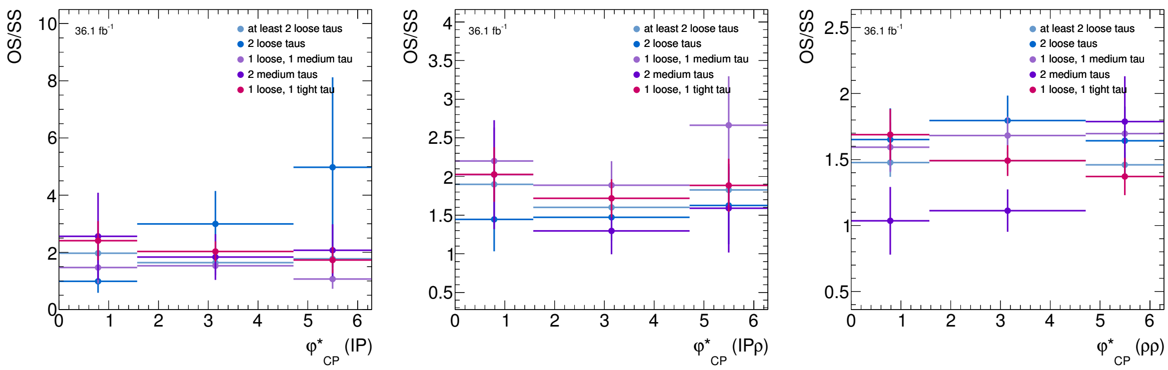

(a) IP-IP (b) IP-ρ (c) $\rho - \rho$

Figure 8.3: OS/SS ratio plotted against φ^*_{CP} for different (anti-) τ-ID regions using Data-(all MC) after applying the $H \to \tau\tau$ preselection.

OS/SS ratio distribution should be flat. To test for each distribution, whether it is compatible with a flat line, it is fitted with a constant.. The individual fit results are displayed in Appendix D. All distributions are compatible with a flat line within their statistical uncertainties. In this thesis, no uncertainty on the extrapolation from the SS to the OS region is included in the measurement of the CP-mixing angle. Nevertheless, in a future Higgs CP-measurement a respective uncertainty should be assigned and included in the fit to the φ^*_{CP} observable. The up- and down-variance histograms can then be obtained by calculating the difference of the actual bin content in the OS/SS ratio histogram compared to the prediction from the flat distribution (obtained by fitting a constant function to the OS/SS ratio histogram) using the anti-τ-ID selection with the maximal statistical power of the test. The proposed procedure is also applied in the measurement of the π^0 directional uncertainties [147].

8.4.5 Systematic uncertainties from the $Z \to \tau\tau$ background estimate

The $Z \to \tau\tau$ background estimate in the φ^*_{CP} signal regions is retrieved from data in the Z CR. Thus, advantageously no systematic uncertainties from theory need to be included for the $Z \to \tau\tau$ background prediction. However, in a future measurement, a $Z \to \tau\tau$ extrapolation uncertainty should be included to account for possible differences in the $Z \to \tau\tau$ shape in the $Z \to \tau\tau$ CRs compared to the $H \to \tau\tau$ SRs.

8.5 Validation of the fit procedure

For each mixing angle hypothesis a separate maximum likelihood fit is performed and the results of all independent fits are combined to determine the CP-mixing angle. Thus, it is important to ensure that the results of the independent fits are comparable. The procedure of the fit is validated in a fit to Asimov data. The Asimov data are SM-like pseudo data, which are produced by taking the sum of all background distributions and the CP-even $H \to \tau\tau$ signal distribution. The observable φ^*_{CP} is segmented into five bins and measured simultaneously in an inclusive VBF or boosted region, which is split up by the respective decay mode and /dsig/$Y_\pm$ requirements. Combining the VBF, boosted low-p_{T} and boosted high-p_{T} region reduces problems caused by limited statistics in the signal or background modelling to a minimum.

8.5.1 The signal-only fit - a test case

Initially a simple test case is created: the CP-mixing angle is measured in Asimov data for a single signal region (e.g. VBF or boosted IP-IP d_0^{sig} low) using only one sample namely the $H \to \tau\tau$ signal sample. As described in Section 6.2.2, unpolarised $H \to \tau\tau$ MC simulations are used to simulate the VBF and ggF signal processes. The unpolarised $H \to \tau\tau$ sample is then reweighted with *TauSpinner* [120] weights to describe the different CP mixing angle hypotheses. Figure 8.4 shows that applying the *TauSpinner* weigths to the unpolarised signal distributions changes the integral and the bin uncertainties in the φ^*_{CP} distribution.

This can cause problems when the results of the 17 independent measurements on the CP-mixing angle ϕ_τ are combined. Accordingly, a change in the integral and uncertainties of the φ^*_{CP} distributions between the different CP mixing angle hypotheses creates artefacts in the distribution of the fitted $H \to \tau\tau$ signal strength μ. In this analysis, only a change in the shape and not the yield of the φ^*_{CP} distribution is measured. Therefore, it is possible to apply a correction on the integral of the φ^*_{CP} distribution without changing the final ΔNLL distribution. The φ^*_{CP} distribution at $\phi_\tau = x$ is thus scaled by the ratio of its integral at $\phi_\tau = X$ over the integral at $\phi_\tau = 0$, separately for each signal-region category. After rescaling the signal φ^*_{CP} distributions, the best-fit result on the $H \to \tau\tau$ signal strength μ deviates only slightly from unity for $\phi_\tau \neq 0$ as it is expected in this simple test case.

However, this integral-correction does not compensate for the artefacts observed in the ΔNLL distribution from a fit to Asimov data. These seem to originate from systematic uncertainties produced by the application of the *TauSpinner* weights. In fact, the *TauSpinner* weights significantly change the bin-by-bin MC uncertainties between the different angles. As a consequence, the ΔNLL values for different CP-mixing angles ϕ_τ are no longer comparable. In order to study this effect further, the bin uncertainties are artificially reduced by scaling the integral of the distributions, i.e. the luminosity L, by a factor of two to 100. Figure 8.5 shows the resulting ΔNLL distributions for a signal-only fit using a single category (VBF or boosted IP-IP d_0^{sig} low) for different luminosities. The results indicate that the bias on the minimum of the ΔNLL distribution, i.e. the measured CP-mixing angle decreases with decreasing bin uncertainties as expected.

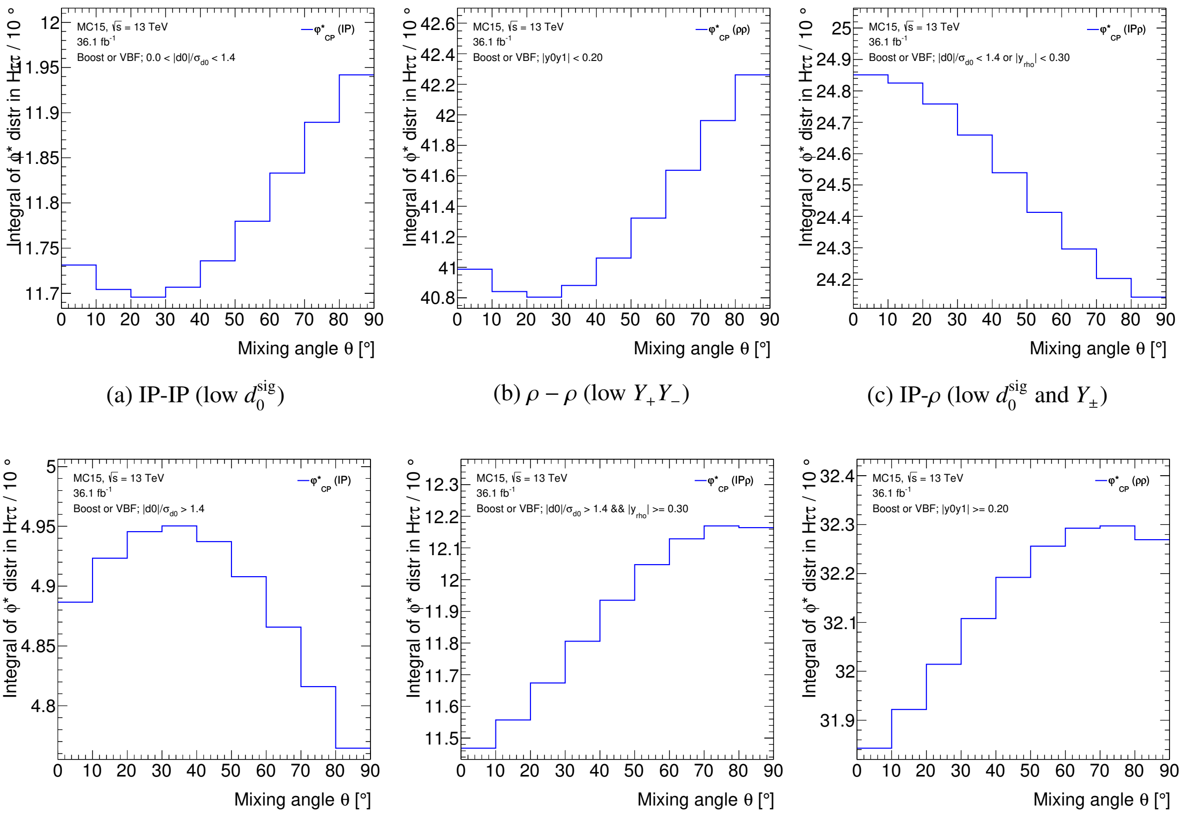

(a) IP-IP (low d_0^{sig}) (b) $\rho-\rho$ (low Y_+Y_-) (c) IP-ρ (low d_0^{sig} and $Y_\pm$)

(d) IP-IP (high d_0^{sig}) (e) IP-ρ (high d_0^{sig} and $Y_\pm$) (f) $\rho-\rho$ (high Y_+Y_-)

Figure 8.4: Integral of the φ^*_{CP} distribution in the VBF or boosted region in the different d_0^{sig} and $Y_\pm$ categories for CP mixing angles between 0 and 90 degrees.

To ensure that the statistical uncertainties are comparable between the different CP-mixing angle hypotheses, the $H \to \tau\tau$ signal templates are generated by drawing N random events from the respective original distributions (Fig. 8.6). This results in the same number of entries in the templates for all mixing angles. Consequently, N random events have to be generated for the nominal $H \to \tau\tau$ signal distributions and all their systematic up- and down-variation histograms in all the signal regions. The number of generated random events N is varied from 10000 to 200000 events to determine the minimum N, such that the φ^*_{CP} distributions are correctly described (Fig. 8.6). Figure 8.6 indicates that 100000 events per distribution are sufficient to correctly describe the φ^*_{CP} distribution from $H \to \tau\tau$ decays without creating an additional bias in the ΔNLL distributions. As a consequence, this method is applied to the $H \to \tau\tau$ signal distributions for all following studies and the presented measurement of the CP-mixing angle, drawing 100000 random events each for the $H \to \tau\tau$ signal distribution and all its systematic variations in all signal regions. This procedure compensates for the variations of the bin-to-bin statistical uncertainties for different mixing angle hypotheses, which would otherwise result in artefacts in the ΔNLL distribution. One drawback of this procedure is that the statistical MC uncertainties on the signal distributions might be underestimated. However, the expected number of signal events in the analysed regions is small enough, that the dominant uncertainty will come from the Poisson uncertainty on the number of expected events.

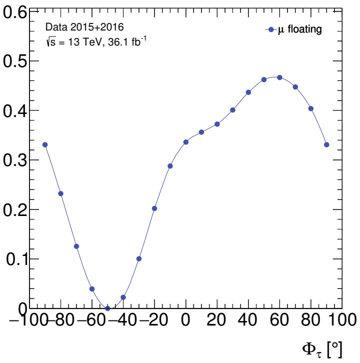

(a) $\mathcal{L} \times 1$

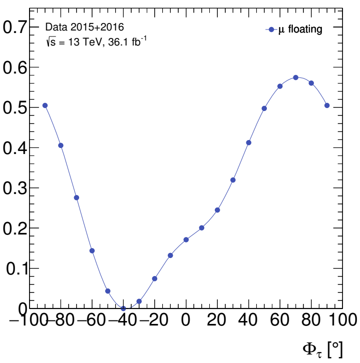

(b) $\mathcal{L} \times 2$

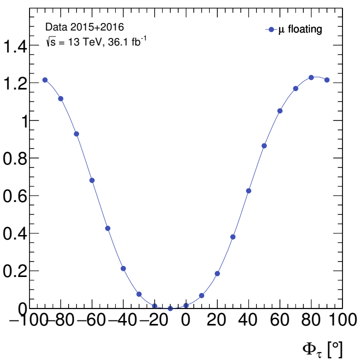

(c) $\mathcal{L} \times 5$

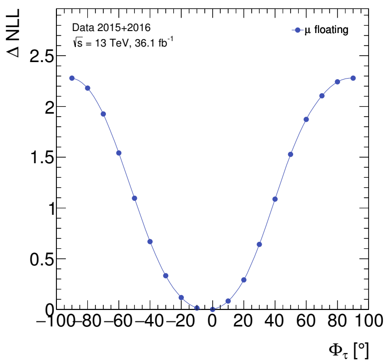

(d) $\mathcal{L} \times 10$

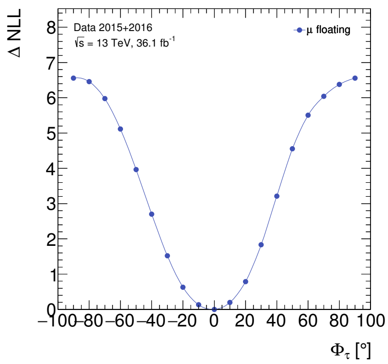

(e) $\mathcal{L} \times 100$

Figure 8.5: ΔNLL curve resulting from fit to the signal only in the IP-IP d_0^{sig} low category with the luminosities $\mathcal{L}$ from two to 100 times the original luminosity.

8.5.2 Including all backgrounds and decay mode combinations

Next, the same measurement is repeated including all background contributions and decay mode combinations. This results in a simultaneous fit to six signal regions: IP-IP low/high d_0^{sig}, IP-ρ low/high $d_0^{\mathrm{sig}}/Y_\pm$ and $\rho-\rho$ low/high Y_+Y_-. Beside the NPs accounting for the bin uncertainties in the signal-, background and Asimov data distributions, the signal strength μ is the only free parameter included in the fit. The background normalisations r_Z and r_{QCD} are fixed to unity.

The post-fit distributions for $\phi_\tau = 0$ (see Fig. G.1) accord in all categories, while for $\phi_\tau = 90$ (see Fig. G.2) slight differences are observed, as expected. The resulting ΔNLL and best-fit μ distributions are displayed in Fig. 8.7. As expected, the width of the ΔNLL curve is enlarged compared to the signal-only fit. The minimum is still compatible with zero, which indicates that artefacts originating from statistical limitations in the background modelling are indetectable or absent. Also, the best-fit μ distribution deviates only minimally from unity for CP-mixing angles $\phi_\tau \neq 0$ as it is expected. Figure 8.7 indicates that no constraint on the CP-mixing angle can be expected from a measurement using the inclusive VBF or boosted categories in the fit due to the large width of the ΔNLL distribution. However, the fit result might be improved using the VBF, boosted low-p_{T}, and boosted high-p_{T} categories instead of the inclusive VBF or boosted ones, because the relative signal contribution to the separate categories is higher than in the inclusive ones.

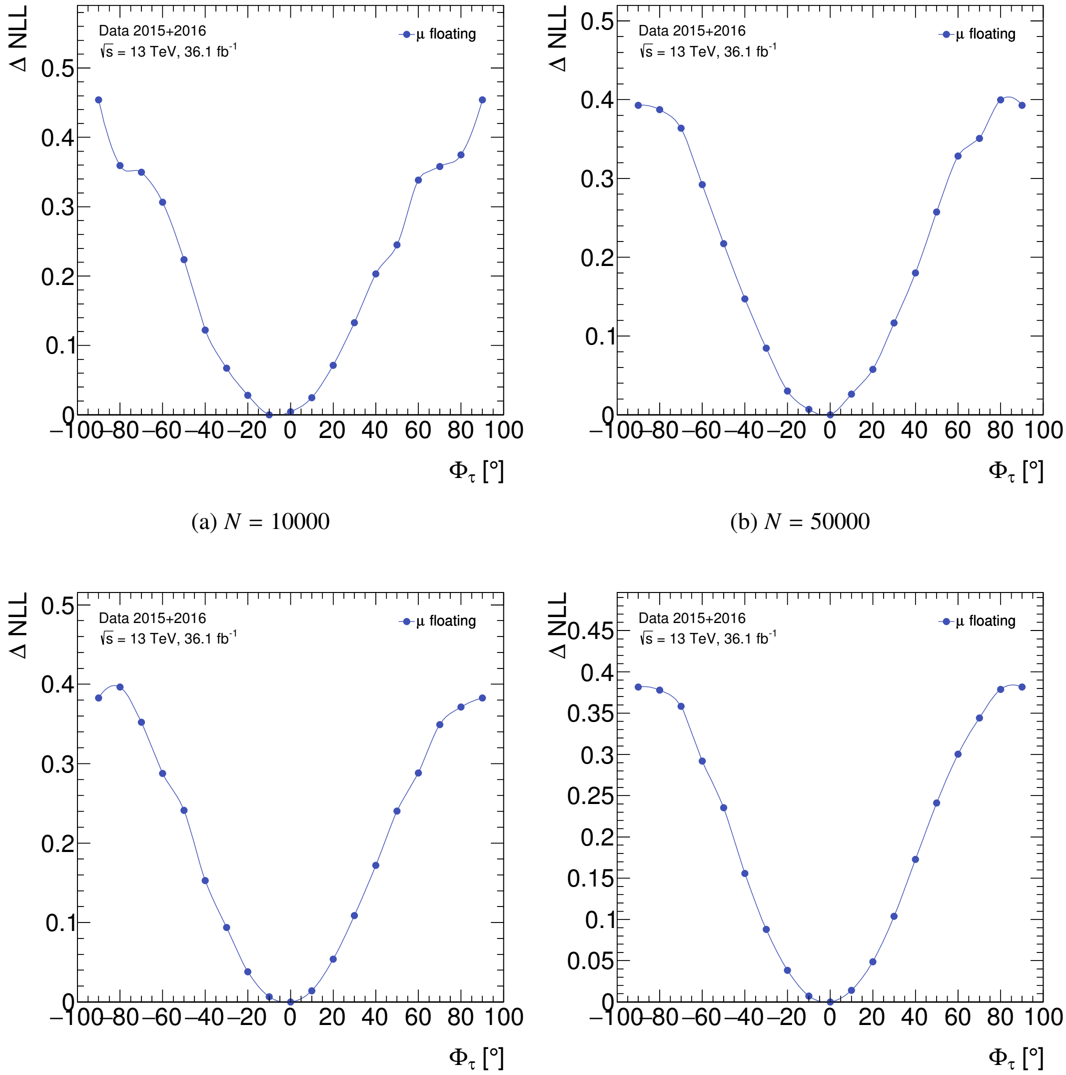

(a) $N = 10000$

(b) $N = 50000$

(c) $N = 100000$

(d) $N = 200000$

Figure 8.6: ΔNLL curve resulting from signal-only fit with 10000 to 200000 random events generated according to the respective $H \to \tau\tau$ distributions.

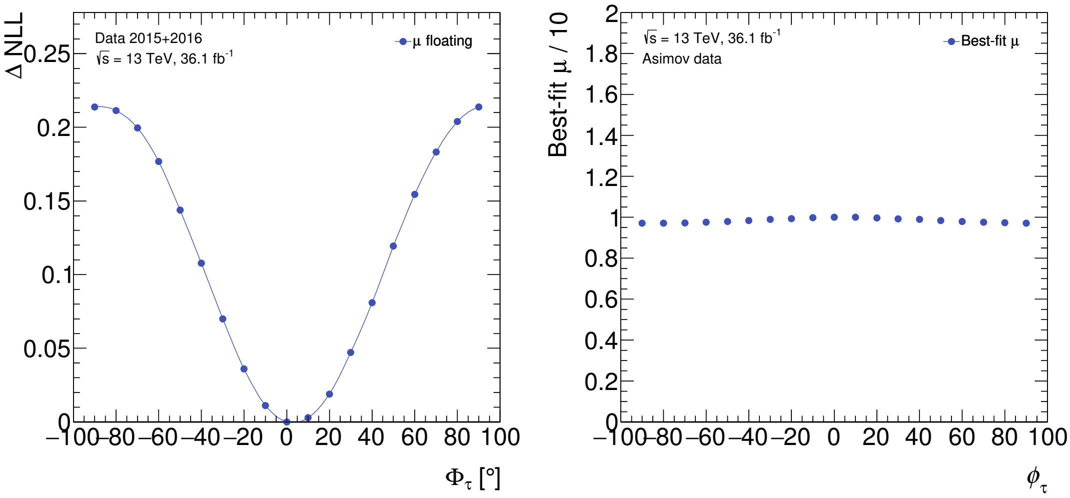

Figure 8.7: ΔNLL curve for the stat only fit using Asimov data with all backgrounds in the merged VBF and boosted categories with the signal strength μ as only free parameter.

8.5.3 Comparison of different fit configurations

To select the optimal configuration, the results of different fit configurations are compared using Asimov data. An ideal fit configuration shows maximum constraining power with minimum bias on the measured CP-mixing angle.

In the validation of the fit procedure, the VBF and boosted categories are merged in order to have sufficient statistics in each signal category. However, the resulting ΔNLL curve (see Fig. 8.7) does not allow to constrain the CP mixing angle. Hence, the benefits of measuring φ^*_{CP} separately in the VBF, boosted low-p_{T} , and boosted high-p_{T} categories are examined in Fig. 8.8(a). Also, the effect of fixing the $H \to \tau\tau$ signal strength μ to unity is studied in Fig. 8.8(b).

The results show, that the ΔNLL distribution obtains a shift towards $\phi_\tau > 0$. However, there are no large difference whether or not μ is allowed to vary in the Asimov fit to the CP-mixing angle. In fact, a μ constrained to unity leads to a slightly smaller width in ΔNLL, because the fit scales down the $H \to \tau\tau$ contributions for CP-mixing angles $\phi_\tau \neq 0$. Thus, for the following comparisons of fit configurations a constrained $H \to \tau\tau$ signal strength is used. The shift in the ΔNLL distribution can be explained by statistical limitations in the background estimates. Due to the need to split up the signal regions by decay modes and d_0^{sig} or $Y_\pm$ significances, the low statistics in the MC samples for signal and background but also the data-driven background models used to describe the $Z \to \tau\tau$ and QCD multijet contributions limit the performance of the maximum likelihood fit. Apart from merging all signal categories, the bin uncertainties in the background distributions can also be reduced by decreasing the number of bins in the φ^*_{CP} distributions. Hence, as a next step, the benefits of using three instead of five bins in φ^*_{CP} are examined. In case of the three bins, a non-equidistant binning is chosen. The borders of the bins are adapted to the expected cosine-shape of the φ^*_{CP} variable. Their ranges are $[0, \pi/2]$, $[\pi/2, 3\pi/2]$ and $[3\pi/2, 2\pi]$. With this choice of binning, the difference between the signal expectation for different CP states is maximal. Figure 8.9(a) shows the ΔNLL curve using three bins instead of five. It is centred at zero as expected in a fit to Asimov data and the width of the ΔNLL curve is reduced by more than a factor of two compared to the fit result using five bins. The latter observation results, however, not from the binning itself, but more from the effect of splitting up the inclusive VBF or boosted signal region into VBF, boosted low-p_{T} , and boosted high-p_{T} regions as indicated from the following

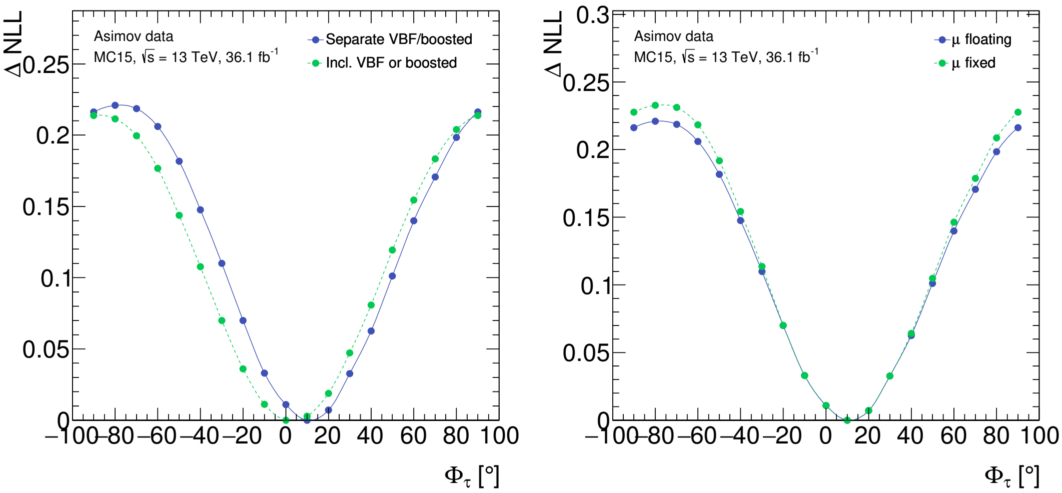

(a) Inclusive/separate SRs (b) Unconstrained/Constrained μ

Figure 8.8: ΔNLL distribution comparing the effect on the CP-mixing angle using one inclusive VBF or boosted vs. separate VBF, boosted low-p_{T} , and boosted high-p_{T} categories (a) and a constrained (fixed) vs. unconstrained (floating) $H \to \tau\tau$ signal strength μ in a fit to Asimov data.

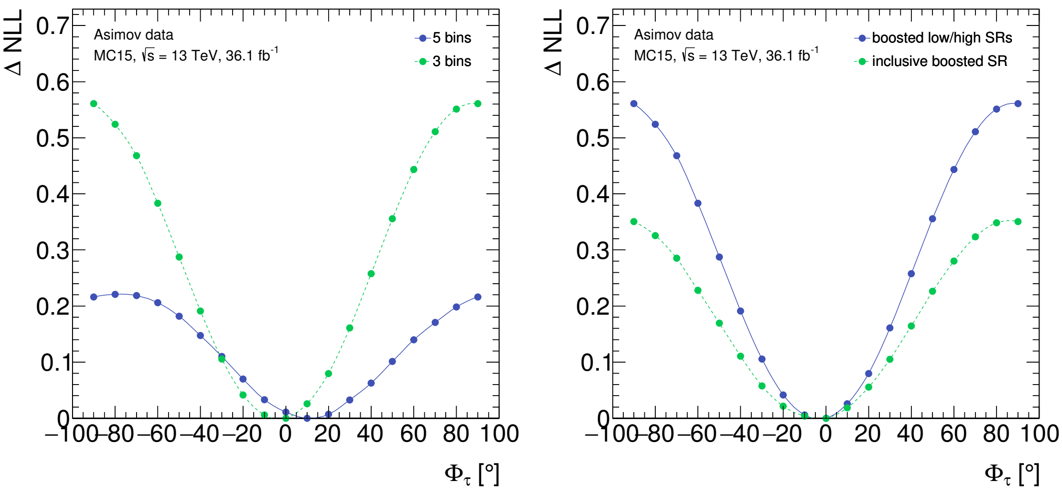

(a) Compare binning (b) Compare merging levels

Figure 8.9: Comparison of the ΔNLL curves using 5- or 3-bins with fixed $H \to \tau\tau$ signal strength μ and minimal merging of categories (a)and merging only the VBF IP-IP and IP-ρ categories or merging also the boost low-p_{T} and high-p_{T} categories (b) in a fit to Asimov data.

comparison: Fig. 8.9(b) compares the *minimal merging*, where only the VBF IP-IP d_0^{sig} and the VBF IP-ρ d_0^{sig}-$Y_\pm$ categories are merged, and the *maximal merging*, where additionally, the boosted low-p_T , and boosted high-p_T categories are convolved into one combined category. In the latter case, four VBF and six boosted signal regions are used in the fit. Figure 8.9 (b) shows that convolving the categories disadvantageously causes a loss of information. Hence, in the final setup of the analysis, the CP-mixing angle is measured simultaneously in the originally proposed 16 signal regions using 3-bins in φ^*_{CP}.

The effect of constraining the $H \to \tau\tau$ signal strength μ to unity is investigated in more detail with the final analysis setup: Figure 8.10 compares the fit results from a fit where μ is constrained (μ fixed) to those from a fit where mu is left unconstrained (μ floating). The fit takes into account NPs for the $H \to \tau\tau$ signal strength, the background normalisation factors r_Z and r_QCD and statistical uncertainties. r_Z and r_QCD are left unconstrained in both cases. Their post-fit values and uncertainties are listed in Table 8.2. Figure 8.10 indicates that there is no significant difference between the ΔNLL curves obtained

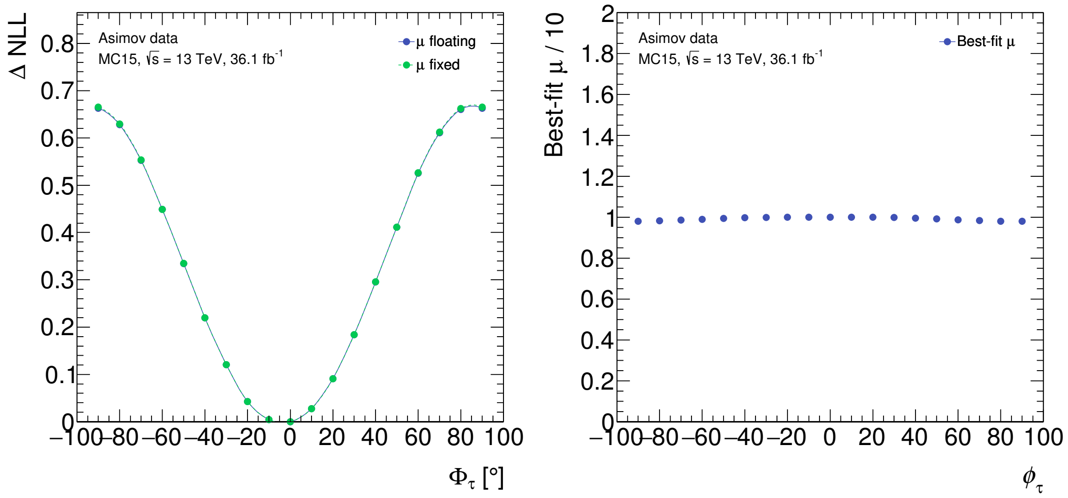

(a) ΔNLL curve

(b) best-fit μ

Figure 8.10: Comparison of the ΔNLL curves using a constrained or unconstrained $H \to \tau\tau$ signal strength μ in the standard 3-bins setup with minimal merging including statistical uncertainties only (a) and the best-fit μ distribution.

with constrained or unconstrained μ. Only for angles $\phi_\tau \geq 70^\circ$, the width of the ΔNLL curve is slightly smaller if μ is fixed to unity. This can be explained based on the post-fit values of the $H \to \tau\tau$ signal strength μ for $\phi_\tau = 0^\circ$ and $\phi_\tau = 90^\circ$: Table 8.2 shows that μ is slightly scaled down for large CP-mixing angles, such that the CP-odd -like $H \to \tau\tau$ distribution better suits the CP-even Asimov data. Thus, the ΔNLL value at large ϕ_τ is slightly reduced when μ is unconstrained compared to when μ is constrained to unity. Furthermore, Table 8.2 indicates that the constraints on the signal and background normalisation factors are similar in the independent fits to different CP mixing angles.

For this thesis the QCD multijet background is estimated from SS data. However, the impact on the measured CP-mixing angle of replacing the data-driven QCD multijet estimate by a flat distribution scaled to the expected yield of the QCD multijet background in each signal region is studied in a fit to Asimov data. The approximation might help to compensate for the large statistical fluctuations in the QCD multijet background. First, it is validated, that the QCD multijet prediction is compatible with a constant distribution by fitting constant functions to the QCD multijet distributions in all signal regions.

NF	$\phi_\tau = 0$	$\phi_\tau = 90$
r_{QCD}	1.0 ± 0.1188	1.0009 ± 0.1409
r_Z	1.0 ± 0.0302	1.0003 ± 0.0695
μ	1.0	1.0

(a) Constrained μ

NF	$\phi_\tau = 0$	$\phi_\tau = 90$
r_{QCD}	1.0 ± 0.1256	1.0012 ± 0.1257
r_Z	1.0 ± 0.0306	1.0003 ± 0.0306
μ	1.0 ± 0.4366	0.9805 ± 0.4402

(b) Unconstrained μ

Table 8.2: QCD and $Z \to \tau\tau$ normalisation factors after the fit to Asimov Data using the SM $H \to \tau\tau$ signal template with a constrained (a) and unconstrained (b) $H \to \tau\tau$ signal strength μ.

Figure 8.11 suggests that the QCD multijet shapes are indeed compatible with constant distributions within the statistical uncertainties. Second, the fit to Asimov data is repeated replacing the data-driven QCD multijet templates by the flat distributions. Finally, the fit results are compared in Fig. 8.12. The results suggest that the ΔNLL curves obtained in both cases are comparable. The uncertainty on the measured mixing angle is even a bit larger when using the approximation of a flat QCD multijet distribution instead of the data-driven estimate.

8.6 Results from the fit to Asimov data

Performing the measurement of the CP-mixing angle in Asimov data allows to verify that the used tools are applied correctly and to derive an expected sensitivity on the Higgs CP-mixing angle. As before, the Asimov data are generated by forming the sum of all background and the CP-even $H \to \tau\tau$ signal distribution. Finally, the complete set of nuisance parameters for systematic uncertainties listed in Table G.1 is included in the fit. As expected, the post-fit φ^*_{CP} and $\Delta\eta_{\tau\tau}$ distributions accord in case the $\phi_\tau = 0$ CP-mixing angle hypothesis is tested (Figs. G.3 to G.6). Comparing the resulting ΔNLL curve to a ΔNLL curve from a fit where no systematic uncertainties are included, as displayed in Fig. 8.13(a), reveals no significant differences. Figure 8.13(a) indicates that the fit is dominated by statistical uncertainties, since there is no difference observed when including systematic uncertainties. The statistical uncertainties will be decreased in the future when more data are included in the fit and. In addition, further systematic uncertainties on e.g. the π^0 resolution, the τ-ID shape, and the extrapolation of the QCD multijet template from the SS to the OS region need to be included. Figure 8.13(b) shows the results of the combined fit compared to separate fits to all signal regions of a specific decay mode combination. From this figure it can be concluded that the constraining power on the CP-mixing angle is largest for 1p0n-1p0n τ decays, where the IP-IP method is applied. The least constraining power is achieved for 1p1n-1p1n τ decays, for which the $\rho - \rho$ method is applied. Furthermore, Fig. 8.13(b) indicates that combining all three decay mode combinations significantly improves the result of the measurement. The combined fit yields a ΔNLL curve which is approximately a factor of two better than the best fit result among the separate fits.

The resulting constraints on the background normalisation factors are listed in Table 8.2(a). As expected, the ratios do not deviate from unity after the fit to Asimov data in case the $\phi_\tau = 0$ CP-mixing angle hypothesis is tested. The estimated relative uncertainties are approximately 11% for r_{QCD} and 3% for r_Z.

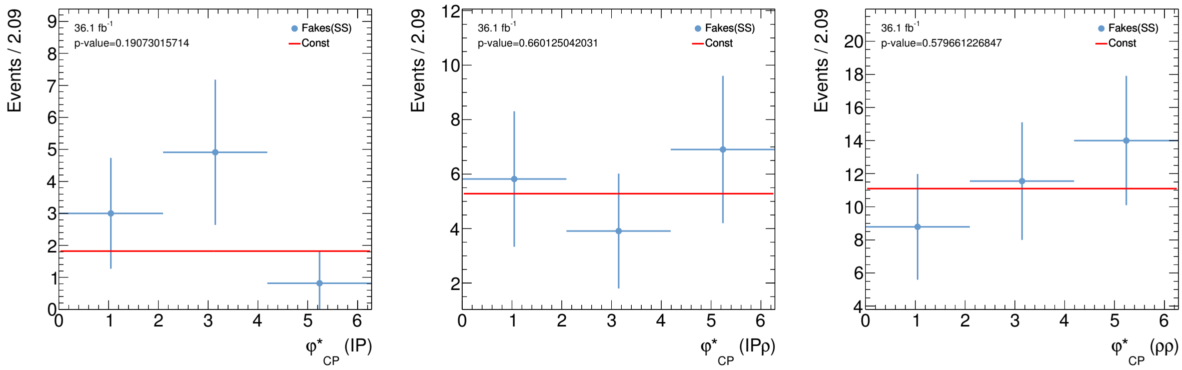

(a) VBF region

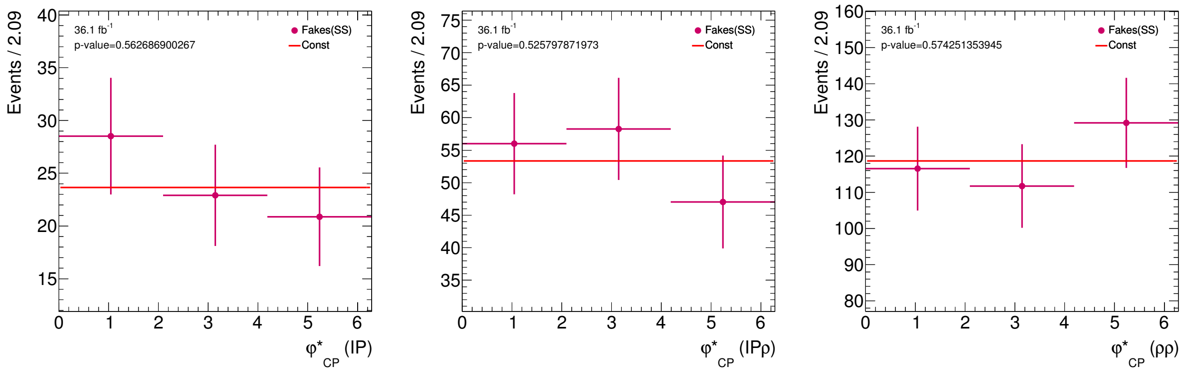

(b) boosted low-p_{T} region

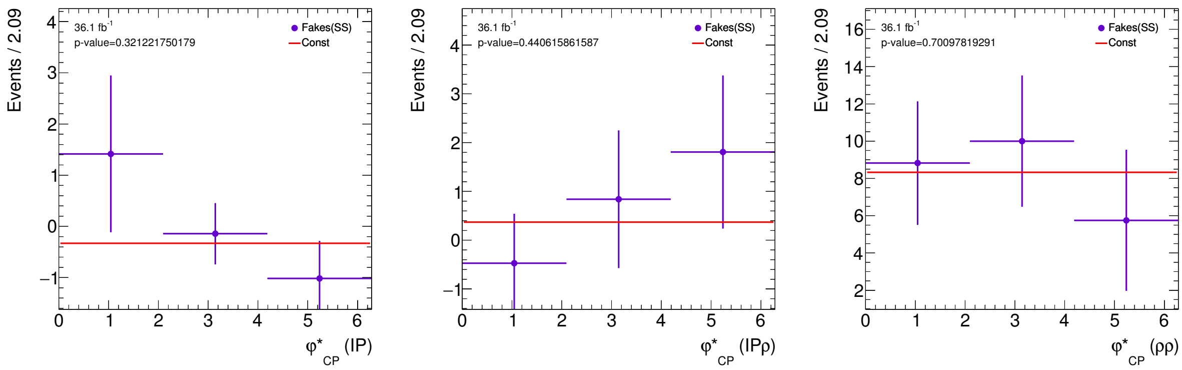

(c) 1p1n-1p1n

Figure 8.11: Compatibility of the QCD multijet background (referenced as Fakes(SS) in the distributions) with a flat distribution. The p-values result from a χ^2 test, evaluating whether the histograms and the fitted constants agree.

8.6.1 Expected sensitivity on the Higgs CP-mixing angle

Figure 8.14 shows the ΔNLL curve for the fit to Asimov data and including systematic and statistical uncertainties and constraining μ to unity. To highlight the parabolic shape of the ΔNLL curve, a parabola is fitted to the innermost region. The expected sensitivity on the CP-mixing angle measured in $H \to \tau\tau$ decays is derived from half the width of the ΔNLL curve at ΔNLL = 0.5. The width is read-off from

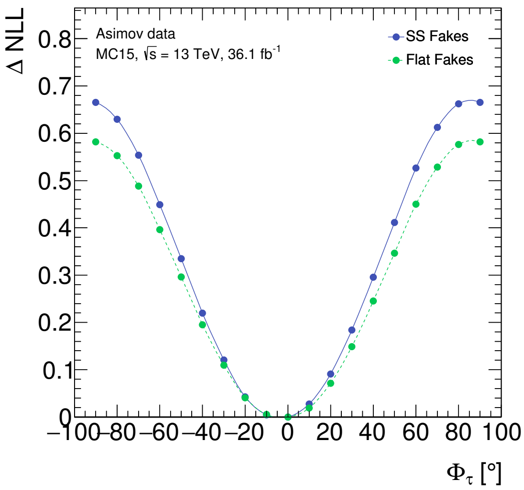

Figure 8.12: ΔNLL curve using data-driven QCD multijet estimate (SS Fakes) compared to the ΔNLL curve obtained when approximating the QCD multijet background by a flat distribution scaled to the expected yield. Both estimates are obtained using a fixed $H \to \tau\tau$ signal strength μ.

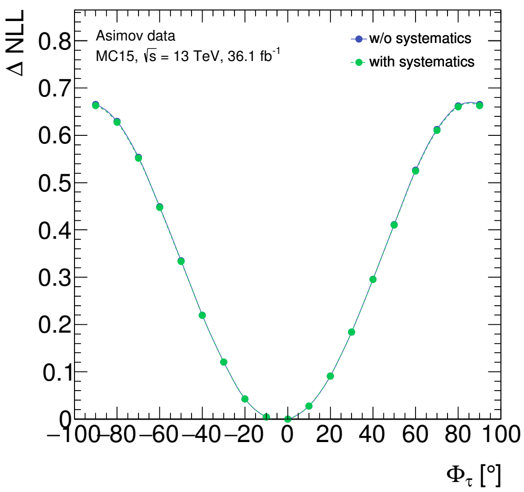

(a) Combined fit of all decay modes

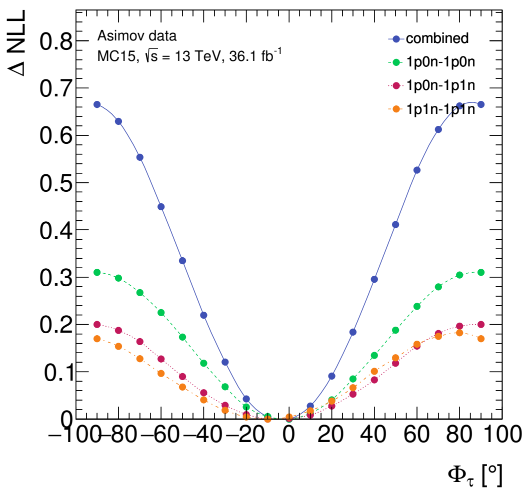

(b) Seperate fits per decay mode, w/o systematics

Figure 8.13: ΔNLL curve obtained by fits to φ^*_{CP} including or excluding systematic uncertainties (a) and separated by decay mode combination without systematic uncertainties (b). All fits were obtained using Asimov data with the $H \to \tau\tau$ signal strength μ being constrained to unity.

the original ΔNLL distribution and amounts to approximately 120°. Hence, the expected accuracy on the measured CP-mixing angle ϕ_τ is approximately 60°. Beside that, Fig. 8.14 allows to determine the expected confidence level at which a pure CP-odd Higgs boson hypothesis can be excluded. To this end, the ΔNLL value at $\phi_\tau = 90^\circ$ is read-off from the distribution. It follows $\Delta\mathrm{NLL}(\phi_\tau = 90^\circ) \approx 0.67$, which corresponds to a $\mathcal{X}^2$ of

$$\mathcal{X}^2(\phi_\tau = 90^\circ) \approx 2\Delta\mathrm{NLL}(\phi_\tau = 90^\circ) \approx 1.34\,.$$

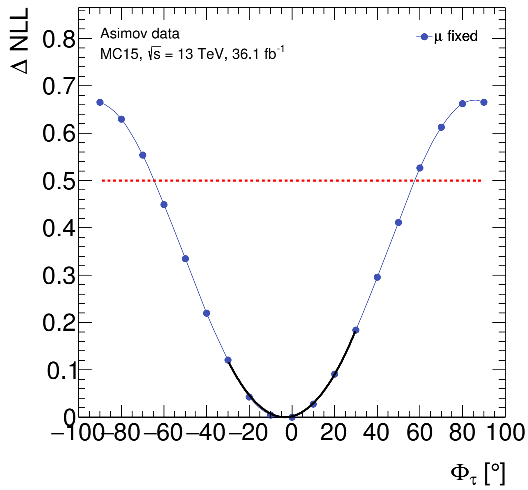

Figure 8.14: ΔNLL curve for the fit to φ^*_{CP} using Asimov data and including systematic and statistical uncertainties. The one sigma uncertainty on the measured mixing angle can be deduced from the width of this curve at 0.5, indicated by the red dashed line. A parabola is fitted to the innermost region of the likelihood distribution to highlight the parabolic shape of the ΔNLL curve.

This results in an expected CL to exclude a pure CP-odd hypothesis of $1 - P(1.37, 1) \approx 75\%$. The corresponding p-value is calculated using ROOT [136]

8.6.2 Constraints on the systematic uncertainties

Figure 8.15 shows the pull distributions for the systematic uncertainties listed in Table G.1 after the fit to Asimov data assuming a CP-mixing angle of $\phi_\tau = 0^\circ$ in the signal distribution. The pull for any nuisance parameter θ is given as:

$$\text{pull} = \frac{\hat{\theta} - \theta_0}{\Delta\theta}, \tag{8.12}$$

where $\hat{\theta}$ is prior value of the NP, θ_0 is the post-fit value and $\Delta\theta$ is the prior uncertainty on the NP. In a fit to Asimov data, where data and prediction agree in all distributions, the pulls of all NPs are centred at zero. The post-fit uncertainties on the NPs are also indicated in the plot. The pulls in Fig. 8.15 are sorted by constraint, starting with the NP which can be constrained the most in this measurement. The results indicate that some of the NPs related to the jet energy resolution can be constrained, especially the *jet_jer_np0* parameter. This is consistent with the results presented in [138]. Since individual fits are performed for each mixing-angle hypothesis, the systematic uncertainties and their pulls could in principle vary for each tested CP mixing angle. However, as can be seen from Fig. G.7, neither the central values, nor the constraints on the included systematic uncertainties change significantly for the CP-odd mixing angle hypothesis with respect to the CP-even one in the fit to Asimov data. The correlations between the different NPs are displayed in Fig. 8.16. To get a better overview, only NPs with more than $\geq 5\%$ correlation are included in this plot. All correlations with a significant impact, i.e. which are $> 30\%$ can be explained by apparent correlations between the respective NPs and thus are expected.

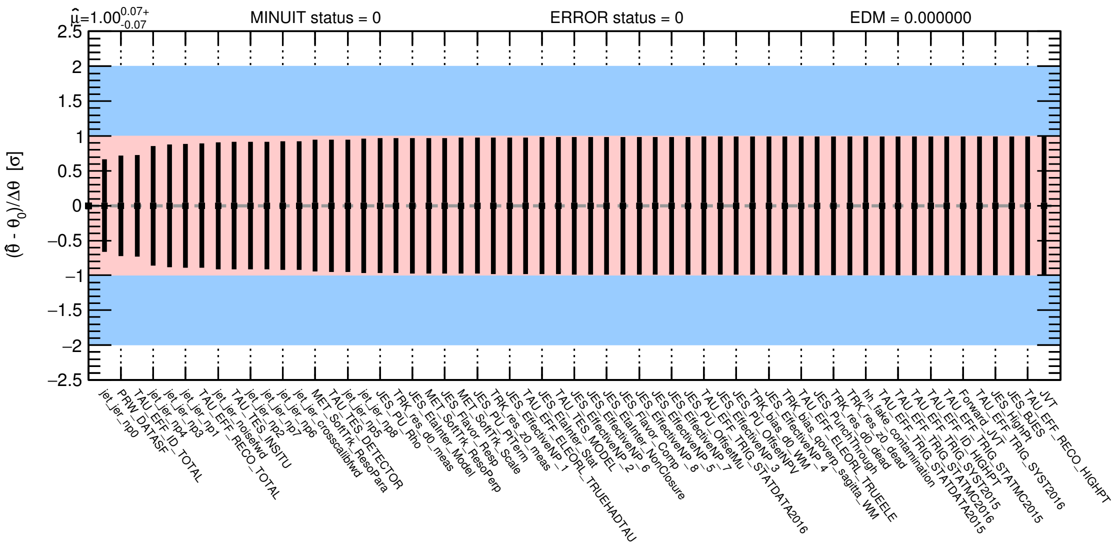

Figure 8.15: Pull distribution of all systematic uncertainty NPs included after a fit to Asimov data sorted by their constraint for $\phi_\tau = 0°$.

8.7 Measurement of the Higgs CP-mixing angle in data

8.7.1 Post-fit distributions

The post-fit $\Delta\eta_{\tau\tau}$ distributions in the VBF, boosted low-p_{T} and boosted high-p_{T} CRs are shown in Fig. 8.17. Figures 8.18 to 8.20 display the post-fit φ^*_{CP} distributions in all signal regions for the fit to the CP-even $H \to \tau\tau$ signal template. After the fit, the agreement between data and the SM predictions is good in all categories. The goodness of fit is indicated by the p-values quoted in the distributions. The post-fit p-values range from $0.63 - 0.99$. The pre- and post-fit yields of signal, backgrounds and data are also summarised in Tables G.2 to G.5, separately for all signal and control regions.

8.7.2 Sensitivity on the CP mixing angle

The resulting negative log-likelihood curves using the 36.1 fb^{-1} of ATLAS data recorded in 2015 and 2016 are shown in Fig. 8.21(a) for a constrained $H \to \tau\tau$ signal strength μ and in Fig. 8.21(b) for an unconstrained μ. In both cases, only statistical uncertainties are included. Please note the different y-axis scales in the two first plots. Figure 8.21(c) shows the μ distribution, which corresponds to the ΔNLL curve in Fig. 8.21(b), where μ is unconstrained. The measured CP-mixing angles and their uncertainties are

$$\phi_\tau = \begin{cases} 10 \pm 41° & \mu \text{ constrained to unity} \\ 10 \pm 37° & \mu \text{ unconstrained.} \end{cases}$$

This indicates that the measured CP-mixing angle is identical for a constrained and unconstrained μ. However, when constraining μ to unity, the uncertainty on ϕ_τ is 10% larger. This can be explained by the fact, that the $H \to \tau\tau$ signal is scaled by a factor of 1.27 on average in case of an unconstrained μ, as can be seen from Fig. 8.21(c). Increasing the signal by $\approx 30\%$ should lead to a reduction of the uncertainty of the CP-mixing angle of about $\sqrt{1.3} \approx 1.1$. Hence, the 10% lower uncertainty coincides with the 10% higher signal strength for an unconstrained μ.

However, since the experimentally determined $H \to \tau\tau$ signal strength suffers from a large uncertainty,

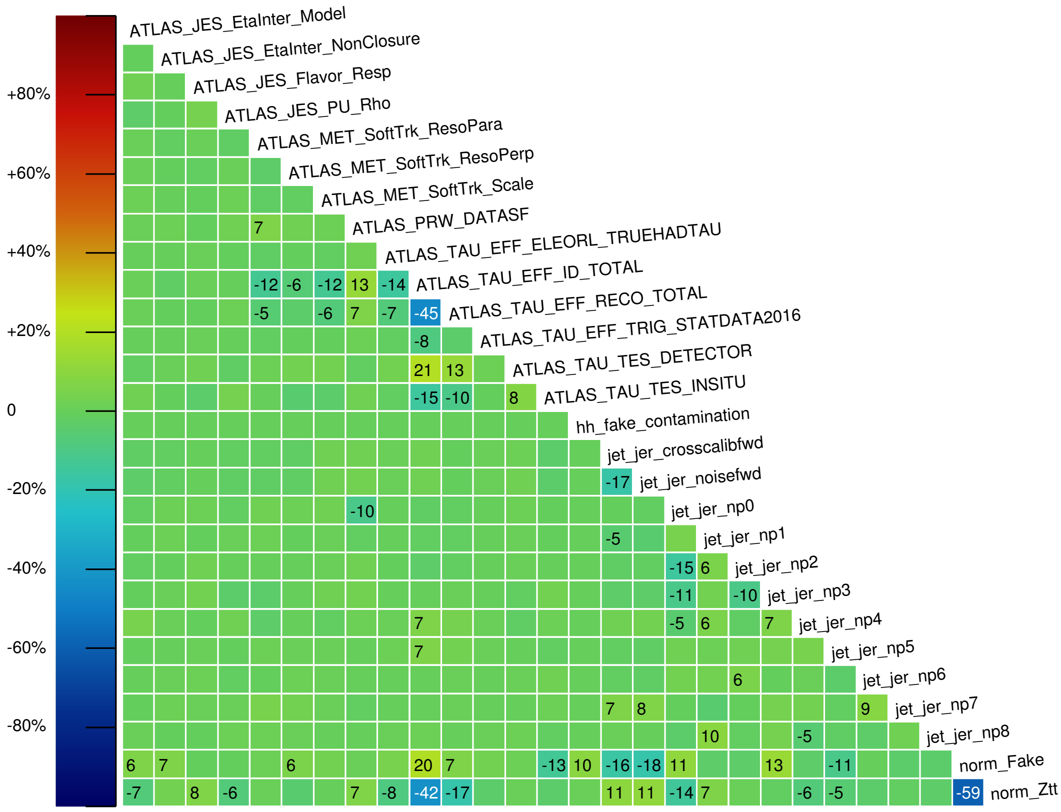

Figure 8.16: Correlation matrix of all NPs with correlations $\geq 5\%$ after the fit to Asimov data.

it is constrained to the SM value in the final measurement of the CP-mixing angle. The normalisations of the $H \to \tau\tau$ signal (μ), the $Z \to \tau\tau$ background (r_Z) and, the QCD background (r_{QCD}) are quoted in Table 8.3 for the fit to the CP-even SM $H \to \tau\tau$ sample ($\phi_\tau = 0^\circ$) and a pure CP-odd sample ($\phi_\tau = 90^\circ$). The difference between the two mixing angles is small and the measured signal and background normalisations are compatible with each other for the independent fits to different mixing angles in all cases.

NF	$\phi_\tau = 0$	$\phi_\tau = 90$
r_{QCD}	1.319 ± 0.154	1.327 ± 0.156
r_Z	1.048 ± 0.072	1.052 ± 0.071
μ	1.0	1.0

(a) μ constrained to unity

NF	$\phi_\tau = 0$	$\phi_\tau = 90$
r_{QCD}	1.321 ± 0.135	1.330 ± 0.134
r_Z	1.019 ± 0.032	1.020 ± 0.032
μ	1.270 ± 0.452	1.177 ± 0.447

(b) unconstrained μ

Table 8.3: $Z \to \tau\tau$ and QCD normalisations for different mixing angles determined from the fit to data with a constrained (a) and an unconstrained (b) $H \to \tau\tau$ signal strength μ.

Figure 8.22 shows the negative log-likelihood curve that results from the fit including statistical and

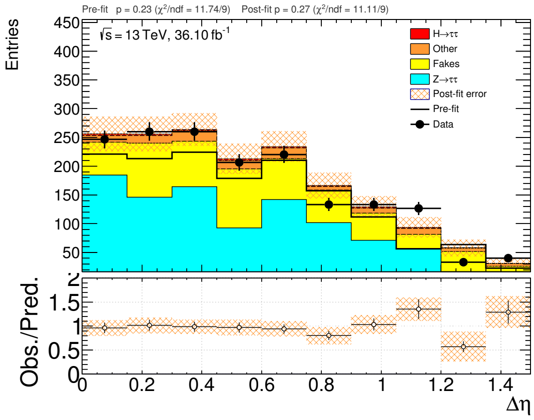

(a) VBF CR

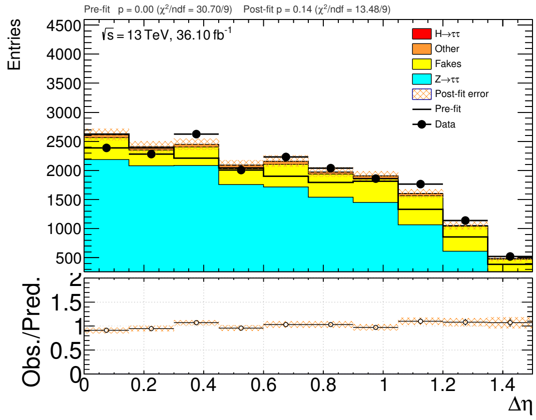

(b) boosted low-p_{T} CR

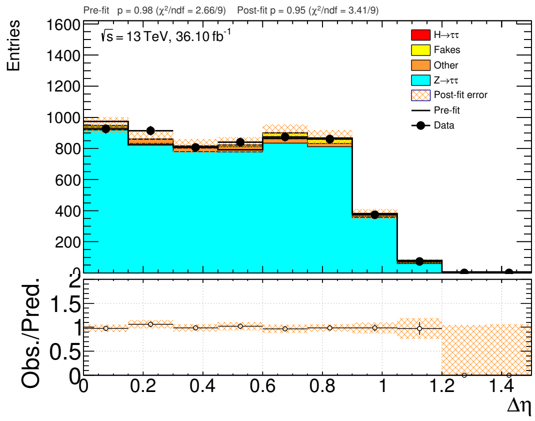

(c) boosted high-p_{T} CR

Figure 8.17: Post-fit $\delta\eta$ distributions in the control regions after the fit to data with a luminosity of $\mathcal{L} \approx 36.1\,\mathrm{fb}^{-1}$ at a CMS energy of $\sqrt{s} = 13\,\mathrm{TeV}$. The black points in the lower plot indicate the ratio of data to the prediction. The statistical uncertainty on the data is indicated by the grey band labelled *Data stat. error*.

systematic uncertainties with μ set to unity. The observed $H \to \tau\tau$ CP-mixing angle in the $36.1\,\mathrm{fb}^{-1}$ of data from 2015+2016 is

$$\phi_\tau = \left(10^{+40}_{-35}\right)^\circ .$$

The uncertainty on the CP-mixing angle is determined from the half width of the ΔNLL curve at 0.5. Consequently, the width of the observed ΔNLL curve (Fig. 8.22) is only about 60% of the width of the expected one (Fig. 8.13). Within the accuracy of the measurement, the observed CP-mixing angle is compatible with the SM-only hypothesis of a pure CP-even Higgs boson. From this measurement, a CP-mixing angle $\phi_\tau > 50^\circ$ and $\phi_\tau < 25^\circ$ can be excluded at 68% CL.

Again, the confidence level at which the hypothesis of a pure CP-odd nature of the Higgs boson can be excluded, is calculated according to Section 8.1. To this end, the ΔNLL value at $\phi_\tau = 90^\circ$ is inferred from the distribution in Fig. 8.21: $\Delta\mathrm{NLL}(\phi_\tau = 90^\circ) \approx 1.25$. The p-value for the corresponding $\chi^2 = 2 \times \Delta\mathrm{NLL}(\phi_\tau = 90^\circ) = 2.5$ is calculated using ROOT [148]. Consequently, the pure CP-odd hypothesis can be excluded at a confidence level of $1 - P(2.5, 1) \approx 89\%$.

For completeness, also the ΔNLL distribution using an unconstrained $H \to \tau\tau$ signal strength μ and

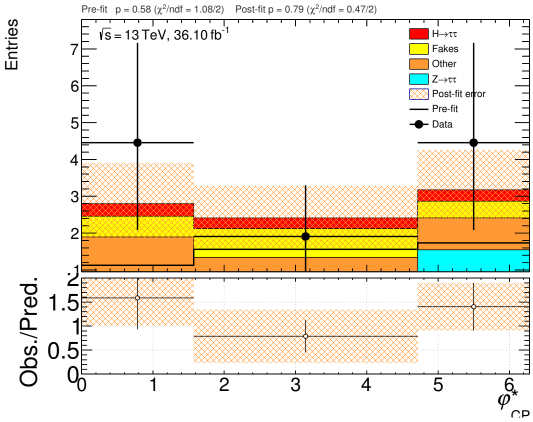

(a) IP-IP

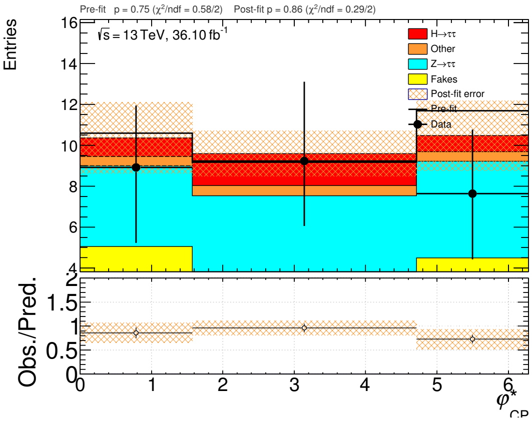

(b) IP-ρ

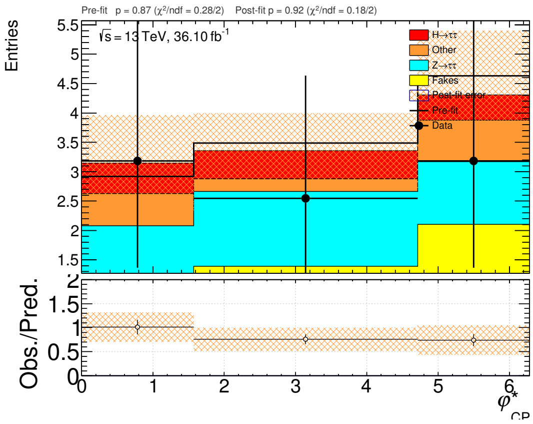

(c) $\rho - \rho$ (high $Y_+ Y_-$)

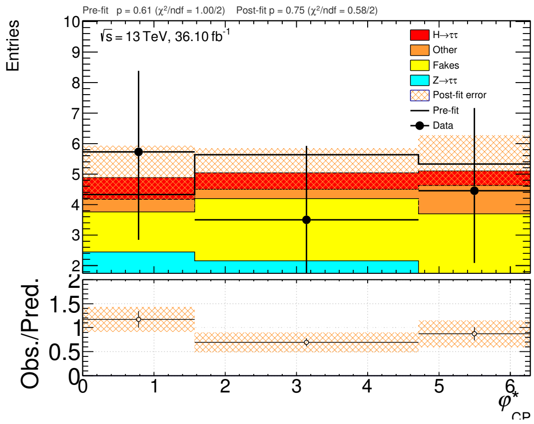

(d) $\rho - \rho$ (low $Y_+ Y_-$)

Figure 8.18: Post-fit φ^*_{CP} distributions in the vbf signal regions after the fit to data with a luminosity of $\mathcal{L} \approx 36.1$ fb^{-1} at a CMS energy of $\sqrt{s} = 13$ TeV.

including all systematic uncertainties is determined in Fig. G.8. Thereby, a $H \to \tau\tau$ signal strength of $\mu = 1.270 \pm 0.452$ was measured testing the SM $H \to \tau\tau$ signal hypothesis, which is compatible with the SM prediction of $\mu = 1.0$ when considering the statistical uncertainties. The resulting ΔNLL curve (see Fig. G.8) is very similar to the one resulting from the fit with μ being set to unity (Fig. 8.22). The variation of the best-fit μ as a function of the CP-mixing angle ϕ_τ is higher, if systematic uncertainties are included.

In order to visualise the total sensitivity on the $H \to \tau\tau$ CP-mixing angle, the φ^*_{CP} distributions in all signal regions are summed up and combined in a single φ^*_{CP} distribution. As signal, two alternative hypotheses of a pure CP-even and a pure CP-odd $H \to \tau\tau$ prediction are sketched in Fig. 8.23(a). Since the different signal regions allow to constrain the CP-nature of the Higgs boson with different strength, it makes sense to combine them with a region-specific weight. This weight is calculated as the inverse squared of the width of the ΔNLL curve that results from a separate fit to the individual region. The likelihood curves for the separate fits and the calculated weights are summarised in Appendix G. The weighted combined φ^*_{CP} distribution is displayed in Fig. 8.23(a). This plot indicates that the data agree with the background plus CP-even $H \to \tau\tau$ signal within the statistical and systematic uncertainties.

In Fig. 8.23(b), again the weighted combined φ^*_{CP} distribution is plotted. However, in this plot, all

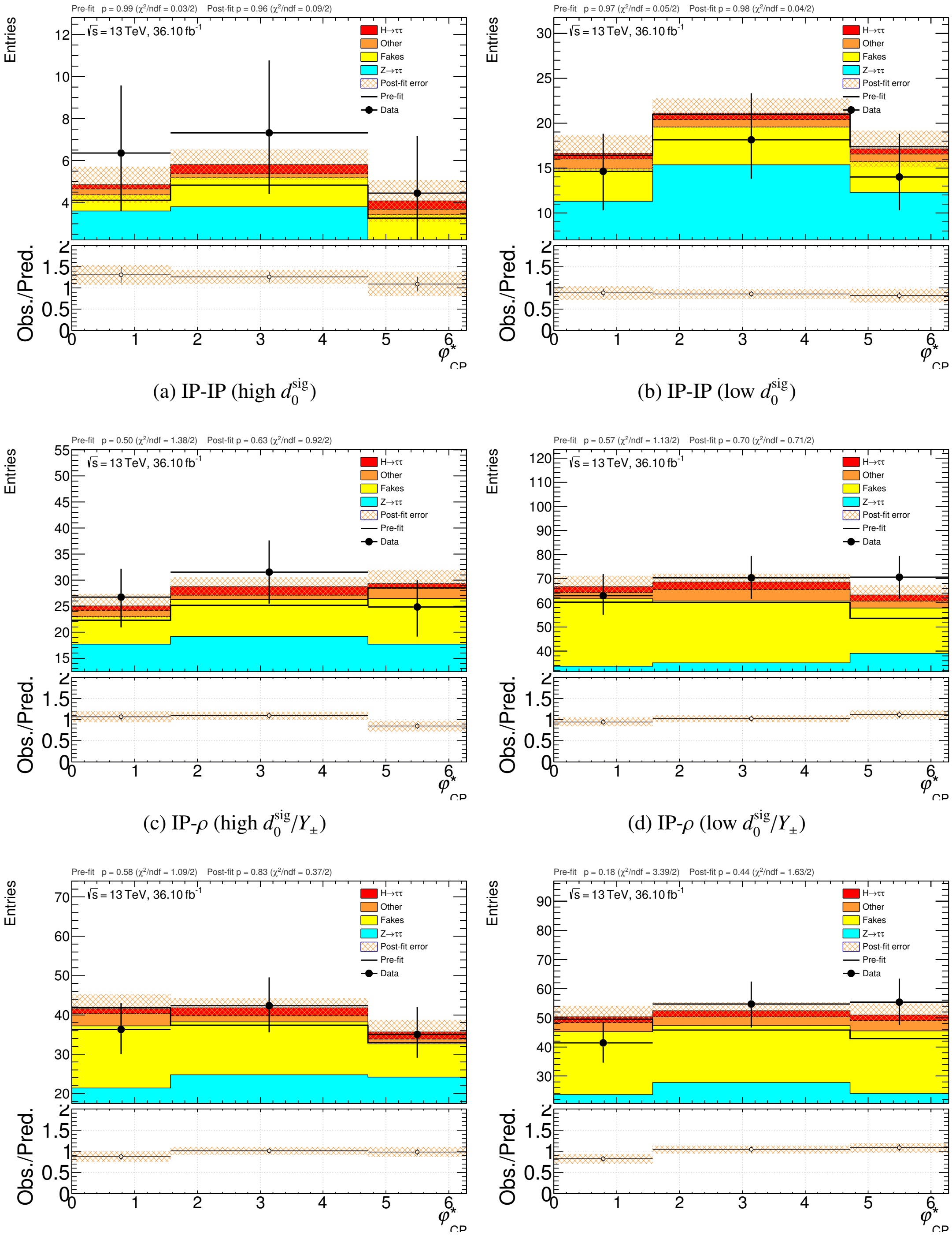

(a) IP-IP (high d_0^{sig})

(b) IP-IP (low d_0^{sig})

(c) IP-ρ (high $d_0^{\mathrm{sig}}/Y_\pm$)

(d) IP-ρ (low $d_0^{\mathrm{sig}}/Y_\pm$)

(e) $\rho-\rho$ (high Y_+Y_-)

(f) $\rho-\rho$ (low Y_+Y_-)

Figure 8.19: Post-fit φ^*_{CP} distributions in the boosted low-p_T signal regions after the fit to data with a luminosity of $\mathcal{L} \approx 36.1\,\mathrm{fb}^{-1}$ at a CMS energy of $\sqrt{s} = 13\,\mathrm{TeV}$.

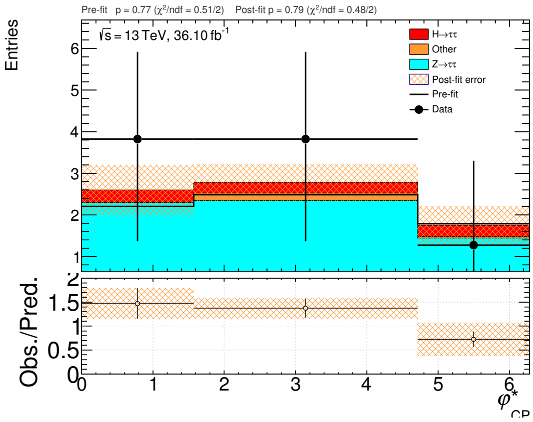

(a) IP-IP (high d_0^{sig})

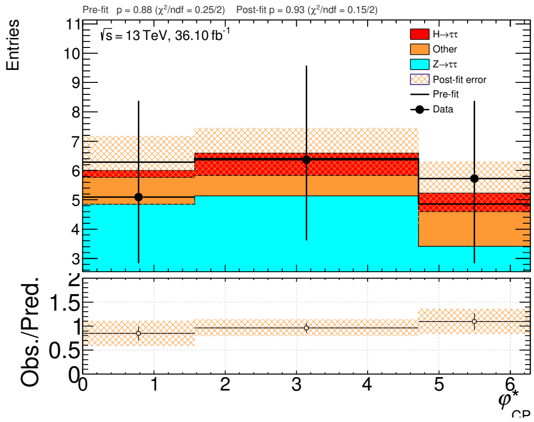

(b) IP-IP (low d_0^{sig})

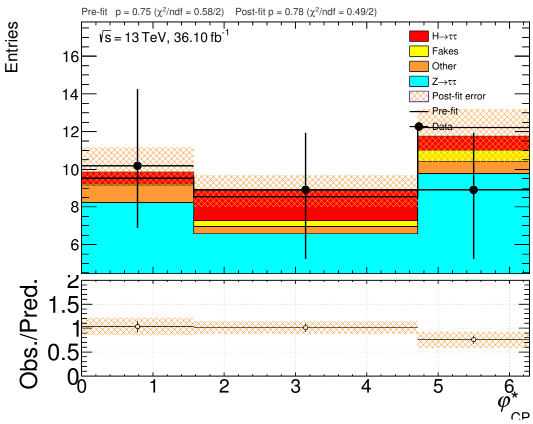

(c) IP-ρ (high $d_0^{\mathrm{sig}}/Y_\pm$)

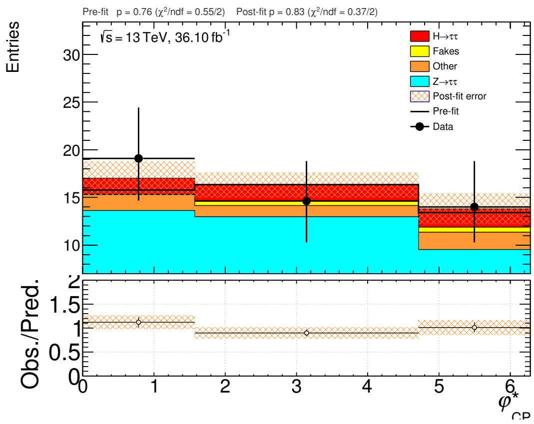

(d) IP-ρ (low $d_0^{\mathrm{sig}}/Y_\pm$)

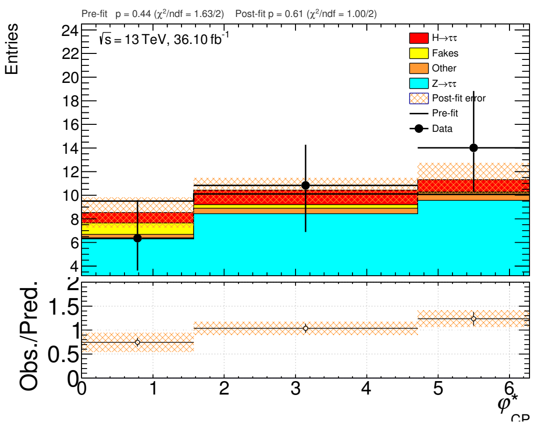

(e) $\rho-\rho$ (high Y_+Y_-)

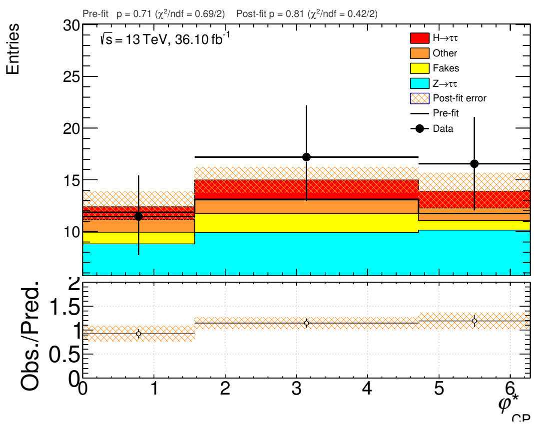

(f) $\rho-\rho$ (low Y_+Y_-)

Figure 8.20: Post-fit φ^*_{CP} distributions in the boosted high-p_{T} signal regions after the fit to data with a luminosity of $\mathcal{L} \approx 36.1\ \mathrm{fb}^{-1}$ at a CMS energy of $\sqrt{s} = 13$ TeV.

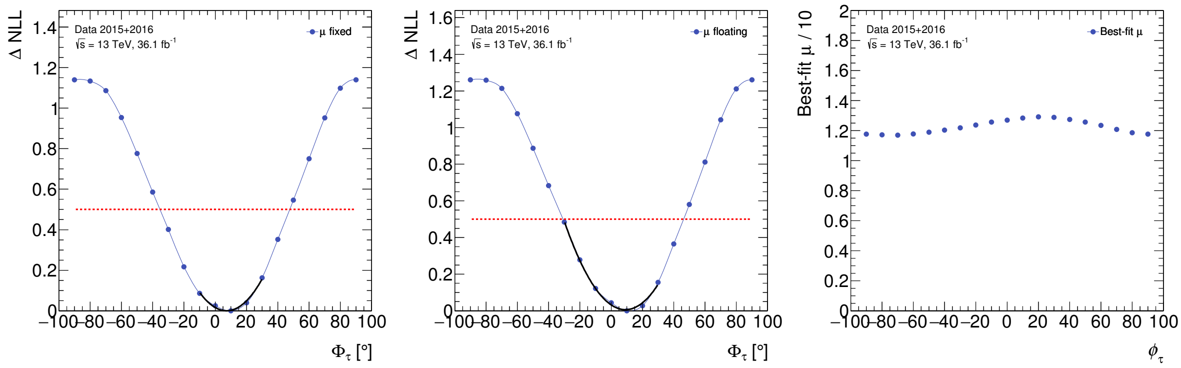

(a) ΔNLL curve (μ constrained) (b) ΔNLL curve (μ unconstrained) (c) best-fit μ

Figure 8.21: ΔNLL curve for the fit to φ^*_{CP} combining all decay modes using data with the $H \to \tau\tau$ signal strength μ constrained to unity (a) and an unconstrained μ (b). The best-fit μ distribution is shown in (c).

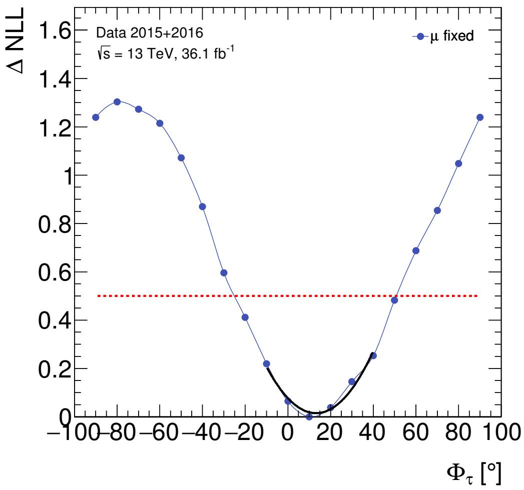

Figure 8.22: ΔNLL curve for the fit to φ^*_{CP} combining all decay modes using data with a constant $H \to \tau\tau$ signal strength μ including systematic and statistical uncertainties.

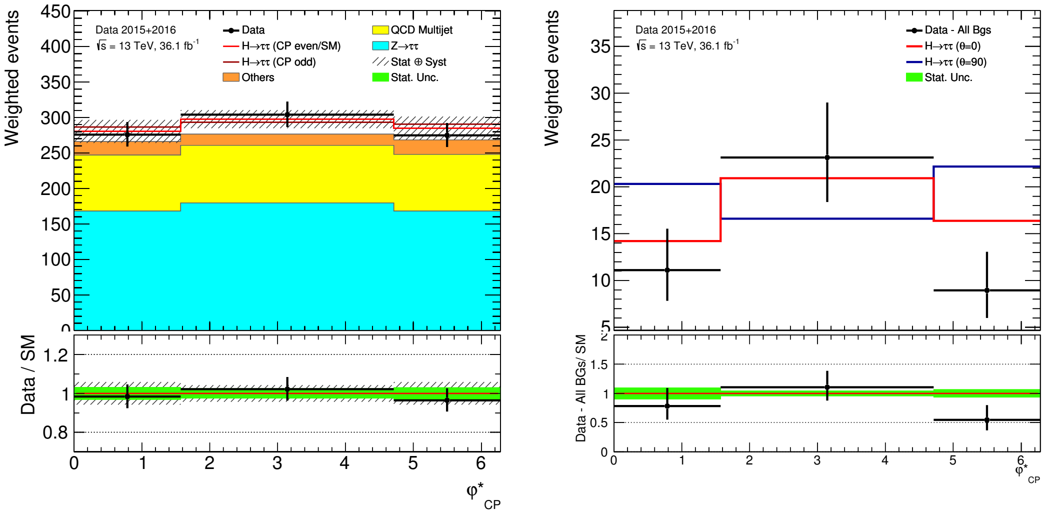

(a) data vs. prediction (b) background-subtracted data vs. $H \to \tau\tau$ signal

Figure 8.23: Combined φ^*_{CP} plot before (a) and after (b) subtracting all background histograms from the data. For comparison, the pure CP-even and CP-odd $H \to \tau\tau$ signal hypotheses are indicated as red (or blue) lines. The lower plots shows the ratio of the (background-subtracted) data to the SM hypothesis.

backgrounds are subtracted from the data. This way, the background-subtracted data points can be directly compared with the different mixing angle hypothesis in the signal templates. As examples, a pure CP-even SM prediction and a hypothetical pure CP-odd BSM signal expectation are sketched. The lower plot shows the background-subtracted data compared to the pure CP-even SM hypothesis. Figure 8.23(b) shows a good agreement between the data and the CP-even SM hypothesis when considering the statistical uncertainties.

8.7.3 Constraints on the nuisance parameters

The pull distributions of the NPs for all systematic uncertainties included in the fit for the $\phi_\tau = 0^\circ$ CP-mixing angle hypothesis are displayed in Fig. 8.24. Figure 8.24 indicates that the strongest constraints are obtained for the NPs related to the jet energy resolution (*jet_jer_np0-8*). The *jet_jer_np0* parameter obtains the strongest constraint, as it was the case for the fit to Asimov data. Some of the NPs related to the Jet energy scale and resolution show a pull which deviates from zero. All observations are consistent with the results presented in the $H \to \tau\tau$ cross section measurement [138], where also the *jet_jer* and τ-ID NPs were pulled in the fit to data. Since the complexity of the fit and the measured observables differ between the two measurement, it is expected that not exactly the same NPs will be constrained or pulled in both measurements. However, the fact that the same type of systematics is constrained and pulled shows the consistency of the two measurements analysing $H \to \tau\tau$ events in similar signal regions.

Of note, the fitting strategy applied in this thesis implements individual fits for each mixing-angle hypothesis. Hence, in principle, the systematic uncertainties and their pulls could differ for each CP mixing angle. However, neither the central values, nor the constraints on the included systematic uncertainties change significantly when fitting the CP-odd mixing angle hypothesis with respect to the CP-even one, as can be seen from Fig. G.9. The correlations $\geq 5\%$ between the different NPs are plotted in Fig. 8.25. All significant correlations (i.e larger 30%) between different NPs agree with the physics

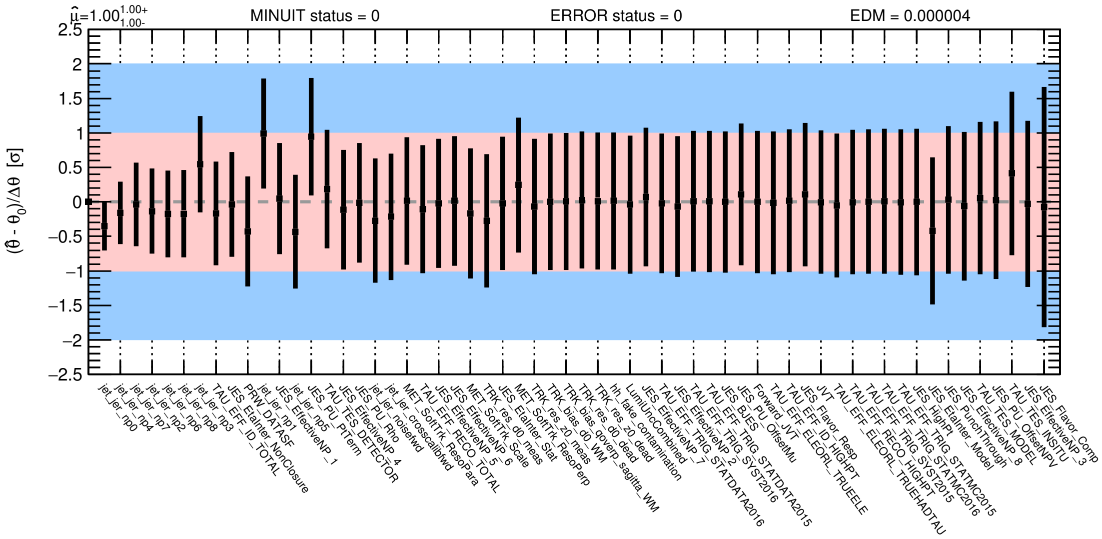

Figure 8.24: Pull distribution of all NPs included in the fit ordered by their constraint for $\phi_\tau = 0°$.

expectation, since the properties related to the respective NPs are anyway correlated.

8.7.4 Luminosity extrapolation

To predict the potential of the method in future applications to more LHC data, the current φ^*_{CP} distributions are scaled to a luminosity of $\mathcal{L} \approx 140\,\mathrm{fb}^{-1}$ corresponding to the full Run-2 dataset and to $\mathcal{L} \approx 3\,000\,\mathrm{fb}^{-1}$ corresponding to the amount of data that is expected from a high-luminosity LHC. Figure 8.26 shows the resulting ΔNLL curves from a fit to Asimov data for the current dataset and for the two datasets obtained by extrapolating the luminosity to $\mathcal{L} \approx 140\,\mathrm{fb}^{-1}$ and $\mathcal{L} \approx 3\,000\,\mathrm{fb}^{-1}$. The accuracy on the CP-mixing angle is determined from half the width of the ΔNLL curve at ΔNLL = 0.5 for all three cases. This highlights that using the full Run-2 dataset would allow to determine the Higgs CP-mixing angle with an one sigma uncertainty of ±42°. Compared to this, the recent ATLAS measurement in $t\bar{t}H$ production (see Section 2.4.3) using $139\,\mathrm{fb}^{-1}$ of ATLAS data excludes a mixing angle larger than 43 at 95% CL[8]. Even though the constraint from the $t\bar{t}H$ analysis is stricter, the expected exclusion limit presented in this thesis is model-independent and uses a pure CP-odd observable. The latter has the advantage that it is sensitive also to the coupling of the CP-odd Higgs boson predicted e.g. by the MSSM or any 2HDM. Therefore, the method used in this thesis is also sensitive to a mixing of the Higgs CP-even and CP-odd CP eigenstates predicted by these models. The CP mixing might remain undetected in CP measurements based on Higgs boson couplings to vector bosons, and also the current ttH CP measurements might be less sensitive to it due to model-dependent cancellations between CP effects and other variations of relative rates of different production mechanisms.

Exploiting an even larger dataset, as it is expected from the high-luminosity LHC, it might be possible to determine the mixing angle with an accuracy of about ±13° as indicated by Fig. 8.26 (c).

Figure 8.27 shows the combined φ^*_{CP} plot using background-subtracted Asimov data generated from a pure CP-even signal and scaled to luminosities of $140\,\mathrm{fb}^{-1}$ and $3\,000\,\mathrm{fb}^{-1}$. In all three distributions, the black points indicate the background-subtracted Asimov data scaled to the respective luminosities. The error bars indicate the statistical uncertainties. In Fig. 8.27(c) a minimal difference between the Asimov data and the CP-even $H \to \tau\tau$ signal distribution visible. This originates from rounding errors in the fit, which processes data always as integer value and thus, information is lost during the conversion to

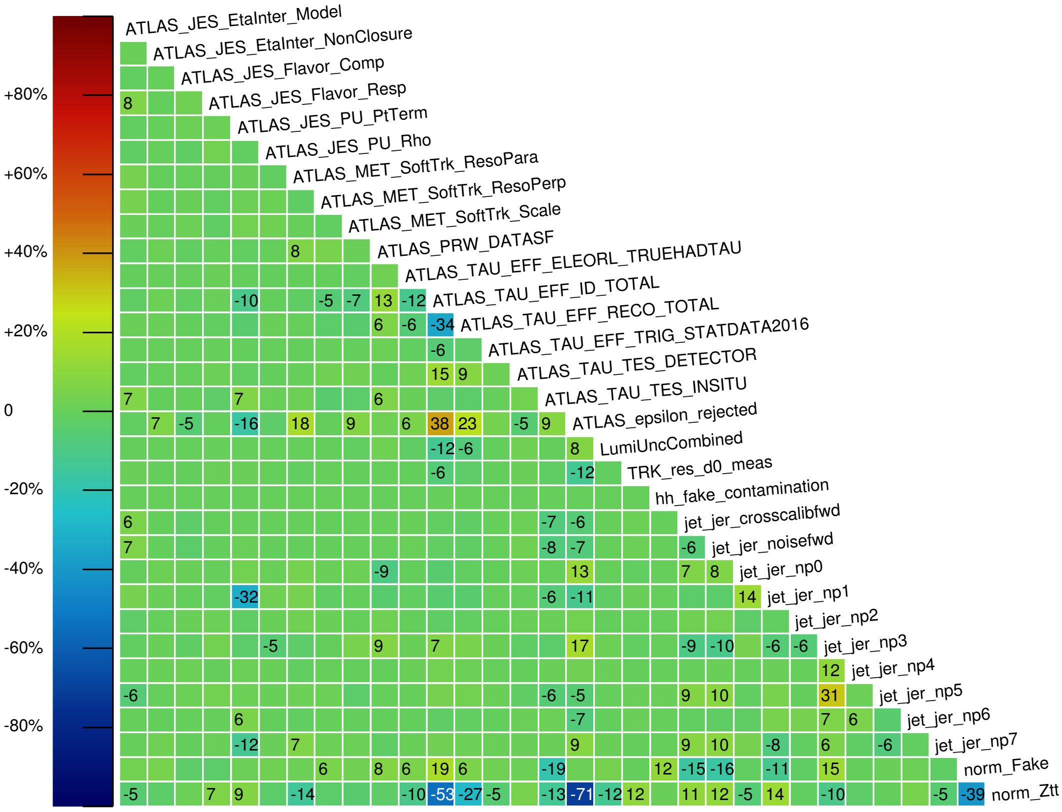

Figure 8.25: Correlation matrix of all NPs with correlations ≥ 5%.

integers: the nominal histogram corresponding to a luminosity of $\mathcal{L} = 36.1\,\text{fb}^{-1}$ is scaled by a factor of 140/36.1 and 3000/36.1. Next, the number of events in Asimov data in each bin is rounded and in turn, especially for high numbers of signal events, such as $3\,000\,\text{fb}^{-1}$, differences due to rounding become visible. However, this does not impact the fit performance, nor the outcome of the luminosity extrapolation studies. The expected separation between a pure CP-even and CP-odd $H \to \tau\tau$ signal increases significantly with increasing luminosities, such that a much more accurate measurement of the Higgs CP-mixing angle will be possible with larger datasets. In the $36.1\,\text{fb}^{-1}$ of data used in this thesis, only ≈ 5 events are used for the distinction between a CP-even and CP-odd $H \to \tau\tau$ signal distribution. However, e.g. in case of the high-luminosity LHC, a difference of ≈ 250 events is expected, using the same binning in φ^*_{CP} and the same fit setup.

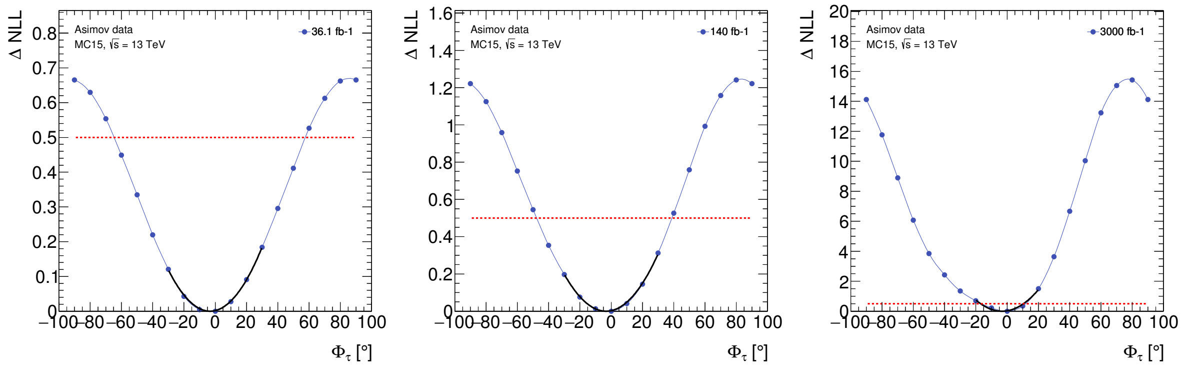

(a) $\mathcal{L}$ = 36.1 fb^{-1} (b) $\mathcal{L}$ = 140 fb^{-1} (c) $\mathcal{L}$ = 3 000 fb^{-1}

Figure 8.26: ΔNLL vs. Higgs CP-mixing angle for the current dataset as well as extrapolated to 140 fb^{-1} and 3 000 fb^{-1}. In all distributions a parabola is fitted to the innermost region. The width at 0.5 indicates the one sigma standard deviation from the centre.

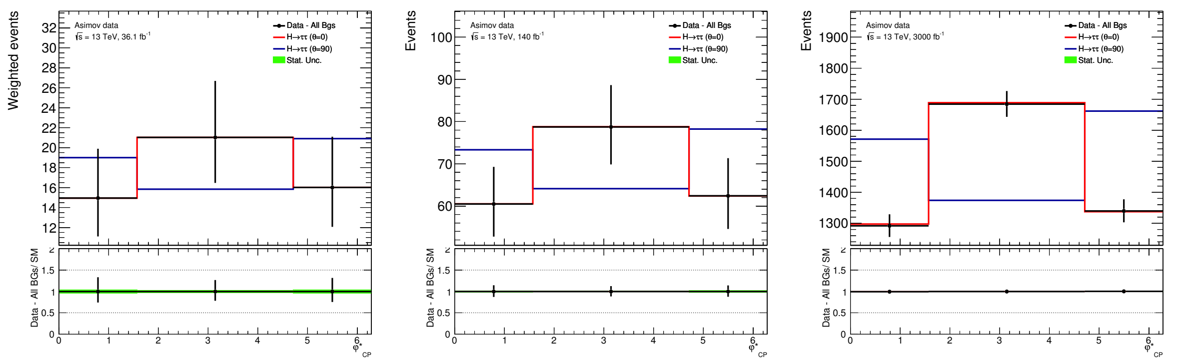

(a) $\mathcal{L}$ = 36.1 fb^{-1} (b) $\mathcal{L}$ = 140 fb^{-1} (c) $\mathcal{L}$ = 3 000 fb^{-1}

Figure 8.27: Combined φ^*_{CP} plot using background subtracted Asimov data generated from a pure CP-even $H \to \tau\tau$ signal sample for 36.1 fb^{-1} and extrapolated to luminosities of $\approx$ 140 fb^{-1} and 3 000 fb^{-1}. For comparison, a pure CP-even and a pure CP-odd $H \to \tau\tau$ signal hypothesis are indicated as red and blue lines. The lower plot shows the ratio of the background subtracted Asimov data to the SM (i.e. pure CP-even) hypothesis, respectively.

CHAPTER 9

Conclusion

After the discovery of the Higgs boson in 2012 at the LHC by the ATLAS and CMS collaborations, many of its properties have been measured to be consistent with the SM expectations. In this dissertation the Higgs bosons behaviour under Charge-Parity (CP) transformation is studied in its decay to two τ leptons using 36.1 fb^{-1} of LHC data recorded by the ATLAS experiment in 2015 and 2016 at a centre-of-mass energy of 13 TeV. For this measurement, events are selected in which both of the τ leptons decay hadronically. The τ particle-flow method used to reconstruct hadronically decaying τ leptons offers a precise τ decay-mode classification, an improved reconstruction of the τ leptons four momentum, and a reconstruction of the π^0 four vector. This allows to reconstruct the τ decay-planes either from the π^0 track IP in 1p0n τ decays or from the visible decay products of the ρ meson in 1p1n τ decays and facilitates the direct measurement of the CP-mixing angle from angular distributions between these τ decay planes. During the work of this dissertation, the two methods to determine the CP-mixing angle have been implemented for the data analysis in ATLAS, validated and applied to $\mathcal{L} = 36.1$ fb^{-1} of ATLAS data collected in 2015 and 2016.

A separate validation of the CP sensitive observables in $Z \to \tau\tau$ decays has been performed. In principle, the φ^*_{CP} shape of $Z \to \tau\tau$ events is flat. However, selecting appropriate regions in phase space, it is possible to restore the dependence of the decay plane angle on the transverse τ spin correlations. A shape similar to the shape expected for $H \to \tau\tau$ decays is observed. To this end, the simulation of transverse τ spin correlations in the $Z \to \tau\tau$ MC samples is analysed in a separate Z-validation region and the reconstruction of the CP sensitive variables is validated in a comparison with theoretical calculations. A measurement of the CP-sensitive variables was only performed to the 2015 dataset with a luminosity of 3.21 fb^{-1}. The 2016 dataset could not be used, due to the requirement of additional jets in the event made at trigger level, removing any φ^*_{CP} dependence in $Z \to \tau\tau$ events is eliminated. Hence, the measurement of φ^*_{CP} in $Z \to \tau\tau$ events can not be used to calibrate the methods for the application in $H \to \tau\tau$ events. However, a good modelling of the CP sensitive variables is observed in the Z-validation region using the 2015 dataset.

The $H \to \tau\tau$ CP-mixing angle ϕ_τ is measured in a binned maximum likelihood on the combined 2015+2016 dataset. The fit is performed in various signal and control regions. The signal regions are similar to the ones used in the $H \to \tau\tau$ cross section measurement [12]. However, in this analysis only events with two 1-prong τ leptons are used and the signal regions are divided further based on the reconstructed τ decay mode combination. The fit procedure is validated using pseudo data and various configurations are compared to find the optimal setup. In the measurement to data, a CP-mixing angle of

$$\phi_\tau = \left(10^{+40}_{-35}\right)^\circ$$

is observed. With this result, a CP-mixing angle larger 50° and smaller −25° can be excluded at 68% CL. Additionally, the confidence level at which a CP-odd Higgs boson can be excluded is calculated and amounts to 89% for the 2015+2016 data. Due to the small number of events in the signal regions, the uncertainty on the measured angle is still large. The results are compatible with the SM expectation of a purely CP-even Higgs boson, predicting a mixing angle of $\phi_\tau = 0$ within the statistical and systematic uncertainties and hence, no sign of new physics has been observed. The derived constraint on the CP-mixing angle is not as strict as the one derived in the recent ATLAS measurement in $t\bar{t}H$ production using 139 fb^{-1} of ATLAS data, which excludes a mixing angle larger than 43 at 95% CL [8]. However, the expected exclusion limit presented in this thesis is model independent and uses a pure CP-odd observable. Thus, it is sensitive, also to the coupling of the CP-odd Higgs boson predicted e.g. by the MSSM or any 2HDM and to a mixing of the Higgs CP-even and CP-odd CP eigenstates predicted by these models. The CP mixing might remain undetected in CP measurements based on Higgs boson couplings to vector bosons and the recent $t\bar{t}H$ CP measurements might be less sensitive to it due e.g. to model dependent cancellations between CP effects.

The maximum likelihood fit is also repeated with an unconstrained $H \to \tau\tau$ signal strength μ and the results agree within the systematic and statistical uncertainties with the SM expectation. The pull distributions and the correlation matrix for all nuisance parameters included in the likelihood fit are in accordance with the results presented in the $H \to \tau\tau$ cross section measurement [138].

Finally, an extrapolation to higher luminosities is performed assuming the full run 2 ATLAS dataset with a luminosity of 140 fb^{-1}, the expected uncertainty on the CP-mixing angle is 42°, which improves the expected uncertainty of 60° from the 36.1 fb^{-1} of data analysed in this thesis significantly. With a luminosity of 3 000 fb^{-1} as it is expected to be delivered by the high-luminosity LHC for example, it would be possible to determine the CP-mixing angle with an accuracy of ±13.

Bibliography

[1] ATLAS Collaboration, *Observation of a new particle in the search for the Standard Model Higgs boson with the ATLAS detector at the LHC*, Phys. Lett. **B716** (2012) 1, arXiv: `1207.7214 [hep-ex]` (cit. on pp. 1, 12, 26).

[2] CMS Collaboration, *Observation of a new boson at a mass of 125 GeV with the CMS experiment at the LHC*, Phys. Lett. **B716** (2012) 30, arXiv: `1207.7235 [hep-ex]` (cit. on pp. 1, 12, 26).

[3] A. D. Sakharov, *Violation of CP Invariance, c Asymmetry, and Baryon Asymmetry of the Universe*, Pisma Zh. Eksp. Teor. Fiz. **5** (1967) 32, [Usp. Fiz. Nauk161,61(1991)] (cit. on pp. 1, 17).

[4] A. D. Sakharov, *Baryonic Asymmetry of the Universe*, Sov. Phys. JETP **49** (1979) 594, [Zh. Eksp. Teor. Fiz.76,1172(1979)] (cit. on pp. 1, 17).

[5] A. D. Sakharov, *Baryon asymmetry of the universe*, Sov. Phys. Usp. **34** (1991) 417 (cit. on pp. 1, 17).

[6] A. M. Sirunyan et al., *Measurements of the Higgs boson width and anomalous HVV couplings from on-shell and off-shell production in the four-lepton final state*, Phys. Rev. D **99** (11 2019) 112003, URL: `https://link.aps.org/doi/10.1103/PhysRevD.99.112003` (cit. on pp. 1, 21, 22).

[7] G. Aad et al., *Higgs boson production cross-section measurements and their EFT interpretation in the 4ℓ decay channel at $\sqrt{s}$ = 13 TeV with the ATLAS detector*, (2020), arXiv: `2004.03447 [hep-ex]` (cit. on pp. 1, 22).

[8] G. Aad et al., *Study of the CP properties of the interaction of the Higgs boson with top quarks using top quark associated production of the Higgs boson and its decay into two photons with the ATLAS detector at the LHC*, (2020), arXiv: `2004.04545 [hep-ex]` (cit. on pp. 1, 22, 145, 150).

[9] A. M. Sirunyan et al., *Measurements of $t\bar{t}H$ production and the CP structure of the Yukawa interaction between the Higgs boson and top quark in the diphoton decay channel*, (2020), arXiv: `2003.10866 [hep-ex]` (cit. on pp. 1, 23).

[10] G. Aad et al., *Test of CP invariance in vector-boson fusion production of the Higgs boson in the $H \to \tau\tau$ channel in proton−proton collisions at $\sqrt{s}$ = 13 TeV with the ATLAS detector*, Phys. Lett. B **805** (2020) 135426, arXiv: `2002.05315 [hep-ex]` (cit. on pp. 1, 22).

[11] A. M. Sirunyan et al., *Constraints on anomalous HVV couplings from the production of Higgs bosons decaying to τ lepton pairs*, Phys. Rev. D **100** (11 2019) 112002, URL: `https://link.aps.org/doi/10.1103/PhysRevD.100.112002` (cit. on pp. 1, 22).

[12] M. Aaboud et al., *Cross-section measurements of the Higgs boson decaying into a pair of τ-leptons in proton-proton collisions at* $\sqrt{s} = 13\,\text{TeV}$ *with the ATLAS detector*, Physical Review D **99** (2019), ISSN: 2470-0029, URL: `http://dx.doi.org/10.1103/PhysRevD.99.072001` (cit. on pp. 2, 75, 149).

[13] *Standard Model infographic developed at the cern webfest*, 2012, URL: `https://cds.cern.ch/record/1473657` (cit. on p. 4).

[14] C. D. Anderson, *The Positive Electron*, Phys. Rev. **43** (6 1933) 491, URL: `https://link.aps.org/doi/10.1103/PhysRev.43.491` (cit. on p. 3).

[15] S. Tomonaga, *On a Relativistically Invariant Formulation of the Quantum Theory of Wave Fields**, Progress of Theoretical Physics **1** (1946) 27, ISSN: 0033-068X, eprint: `https://academic.oup.com/ptp/article-pdf/1/2/27/24027031/1-2-27.pdf`, URL: `https://doi.org/10.1143/PTP.1.27` (cit. on p. 4).

[16] J. Schwinger, *Quantum Electrodynamics. I. A Covariant Formulation*, Phys. Rev. **74** (10 1948) 1439, URL: `https://link.aps.org/doi/10.1103/PhysRev.74.1439` (cit. on p. 4).

[17] R. P. Feynman, *Relativistic Cut-Off for Quantum Electrodynamics*, Phys. Rev. **74** (10 1948) 1430, URL: `https://link.aps.org/doi/10.1103/PhysRev.74.1430` (cit. on p. 4).

[18] E. Fermi, *Versuch einer Theorie der β-Strahlen. I*, Zeitschrift für Physik **88** (1934) 161, ISSN: 0044-3328, URL: `https://doi.org/10.1007/BF01351864` (cit. on pp. 5, 6).

[19] S. L. Glashow, *The renormalizability of vector meson interactions*, Nucl. Phys. **10** (1959) 107 (cit. on pp. 5, 6).

[20] A. Salam and J. C. Ward, *Weak and electromagnetic interactions*, Il Nuovo Cimento **11** (1959) 568 (cit. on pp. 5, 6).

[21] S. Weinberg, *A Model of Leptons*, Phys. Rev. Lett. **19** (21 1967) 1264, URL: `https://link.aps.org/doi/10.1103/PhysRevLett.19.1264` (cit. on pp. 5, 6).

[22] H. Fritzsch, M. Gell-Mann and H. Leutwyler, *Advantages of the color octet gluon picture*, Physics Letters B **47** (1973) 365, ISSN: 0370-2693, URL: `http://www.sciencedirect.com/science/article/pii/0370269373906254` (cit. on p. 5).

[23] D. J. Gross and F. Wilczek, *Ultraviolet Behavior of Non-Abelian Gauge Theories*, Phys. Rev. Lett. **30** (26 1973) 1343, URL: `https://link.aps.org/doi/10.1103/PhysRevLett.30.1343` (cit. on p. 5).

[24] H. D. Politzer, *Reliable Perturbative Results for Strong Interactions?*, Phys. Rev. Lett. **30** (26 1973) 1346, URL: `https://link.aps.org/doi/10.1103/PhysRevLett.30.1346` (cit. on p. 5).

[25] M. Thomson, *Modern Particle Physics*, Cambridge University Press, 2013 (cit. on pp. 6, 8, 11, 13, 16).

[26] M. Tanabashi et al., *Review of Particle Physics*, Phys. Rev. D **98** (3 2018) 030001, URL: `https://link.aps.org/doi/10.1103/PhysRevD.98.030001` (cit. on pp. 6, 8, 9, 12–14, 17–21).

[27] F. J. Hasert et al., *Observation of Neutrino Like Interactions Without Muon Or Electron in the Gargamelle Neutrino Experiment*, Phys. Lett. **46B** (1973) 138, [,5.15(1973)] (cit. on p. 6).

[28] F. J. Hasert et al., *Observation of Neutrino Like Interactions without Muon or Electron in the Gargamelle Neutrino Experiment*, Nucl. Phys. **B73** (1974) 1 (cit. on p. 6).

[29] *Nobel Prize for Physics, 1979*, CERN Courier **19** (1979) 395, URL: `http://cds.cern.ch/record/1730492` (cit. on p. 6).

[30] G. Arnison et al., *Experimental Observation of Isolated Large Transverse Energy Electrons with Associated Missing Energy at s**(1/2) = 540-GeV*, Phys. Lett. **122B** (1983) 103, [,611(1983)] (cit. on p. 6).

[31] M. Banner et al., *Observation of Single Isolated Electrons of High Transverse Momentum in Events with Missing Transverse Energy at the CERN anti-p p Collider*, Phys. Lett. **122B** (1983) 476, [,7.45(1983)] (cit. on p. 6).

[32] G. Arnison et al., *Experimental Observation of Lepton Pairs of Invariant Mass Around 95-GeV/c**2 at the CERN SPS Collider*, Phys. Lett. **126B** (1983) 398, [,7.55(1983)] (cit. on p. 6).

[33] P. Bagnaia et al., *Evidence for Z0 → e^+e^- at the CERN anti-p p Collider*, Phys. Lett. **129B** (1983) 130, [,7.69(1983)] (cit. on p. 6).

[34] F. Englert and R. Brout, *Broken Symmetry and the Mass of Gauge Vector Mesons*, Phys. Rev. Lett. **13** (9 1964) 321, URL: `https://link.aps.org/doi/10.1103/PhysRevLett.13.321` (cit. on p. 9).

[35] P. W. Higgs, *Broken symmetries, massless particles and gauge fields*, Phys. Lett. **12** (1964) 132 (cit. on p. 9).

[36] P. W. Higgs, *Broken Symmetries and the Masses of Gauge Bosons*, Phys. Rev. Lett. **13** (1964) 508, [,160(1964)] (cit. on p. 9).

[37] M. Aaboud et al., *Cross-section measurements of the Higgs boson decaying into a pair of τ-leptons in proton-proton collisions at $\sqrt{s} = 13$ TeV with the ATLAS detector*, Phys. Rev. **D99** (2019) 072001, arXiv: `1811.08856 [hep-ex]` (cit. on p. 12).

[38] A. M. Sirunyan et al., *Observation of the Higgs boson decay to a pair of τ leptons with the CMS detector*, Phys. Lett. **B779** (2018) 283, arXiv: `1708.00373 [hep-ex]` (cit. on p. 12).

[39] M. L. Perl et al., *Evidence for Anomalous Lepton Production in $e^+ - e^-$ Annihilation*, Phys. Rev. Lett. **35** (22 1975) 1489, URL: `https://link.aps.org/doi/10.1103/PhysRevLett.35.1489` (cit. on p. 13).

[40] F. Zwicky, *Die Rotverschiebung von extragalaktischen Nebeln*, Helvetica Physica Acta **6** (1933) 110, URL: `https://ui.adsabs.harvard.edu/abs/1933AcHPh...6..110Z` (cit. on p. 15).

[41] A. Del Popolo, "Non-baryonic dark matter in cosmology", *American Institute of Physics Conference Series*, ed. by L. A. Uren-López, R. Becerril-Bárcenas and R. Linares-Romero, vol. 1548, American Institute of Physics Conference Series, 2013 2 (cit. on p. 15).

[42] N. Aghanim et al., *Planck 2018 results. VI. Cosmological parameters*, (2018), arXiv: `1807.06209 [astro-ph.CO]` (cit. on p. 15).

[43] C. CSÁKI, *THE MINIMAL SUPERSYMMETRIC STANDARD MODEL*, Modern Physics Letters A **11** (1996) 599, ISSN: 1793-6632, URL: `http://dx.doi.org/10.1142/S021773239600062X` (cit. on p. 15).

[44] G. Branco et al., *Theory and phenomenology of two-Higgs-doublet models*, Physics Reports **516** (2012) 1, ISSN: 0370-1573, URL: `http://dx.doi.org/10.1016/j.physrep.2012.02.002` (cit. on p. 15).

[45] *Dark matter summary plots*, tech. rep. ATL-PHYS-PUB-2019-030, CERN, 2019, URL: `https://cds.cern.ch/record/2684864` (cit. on p. 15).

[46] E. Aprile et al., *Search for Light Dark Matter Interactions Enhanced by the Migdal effect or Bremsstrahlung in XENON1T*, Phys. Rev. Lett. **123** (2019) 241803, arXiv: `1907.12771 [hep-ex]` (cit. on p. 15).

[47] X. Ren et al., *Constraining Dark Matter Models with a Light Mediator at the PandaX-II Experiment*, Phys. Rev. Lett. **121** (2 2018) 021304, URL: `https://link.aps.org/doi/10.1103/PhysRevLett.121.021304` (cit. on p. 15).

[48] L. Roszkowski, E. M. Sessolo and S. Trojanowski, *WIMP dark matter candidates and searches—current status and future prospects*, Rept. Prog. Phys. **81** (2018) 066201, arXiv: `1707.06277 [hep-ph]` (cit. on p. 15).

[49] H. Georgi and S. L. Glashow, *Unity of All Elementary-Particle Forces*, Phys. Rev. Lett. **32** (8 1974) 438, URL: `https://link.aps.org/doi/10.1103/PhysRevLett.32.438` (cit. on p. 16).

[50] P. A. R. Ade et al., *Planck 2015 results. XIII. Cosmological parameters*, Astron. Astrophys. **594** (2016) A13, arXiv: `1502.01589 [astro-ph.CO]` (cit. on p. 17).

[51] M. Kobayashi and T. Maskawa, *CP-Violation in the Renormalizable Theory of Weak Interaction*, Progress of Theoretical Physics **49** (1973) 652, ISSN: 0033-068X, eprint: `https://academic.oup.com/ptp/article-pdf/49/2/652/5257692/49-2-652.pdf`, URL: `https://doi.org/10.1143/PTP.49.652` (cit. on p. 17).

[52] N. Cabibbo, *Unitary Symmetry and Leptonic Decays*, Phys. Rev. Lett. **10** (12 1963) 531, URL: `https://link.aps.org/doi/10.1103/PhysRevLett.10.531` (cit. on p. 17).

[53] J. H. Christenson et al., *Evidence for the 2π Decay of the K_2^0 Meson*, Phys. Rev. Lett. **13** (4 1964) 138, URL: `https://link.aps.org/doi/10.1103/PhysRevLett.13.138` (cit. on p. 17).

[54] B. Aubert et al., *Observation of CP Violation in the B^0 Meson System*, Phys. Rev. Lett. **87** (9 2001) 091801, URL: `https://link.aps.org/doi/10.1103/PhysRevLett.87.091801` (cit. on p. 17).

[55] K. Abe et al., *Observation of Large CP Violation in the Neutral B Meson System*, Phys. Rev. Lett. **87** (9 2001) 091802, URL: `https://link.aps.org/doi/10.1103/PhysRevLett.87.091802` (cit. on p. 17).

[56] H. Burkhardt et al., *First Evidence for Direct CP Violation*, Phys. Lett. **B206** (1988) 169 (cit. on p. 17).

[57] V. Fanti et al., *A New measurement of direct CP violation in two pion decays of the neutral kaon*, Phys. Lett. **B465** (1999) 335, arXiv: `hep-ex/9909022 [hep-ex]` (cit. on p. 17).

[58] A. Alavi-Harati et al., *Observation of Direct CP Violation in $K_{S,L} \to \pi\pi$ Decays*, Phys. Rev. Lett. **83** (1 1999) 22, URL: `https://link.aps.org/doi/10.1103/PhysRevLett.83.22` (cit. on p. 17).

[59] B. Aubert et al., *Direct CP Violating Asymmetry in $B^0 \to K^+\pi^-$ Decays*, Phys. Rev. Lett. **93** (13 2004) 131801, URL: `https://link.aps.org/doi/10.1103/PhysRevLett.93.131801` (cit. on p. 17).

[60] K. Abe et al., "Improved measurements of direct CP violation in B —> K+ pi-, K+ pi0 and pi+ pi0 decays", *Proceedings, 2005 Europhysics Conference on High Energy Physics (EPS-HEP 2005): Lisbon, Portugal, July 21-27, 2005*, 2005, arXiv: `hep-ex/0507045 [hep-ex]` (cit. on p. 17).

[61] A. Poluektov et al., *Evidence for direct CP violation in the decay B->D(*)K, D->KsPi+Pi- and measurement of the CKM phase phi3*, Phys. Rev. **D81** (2010) 112002, arXiv: `1003.3360 [hep-ex]` (cit. on p. 17).

[62] P. del Amo Sanchez et al., *Measurement of CP observables in $B^\pm \to D_{CP}K^\pm$ decays and constraints on the CKM angle γ*, Phys. Rev. D **82** (7 2010) 072004, URL: `https://link.aps.org/doi/10.1103/PhysRevD.82.072004` (cit. on p. 17).

[63] R. Aaij et al., *Observation of CP violation in $B^\pm \to DK^\pm$ decays*, Phys. Lett. **B712** (2012) 203, [Erratum: Phys. Lett.B713,351(2012)], arXiv: `1203.3662 [hep-ex]` (cit. on p. 17).

[64] R. Aaij et al., *Evidence for CP Violation in Time-Integrated $D^0 \to h^-h^+$ Decay Rates*, Phys. Rev. Lett. **108** (11 2012) 111602, URL: `https://link.aps.org/doi/10.1103/PhysRevLett.108.111602` (cit. on p. 17).

[65] T. Aaltonen et al., *Measurements of Direct CP Violating Asymmetries in Charmless Decays of Strange Bottom Mesons and Bottom Baryons*, Phys. Rev. Lett. **106** (18 2011) 181802, URL: `https://link.aps.org/doi/10.1103/PhysRevLett.106.181802` (cit. on p. 17).

[66] Z. Maki, M. Nakagawa and S. Sakata, *Remarks on the Unified Model of Elementary Particles*, Progress of Theoretical Physics **28** (1962) 870, ISSN: 0033-068X, eprint: `https://academic.oup.com/ptp/article-pdf/28/5/870/5258750/28-5-870.pdf`, URL: `https://doi.org/10.1143/PTP.28.870` (cit. on p. 17).

[67] K. Abe et al., *Constraint on the matter–antimatter symmetry-violating phase in neutrino oscillations*, Nature **580** (2020) 339, arXiv: `1910.03887 [hep-ex]` (cit. on p. 17).

[68] E. Accomando et al., *Workshop on CP Studies and Non-Standard Higgs Physics*, (2006), arXiv: `hep-ph/0608079 [hep-ph]` (cit. on p. 17).

[69] G. Aad et al., *Study of the spin and parity of the Higgs boson in diboson decays with the ATLAS detector*, Eur. Phys. J. **C75** (2015) 476, [Erratum: Eur. Phys. J.C76,no.3,152(2016)], arXiv: `1506.05669 [hep-ex]` (cit. on pp. 21, 22).

[70] CMS Collaboration, *Constraints on the spin-parity and anomalous HVV couplings of the Higgs boson in proton collisions at 7 and 8 TeV*, Phys. Rev. **D92** (2015) 012004, arXiv: `1411.3441 [hep-ex]` (cit. on p. 21).

[71] A. Djouadi and G. Moreau, *The couplings of the Higgs boson and its CP properties from fits of the signal strengths and their ratios at the 7+8 TeV LHC*, The European Physical Journal C **73** (2013), ISSN: 1434-6052, URL: http://dx.doi.org/10.1140/epjc/s10052-013-2512-9 (cit. on pp. 23, 24).

[72] C. communication group, URL: multimedia-gallery.web.cern.ch/multimedia-gallery/Brochures.aspx (cit. on p. 25).

[73] J. Pequenao, "Computer generated image of the whole ATLAS detector", 2008, URL: https://cds.cern.ch/record/1095924 (cit. on p. 26).

[74] G. Aad et al., *The ATLAS Experiment at the CERN Large Hadron Collider*, JINST **3** (2008) S08003 (cit. on pp. 28–30).

[75] G. Aad et al., *The ATLAS Experiment at the CERN Large Hadron Collider*, JINST **3** (2008) S08003. 437 p, Also published by CERN Geneva in 2010, URL: https://cds.cern.ch/record/1129811 (cit. on pp. 28–30, 34).

[76] M. Capeans et al., *ATLAS Insertable B-Layer Technical Design Report*, (2010) (cit. on p. 28).

[77] A. La Rosa, *The ATLAS Insertable B-Layer: from construction to operation*, JINST **11** (2016) C12036, arXiv: 1610.01994 [physics.ins-det] (cit. on p. 28).

[78] M. Aaboud et al., *Performance of the ATLAS Trigger System in 2015*, Eur. Phys. J. **C77** (2017) 317, arXiv: 1611.09661 [hep-ex] (cit. on p. 30).

[79] D. Caforio, *Luminosity Measurement Using Cherenkov Integrating Detector (LUCID) in ATLAS*, (2008), URL: https://cds.cern.ch/record/1742259 (cit. on p. 30).

[80] H. Bertelsen et al., *Operation of the upgraded ATLAS Central Trigger Processor during the LHC Run 2*, Journal of Instrumentation **11** (2016) C02020, URL: https://doi.org/10.1088%2F1748-0221%2F11%2F02%2Fc02020 (cit. on p. 31).

[81] URL: https://twiki.cern.ch/twiki/bin/view/AtlasPublic/TriggerOperationPublicResults#L1_Trigger_Rate (cit. on p. 31).

[82] M. Aaboud et al., *Electron reconstruction and identification in the ATLAS experiment using the 2015 and 2016 LHC proton-proton collision data at* $\sqrt{s}$ *= 13 TeV*, Eur. Phys. J. **C79** (2019) 639, arXiv: 1902.04655 [physics.ins-det] (cit. on p. 31).

[83] M. Aaboud et al., *Measurement of the photon identification efficiencies with the ATLAS detector using LHC Run-1 data*, Eur. Phys. J. **C76** (2016) 666, arXiv: 1606.01813 [hep-ex] (cit. on p. 31).

[84] W. Lampl et al., *Calorimeter Clustering Algorithms: Description and Performance*, tech. rep. ATL-LARG-PUB-2008-002. ATL-COM-LARG-2008-003, CERN, 2008, URL: https://cds.cern.ch/record/1099735 (cit. on p. 31).

[85] M. Aaboud et al., *Measurement of the photon identification efficiencies with the ATLAS detector using LHC Run 2 data collected in 2015 and 2016*, The European Physical Journal C **79** (2019) 205, ISSN: 1434-6052, URL: https://doi.org/10.1140/epjc/s10052-019-6650-6 (cit. on p. 32).

[86] A. Salzburger, *Optimisation of the ATLAS Track Reconstruction Software for Run-2*, tech. rep. ATL-SOFT-PROC-2015-056. 7, CERN, 2015, URL: https://cds.cern.ch/record/2018442 (cit. on p. 32).

[87] G. Aad et al., *Muon reconstruction performance of the ATLAS detector in proton–proton collision data at $\sqrt{s}$ =13 TeV*, Eur. Phys. J. **C76** (2016) 292, arXiv: `1603.05598 [hep-ex]` (cit. on p. 32).

[88] M. Cacciari, G. P. Salam and G. Soyez, *The Anti-k(t) jet clustering algorithm*, JHEP **0804** (2008) 063, arXiv: `0802.1189 [hep-ph]` (cit. on p. 33).

[89] ATLAS Collaboration, *Topological cell clustering in the ATLAS calorimeters and its performance in LHC Run 1*, Submitted to Eur. Phys. J. C (2016), arXiv: `1603.02934 [hep-ex]` (cit. on p. 34).

[90] *Reconstruction, Energy Calibration, and Identification of Hadronically Decaying Tau Leptons in the ATLAS Experiment for Run-2 of the LHC*, tech. rep. ATL-PHYS-PUB-2015-045, CERN, 2015, URL: `https://cds.cern.ch/record/2064383` (cit. on pp. 34, 122).

[91] *Measurement of the tau lepton reconstruction and identification performance in the ATLAS experiment using pp collisions at* $\sqrt{s}$ = 13 TeV, tech. rep. ATLAS-CONF-2017-029, CERN, 2017, URL: `https://cds.cern.ch/record/2261772` (cit. on pp. 34, 39, 120, 122).

[92] G. Aad et al., *Reconstruction of hadronic decay products of tau leptons with the ATLAS experiment*, Eur. Phys. J. **C76** (2016) 295, arXiv: `1512.05955 [hep-ex]` (cit. on pp. 35–38).

[93] M. Aaboud et al., *Performance of missing transverse momentum reconstruction with the ATLAS detector using proton-proton collisions at $\sqrt{s}$ = 13 TeV*, Eur. Phys. J. **C78** (2018) 903, arXiv: `1802.08168 [hep-ex]` (cit. on pp. 35, 123).

[94] *Forward Jet Vertex Tagging: A new technique for the identification and rejection of forward pileup jets*, tech. rep. ATL-PHYS-PUB-2015-034, CERN, 2015, URL: `https://cds.cern.ch/record/2042098` (cit. on p. 35).

[95] M. Aaboud et al., *Jet reconstruction and performance using particle flow with the ATLAS Detector*, Eur. Phys. J. **C77** (2017) 466, arXiv: `1703.10485 [hep-ex]` (cit. on pp. 36, 39, 40, 43).

[96] S. Berge, W. Bernreuther and S. Kirchner, *Determination of the Higgs CP-mixing angle in the tau decay channels at the LHC including the Drell?Yan background*, Eur. Phys. J. **C74** (2014) 3164, arXiv: `1408.0798 [hep-ph]` (cit. on pp. 63–66, 70–73, 95).

[97] S. Berge, W. Bernreuther and S. Kirchner, *Prospects of constraining the Higgs boson's CP nature in the tau decay channel at the LHC*, Phys. Rev. **D92** (2015) 096012, arXiv: `1510.03850 [hep-ph]` (cit. on pp. 63, 65, 66, 68–70).

[98] S. Berge, W. Bernreuther and S. Kirchner, *Determination of the Higgs CP-mixing angle in the tau decay channels*, Nucl. Part. Phys. Proc. **273-275** (2016) 841, arXiv: `1410.6362 [hep-ph]` (cit. on p. 64).

[99] K. Desch, Z. Was and M. Worek, *Measuring the Higgs boson parity at a linear collider using the tau impact parameter and tau —> rho nu decay*, Eur. Phys. J. **C29** (2003) 491, arXiv: `hep-ph/0302046 [hep-ph]` (cit. on p. 65).

[100] G. R. Bower et al., *Measuring the Higgs boson's parity using tau —> rho nu*, Phys. Lett. **B543** (2002) 227, arXiv: `hep-ph/0204292 [hep-ph]` (cit. on pp. 65–67).

[101] Z. Was and M. Worek, *Transverse spin effects in H/A —> tau+ tau-: tau+- —> nu X+-, Monte Carlo approach*, Acta Phys. Polon. **B33** (2002) 1875, arXiv: `hep-ph/0202007 [hep-ph]` (cit. on pp. 65, 66).

[102] K. Desch et al., *Probing the CP nature of the Higgs boson at linear colliders with tau spin correlations: The Case of mixed scalar - pseudoscalar couplings*, Phys. Lett. **B579** (2004) 157, arXiv: `hep-ph/0307331 [hep-ph]` (cit. on pp. 65, 66).

[103] S. Berge and W. Bernreuther, *Determining the CP parity of Higgs bosons at the LHC in the tau to 1-prong decay channels*, Phys. Lett. **B671** (2009) 470, arXiv: `0812.1910 [hep-ph]` (cit. on pp. 65, 66).

[104] S. Berge, W. Bernreuther and J. Ziethe, *Determining the CP parity of Higgs Bosons via their τ-decay channels at the Large Hadron Collider*, Physical Review Letters **100** (2008), ISSN: 1079-7114, URL: `http://dx.doi.org/10.1103/PhysRevLett.100.171605` (cit. on p. 66).

[105] S. Berge et al., *How to pin down the CP quantum numbers of a Higgs boson in its tau decays at the LHC*, Phys. Rev. **D84** (2011) 116003, arXiv: `1108.0670 [hep-ph]` (cit. on pp. 67, 68).

[106] M. Hübner, *Effects of tau decay product reconstruction in a Higgs CP analysis with the ATLAS experiment*, unpublished, MA thesis: Mathematisch-Naturwissenschaftlichen Fakultät der Rheinischen Friedrich-Wilhelms-Universität Bonn, 2016 (cit. on pp. 69, 77).

[107] J. Dormans, *NLO QCD Corrections to Z + jet Production at the LHC*, unpublished, MA thesis: Fakultät für Mathematik, Informatik und Naturwissenschaften der RWTH Aachen, 2016 (cit. on pp. 72, 73, 81, 99).

[108] A. Elagin et al., *A New Mass Reconstruction Technique for Resonances Decaying to di-tau*, Nucl. Instrum. Meth. **A654** (2011) 481, arXiv: `1012.4686 [hep-ex]` (cit. on p. 77).

[109] T. A. Collaboration, URL: `https://twiki.cern.ch/twiki/bin/view/AtlasPublic/LuminosityPublicResultsRun2#Luminosity_summary_plots_for_AN3` (visited on 22/08/2019) (cit. on pp. 87, 89).

[110] J. Allison et al., *Recent developments in Geant4*, Nucl. Instrum. Meth. **A835** (2016) 186 (cit. on p. 88).

[111] J. Allison et al., *Geant4 developments and applications*, IEEE Trans. Nucl. Sci. **53** (2006) 270 (cit. on p. 88).

[112] S. Agostinelli et al., *GEANT4: A Simulation toolkit*, Nucl. Instrum. Meth. **A506** (2003) 250 (cit. on p. 88).

[113] T. Sjöstrand et al., *An Introduction to PYTHIA 8.2*, Comput. Phys. Commun. **191** (2015) 159, arXiv: `1410.3012 [hep-ph]` (cit. on pp. 88, 89).

[114] P. Nason, *A New method for combining NLO QCD with shower Monte Carlo algorithms*, JHEP **11** (2004) 040, arXiv: `hep-ph/0409146 [hep-ph]` (cit. on p. 89).

[115] S. Frixione, P. Nason and C. Oleari, *Matching NLO QCD computations with parton shower simulations: the POWHEG method*, Journal of High Energy Physics **2007** (2007) 070, ISSN: 1029-8479, URL: `http://dx.doi.org/10.1088/1126-6708/2007/11/070` (cit. on p. 89).

[116] S. Alioli et al., *A general framework for implementing NLO calculations in shower Monte Carlo programs: the POWHEG BOX*, Journal of High Energy Physics **2010** (2010), ISSN: 1029-8479, URL: `http://dx.doi.org/10.1007/JHEP06(2010)043` (cit. on p. 89).

[117] E. Bagnaschi et al.,
Higgs production via gluon fusion in the POWHEG approach in the SM and in the MSSM,
Journal of High Energy Physics **2012** (2012), ISSN: 1029-8479,
URL: `http://dx.doi.org/10.1007/JHEP02(2012)088` (cit. on p. 89).

[118] H.-L. Lai et al., *New parton distributions for collider physics*, Phys. Rev. **D82** (2010) 074024,
arXiv: `1007.2241 [hep-ph]` (cit. on p. 89).

[119] J. Rojo et al.,
The PDF4LHC report on PDFs and LHC data: results from Run I and preparation for Run II,
Journal of Physics G: Nuclear and Particle Physics **42** (2015) 103103, ISSN: 1361-6471,
URL: `http://dx.doi.org/10.1088/0954-3899/42/10/103103` (cit. on p. 89).

[120] T. Przedzinski, E. Richter-Was and Z. Was,
TauSpinner: a tool for simulating CP effects in $H \to \tau\tau$ decays at LHC,
Eur. Phys. J. **C74** (2014) 3177, arXiv: `1406.1647 [hep-ph]` (cit. on pp. 90, 119, 126).

[121] E. Bothmann et al., *Event Generation with SHERPA 2.2*, (2019), arXiv: `1905.09127 [hep-ph]`
(cit. on p. 95).

[122] P. Richardson, *Spin correlations in Monte Carlo simulations*, JHEP **11** (2001) 029,
arXiv: `hep-ph/0110108 [hep-ph]` (cit. on p. 95).

[123] P. Ilten, *Pythia 8: Simulating Tau-Lepton Decays*, Nucl. Part. Phys. Proc. **260** (2015) 56
(cit. on pp. 95, 100).

[124] P. Ilten, *Private communication*, 2016 (cit. on p. 95).

[125] S. Berge, *Private communication*, 2016 (cit. on pp. 95–97, 99).

[126] S. Höche et al., *Beyond Standard Model calculations with Sherpa*, Eur. Phys. J. **C75** (2015) 135,
arXiv: `1412.6478 [hep-ph]` (cit. on p. 100).

[127] P. Ilten, *Tau Decays in Pythia 8*, Nucl. Phys. Proc. Suppl. **253-255** (2014) 77,
arXiv: `1211.6730 [hep-ph]` (cit. on p. 100).

[128] *Observation of the SM scalar boson decaying to a pair of τ leptons with the CMS experiment at the LHC*, tech. rep. CMS-PAS-HIG-16-043, CERN, 2017,
URL: `http://cds.cern.ch/record/2264522` (cit. on pp. 110, 111).

[129] T. A. Collaboration, *TrigTauEmulationTool*,
URL: `https://svnweb.cern.ch/trac/atlasoff/browser/Trigger/TrigAnalysis/TrigTauAnalysis/TrigTauEmulation?order=name` (visited on 10/08/2017)
(cit. on p. 111).

[130] A. Tuna and H. Williams, *Evidence for decays of the Higgs boson to tau leptons at ATLAS*,
Presented 06 Apr 2015, PhD Thesis, 2015, URL: `https://cds.cern.ch/record/2013235`
(cit. on p. 113).

[131] S. Maeland, *Pixel detector performance and study of CP invariance in H to tau tau decays with the ATLAS detector*, 2018, URL: `https://bora.uib.no/handle/1956/18106`
(cit. on p. 117).

[132] S. P. Y. Yuen, *Analysis of the Higgs boson decay in the $H \to \tau_{had}\tau_{had}$ channel and CP properties with $\sqrt{s} = 13$ TeV collisions at the ATLAS detector*, Presented 2019, 2018,
URL: `https://cds.cern.ch/record/2648539` (cit. on p. 117).

[133] G. Cowan, *Statistical data analysis*, 1998, ISBN: 978-0-19-850156-5 (cit. on p. 117).

[134] L.-G. Xia,
Study of constraint and impact of a nuisance parameter in maximum likelihood method,
J. Phys. **G46** (2019) 085004, arXiv: `1805.03961 [physics.data-an]` (cit. on p. 118).

[135] *FitBox*,
URL: `https://gitlab.cern.ch/ATauLeptonAnalysiS/FitBox` (visited on 07/05/2020)
(cit. on p. 119).

[136] I. Antcheva et al.,
ROOT — A C++ framework for petabyte data storage, statistical analysis and visualization,
Computer Physics Communications **180** (2009) 2499, ISSN: 0010-4655,
URL: `http://dx.doi.org/10.1016/j.cpc.2009.08.005` (cit. on pp. 119, 136).

[137] K. Cranmer et al.,
HistFactory: A tool for creating statistical models for use with RooFit and RooStats, (2012)
(cit. on p. 119).

[138] A. Andreazza et al.,
Measurement of the $H \to \tau^+\tau^-$ cross-section in 13 TeV Collisions with the ATLAS Detector,
tech. rep. ATL-COM-PHYS-2017-446, CERN, 2017,
URL: `https://cds.cern.ch/record/2261605` (cit. on pp. 120, 136, 144, 150).

[139] A. Andreazza et al., *Cross-section measurement of Higgs bosons that decay to a pair of tau leptons in proton–proton collisions at $\sqrt{s} = 13$ TeV with the ATLAS detector*,
tech. rep. ATL-COM-PHYS-2018-264, CERN, 2018,
URL: `https://cds.cern.ch/record/2309974` (cit. on pp. 120, 123).

[140] A. T. working group, *2017 Tau Recommendations*, 2017, URL: `https://twiki.cern.ch/twiki/bin/view/AtlasProtected/TauRecommendationsMoriond2017` (cit. on p. 120).

[141] G. Aad et al., *Identification and energy calibration of hadronically decaying tau leptons with the ATLAS experiment in pp collisions at $\sqrt{s}$=8 TeV*, Eur. Phys. J. **C75** (2015) 303,
arXiv: `1412.7086 [hep-ex]` (cit. on p. 120).

[142] *Tagging and suppression of pileup jets with the ATLAS detector*,
tech. rep. ATLAS-CONF-2014-018, CERN, 2014,
URL: `https://cds.cern.ch/record/1700870` (cit. on p. 122).

[143] M. Aaboud et al., *Jet energy scale measurements and their systematic uncertainties in proton-proton collisions at $\sqrt{s} = 13$ TeV with the ATLAS detector*,
Phys. Rev. **D96** (2017) 072002, arXiv: `1703.09665 [hep-ex]` (cit. on p. 123).

[144] *Jet Calibration and Systematic Uncertainties for Jets Reconstructed in the ATLAS Detector at $\sqrt{s} = 13$ TeV*, tech. rep. ATL-PHYS-PUB-2015-015, CERN, 2015,
URL: `https://cds.cern.ch/record/2037613` (cit. on p. 123).

[145] M. Aaboud et al.,
Luminosity determination in pp collisions at $\sqrt{s} = 8$ TeV using the ATLAS detector at the LHC,
Eur. Phys. J. **C76** (2016) 653, arXiv: `1608.03953 [hep-ex]` (cit. on p. 123).

[146] A. T. C. group,
Tracking CP Pre-Recommendations for 2017 Winter Conferences, 2015+2016/20.7, 2017,
URL: `https://twiki.cern.ch/twiki/bin/viewauth/AtlasProtected/TrackingCPMoriond2017`
(cit. on p. 123).

[147] A. Manthei,
Studies towards constraining the CP properties of the Higgs boson in its decays to tau leptons, unpublished, MA thesis: Mathematisch-Naturwissenschaftlichen Fakultät der Rheinischen Friedrich-Wilhelms-Universität Bonn, 2019 (cit. on pp. 124, 125).

[148] R. Brun and F. Rademakers, *ROOT: An object oriented data analysis framework*, Nucl. Instrum. Meth. A **389** (1997) 81, ed. by M. Werlen and D. Perret-Gallix (cit. on p. 139).

APPENDIX A

Reconstruction of the 3D impact parameter

This chapter describes the approximation of the 3D impact parameter from the measured 2D point of closest approach of the charged pion track, the primary vertex and the charged pion 4 momentum.

The pion track is parametrised to approximate the 3D impact parameter. The pion track is approximated with a straight-line using the vector pointing to the 2D point of closest approach as support-vector $\vec{b}$ and the pion momentum vector as directional vector.

$$\vec{b} = \begin{pmatrix} |d_0| \cos \Phi_{xy} \\ |d_0| \sin \Phi_{xy} \\ z0 \end{pmatrix} \tag{A.1}$$

The support-vector can be obtained from the 2D point of closest approach, as indicated in Eq. (A.1), whereas $\Phi_{xy} = \Phi^{\pi} + \frac{\pi}{2} \cdot \mathrm{sign}(d0)$ denotes the angle of this vector in the xy-plane. The parametrisation of the pion track is then given as

$$\Pi : \vec{b} + k \cdot \vec{P_{\pi}},$$

and the distance between the pion track and the primary vertex can be written as

$$\vec{d} = \Pi - \vec{PV} = \vec{b} + k \cdot \vec{P_{\pi}} - \vec{PV}.$$

To determine the the 3D point of closest approach from the measured quantities, the value of k needs to be determined, for which the distance between the pion track and the primary vertex is minimal. This is the case if $\vec{d}$ and $\vec{P_{\pi}}$ are orthogonal, i.e. if

$$\begin{aligned} \vec{d} \cdot \vec{P_{\pi}} &= 0 \\ \Leftrightarrow \vec{b} \cdot \vec{P_{\pi}} + k \cdot \vec{P_{\pi}} \cdot \vec{P_{\pi}} - \vec{PV} \cdot \vec{P_{\pi}} &= 0 \\ \Leftrightarrow k = \frac{\left(\vec{PV} - \vec{b}\right) \cdot \vec{P_{\pi}}}{\vec{P_{\pi}} \cdot \vec{P_{\pi}}} &= \frac{\left(\vec{PV} - \vec{b}\right) \cdot \vec{P_{\pi}}}{\left|\vec{P_{\pi}}\right|^2} \end{aligned}$$

Once $\tilde{k}$ is determined, the impact parameter can be calculated as

$$\vec{n} = \vec{PV} + \vec{d}(\tilde{k}) = \vec{b} + \tilde{k} \cdot \vec{P_{\pi}}$$

This vector is normalised and referenced as $\hat{\vec{n}} = \frac{\vec{n}}{|\vec{n}|}$ in the following.

Since the sensitivity is much larger in the $\pi^{+} \pi^{-}$-ZMF than in the laboratory frame, a Lorentz boost from the laboratory frame into this frame is performed. However, only the 3d impact parameter is measured in the laboratory frame. Thus, the true IP in the $\pi^+\ \pi^-$-ZMF can not be determined with this method. Instead, space-like 4d impact parameter vectors

$$\hat{n} = \begin{pmatrix} 0 \\ \hat{\vec{n}} \end{pmatrix}$$

are defined and then boosted in the $\pi^+\ \pi^-$ frame, defined as:

$$\hat{n^*} = \begin{pmatrix} n_0^* \\ \vec{n^*} \end{pmatrix}$$

Similarly, the pion momentum four vector $\vec{P_\pi}$ is boosted in the $(\pi^+\pi^-)$ rest-frame. The boosted vector is referenced as $\vec{P_\pi}^*$.

To calculate the angle between the two τ decay-planes, the component of n^* orthogonal to the charged pion vector needs to be determined. It is given as:

$$\begin{aligned} \vec{n}^*_\perp &= \vec{n}^* - \vec{n}^*_{\|} \\ &= \vec{n}^* - \frac{\vec{n}^* \cdot \vec{P_\pi}^*}{|\vec{P_\pi}^*|^2} \cdot \vec{P_\pi}^*. \end{aligned}$$

APPENDIX **B**

Asymmetry dependence on the event selection requirements in $H \to \tau\tau$ events

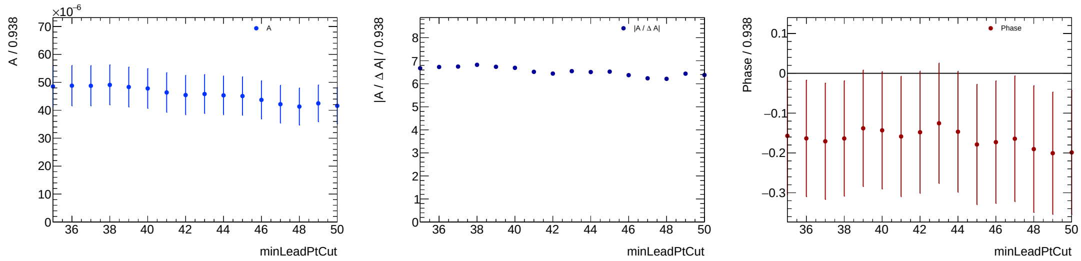

(a) Variation of the minimum leading p_{T} cut

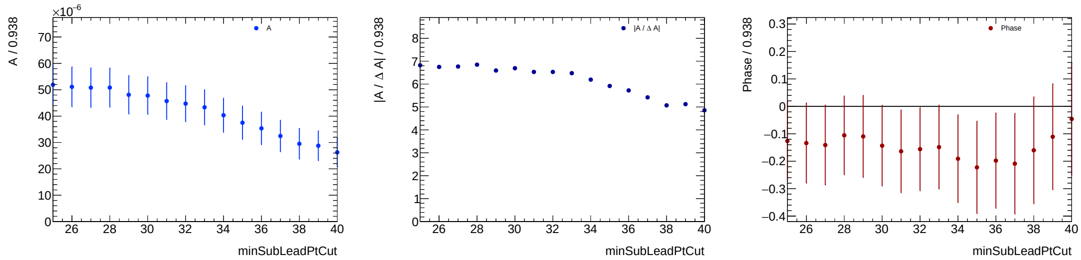

(b) Variation of the minimum subleading p_{T} cut

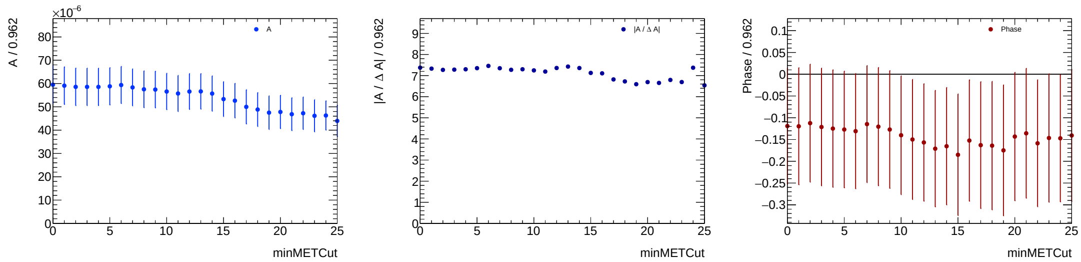

(c) Variation of the minimum $E_{\mathrm{T}}^{\mathrm{miss}}$ cut

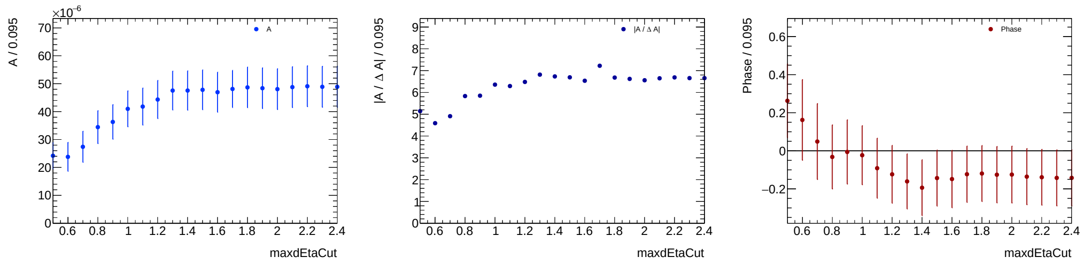

(d) Variation of the maximum $\Delta\eta_{\tau\tau}$ cut

Figure B.1: Impact of the leading and subleading τ p_{T}, $E_{\mathrm{T}}^{\mathrm{miss}}$ and $\Delta\eta_{\tau\tau}$ requirements on the amplitude and phase of the φ^{*}_{CP} distribution in $H \to \tau\tau$ events.

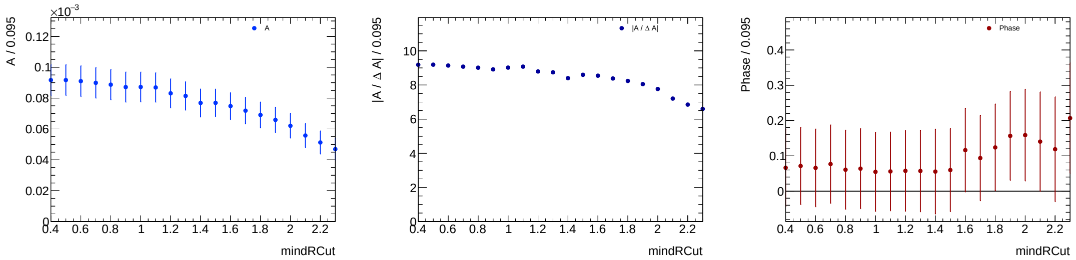

(a) Variation of the minimum $\Delta R_{\tau\tau}$ cut

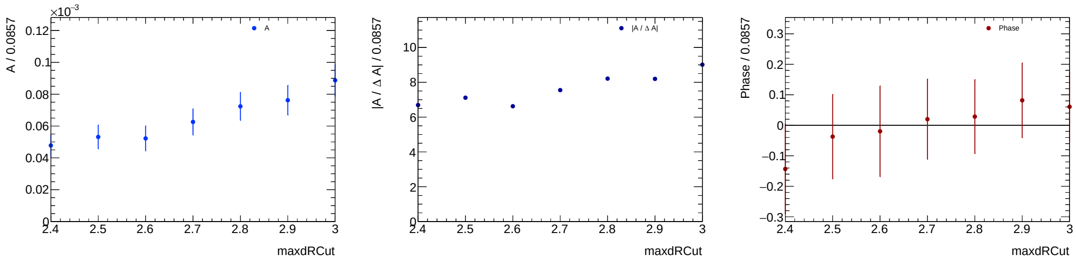

(b) Variation of the maximum $\Delta R_{\tau\tau}$ cut

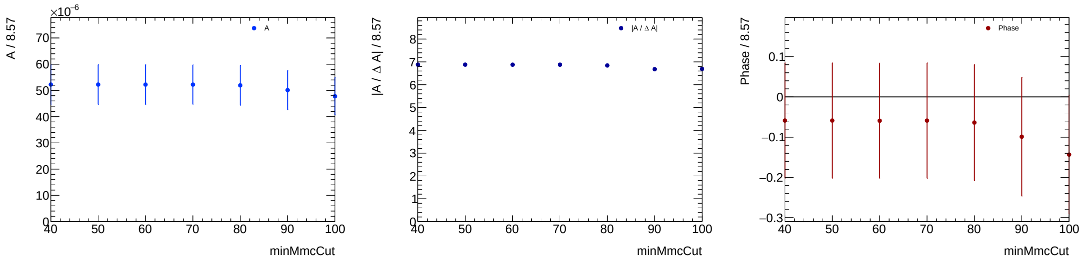

(c) Variation of the minimum mmc mass cut

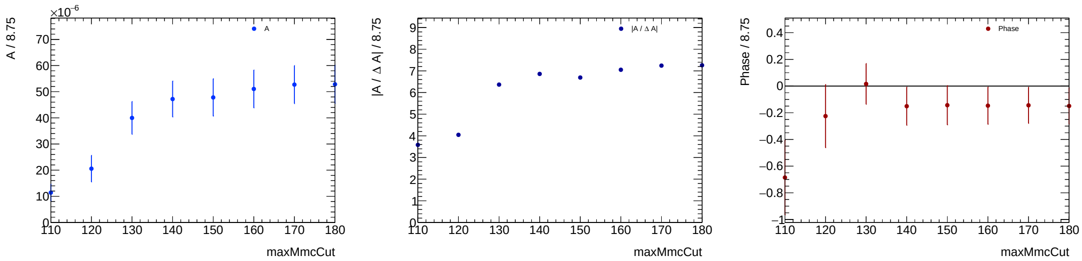

(d) Variation of the maximum mmc mass cut

Figure B.2: Impact of $\Delta R_{\tau\tau}$ and $m_{\tau\tau}^{\text{MMC}}$ requirements on the amplitude and phase of the φ^*_{CP} distribution in $H \to \tau\tau$ events.

APPENDIX C

Validation of the unpolarised $H \to \tau\tau$ sample

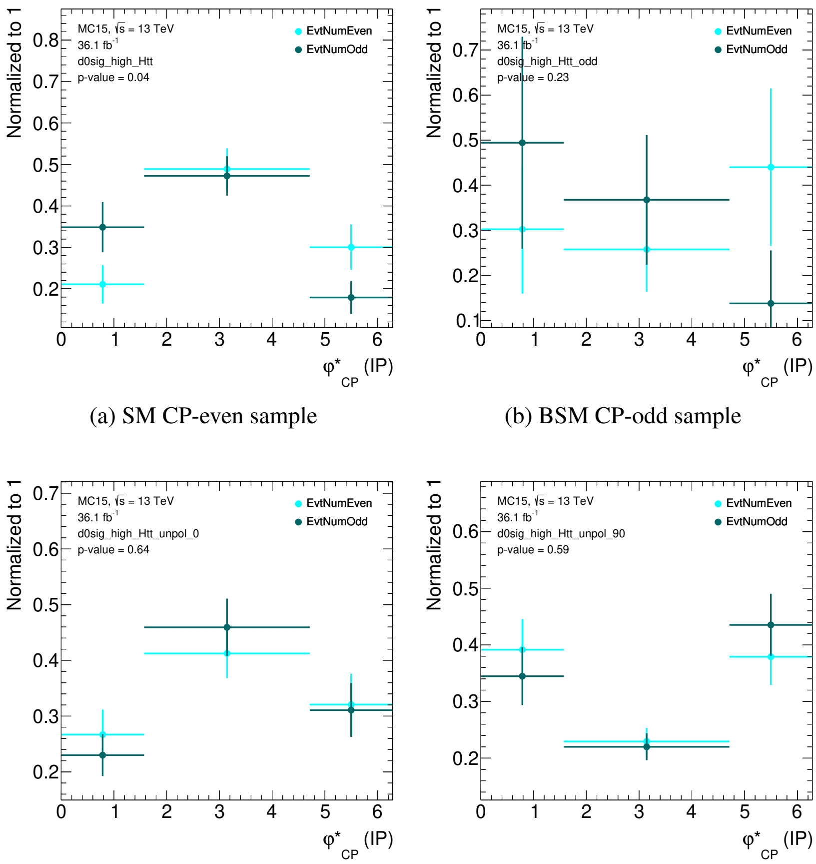

(a) SM CP-even sample

(b) BSM CP-odd sample

(c) unpol. $H \to \tau\tau$ sample ($\phi_\tau = 0^\circ$)

(d) unpol. $H \to \tau\tau$ sample ($\phi_\tau = 90^\circ$)

Figure C.1: The φ^*_{CP} distribution comparing two randomly chosen, equally sized subsets of the CP-even or CP-odd $H \to \tau\tau$ signal samples in the IP-IP d_0^{sig} high preselection region.

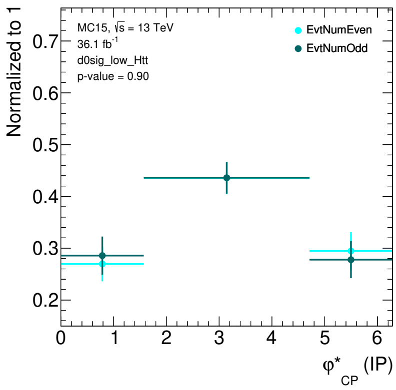

(a) SM CP-even sample

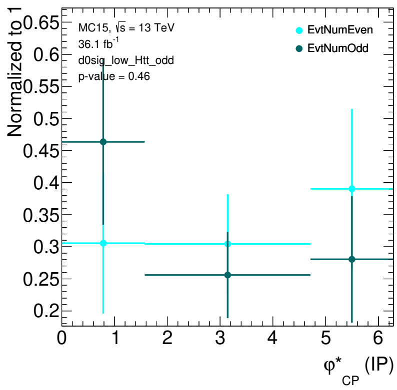

(b) BSM CP-odd sample

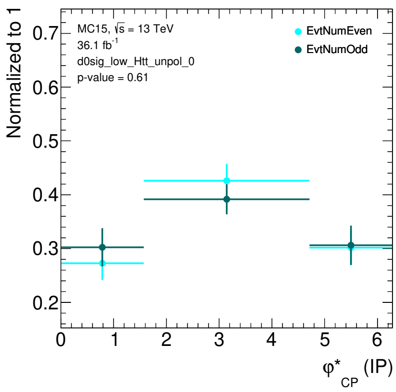

(c) unpol. $H \to \tau\tau$ sample ($\phi_\tau = 0°$)

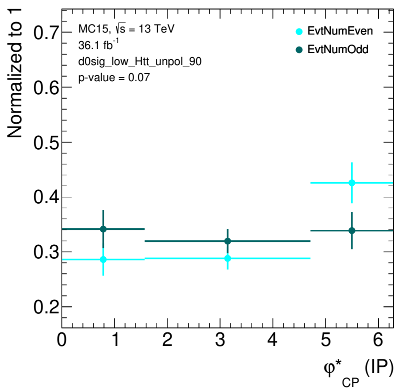

(d) unpol. $H \to \tau\tau$ sample ($\phi_\tau = 90°$)

Figure C.2: The φ^*_{CP} distribution comparing two randomly chosen, equally sized subsets of the CP-even or CP-odd $H \to \tau\tau$ signal samples in the IP-IP d_0^{sig} low preselection region.

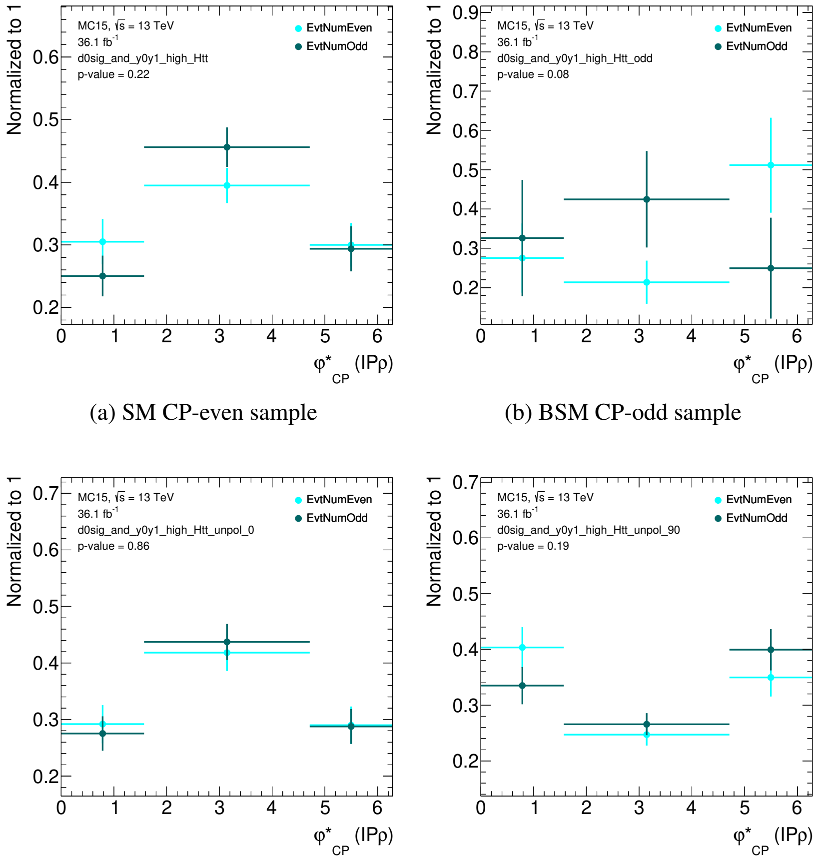

(a) SM CP-even sample

(b) BSM CP-odd sample

(c) unpol. $H \to \tau\tau$ sample ($\phi_\tau = 0^\circ$)

(d) unpol. $H \to \tau\tau$ sample ($\phi_\tau = 90^\circ$)

Figure C.3: The φ^*_{CP} distribution comparing two randomly chosen, equally sized subsets of the CP-even or CP-odd $H \to \tau\tau$ signal samples in the IP-ρ $d_0^{\mathrm{sig}}/Y_\pm$ high preselection region.

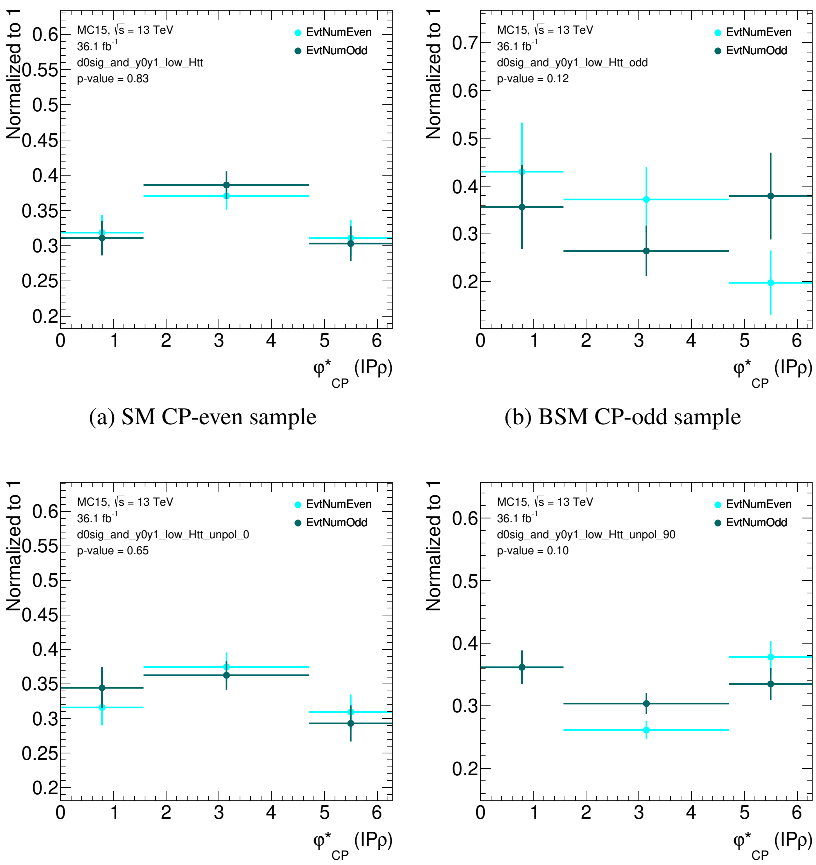

(a) SM CP-even sample

(b) BSM CP-odd sample

(c) unpol. $H \to \tau\tau$ sample ($\phi_\tau = 0^\circ$)

(d) unpol. $H \to \tau\tau$ sample ($\phi_\tau = 90^\circ$)

Figure C.4: The φ^*_{CP} distribution comparing two randomly chosen, equally sized subsets of the CP-even or CP-odd $H \to \tau\tau$ signal samples in the IP-ρ $d_0^{\text{sig}}/Y_\pm$ low preselection region.

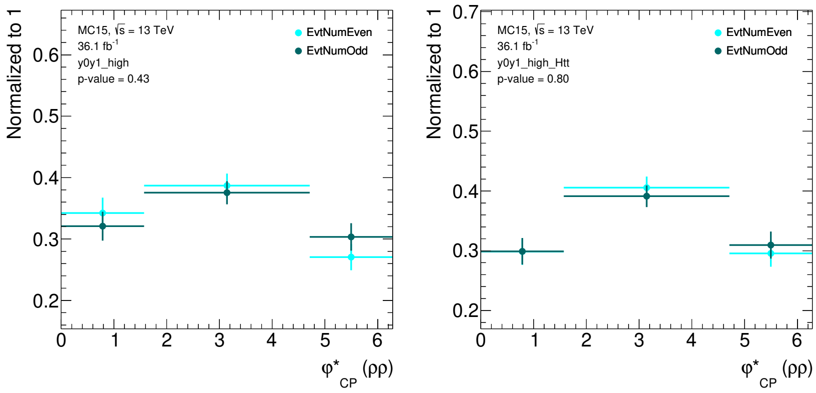

(a) SM CP-even sample (b) BSM CP-odd sample

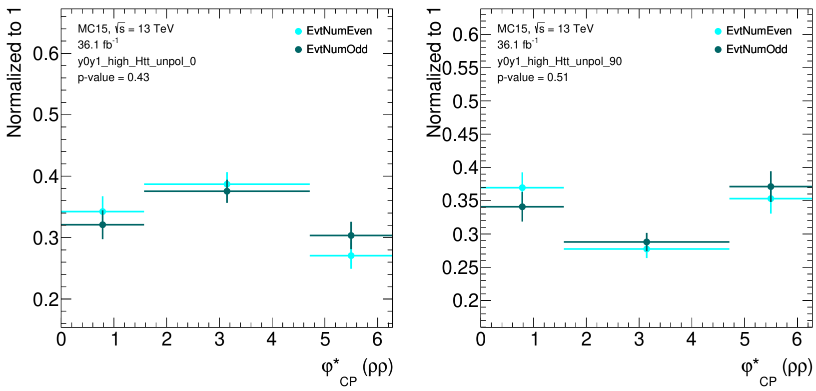

(c) unpol. $H \to \tau\tau$ sample ($\phi_\tau = 0^\circ$) (d) unpol. $H \to \tau\tau$ sample ($\phi_\tau = 90^\circ$)

Figure C.5: The φ^*_{CP} distribution comparing two randomly chosen, equally sized subsets of the CP-even or CP-odd $H \to \tau\tau$ signal samples in the $\rho - \rho$ $Y_+ Y_-$ high preselection region.

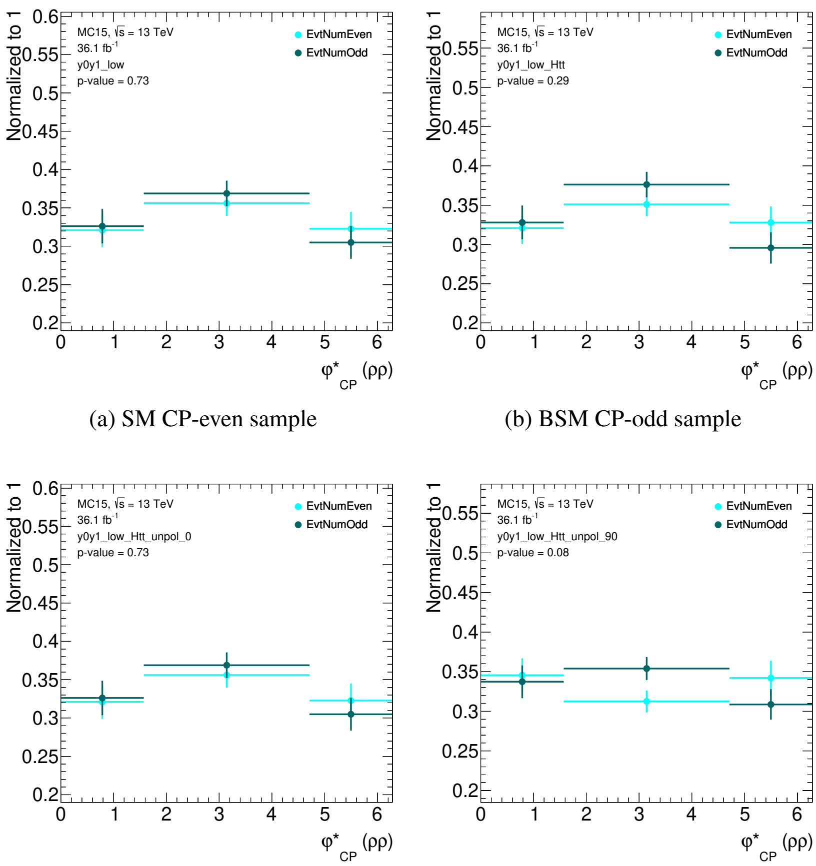

(a) SM CP-even sample

(b) BSM CP-odd sample

(c) unpol. $H \to \tau\tau$ sample ($\phi_\tau = 0^\circ$)

(d) unpol. $H \to \tau\tau$ sample ($\phi_\tau = 90^\circ$)

Figure C.6: The φ^*_{CP} distribution comparing two randomly chosen, equally sized subsets of the CP-even or CP-odd $H \to \tau\tau$ signal samples in the $\rho - \rho$ Y_+Y_- low preselection region.

APPENDIX D

Systematic uncertainties on the QCD multijet background

D.1 Fit of straight line to OS/SS distributions in various anti-τ-ID regions

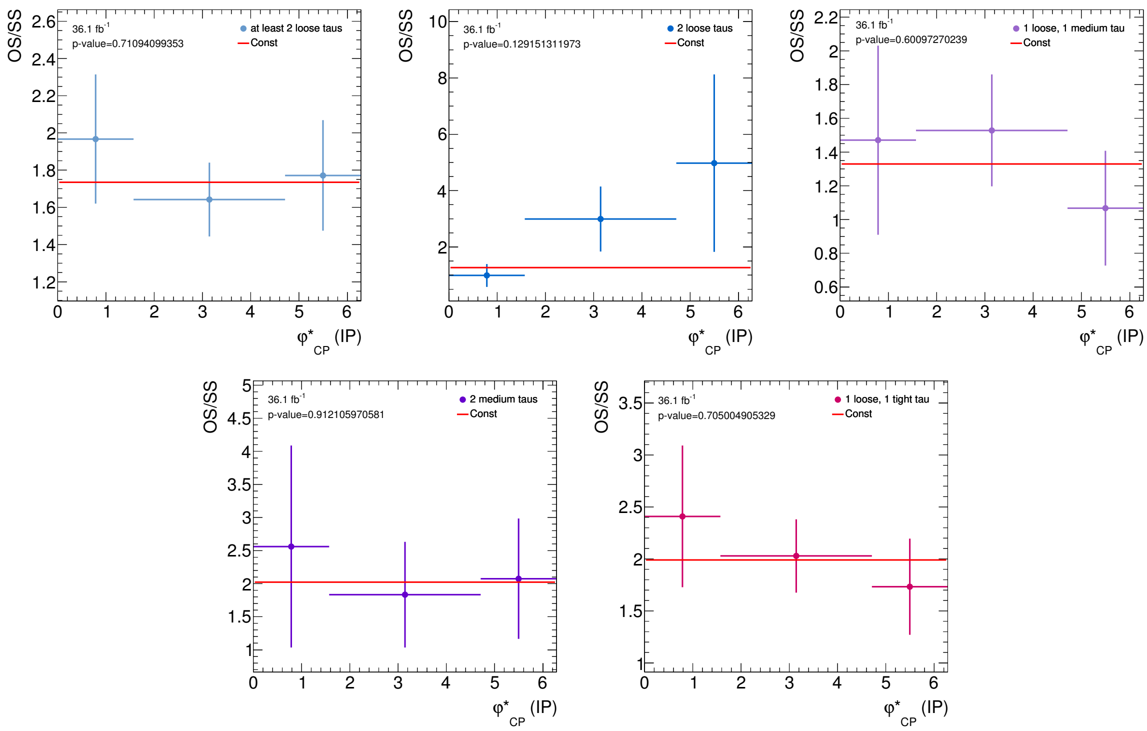

Figure D.1: OS/SS shapes in various anti-τ-ID regions for 1p0n-1p0n τ decays. A straight line is fitted to each of the distributions and the p-value is quoted to measure the compatibility of the OS/SS shape with a flat distribution.

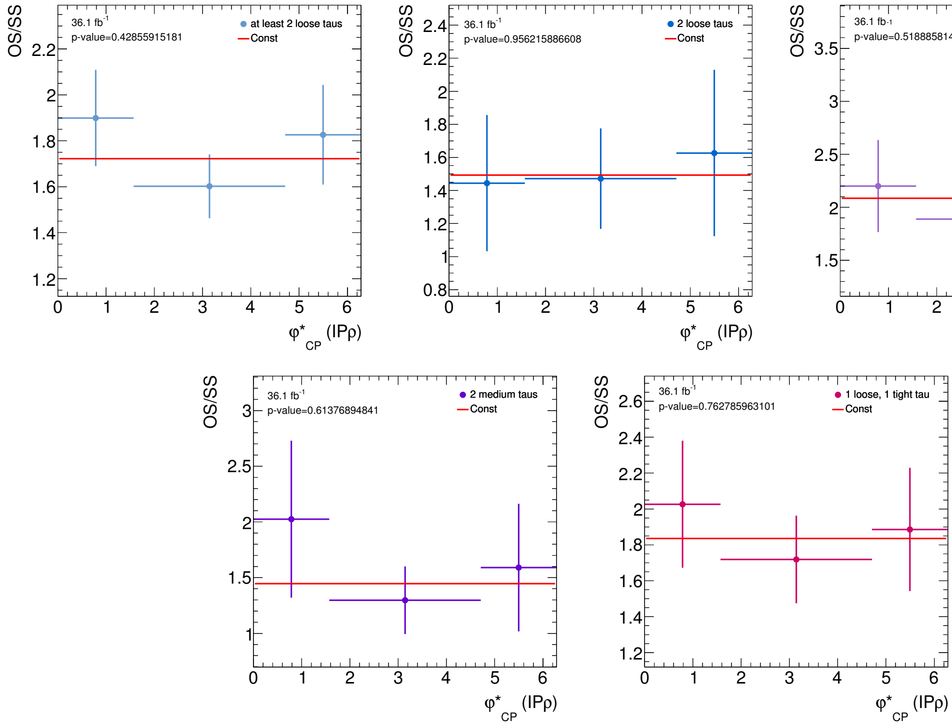

Figure D.2: OS/SS shapes in various anti-τ-ID regions for 1p0n-1p1n τ decays. A straight line is fitted to each of the distributions and the p-value is quoted to measure the compatibility of the OS/SS shape with a flat distribution.

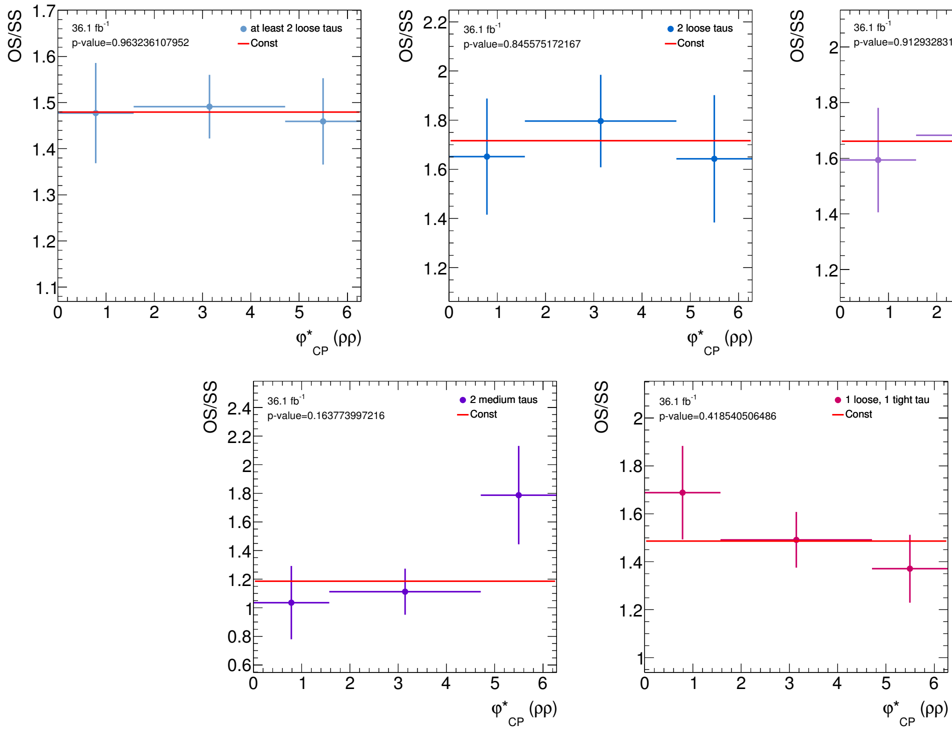

Figure D.3: OS/SS shapes in various anti-τ-ID regions for 1p1n-1p1n τ decays. A straight line is fitted to each of the distributions and the p-value is quoted to measure the compatibility of the OS/SS shape with a flat distribution.

APPENDIX E

Additional plots from the optimisation of the jet particle flow algorithm

Distributions of R^0 and R^+ in bins of different jet p_{T}'s:

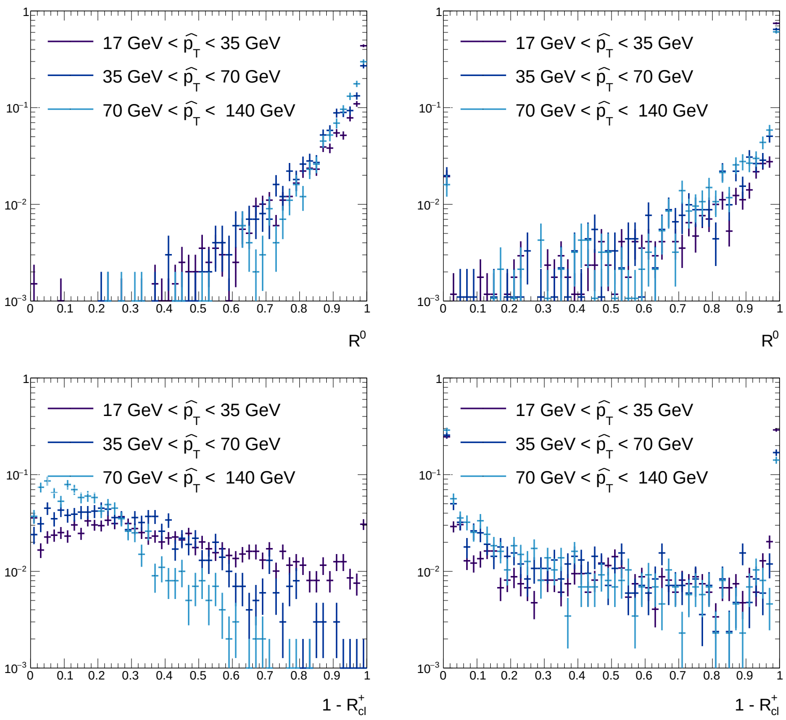

Figure E.1: R^0 and R^+ in the barrel (left) and endcap (right) Presampler.

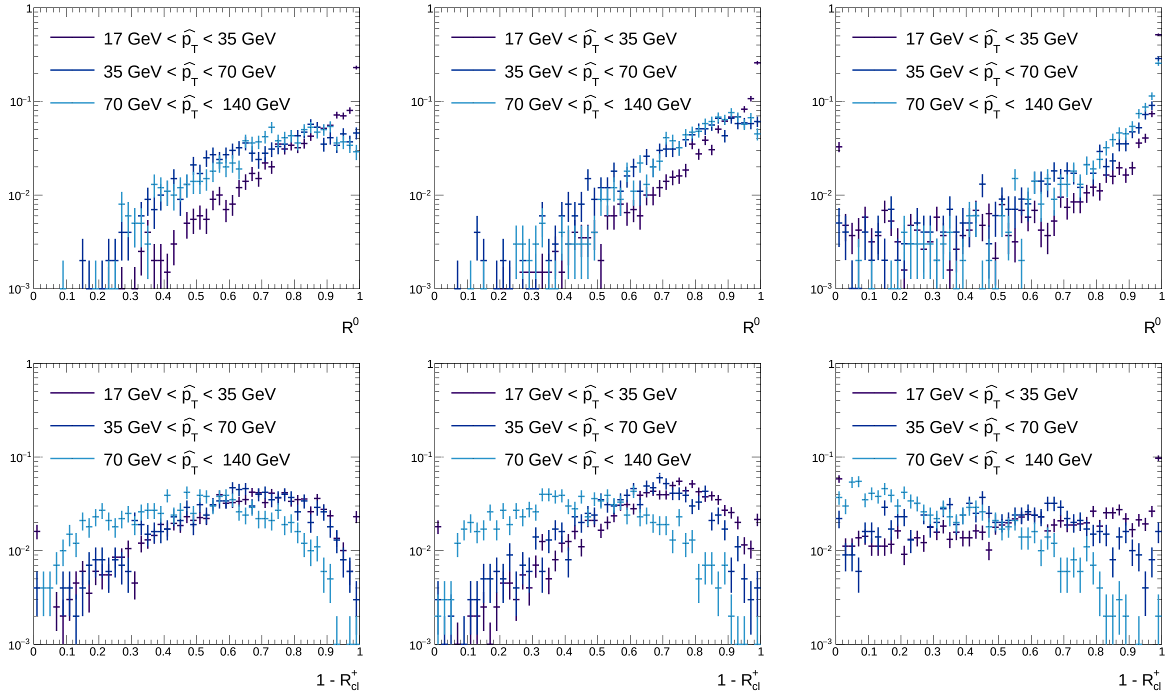

Figure E.2: R^0 and R^+ in EMB 1–3.

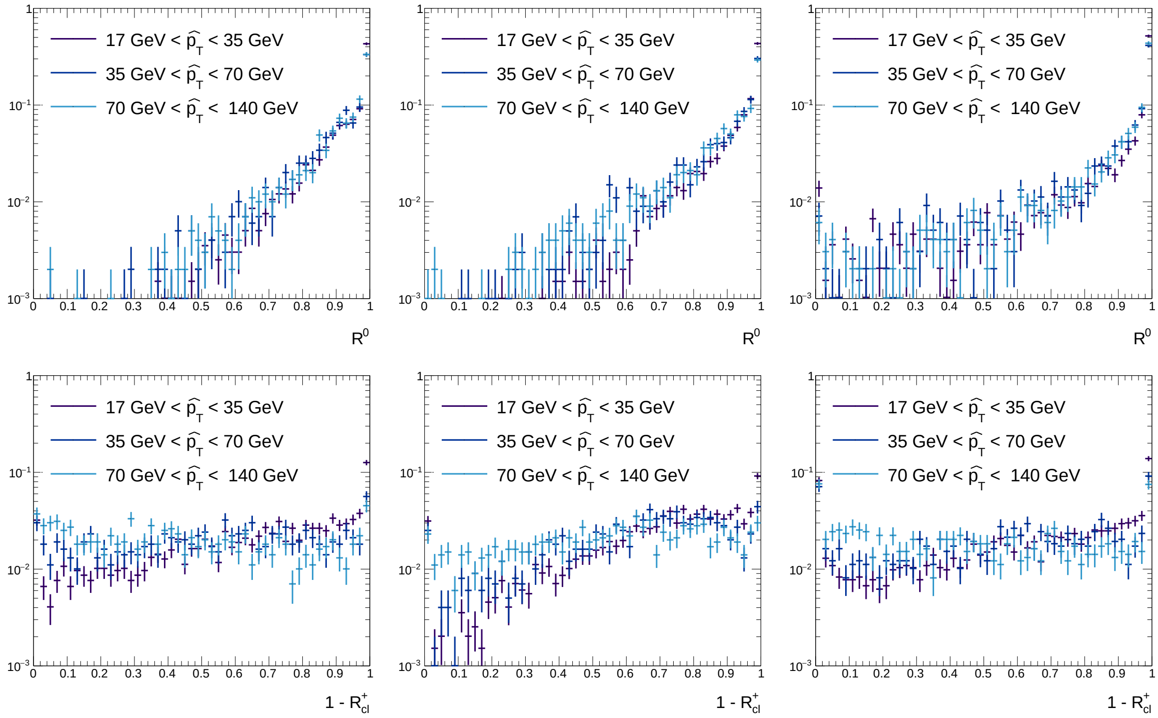

Figure E.3: R^0 and R^+ in EME 1–3.

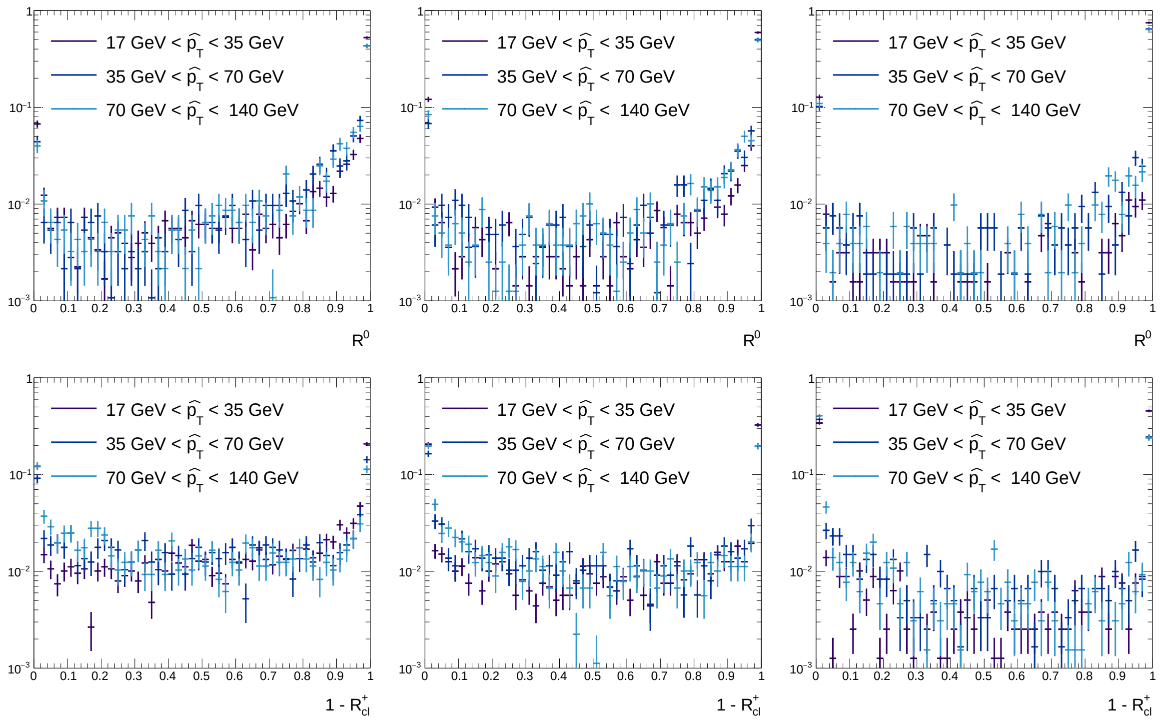

Figure E.4: R^0 and R^+ in HEC 0–2.

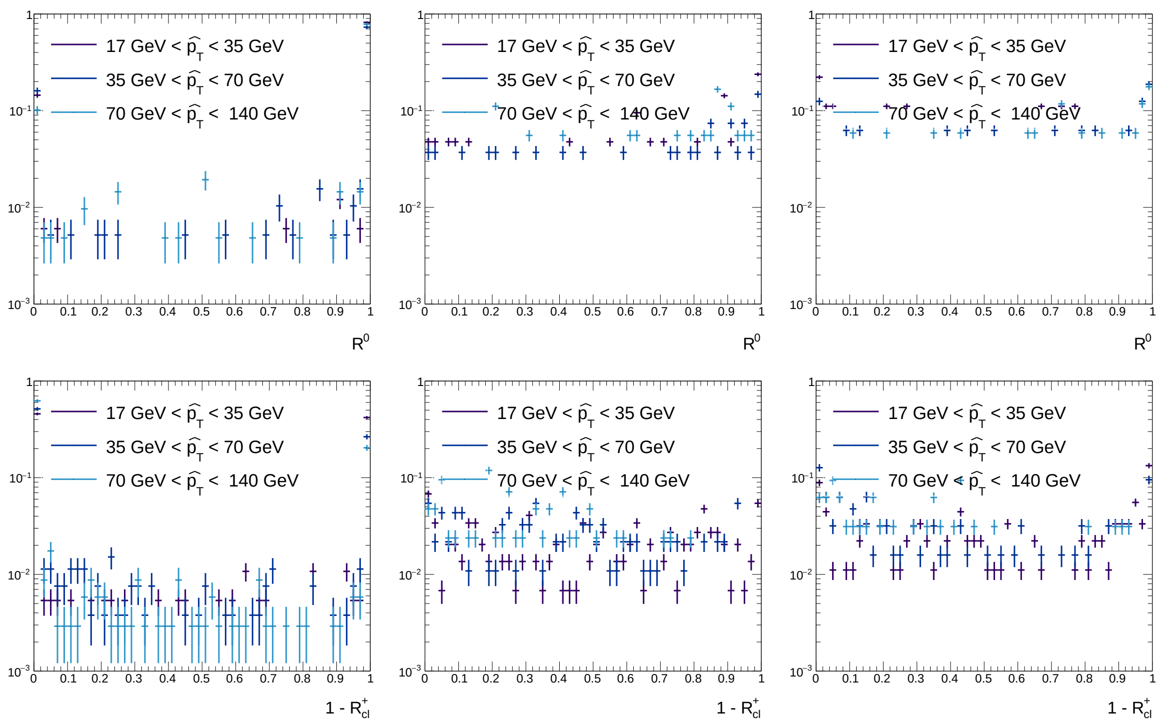

Figure E.5: R^0 and R^+ in HEC 3, Tile 1 and Tile 2.

APPENDIX F

Further validation of background estimates

F.1 Shape comparison of OS and SS data in the signal regions

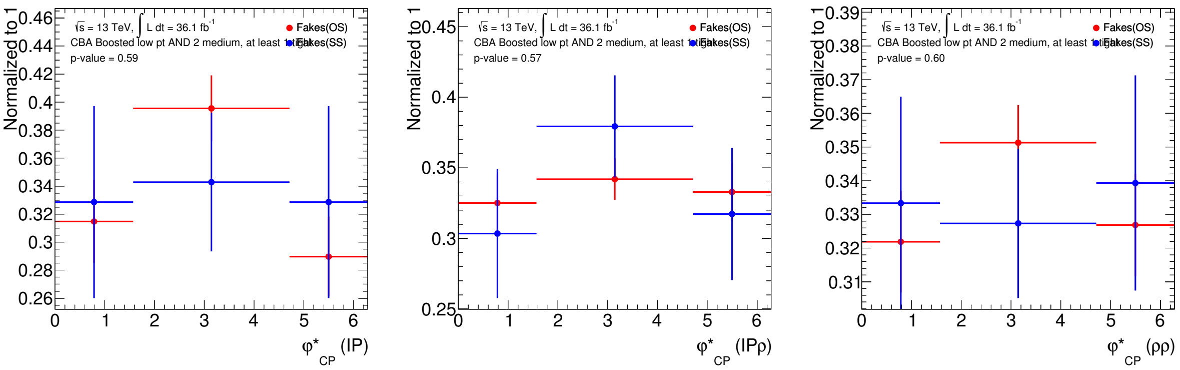

(a) tau ID

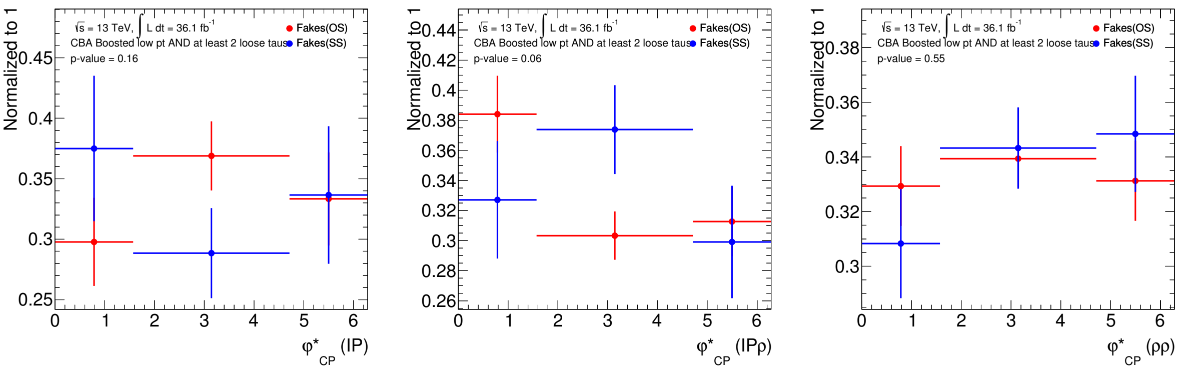

(b) anti-tau ID

Figure F.1: Comparison of the shape of OS and SS data after subtraction of all mc backgrounds. Applying the boost low p_{T} selection with the standard tau ID requirement (a) and applying the boost low p_{T} selection with the anti-tau ID requirement, i.e. not medium-tight and at least 2 loose tau leptons(b).

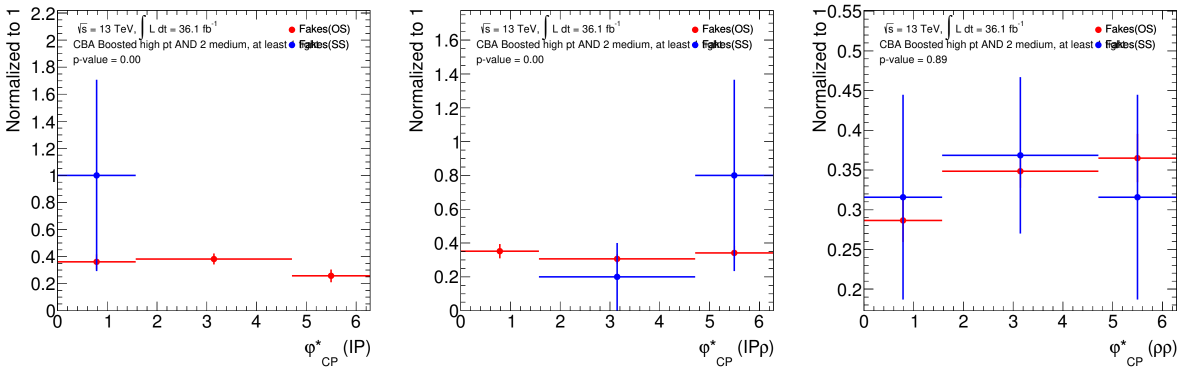

(a) tau ID

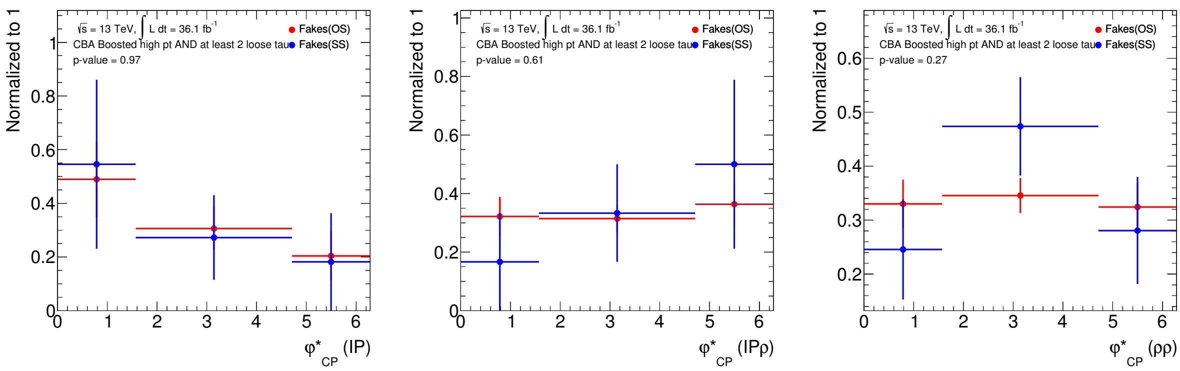

(b) anti-tau ID

Figure F.2: Comparison of the shape of OS and SS data after subtraction of all mc backgrounds. Applying the boost high p_{T} selection with the standard tau ID requirement (a) and applying the boost high p_{T} selection with the anti-tau ID requirement, i.e. not medium-tight and at least 2 loose tau leptons(b).

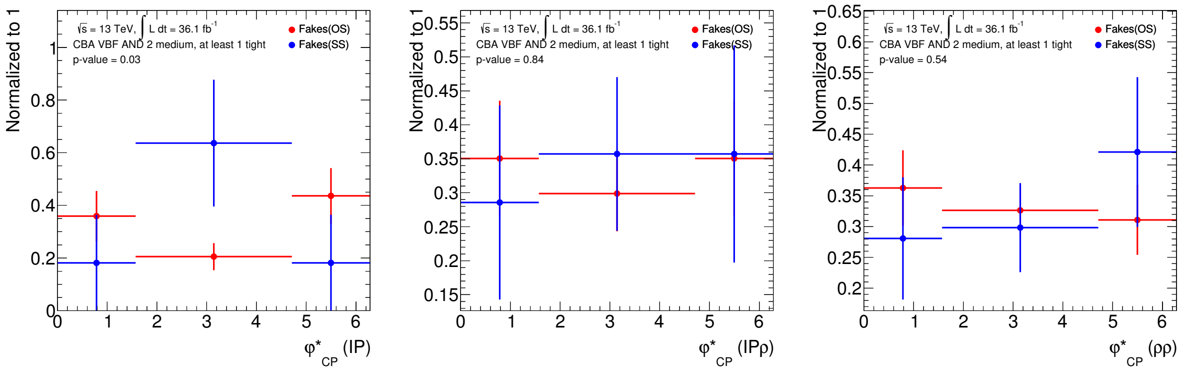

(a) tau ID

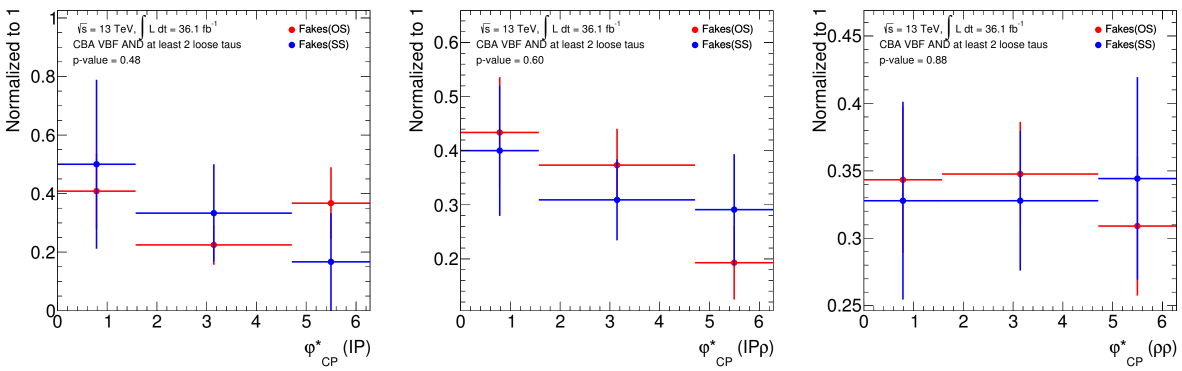

(b) anti-tau ID

Figure F.3: Comparison of the shape of OS and SS data after subtraction of all mc backgrounds. Applying the vbf selection with the standard tau ID requirement (a) and applying the vbf selection with the anti-tau ID requirement, i.e. not medium-tight and at least 2 loose tau leptons(b).

F.2 Shape of the Sherpa2.2 $Z \to \tau\tau$ background in the signal regions comparing the Higgs and Z mass windows

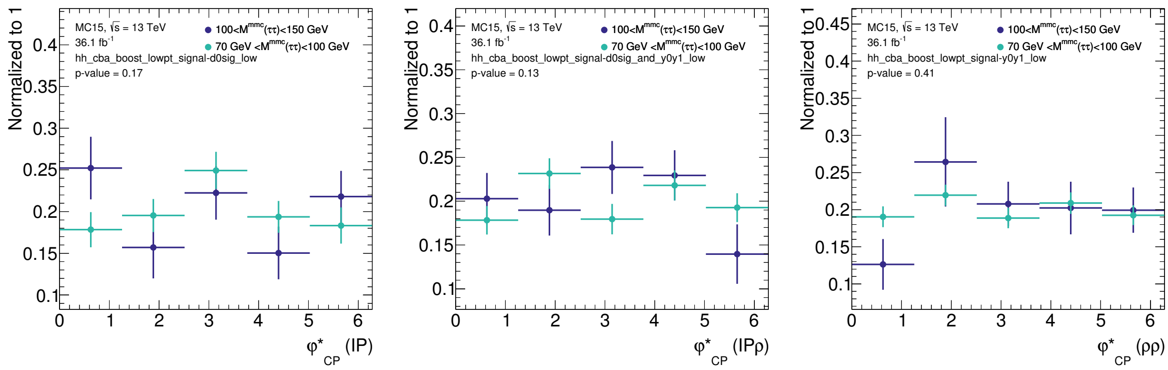

(a) IP-IP (low d_0^{sig}) (b) IP-ρ (low d_0^{sig}, low $Y_\pm$) (c) $\rho-\rho$ (low Y_+Y_-)

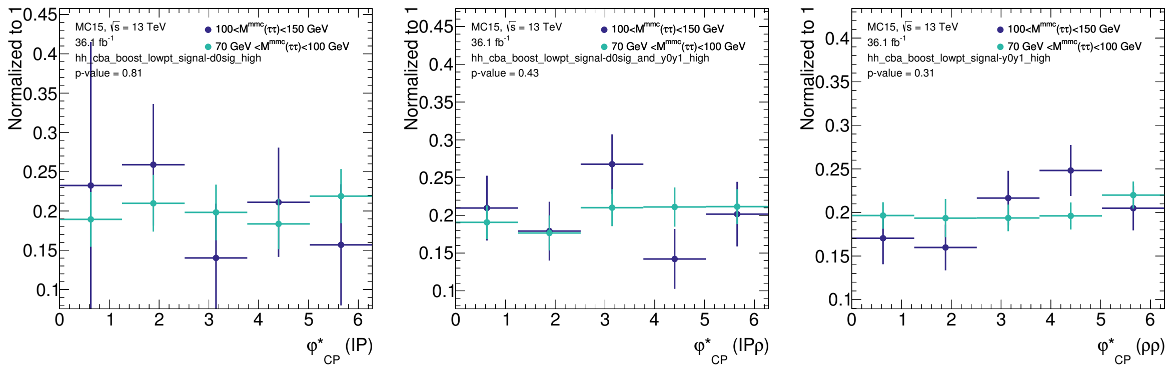

(d) IP-IP (high d_0^{sig}) (e) IP-ρ (high $d_0^{\mathrm{sig}}/ Y_\pm$) (f) $\rho-\rho$ (high Y_+Y_-)

Figure F.4: φ^*_{CP} distribution of Sherpa2.2 $Z \to \tau\tau$ in the boost low p_{T} signal region in the H and Z mass window

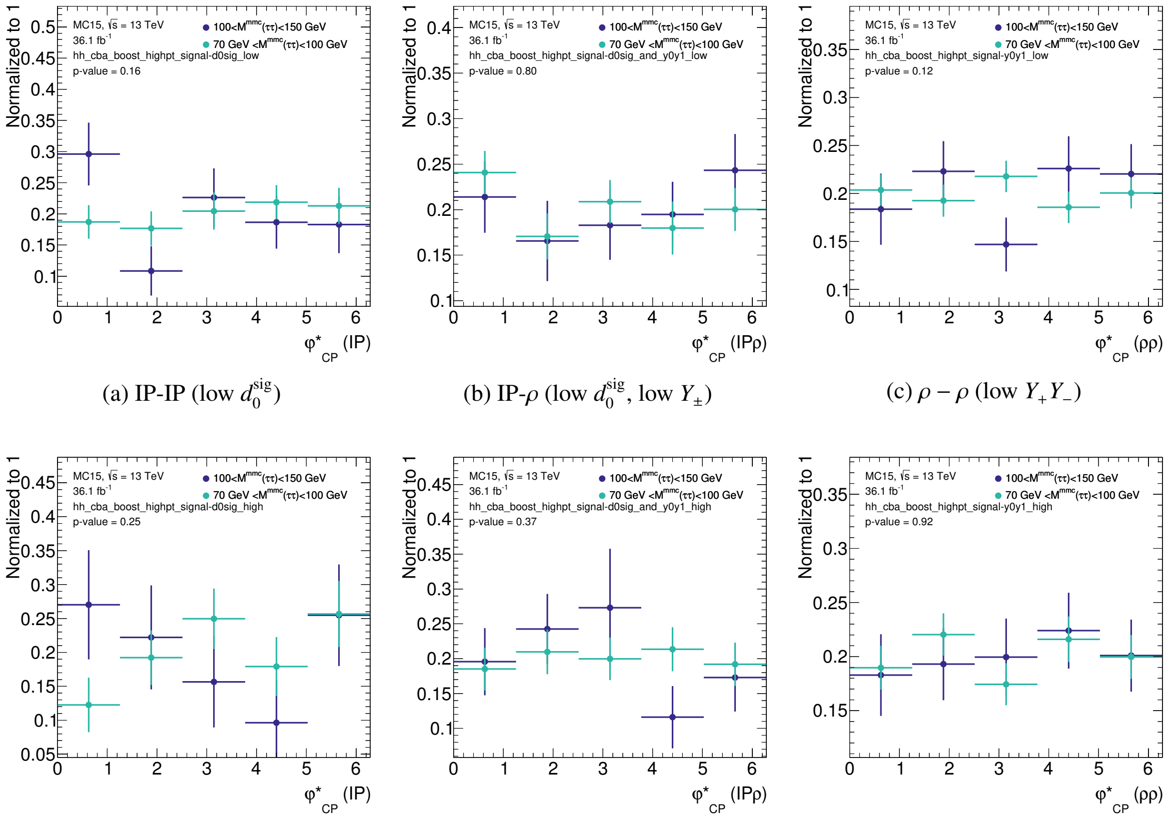

(a) IP-IP (low d_0^{sig})

(b) IP-ρ (low d_0^{sig}, low $Y_\pm$)

(c) $\rho-\rho$ (low Y_+Y_-)

(d) IP-IP (high d_0^{sig})

(e) IP-ρ (high d_0^{sig}/ $Y_\pm$)

(f) $\rho-\rho$ (high Y_+Y_-)

Figure F.5: φ^*_{CP} distribution of SHERPA2.2 $Z \to \tau\tau$ in the boost high p_{T} signal region in the H and Z mass window

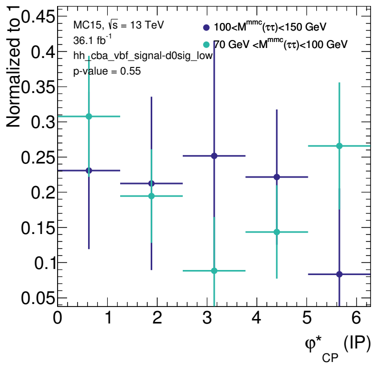

(a) IP-IP (low d_0^{sig})

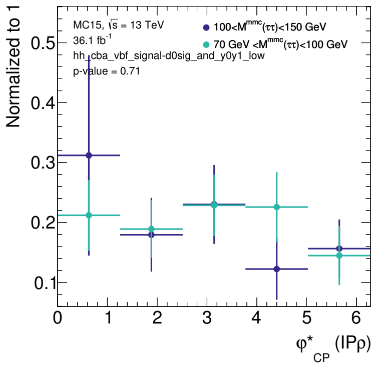

(b) IP-ρ (low d_0^{sig}, low $Y_\pm$)

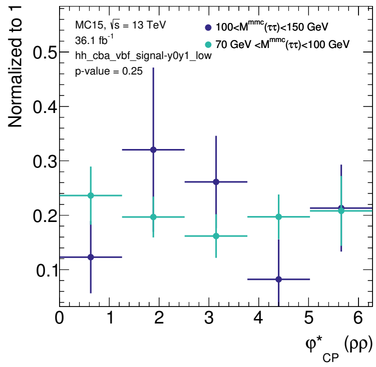

(c) $\rho-\rho$ (low Y_+Y_-)

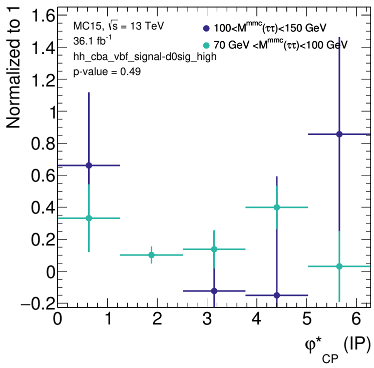

(d) IP-IP (high d_0^{sig})

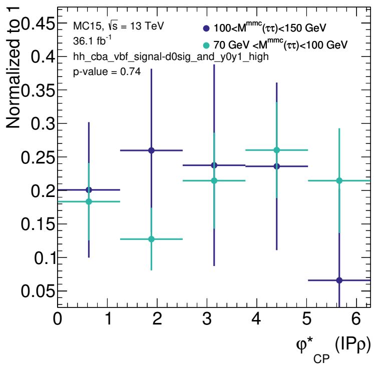

(e) IP-ρ (high d_0^{sig}/ $Y_\pm$)

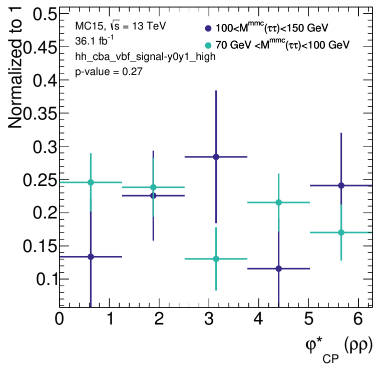

(f) $\rho-\rho$ (high Y_+Y_-)

Figure F.6: φ^*_{CP} distribution of Sherpa2.2 $Z \to \tau\tau$ in the vbf signal region in the H and Z mass window

APPENDIX G

Supplementary material to the Higgs CP-measurement

Nuisance parameter
Forward_JVT
JES_BJES
JES_EffectiveNP_1
JES_EffectiveNP_2
JES_EffectiveNP_3
JES_EffectiveNP_4
JES_EffectiveNP_5
JES_EffectiveNP_6
JES_EffectiveNP_7
JES_EffectiveNP_8
JES_EtaInter_Model
JES_EtaInter_NonClosure
JES_EtaInter_Stat
JES_Flavor_Comp
JES_Flavor_Resp
JES_HighPt
JES_PU_OffsetMu
JES_PU_OffsetNPV
JES_PU_PtTerm
JES_PU_Rho
JES_PunchThrough
JVT
MET_SoftTrk_ResoPara
MET_SoftTrk_ResoPerp
MET_SoftTrk_Scale
PRW_DATASF
TAU_EFF_ELEORL_TRUEELE
TAU_EFF_ELEORL_TRUEHADTAU
TAU_EFF_ID_HIGHPT
TAU_EFF_ID_TOTAL
TAU_EFF_RECO_HIGHPT
TAU_EFF_RECO_TOTAL
TAU_EFF_TRIG_STATDATA2015
TAU_EFF_TRIG_STATDATA2016
TAU_EFF_TRIG_STATMC2015
TAU_EFF_TRIG_STATMC2016
TAU_EFF_TRIG_SYST2015
TAU_EFF_TRIG_SYST2016
TAU_TES_DETECTOR
TAU_TES_INSITU
TAU_TES_MODEL
LumiUncCombined
TRK_bias_d0_WM
TRK_bias_qoverp_sagitta_WM
TRK_res_d0_dead
TRK_res_d0_meas
TRK_res_z0_dead
TRK_res_z0_meas
hh_fake_contamination
jet_jer_crosscalibfwd
jet_jer_noisefwd
jet_jer_np0
jet_jer_np1
jet_jer_np2
jet_jer_np3
jet_jer_np4
jet_jer_np5
jet_jer_np6
jet_jer_np7
jet_jer_np8

Table G.1: Systematic uncertainties included in the fit of the CP-mixing angle.

G.1 Supplementary plots from the fit to Asimov data

G.1.1 Post-fit distributions for the combined VBF and boosted categories

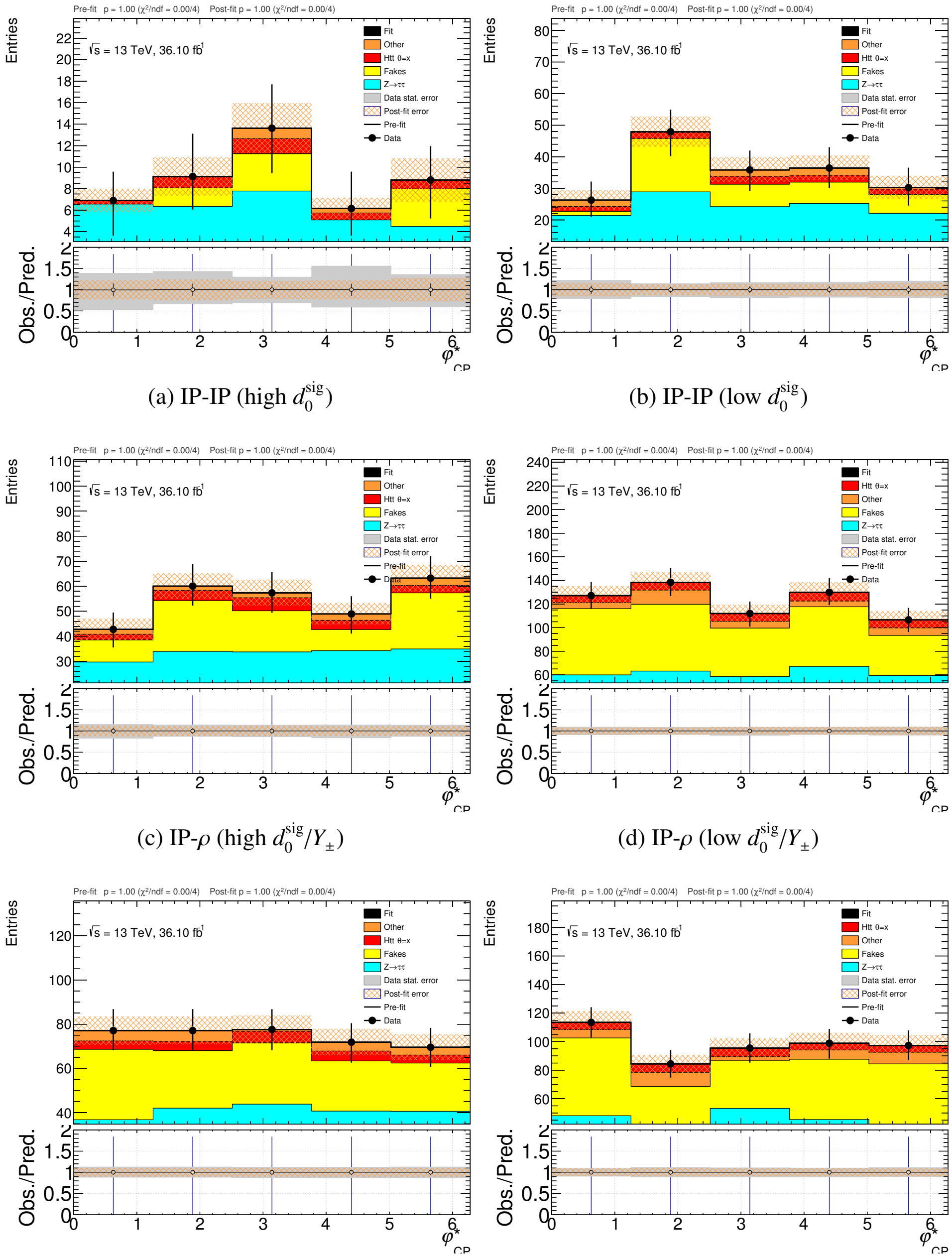

(a) IP-IP (high d_0^{sig})

(b) IP-IP (low d_0^{sig})

(c) IP-ρ (high $d_0^{\mathrm{sig}}/Y_\pm$)

(d) IP-ρ (low $d_0^{\mathrm{sig}}/Y_\pm$)

(e) $\rho-\rho$ (high Y_+Y_-)

(f) $\rho-\rho$ (high Y_+Y_-)

Figure G.1: Post-fit distributions for $\phi_\tau = 0^\circ$ using Asimov data in the VBF or boosted categories segmented into the six decay mode and $d_0^{\mathrm{sig}}/Y_\pm$ categories.

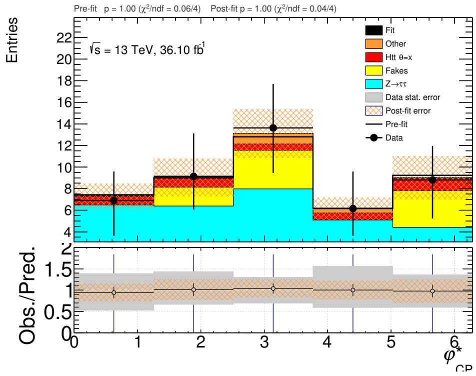

(a) IP-IP (high d_0^{sig})

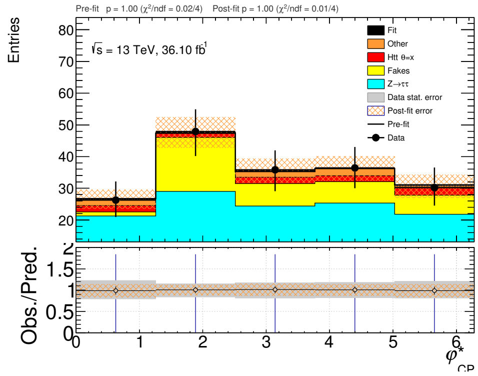

(b) IP-IP (low d_0^{sig})

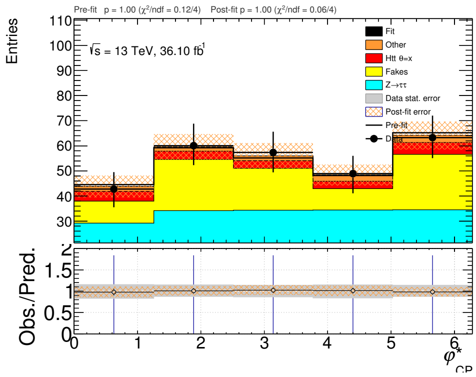

(c) IP-ρ (high $d_0^{\mathrm{sig}}/Y_{\pm}$)

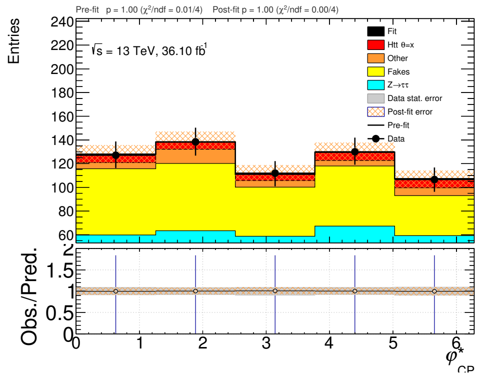

(d) IP-ρ (low $d_0^{\mathrm{sig}}/Y_{\pm}$)

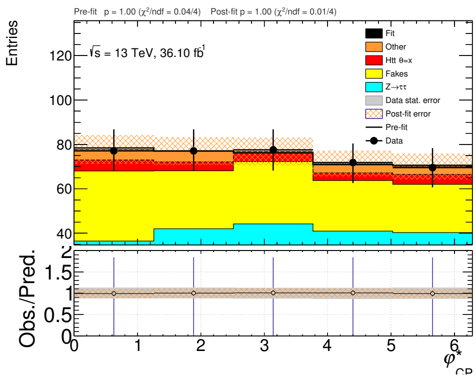

(e) $\rho-\rho$ (high $Y_{+}Y_{-}$)

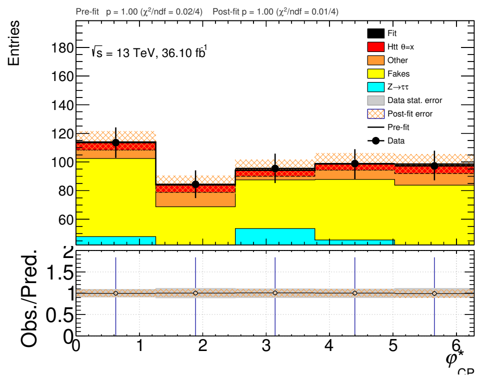

(f) $\rho-\rho$ (low $Y_{+}Y_{-}$)

Figure G.2: Post-fit distributions for $\phi_{\tau} = 90^{\circ}$ using Asimov data in the VBF or boosted categories segmented into the six decay mode and $d_0^{\mathrm{sig}}/Y_{\pm}$ categories.

G.1.2 Post-fit distributions for all signal and control regions

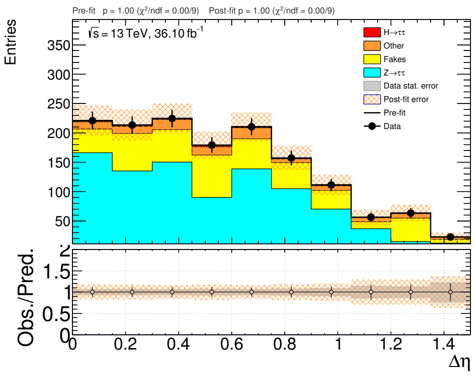

(a) VBF CR

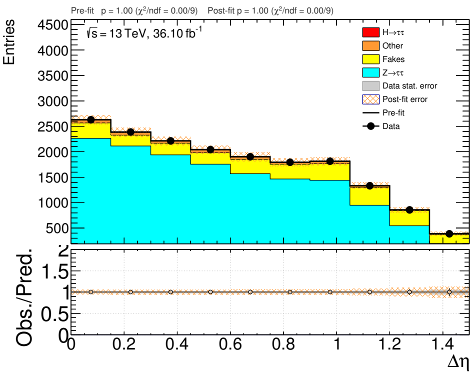

(b) boosted low-p_T CR

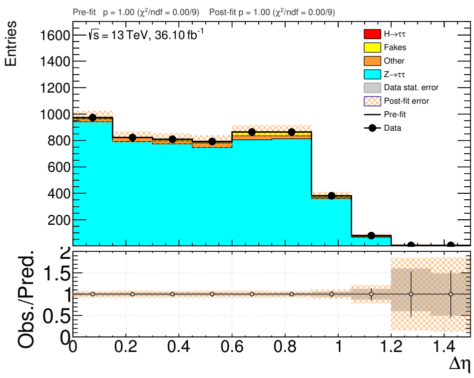

(c) boosted high-p_T CR

Figure G.3: Post-fit $\delta\eta$ distributions in the VBF, boosted low-p_T , and boosted high-p_T CR after the fit to Asimov data with a luminosity of $\mathcal{L} \approx 36.1\ \text{fb}^{-1}$ at a CMS energy of $\sqrt{s} = 13\,\text{TeV}$.

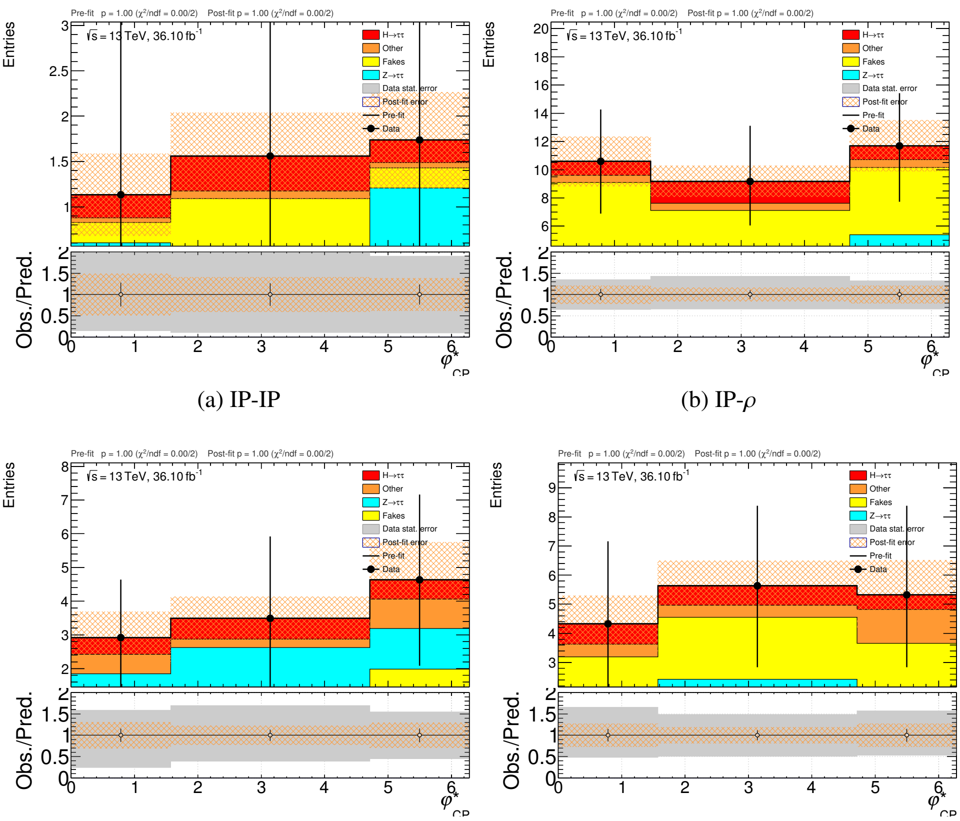

(a) IP-IP

(b) IP-ρ

(c) $\rho-\rho$ (high $Y_{+}Y_{-}$)

(d) $\rho-\rho$ (low $Y_{+}Y_{-}$)

Figure G.4: Post-fit φ^{*}_{CP} distributions in the VBF signal regions after the fit to Asimov data with a luminosity of $\mathcal{L} \approx 36.1\ \mathrm{fb}^{-1}$ at a CMS energy of $\sqrt{s} = 13\,\mathrm{TeV}$.

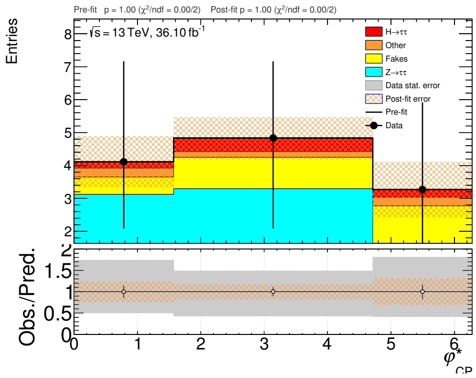

(a) IP-IP (high d_0^{sig})

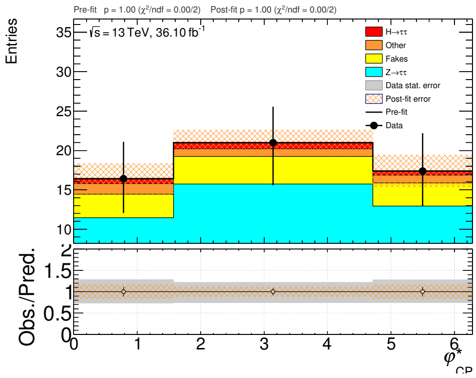

(b) IP-IP (low d_0^{sig})

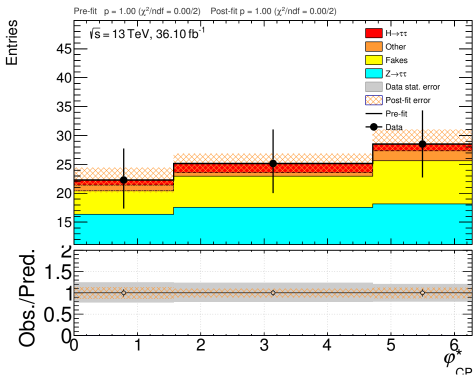

(c) IP-ρ (high $d_0^{\mathrm{sig}}/Y_{\pm}$)

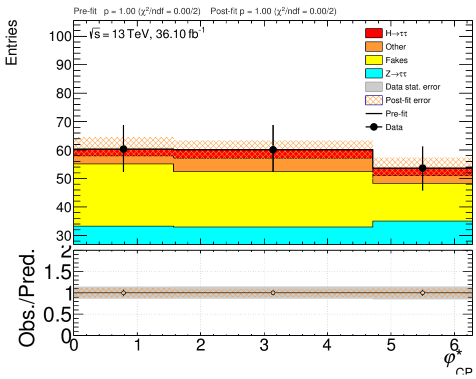

(d) IP-ρ (low $d_0^{\mathrm{sig}}/Y_{\pm}$)

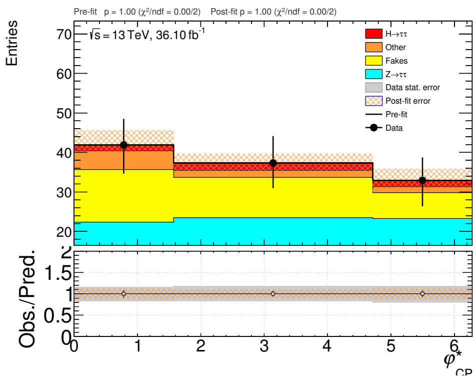

(e) $\rho-\rho$ (high Y_+Y_-)

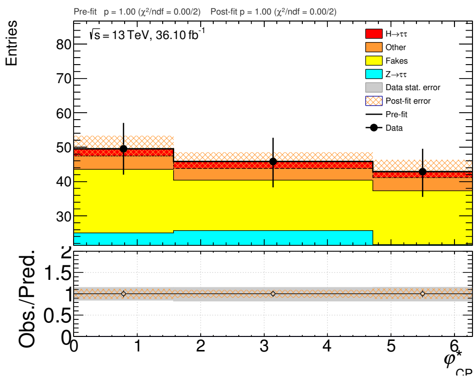

(f) $\rho-\rho$ (low Y_+Y_-)

Figure G.5: Post-fit φ^*_{CP} distributions in theboosted low-p_{T} signal regions after the fit to Asimov data with a luminosity of $\mathcal{L} \approx 36.1\,\mathrm{fb}^{-1}$ at a CMS energy of $\sqrt{s} = 13\,\mathrm{TeV}$.

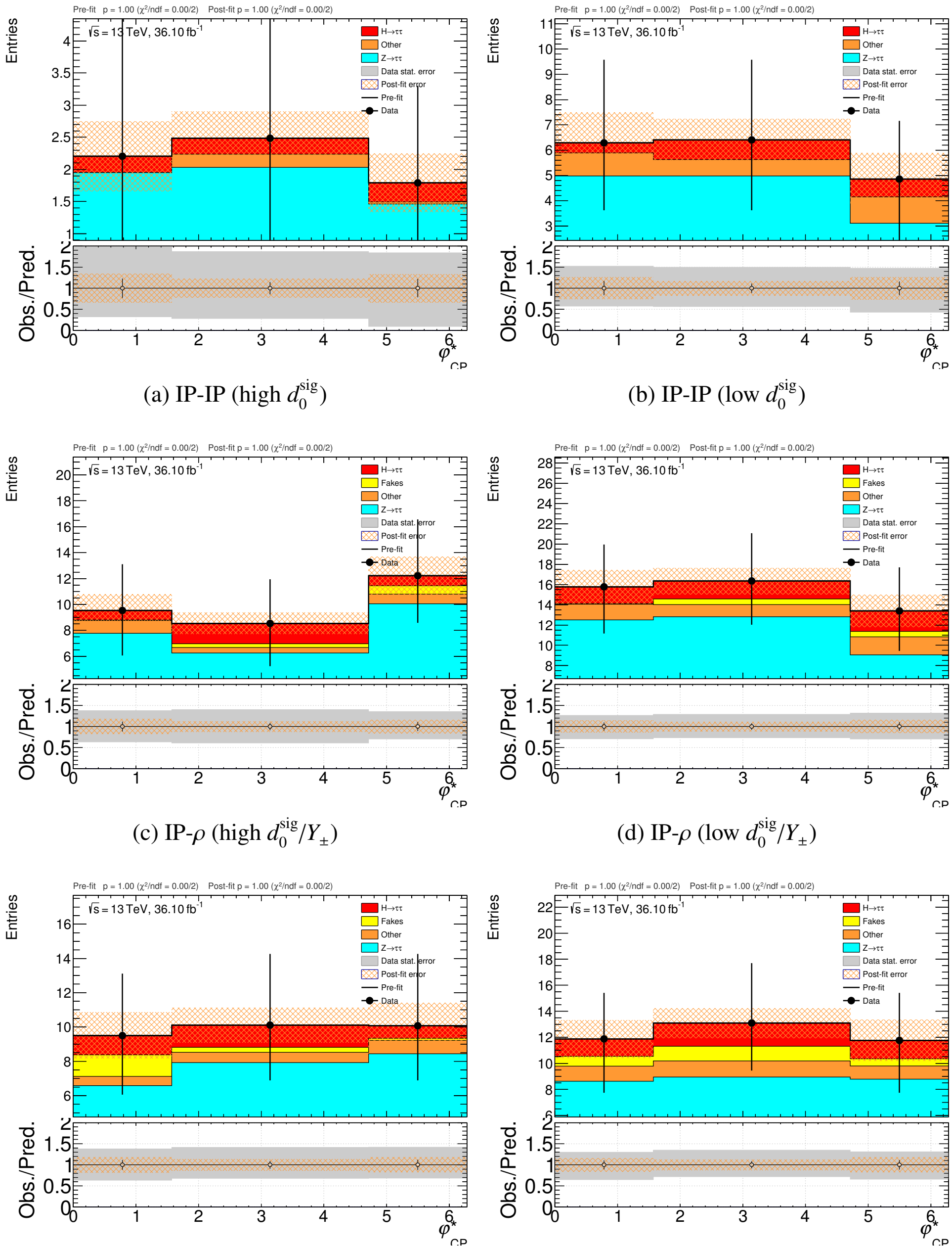

(a) IP-IP (high d_0^{sig})

(b) IP-IP (low d_0^{sig})

(c) IP-ρ (high $d_0^{\mathrm{sig}}/Y_{\pm}$)

(d) IP-ρ (low $d_0^{\mathrm{sig}}/Y_{\pm}$)

(e) $\rho-\rho$ (high Y_+Y_-)

(f) $\rho-\rho$ (low Y_+Y_-)

Figure G.6: Post-fit φ^*_{CP} distributions in the boosted high-p_{T} signal regions after the fit to Asimov data with a luminosity of $\mathcal{L} \approx 36.1\,\mathrm{fb}^{-1}$ at a CMS energy of $\sqrt{s} = 13\,\mathrm{TeV}$.

G.1.3 Pull distribution of all NPs for ϕ_τ = 90°

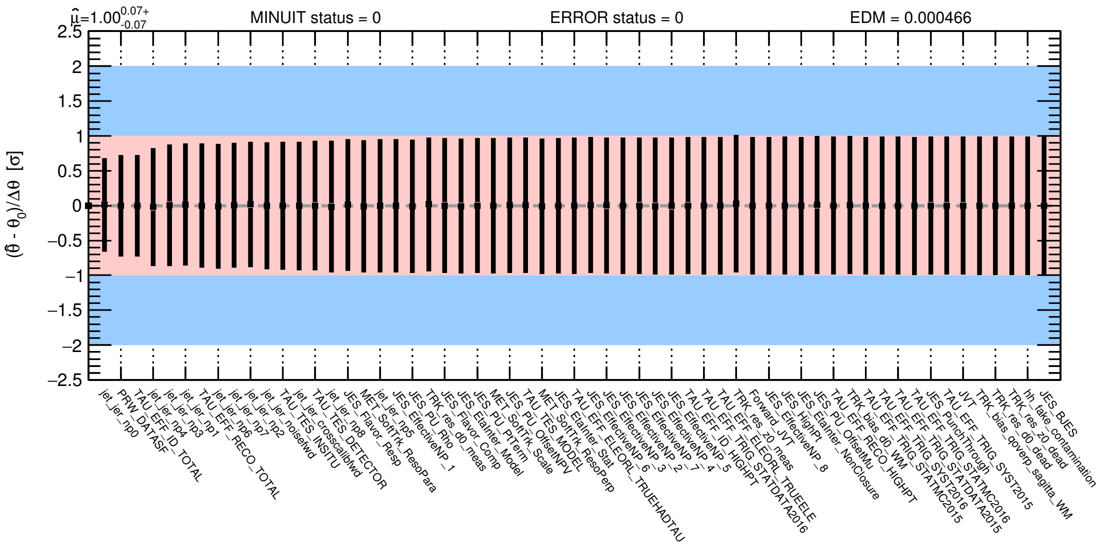

Figure G.7: Pull distribution of all systematic uncertainty NPs included after a fit to Asimov data sorted by their constraint for $\phi_\tau = 90^\circ$.

G.2 Pre- and post-fit event yields using 2015+2016 data

Tables G.2, G.4 and G.5 display the pre- and post-fit yields of the signal and background expectation and 2015+2016 data. The total sum of signal and background is summarised in Total and compared to data in Data/Total. Ratio denotes the quotient of the number of events after to the number of events before the fit.

Region	Sample	Prefit	Postfit	Ratio
VBF CR	$Z \to \tau\tau$	920.3397 ± 111.4252	985.6764 ± 54.8996	1.07 ± 0.14
	Fake	416.8826 ± 65.6052	584.7414 ± 38.2299	1.40 ± 0.24
	$H \to \tau\tau$	15.7167 ± 14.0805	17.9783 ± 1.3110	1.14 ± 1.03
	Others	106.8782 ± 34.1530	111.9336 ± 7.7315	1.05 ± 0.34
	Total	1459.8173 ± 134.4779	1700.3297 ± 67.3571	1.16 ± 0.12
	Data	1659^{+40}_{-41}		
	Data/Total	$1.1371^{+0.1083}_{-0.1085}$	$0.9763^{+0.0453}_{+0.0456}$	
boosted low-p_T	$Z \to \tau\tau$	14239.3126 ± 424.7525	14715.4702 ± 253.2067	1.03 ± 0.04
	Fake	2695.8992 ± 171.8922	3631.4459 ± 141.6832	1.35 ± 0.10
	$H \to \tau\tau$	38.0279 ± 20.5666	38.5940 ± 6.2900	1.01 ± 0.57
	Others	388.7434 ± 67.9910	378.4486 ± 12.5088	0.97 ± 0.17
	Total	17361.9831 ± 463.6889	18763.9587 ± 290.4888	1.08 ± 0.03
	Data	18860^{+137}_{-136}		
	Data/Total	$1.0863^{+0.0301}_{-0.0301}$	$1.0051^{+0.0172}_{+0.0172}$	
boosted high-p_T	$Z \to \tau\tau$	5301.3285 ± 266.3525	5368.9301 ± 119.8380	1.01 ± 0.06
	Fake	94.7058 ± 29.8939	124.7822 ± 9.5904	1.32 ± 0.43
	$H \to \tau\tau$	18.6657 ± 14.9291	16.2369 ± 2.9935	0.87 ± 0.71
	Others	184.4734 ± 44.9672	172.4062 ± 7.5522	0.93 ± 0.23
	Total	5599.1734 ± 272.1805	5682.3555 ± 120.4953	1.01 ± 0.05
	Data	5666^{+75}_{-75}		
	Data/Total	$1.0121^{+0.0510}_{-0.0510}$	$0.9972^{+0.0249}_{+0.0250}$	

Table G.2: Prefit, Postfit, and Ratio yields in the VBF, boosted low-p_T and boosted high-p_T CRs.

Region	Sample	Prefit	Postfit	Ratio
VBF IP-IP	$Z \to \tau\tau$	2.3403 ± 1.0869	2.9705 ± 0.5469	1.27 ± 0.63
	Fake	1.0044 ± 0.6404	1.7960 ± 0.5638	1.79 ± 1.27
	$H \to \tau\tau$	0.8867 ± 0.6193	0.9457 ± 0.2083	1.07 ± 0.78
	Others	0.1946 ± 0.2913	2.6825 ± 1.7356	13.79 ± 22.49
	Total	4.4260 ± 1.4352	8.3947 ± 1.9165	1.90 ± 0.75
	Data	10^{+3}_{-3}		
	Data/Total	$2.4452^{+1.1110}_{-1.1906}$	$1.2892^{+0.5050}_{+0.5531}$	
VBF IP-ρ	$Z \to \tau\tau$	13.6077 ± 2.5319	12.8375 ± 1.2410	0.94 ± 0.20
	Fake	12.7513 ± 2.4502	12.9272 ± 1.6023	1.01 ± 0.23
	$H \to \tau\tau$	3.5090 ± 1.2301	3.2454 ± 0.3504	0.92 ± 0.34
	Others	1.5833 ± 0.8527	1.4157 ± 0.2608	0.89 ± 0.51
	Total	31.4513 ± 3.8280	30.4257 ± 2.0732	0.97 ± 0.13
	Data	25^{+5}_{-5}		
	Data/Total	$0.8198^{+0.1954}_{-0.2083}$	$0.8474^{+0.1830}_{+0.1976}$	
VBF $\rho-\rho$, low Y_+Y_-	$Z \to \tau\tau$	6.3100 ± 1.6585	6.2990 ± 0.7718	1.00 ± 0.29
	Fake	5.0988 ± 1.5242	5.3480 ± 0.8188	1.05 ± 0.35
	$H \to \tau\tau$	1.8612 ± 0.9015	1.7215 ± 0.2613	0.92 ± 0.47
	Others	2.0157 ± 1.0249	1.6544 ± 0.4690	0.82 ± 0.48
	Total	15.2857 ± 2.6338	15.0228 ± 1.2467	0.98 ± 0.19
	Data	13^{+4}_{-4}		
	Data/Total	$0.8954^{+0.3044}_{-0.3177}$	$0.9111^{+0.2774}_{+0.2926}$	
VBF $\rho-\rho$, high Y_+Y_-	$Z \to \tau\tau$	3.7693 ± 1.2984	3.6041 ± 0.5039	0.96 ± 0.36
	Fake	3.8928 ± 1.3887	4.3128 ± 0.7462	1.11 ± 0.44
	$H \to \tau\tau$	1.6737 ± 0.8700	1.4327 ± 0.2314	0.86 ± 0.47
	Others	1.7041 ± 0.9335	1.4655 ± 0.2982	0.86 ± 0.50
	Total	11.0399 ± 2.2897	10.8151 ± 0.9763	0.98 ± 0.22
	Data	8^{+3}_{-3}		
	Data/Total	$0.8073^{+0.3217}_{-0.3731}$	$0.8241^{+0.2901}_{+0.3484}$	

Table G.3: Prefit, Postfit, and Ratio yields in the VBF SRs.

Region	Sample	Prefit	Postfit	Ratio
boosted low-p_T IP-IP, low d_0^{sig}	$Z \to \tau\tau$	40.1483 ± 4.2302	38.9811 ± 2.6014	0.97 ± 0.12
	Fake	9.3900 ± 2.0443	11.2381 ± 1.1949	1.20 ± 0.29
	$H \to \tau\tau$	1.9289 ± 0.9117	1.8955 ± 0.2968	0.98 ± 0.49
	Others	3.2953 ± 1.2181	2.7513 ± 0.3906	0.83 ± 0.33
	Total	54.7626 ± 4.9385	54.8661 ± 2.9044	1.00 ± 0.10
	Data	46^{+7}_{-7}		
	Data/Total	$0.8544^{+0.1499}_{-0.1579}$	$0.8528^{+0.1360}_{+0.1448}$	
boosted low-p_T IP-IP, high d_0^{sig}	$Z \to \tau\tau$	7.9203 ± 1.8086	9.0827 ± 0.9400	1.15 ± 0.29
	Fake	2.7572 ± 1.1528	3.9106 ± 0.5460	1.42 ± 0.63
	$H \to \tau\tau$	0.8404 ± 0.5991	1.0314 ± 0.2015	1.23 ± 0.91
	Others	0.6992 ± 0.5731	0.7281 ± 0.1209	1.04 ± 0.87
	Total	12.2171 ± 2.2995	14.7528 ± 1.1122	1.21 ± 0.24
	Data	18^{+5}_{-4}		
	Data/Total	$1.4851^{+0.5077}_{-0.4524}$	$1.2298^{+0.3630}_{+0.3089}$	
boosted low-p_T IP-ρ, low $d_0^{\mathrm{sig}}/Y_\pm$	$Z \to \tau\tau$	101.2684 ± 6.8028	108.0141 ± 5.4232	1.07 ± 0.09
	Fake	54.5498 ± 4.8458	72.2544 ± 5.2911	1.32 ± 0.15
	$H \to \tau\tau$	7.9289 ± 1.8829	8.0741 ± 0.7565	1.02 ± 0.26
	Others	10.3228 ± 2.1005	10.3306 ± 1.2648	1.00 ± 0.24
	Total	174.0699 ± 8.8158	198.6731 ± 7.7188	1.14 ± 0.07
	Data	204^{+14}_{-13}		
	Data/Total	$1.1722^{+0.1035}_{-0.0992}$	$1.0270^{+0.0843}_{+0.0802}$	
boosted low-p_T IP-ρ, high $d_0^{\mathrm{sig}}/Y_\pm$	$Z \to \tau\tau$	52.1027 ± 4.8774	54.5716 ± 3.1305	1.05 ± 0.11
	Fake	16.9405 ± 2.8504	21.1293 ± 1.8142	1.25 ± 0.24
	$H \to \tau\tau$	3.6184 ± 1.2640	3.4037 ± 0.3733	0.94 ± 0.34
	Others	3.3227 ± 1.3010	3.9894 ± 0.7401	1.20 ± 0.52
	Total	75.9844 ± 5.9333	83.0940 ± 3.7119	1.09 ± 0.10
	Data	83^{+10}_{-9}		
	Data/Total	$1.0934^{+0.1576}_{-0.1478}$	$0.9998^{+0.1291}_{+0.1191}$	
boosted low-p_T $\rho-\rho$, low Y_+Y_-	$Z \to \tau\tau$	72.5232 ± 5.6717	75.5732 ± 4.1704	1.04 ± 0.10
	Fake	48.7751 ± 4.7024	62.4363 ± 4.7483	1.28 ± 0.16
	$H \to \tau\tau$	5.8768 ± 1.6147	6.0687 ± 0.5821	1.03 ± 0.30
	Others	11.0772 ± 2.2530	9.6750 ± 1.9378	0.87 ± 0.25
	Total	138.2523 ± 7.8717	153.7532 ± 6.6357	1.11 ± 0.08
	Data	151^{+12}_{-12}		
	Data/Total	$1.0959^{+0.1086}_{-0.1088}$	$0.9854^{+0.0905}_{+0.0907}$	
boosted low-p_T $\rho-\rho$, high Y_+Y_-	$Z \to \tau\tau$	69.1509 ± 5.6011	70.3258 ± 3.9322	1.02 ± 0.10
	Fake	30.0191 ± 3.5771	37.7102 ± 3.0774	1.26 ± 0.18
	$H \to \tau\tau$	4.9807 ± 1.4942	5.1260 ± 0.5096	1.03 ± 0.33
	Others	8.0172 ± 1.8532	5.8816 ± 1.4942	0.73 ± 0.25
	Total	112.1679 ± 7.0594	119.0435 ± 5.2369	1.06 ± 0.08
	Data	113^{+10}_{-10}		
	Data/Total	$1.0131^{+0.1133}_{-0.1153}$	$0.9546^{+0.0977}_{+0.0998}$	

Table G.4: Prefit, Postfit, and Ratio yields in the boosted low-p_T SRs.

Region	Sample	Prefit	Postfit	Ratio
boosted high-p_T IP-IP, low d_0^{sig}	$Z \to \tau\tau$	13.0651 ± 2.3626	13.3932 ± 1.3751	1.03 ± 0.21
	$H \to \tau\tau$	1.8791 ± 0.9257	1.6420 ± 0.3519	0.87 ± 0.47
	Others	2.6028 ± 1.1132	2.8026 ± 0.5523	1.08 ± 0.51
	Total	17.5470 ± 2.7709	17.8378 ± 1.5231	1.02 ± 0.18
	Data	17^{+5}_{-4}		
	Data/Total	$0.9796^{+0.3250}_{-0.2884}$	$0.9636^{+0.2929}_{+0.2532}$	
boosted high-p_T IP-IP, high d_0^{sig}	$Z \to \tau\tau$	5.4416 ± 1.5385	6.0963 ± 0.7478	1.12 ± 0.35
	$H \to \tau\tau$	0.7942 ± 0.6073	0.8333 ± 0.2603	1.05 ± 0.87
	Others	0.2438 ± 0.2977	0.2099 ± 0.0824	0.86 ± 1.10
	Total	6.4797 ± 1.6806	7.1396 ± 0.7961	1.10 ± 0.31
	Data	8^{+3}_{-3}		
	Data/Total	$1.3755^{+0.5885}_{-0.6708}$	$1.2483^{+0.4470}_{+0.5340}$	
boosted high-p_T IP-ρ, low $d_0^{sig}/Y_\pm$	$Z \to \tau\tau$	34.3791 ± 3.8616	36.1620 ± 2.2917	1.05 ± 0.14
	Fake	1.1623 ± 0.7399	1.0902 ± 0.2014	0.94 ± 0.62
	$H \to \tau\tau$	5.4459 ± 1.5882	5.2333 ± 0.5535	0.96 ± 0.30
	Others	4.5334 ± 1.4645	4.6554 ± 0.7920	1.03 ± 0.37
	Total	45.5207 ± 4.4863	47.1409 ± 2.4952	1.04 ± 0.12
	Data	47^{+7}_{-7}		
	Data/Total	$1.0489^{+0.1882}_{-0.1960}$	$1.0128^{+0.1610}_{+0.1694}$	
boosted high-p_T IP-ρ, high $d_0^{sig}/Y_\pm$	$Z \to \tau\tau$	24.0755 ± 3.3967	24.5684 ± 1.8131	1.02 ± 0.16
	Fake	0.9920 ± 0.7226	0.9493 ± 0.2127	0.96 ± 0.73
	$H \to \tau\tau$	3.0687 ± 1.1351	2.9744 ± 0.3459	0.97 ± 0.38
	Others	2.1594 ± 1.0073	1.9821 ± 0.4860	0.92 ± 0.48
	Total	30.2956 ± 3.7898	30.4743 ± 1.9205	1.01 ± 0.14
	Data	28^{+6}_{-5}		
	Data/Total	$0.9246^{+0.2392}_{-0.2089}$	$0.9192^{+0.2161}_{+0.1824}$	
boosted high-p_T $\rho-\rho$, low Y_+Y_-	$Z \to \tau\tau$	26.3554 ± 3.4548	28.8503 ± 2.0375	1.09 ± 0.16
	Fake	2.4276 ± 1.0066	3.8865 ± 0.8103	1.60 ± 0.74
	$H \to \tau\tau$	4.5370 ± 1.4180	4.7188 ± 0.4356	1.04 ± 0.34
	Others	3.4009 ± 1.2265	3.8421 ± 0.6742	1.13 ± 0.45
	Total	36.7210 ± 4.0576	41.2977 ± 2.3351	1.12 ± 0.14
	Data	45^{+7}_{-6}		
	Data/Total	$1.2309^{+0.2467}_{-0.2316}$	$1.0945^{+0.1932}_{+0.1778}$	
boosted high-p_T $\rho-\rho$, high Y_+Y_-	$Z \to \tau\tau$	69.1509 ± 5.6011	70.3258 ± 3.9322	1.02 ± 0.10
	Fake	30.0191 ± 3.5771	37.7102 ± 3.0774	1.26 ± 0.18
	$H \to \tau\tau$	4.9807 ± 1.4942	5.1260 ± 0.5096	1.03 ± 0.33
	Others	8.0172 ± 1.8532	5.8816 ± 1.4942	0.73 ± 0.25
	Total	112.1679 ± 7.0594	119.0435 ± 5.2369	1.06 ± 0.08
	Data	113^{+10}_{-10}		
	Data/Total	$1.0131^{+0.1133}_{-0.1153}$	$0.9546^{+0.0977}_{+0.0998}$	

Table G.5: Prefit, Postfit, and Ratio yields in the boosted high-p_T SRs.

G.3 Supplementary plots from the fit to 2015+2016 data

G.3.1 Results from a fit with unconstraint μ and systematic uncertainties

Figure G.8 shows a comparison of the ΔNLL curves with fixed and floating/variable $H \to \tau\tau$ signal strength in the maximum likelihood fit to data including all systematic uncertainties. From these distributions, it can be seen that the variation of μ in Fig. G.8 (c) leads to a slightly smaller uncertainty on ϕ_τ. The $H \to \tau\tau$ signal strength is scaled up the most at angles ϕ_τ close the one minimum of the ΔNLL curve and scaled down the most for angles $\phi_\tau^{\mathrm{min}} \pm 90$ in order to minimise the disagreement between data and expectation in all cases.

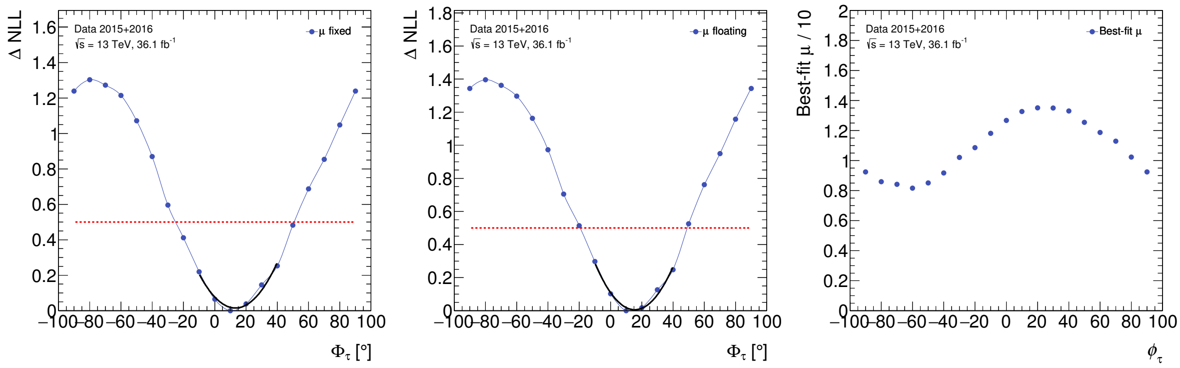

(a) ΔNLL curve (fixed μ) (b) ΔNLL curve (floating μ) (c) μ distribution (floating μ)

Figure G.8: ΔNLL curve for the fit to φ^*_{CP} combining all decay modes using data with a constant $H \to \tau\tau$ signal strength μ including systematic and statistical uncertainties.

G.3.2 Pull distribution for $\phi_\tau = 90^\circ$

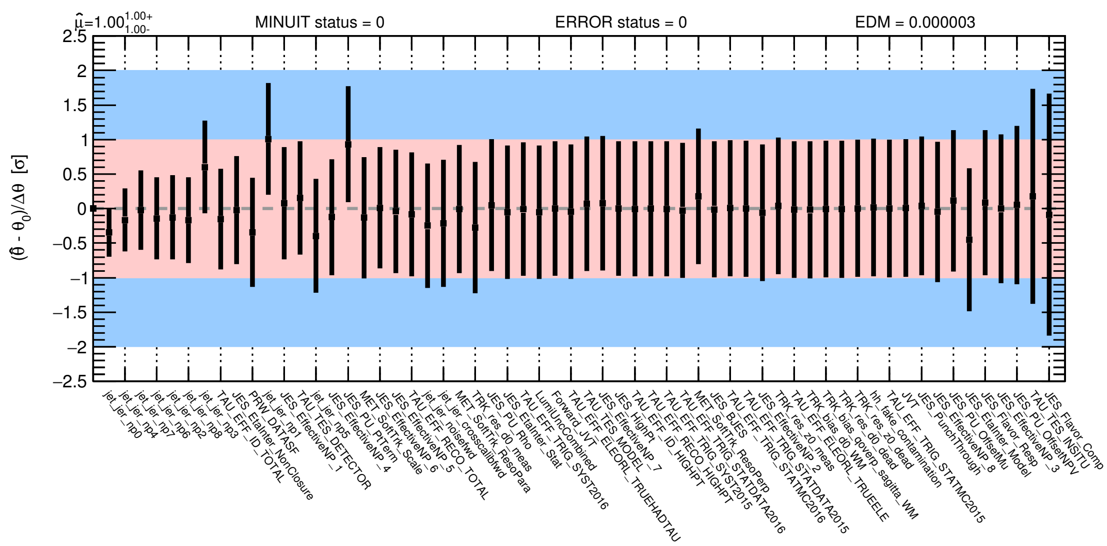

Figure G.9: Pull distribution of all NPs included in the fit sorted by their constraint for $\phi_\tau = 90^\circ$.

G.4 ΔNLL curves, uncertainties and weights from separate fits to each SR

A separate fit of the CP mixing angle is performed to each φ^*_{CP} SR using Asimov data in order to determine the region-specific weights applied in the combination of all φ^*_{CP} distributions. The resulting $-\log \mathcal{L}$ curves as a function of the CP-mixing angle are displayed in Figs. G.10 to G.12.

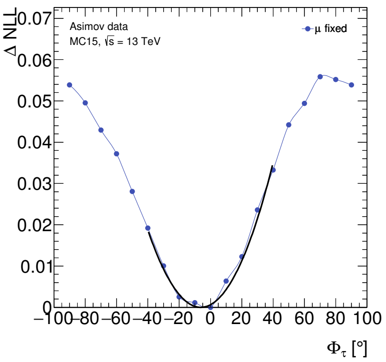

(a) IP-IP

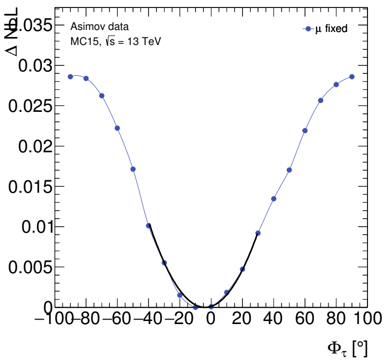

(b) IP-ρ

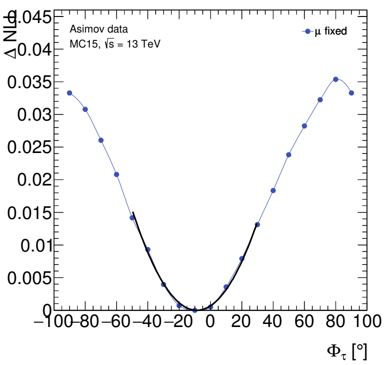

(c) $\rho - \rho$ (high Y_+Y_-)

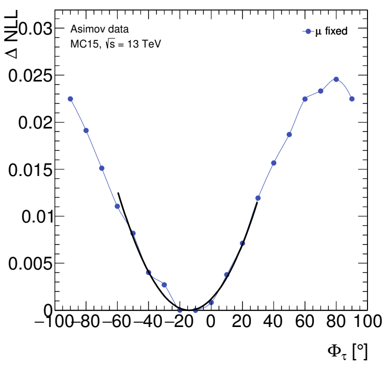

(d) $\rho - \rho$ (low Y_+Y_-)

Figure G.10: $-\log \mathcal{L}$ vs CP mixing angle from separate fits for the VBF signal regions

For each likelihood curve, a parabola is fitted around the minimum and the 1σ uncertainty to the respective result is derived from the width of this parabola at $-\log \mathcal{L} = 0.5$. The inverse square of the resulting 1σ uncertainties is used as weight to the respective region in the combined φ^*_{CP} plot. The uncertainties and the calculated weights are listed in Table G.6.

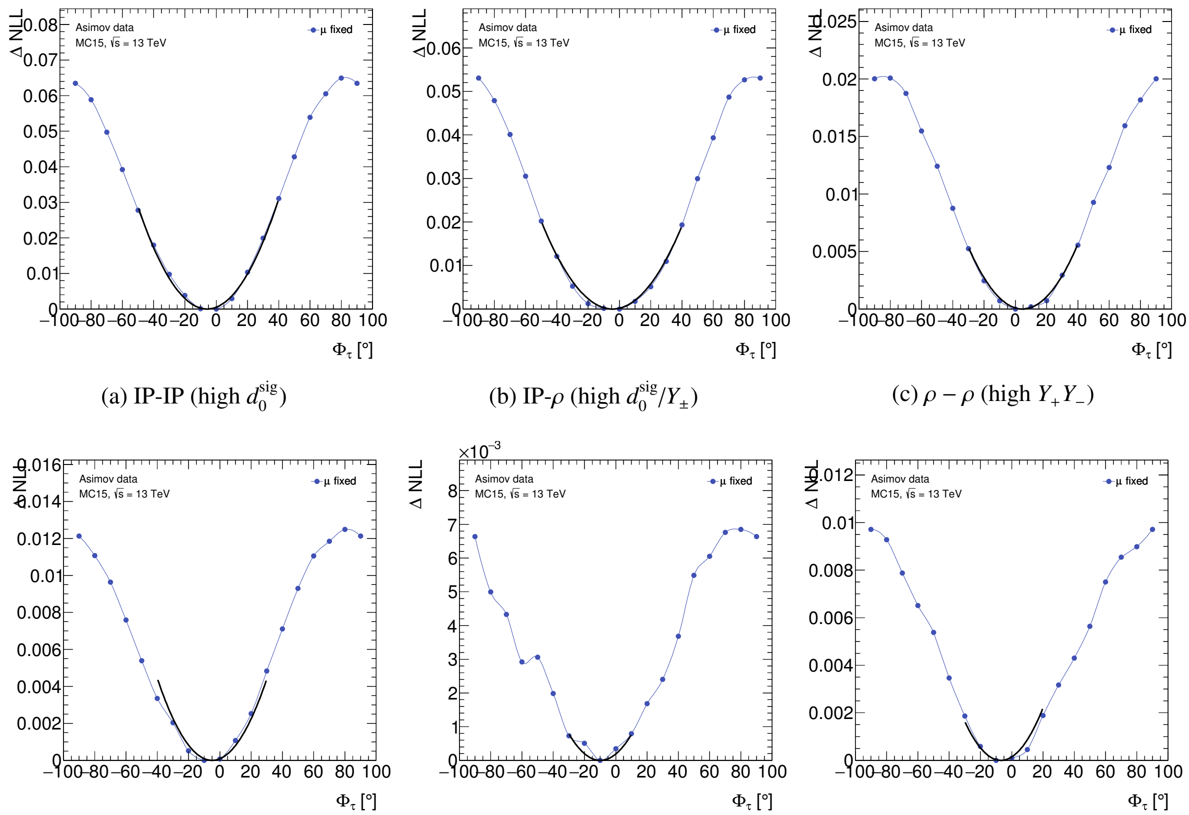

(a) IP-IP (high d_0^{sig}) (b) IP-ρ (high $d_0^{\mathrm{sig}}/Y_{\pm}$) (c) $\rho - \rho$ (high $Y_+ Y_-$)

(d) IP-IP (low d_0^{sig}) (e) IP-ρ (low $d_0^{\mathrm{sig}}/Y_{\pm}$) (f) $\rho - \rho$ (low $Y_+ Y_-$)

Figure G.11: $-\log \mathcal{L}$ vs CP mixing angle from separate fits for the boosted low-p_{T} signal regions

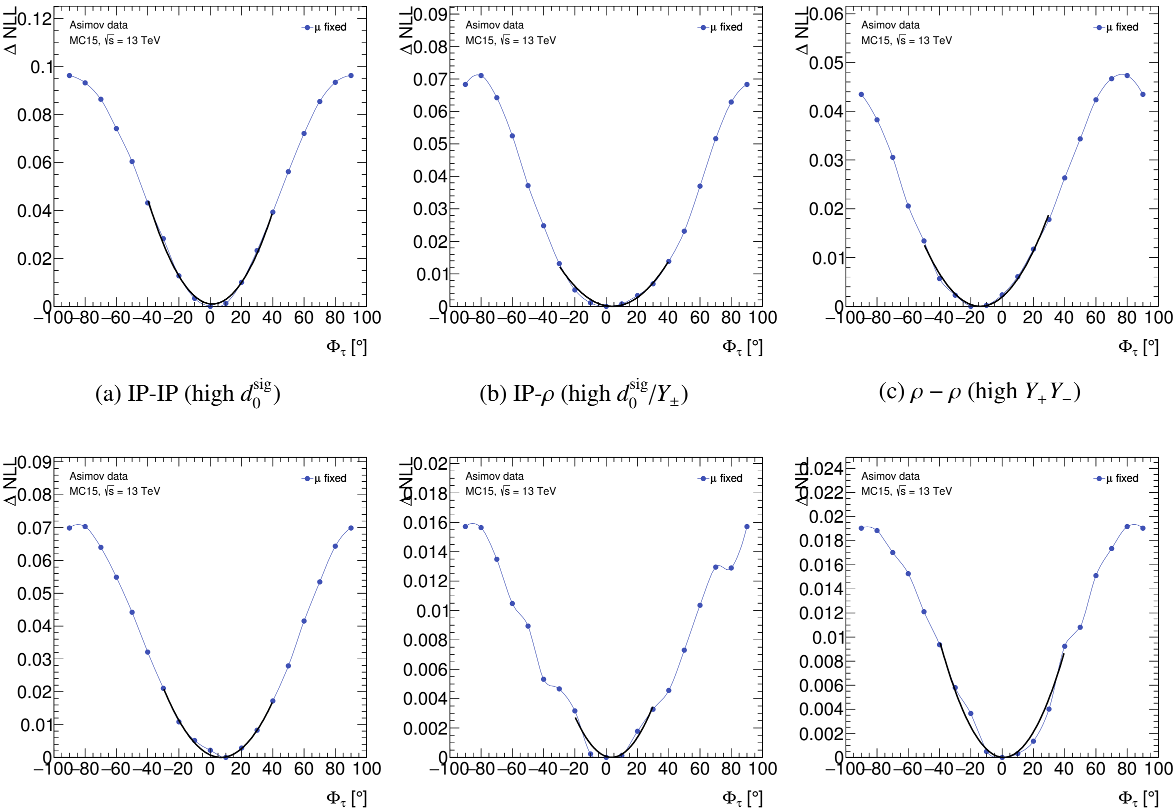

(a) IP-IP (high d_0^{sig})

(b) IP-ρ (high $d_0^{\mathrm{sig}}/Y_\pm$)

(c) $\rho-\rho$ (high Y_+Y_-)

(d) IP-IP (low d_0^{sig})

(e) IP-ρ (low $d_0^{\mathrm{sig}}/Y_\pm$)

(f) $\rho-\rho$ (low Y_+Y_-)

Figure G.12: $-\log\mathcal{L}$ vs CP mixing angle from separate fits for the boosted high-p_T signal regions

region	1σ	weight
boosted high-p_T IP-IP, high d_0^{sig}	139	0.0000517571554267377
boosted high-p_T IP-IP, low d_0^{sig}	179	0.0000312100121719047
boosted low-p_T IP-IP, high d_0^{sig}	184	0.0000295368620037807
boosted low-p_T IP-IP, low d_0^{sig}	372	0.00000722626893282464
VBF IP-IP	174	0.0000330294622803541
boosted high-p_T IP-ρ, high $d_0^{sig}/Y_\pm$	215	0.0000216333153055706
boosted high-p_T IP-ρ, low $d_0^{sig}/Y_\pm$	315	0.0000100781053162006
boosted low-p_T IP-ρ, high $d_0^{sig}/Y_\pm$	227	0.0000194065477692173
boosted low-p_T IP-ρ, low $d_0^{sig}/Y_\pm$	507	0.00000389030885161973
VBF IP-ρ	247	0.000016391024275107
boosted high-p_T $\rho-\rho$, high Y_+Y_-	225	0.0000197530864197531
boosted high-p_T $\rho-\rho$, low Y_+Y_-	294	0.0000115692535517608
boosted low-p_T $\rho-\rho$, high Y_+Y_-	333	0.00000901802703604505
boosted low-p_T $\rho-\rho$, low Y_+Y_-	404	0.00000612685030879326
VBF $\rho-\rho$, high Y_+Y_-	235	0.0000181077410593029
VBF $\rho-\rho$, low Y_+Y_-	287	0.0000121404897473564

Table G.6: 1σ uncertainties and weights derived from separate fits to each signal region.

List of Figures

List of Tables

Acknowledgements

During my time at the Physics Institute in Bonn I received support from many people for which I am very thankful. In particular I show my gratitude to Prof. Dr. Klaus Desch for giving me the opportunity to work in his research group, for his support throughout my whole scientific career and for sharing his knowledge and expertise with me.

I am also very grateful to Prof. Dr. Ian Brock for his encouragement especially during my ATLAS qualification task and all the valuable discussions we had. No less I thank Priv. Doz. Dr. Philip Bechtle for all the inspiring discussions, Dr. Christian Grefe for always supporting and motivating me, and Dr. Peter Wagner for all the scientific exchange. I also acknowledge the constructive collaboration with Dr. Stefan Berge on the theoretical foundation of this measurement. I thank all my colleagues for the wonderful time in this research group, their support and all the fruitful conversations we had. In particular, I want to thank Michael Hübner and Alina Manthei.

I am grateful to Prof. Dr. Herbert Dreiner for the amazing physics shows we performed together and for fascinating me for outreach. I also want to thank Dr. Barbara Valeriani-Kaminski for her support and the inspiring collaboration in outreach.

Last but not least, I want to thank my family and friends for their endless support and for just being there. A special thanks to my husband for his patience and endless encouragement and to my daughter for her patience, especially during the last period of my thesis. I am very grateful to my mother for always believing in me and supporting me as well as to my brother for encouraging me wherever needed.